Ingo Sänger

Magnetic - Field - Induced
Second Harmonic Generation
in Semiconductors and Insulators

Magnetic - Field - Induced Second Harmonic Generation in Semiconductors and Insulators

Dissertation

presented to the Institute of Physics of the University of Dortmund, Germany, in partial fulfilment of the requirements for the degree of Doktor rer. nat.

presented by

Ingo Sänger

Dortmund, March 2006

Accepted by the faculty of the Institute of Physics of the University of Dortmund, Germany.

Day of the oral exam: 12th May 2006

Examination board:

Priv.-Doz. Dr. Dmitri R. Yakovlev

Prof. Dr. Metin Tolan

Prof. Dr. Bernhard Spaan

Dr. Vasily Temnov

Contents

Motivation

Since the invention of lasers in the 1960s, nonlinear optical techniques established a new field of research [1, 2, 3, 4]. Although the second harmonic generation (SHG) is the lowest-order nonlinear process, it can provide a lot of important information about the electronic and magnetic structure of solids [5, 6, 7]. With its larger number of degrees of freedom SHG reveals new and complementary information in comparison to linear optics [8, 9, 10]. The leading-order contribution to SHG induced by the interaction of light and matter can be described in the electric-dipole (ED) approximation. This process is forbidden in non-centrosymmetric crystals from the symmetry point of view [3, 8, 7]. Especially in the case of centrosymmetric materials the SHG process can be sensitive to surfaces or interfaces due to the breaking of the inversion symmetry at the boundary [11, 12, 13, 14]. Beside the optical degrees of freedom as spectral, spatial or temporal resolution as well as the choice of light polarization, external perturbations can provide additional degrees of freedom in order to study electronic or magnetic properties. Usually perturbations of the material system are introduced by means of applied electric or magnetic fields or external pressure. In the case of an applied electric field, which is described by a polar vector, the inversion symmetry is broken in any case. As a result of the reduced symmetry, the generation of an electric-field-induced second harmonic (EFISH) contribution becomes allowed [15], which enables to probe the charge of the electrons. Due to their axial nature, an applied magnetic field or a spontaneous magnetic ordering break the time-inversion symmetry. This breaking of the symmetry leads to a magnetic-field-induced second harmonic (MFISH) [16, 17] or a magnetic second harmonic (MSHG) [7] contribution, respectively, which provides an opportunity to probe the spin of the electrons. A complementary use of MFISH and EFISH as sensors to spin and charge enables to study both, charge and spin properties, by means of nonlinear optics.

A recent field of research are spin phenomena and their possible applications in e.g. spintronics and quantum computation [18, 19]. Big research effort is not only made to develop technological applications in electronics and optoelectronics, but also for fundamental study of spin phenomena. Most of the fundamental studies of optical spin manipulation are accomplished by using linear optical techniques as e.g. magneto-optical spectroscopy [20, 21, 22]. Applications of nonlinear magneto-optical techniques to this field are scarce. In order to discover nonlinear spin effects, detailed studies are required. For this purpose especially the nonlinear techniques of MFISH and EFISH might be promising tools to study charge and spin phenomena. In this work the novel technique of MFISH is used to probe the spin properties of semiconductors (GaAs,

CdTe and (Cd,Mn)Te) and isolators (CuB_2O_4 and NiO).

One of the main foci of this work is the study of the magnetic properties of semiconductors. Up to now, semiconductors have been probed by SHG only under restricted experimental conditions (single optical wave lengths, room temperature and without application of magnetic fields). However, examples of SHG over a wide spectral range are scarce [23, 24]. Only recently, studies of SHG over wide spectral ranges at low temperatures and supplementary application of a magnetic field were reported [16, 25]. Broad spectral features near the band gap related to magnetic ordering have been found in the ferromagnetic semiconductor (Ga,Mn)As [26]. Theoretical calculations can be only found for crystallographic SHG susceptibilities [27, 28, 29], but for SHG in semiconductors in an applied magnetic field theoretical calculations are still missing.

A possible classification of semiconductors can be given according to their magnetic properties, which are of main interest for this work. Undoped semiconductors with a spin-compensated atomic or ionic structure as e.g. Si, Ge, GaAs and CdTe are diamagnets. The interaction with a magnetic field is rather weak and determined mostly by orbital magnetic momentums [30]. Semiconductors doped with magnetic impurities, which contribute uncompensated spins, can reveal possible paramagnetic behavior. The interaction of a paramagnet with a magnetic field is much stronger than for a diamagnet and is determined mostly by the magnetic momentums of the uncompensated spins. As a consequence of the different microscopic mechanisms the signs of the magnetic susceptibilities are opposite for dia- and paramagnets. In this work, amongst others, the material system (Cd,Mn)Te was chosen by two reasons. On the one hand the dilution with Mn ions induces via exchange interaction a giant Zeeman splitting of the valence and conduction bands, which can raise up to about 120 meV depending on the Mn concentration. On the other hand, without Mn, CdTe provides a diamagnetic reference system. Another class is given by magnetically ordered semiconductors. Here the exchange interaction can lead to a possible ferromagnetic or antiferromagnetic ordering below a critical temperature. Magnetic semiconductors revealed a plenty of new electronic, magnetic and optical properties. Exemplarily, unusually large magneto-optical effects as giant Faraday rotation [31] or nonreciprocal linear birefringence in the Voigt configuration [32] are observed.

Another focus of this work is on the investigation of long-range magnetically ordered materials. Due to its possible macroscopic spontaneous magnetization, ferromagnetism was discovered and practically used even two millennia ago. One of the oldest application is the use of magnetite crystals (Fe_3O_4) as compass needles. In our day ferromagnetic properties are exploited e.g. to convert kinetic energy into electric current and vice versa via generators and motors, respectively. Another application of ferromagnetism is the data storage. All these effects are based on the macroscopic magnetization in ferromagnets. In opposite to ferromagnetism, antiferromagnetism was predicted first by Néel in 1932 [33] and demonstrated by Bizette, Squire and Tsai in 1938 [34]. Since antiferromagnets do not possess a macroscopic magnetization, a technical application was not considered for a long time. Nowadays the importance of antiferromagnetic compounds for practical applications has increased strongly. Examples for applications of antiferromagnetic systems are mostly on the field of data storage and based on

the exchange bias effect [35]. Furthermore antiferromagnetic materials are expected to enable fast spin manipulation since no magnetization is present [36]. Another example are high-temperature superconductors, which reveal also antiferromagnetic phases in their magnetic phase diagrams [37].

As examples for antiferromagnetic insulators, copper borate and nickel oxide are chosen to study the magnetic properties by means of SHG. Nickel oxide is one of the most promising antiferromagnetic materials for device application. An important application is the data storage using the exchange bias effect [35]. The effect of exchange bias is based on the directional coupling between the spins in an antiferromagnet and those in an adjacent ferromagnet. The development of magnetic read heads [38] and magnetic memory cells [39] was already reported. Furthermore the ultrafast manipulation of the antiferromagnetic order parameter of NiO is very promising [40, 41]. In the case of copper borate no device application is in sight yet. Nevertheless it possesses a rather complicated magnetic structure with different magnetic phases and thus is a good material to point out the power of the MFISH technique to investigate antiferromagnetic ordering phenomena.

Outline

In Ch. 1, a brief review of some important topics of magnetism in solids, semiconductor physics and nonlinear optics is given.

In Ch. 2, a study of magnetic-field-induced second harmonic generation (MFISH) in the diamagnetic III-V and II-VI semiconductors gallium arsenide (GaAs) and cadmium telluride (CdTe) over broad spectral ranges and at varying temperatures is presented [16, 42, 43]. The applied magnetic field breaks the time-inversion symmetry of a diamagnetic compound and induces new optical nonlinearities. SHG spectra with complicated polarization properties and characteristic magnetic-field and temperature dependencies are observed. The rotational anisotropy of the SHG signal distinctly differs from that of the electric-dipole approximation. It will be shown by model calculations, that the MFISH process is based on nonlinear magneto-optical spatial-dispersion and the electric-dipole term. In diamagnetic semiconductors, the Zeeman splitting is much smaller than the Landau-level splitting and the dominant SHG mechanism is based on the Landau-orbital quantization, whereas the SHG intensity depends quadratically on the applied magnetic field.

In Ch. 3, MFISH in the diluted magnetic semiconductor cadmium manganese telluride ($Cd_{1-x}Mn_xTe$) is investigated [44, 45, 46]. In opposite to the MFISH mechanism in diamagnetic semiconductors, in paramagnetic semiconductors a new mechanism based on the spin quantization and giant Zeeman splitting of electronic states is found. The interplay of both mechanisms is studied as a function of the Mn concentration. By contrast to linear optics, the complete set of eight possible electronic transitions between different spin-states of the valence and conduction bands is observed in $Cd_{1-x}Mn_xTe$ using MFISH. It will be shown, that the MFISH intensity is proportional to the magnetization induced by an applied magnetic field. Subsequently, MFISH will be used to study spin glass phase magnetic properties.

In Ch. 4, the complex magnetic structure of the antiferromagnetic compound copper borate (CuB_2O_4) is investigated by linear and (more detailed) by nonlinear optical techniques [25, 47, 7, 48]. Three different types of optical magnetic-field-induced second harmonic (MFISH) generation are observed in CuB_2O_4. Unusually sharp and intense electronic transitions in MFISH and linear absorption spectra provide selective access to the two non-equivalent Cu^{2+} sublattices. The magnetic phase diagram for both sublattices is determined by MFISH. The magnetic structure is dominated by antiferromagnetic order at the 4b site. The magnetic ordering is transferred via sublattice interactions to the 8d site where it coexists with a discoupled paramagnetic component.

In Ch. 5, the distribution of antiferromagnetic S and T domains in NiO is investigated by optical magnetic second harmonic generation (MSHG) [49, 7]. The anisotropy of the MSHG signal from individual domains and from typical superpositions of domains in NiO is derived from symmetry considerations. Subsequently, experiments on two types of samples are discussed. Untreated NiO samples possess a random distribution of all S and T domains with a lateral size in the order of $\lesssim 1 \ \mu$m. NiO samples annealed in oxygen possess a distribution of T domains of $\sim 100 \ \mu$m make up by a random distribution of the three corresponding S domains of $\lesssim 1 \ \mu$m is observed. Next to a T domain wall large S domains of $\sim 10 \ \mu$m are formed because of a tendency of the Ni^{2+} spins to orient along the stacking direction of ferromagnetic planes in the adjacent T domain. Considering practical application, correlations between the ultrafast magnetization dynamics [40] and the density of domain walls can be of big importance. Therefore MSHG is not only an alternative technique for probing domain structures in NiO, but indispensable for studying contemporary aspects of antiferromagnetism.

Chapter 1

Introduction

In this section an introduction to the physical basis of this work is provided. Magnetism in solids and semiconductor basics are of capital importance for this work. Furthermore the experimental technique of nonlinear optics is considered.

1.1 Magnetism

Magnetism in matter originates mainly from the magnetic moments of the electrons. Thereby the spin and the orbital momentum contribute to the magnetism. In opposite to electrons the magnetic moments of the nucleons are negligible compared to the magnetic moments of electrons, which is a result of the mass difference between neutrons or protons and electrons. In this Chapter the magnetism resulting from localized ionic magnetic moments will be discussed. A consideration of the magnetic properties induced by free carriers is given in Ch. 1.2. According to Hund's rule the atomic orbitals of the ions building up the crystal are filled with electrons, whereas electronic spins can partly compensate each other. Thus only partially filled orbitals with unpaired electrons can result in a magnetic moment of the ion [30].

1.1.1 Disordered magnetic systems

In the case of absent long-range interaction between the magnetic moments and without an external magnetic field, a system of disordered magnetic moments is present. An alignment of such non-correlated magnetic moments is possible by applying an external magnetic field. The dependence of the magnetization $\mathbf{M}$ of the system on the magnetic field strength $\mathbf{H}$ is described by the magnetic susceptibility χ_{mag}:

$$\mathbf{M} = \mu_0 \chi_{mag} \mathbf{H}, \tag{1.1}$$

where μ_0 is the permeability. The magnetic susceptibility varies by orders of magnitude for the different types of magnetism discussed below.

1.1.1.1 Diamagnetism

Diamagnetism can be described by the induction of a circular current by an external magnetic field. The circular current is caused by the Lorentz force acting on the orbital and band electrons of the material. According to Lenz's rule the induced magnetic moments of the electrons are aligned reverse to the applied magnetic field. Therefore the magnetic susceptibility is negative $\chi_{Dia} < 0$. Larmor diamagnetism is a form of magnetism, which is present in all materials and is in the order of magnitude of 10^{-4}. In the case that other forms of magnetism are present in a material, diamagnetism can be neglected. In opposite to other forms of magnetism, diamagnetism does not depend on the temperature. A model of an ideal diamagnet is a superconductor. According to the Meißner-Ochsenfeld effect the magnetic moments fully insulate the external magnetic field. This is described by $\chi_{SC} = -1$.

1.1.1.2 Paramagnetism

Beside diamagnetism other forms of magnetism can exist. The magnetic properties discussed below originate from the magnetic moments of ions possessing only partially filled orbitals. Unpaired electrons of the partially filled orbitals contribute a magnetic moment due to their spin and angular momentum. In the case that no long-range ordering exists, without magnetic field the directions of the magnetic moments are distributed statistically. Due to the statistical distribution the macroscopic average of the magnetic moments vanishes whereby the time-inversion symmetry remains a symmetry of the system. The application of a magnetic field leads to a breaking of the symmetry, since an alignment of the magnetic moments along the magnetic field direction is induced. Paramagnetism is described by a positive magnetic susceptibility $\chi_{Para} > 0$.

The Langevin paramagnetism is based on a model system of free magnetic moments $\mu = g_J \mu_B J$ without interaction. The magnetization can be calculated thermodynamically and is given by

$$M = n g_J \mu_B J B_J(y) \,, \tag{1.2}$$

where n is the number of magnetic moments per unit volume,

$$g_J = 1 + \frac{J(J+1) + S(S+1) - L(L+1)}{2J(J+1)} \tag{1.3}$$

is the Landé factor, J is the total angular momentum and

$$B_J(y) = \frac{2J+1}{2J} \coth(\frac{2J+1}{2J}y) - \frac{1}{2J\coth(\frac{y}{2J})} \tag{1.4}$$

is the Brillouin function with the argument $y = \frac{g_J \mu_B J B}{k_B T}$. The special case, that the argument y of the Brillouin function is small, which is fulfilled at high temperature and weak magnetic fields, leads to the classical Curie law

$$\chi_{para} = \frac{C}{T} \,, \tag{1.5}$$

where C is the Curie constant. In the special case of low temperature and high magnetic fields the Brillouin function in Eq. (1.2) amounts to the value 1 and the saturated magnetization is given by $M_S = n g_J \mu_B J$.

In addition, for $J = 0$ Van Vleck paramagnetism exists, which does not depend on the temperature. This contribution is induced by excited states. Since the Van Vleck paramagnetism is weak compared to χ_{para} for $J \neq 0$, it will be not considered here.

Another paramagnetic contribution to the magnetic susceptibility is given by the Pauli paramagnetism, which is important for metals, where the electrons are delocalized.

1.1.2 Ordered magnetic systems

In diamagnetic and paramagnetic materials discussed above, at zero magnetic field the magnetic symmetry coincides with the crystallographic symmetry. In contrast, a spontaneous ordering leads to a reduction of the magnetic symmetry. Long-range interaction causes an collective alignment of the magnetic moments. The time-inversion symmetry is broken, since time-inversion causes a reversal of the spins.

In order to describe the magnetic ordering in ferromagnetic, ferrimagnetic and antiferromagnetic materials, the Heisenberg model [50] will be considered. The Heisenberg model takes into account the exchange interaction between electrons on the basis of the Coulomb interaction and the Pauli principle. The Heisenberg Hamilton operator is given by

$$\hat{H}_{Exchange} = -2 \sum_{i \neq j} J_{ij} \mathbf{S}_i \cdot \mathbf{S}_j \,, \tag{1.6}$$

where J_{ij} is the exchange integral. J_{ij} displays the overlap of the wave functions of two spins located at the lattice sites i and j.

1.1.2.1 Ferromagnetism

In ferromagnetic materials the exchange integral J_{ij} is positive. Thus the exchange energy is minimal in the case of a parallel alignment of the spins. The ferromagnetic susceptibility depends strongly on the temperature. Below a critical temperature T_C, namely the Curie temperature, the spins are aligned ferromagnetically. The order parameter is the magnetization. With raising temperature the order parameter decreases and vanishes at T_C. At T_C a phase transition of second order (no latent heat) [51] occurs. Above T_C paramagnetism is present. Due to the thermal energy above T_C no ordering of the magnetic moments is possible.

Application of a magnetic field leads to an alignment of spins and thus a macroscopic magnetization. The magnetic susceptibility is on the order of magnitude of 10^2-10^6. For $T > T_C$ the temperature dependence of the magnetic susceptibility is given by the Curie-Weiss law

$$\chi = \frac{C}{T - T_C} \,. \tag{1.7}$$

Figure 1.1: *Hysteresis of a ferromagnet below T_C: Dependence of the magnetization M on the magnetic field strength H. M_S: saturated magnetization, M_r: remanent magnetization, H_C: coercive field strength.*
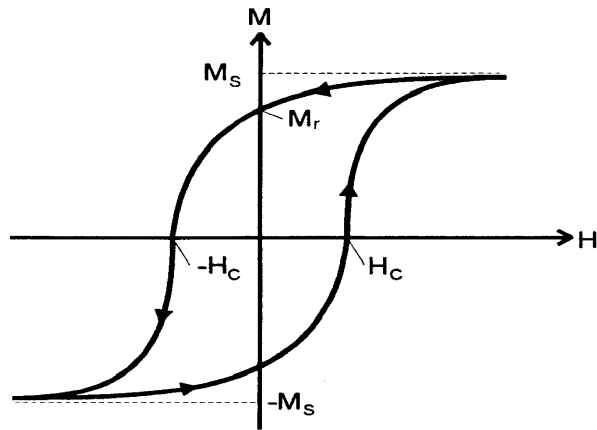
Below T_C a characteristic dependence of the magnetization on the magnetic field strength, namely the hysteresis (B-H curve), can be observed. Fig. 1.1 shows a hysteresis, which is obtained from a periodic variation of the magnetic field. With increasing magnetic field strength the magnetization asymptotically saturates (M_S) and all magnetic moments are aligned along the direction of the magnetic field. After reducing the magnetic field strength to zero, the magnetization M_r remains. The remanent magnetization vanishes at the reverse coercive field strength $-H_C$ or for $T > T_C$. The variation of the magnetization is based on two processes. On the one hand at low magnetic field strengths, where the external magnetic field is applied along one of the crystallographic axes (easy axes), the domain walls are shifted. The shifts of the domain walls increase the size of the domains possessing a magnetization, which is parallel to the magnetic field. On the other hand at high magnetic field strengths, where the magnetic field is not applied parallel to a crystallographic axis, a tilting of the magnetic moments along the direction of the magnetic field is induced.

1.1.2.2 Ferrimagnetism

Ferrimagnetism is observed in materials with at least two ferromagnetically ordered sublattices with opposed magnetization. If the spins of the sublattices do not fully compensate each other, a macroscopic magnetization can be observed. The exchange integral between spins of the same sublattice is positive, whereas the exchange integral between spins of opposed sublattices are negative. Similar to ferromagnetic materials, the formation of domains can lead to a macroscopic magnetization. The order parameter is the magnetization. In opposite to ferromagnetism, in general different temperature dependencies of the magnetization of the sublattices are present. Thus the macroscopic magnetization within the domains might vanish for a compensation temperature [52].

1.1.2.3 Antiferromagnetism

Antiferromagnetism is a special case of ferrimagnetism, where the magnetic moments of the sublattices fully compensate each other within the unit cell. The exchange inte-

gral is negative. In opposite to ferrimagnetism and ferromagnetism, the macroscopic magnetization vanishes in the case of antiferromagnetism.

Above the Néel temperature T_N the paramagnetic phase is present. The temperature dependence of the magnetic susceptibility in the paramagnetic phase is given by

$$\chi = \frac{C}{T + \Theta} \, , \tag{1.8}$$

where C and Θ, the paramagnetic Néel temperature, are material-specific constants. Below the phase transition of second order the spins are aligned antiferromagnetically. Due to the vanishing of the magnetization, the order parameter is defined to be a non-vanishing linear combination of the magnetic moments of the unit cell. This definition is not unique. A constraint for the choice of the magnetic order parameter is that the magnetic order parameter has to possess the same symmetry as the magnetic system. In opposite to the magnetization in ferri- and ferromagnetic materials, the antiferromagnetic order parameter is no physical property.

Beside antiferromagnetism possible ferromagnetic components can be present. The so-called parasitic ferromagnetism results from a slight misalignment or tilting of the antiferromagnetically ordered spins. The weak ferromagnetic susceptibility is on the order of magnitude of 10^{-3}-10^{-5}. Possible explanations are the influence of relativistic effects [53], magnetic impurities [54] or domain walls [55].

A phase transition from the antiferromagnetic to the ferromagnetic phase is described by the metamagnetism, where the spins are aligned along the direction of a strong magnetic field. In opposite to ferromagnetism, the antiferromagnetic exchange interaction is overcome by the magnetic field. This effect requires high magnetic fields on the order of magnitude of 100 T [56].

According to the spin dimensionality n, different models to describe the alignment of the spins are distinguished. Thereby the spin alignment with the minimal exchange energy is formed. The Ising model (n=1) describes a system of spins, where the spins are aligned along one (easy) axis. If the spins are aligned within the (easy) plane, the XY model (n=2) can be used. The Heisenberg model (n=3) describes a three-dimensional spin order. Further models as well as the universality classes of phase transitions are introduced in the Refs. [57, 58, 59].

A frustration of a spin arrangement appears, if no optimal solution for the exchange coupling exists. The antiferromagnetic exchange interaction leads to a minimal exchange energy in the case of antiparallel aligned spins. An example for a frustrated spin arrangement is the triangular arrangement of spins [60] in the one-dimensional Ising model. Thereby only two spins can be aligned antiparallel leading to a minimization of the exchange energy, whereas the orientation of the third spin can not be explained in terms of the exchange energy.

1.1.2.4 Domains

Although in ferromagnetic materials the spontaneous magnetization is saturated below T_C, a vanishing of the macroscopic magnetization is possible. The vanishing of

the macroscopic magnetization can be explained by the presence of domains. Within a domain the spins are saturated, but different domains might have different order parameters, which are correlated to the spin orientations. Thus a compensation of the magnetization of different domains is possible leading to a vanishing macroscopic magnetization. In the case of antiferromagnetic domains, a distinction by means of the antiferromagnetic order parameter is possible. Ferromagnetic and antiferromagnetic domains were postulated by Weiss [61] and Néel [62], respectively. Experimentally ferromagnetic domains were observed by Barkhausen [63], Hondo and Kaya [64] and the existence of antiferromagnetic domains was demonstrated by Slack [65] and Roth [66].

The formation of the domains, e.g. the size and the shape, depends on the total energy of the system [67, 68]. The domain structure, which minimizes the free enthalpy G, is formed. In the following the most important contributions to the free enthalpy are discussed for the ferri- and ferromagnetism:

- The magnetostatic field energy is given by the energy of the magnetic field caused by the magnetization. This contribution raises with the domain size and thus prefers the formation of small domains.

- The exchange energy is calculated by the Heisenberg model and the exchange integral. Due to the coupling of the spins large domains are energetically preferred.

- The wall energy takes into account the transition zones between different domains, which are called Bloch walls in the case of ferromagnetism. Between different domains the magnetization changes within the distance of many lattice constants. In order to overcome the exchange energy the wall energy is required.

- The anisotropy energy results from preferential directions for the magnetization due to the crystallographic structure. The alignment of the spins along such easy axes leads to a lower anisotropy energy. The other way round, a rotation of the magnetization by an applied magnetic field requires anisotropy energy.

- The mechanical tension energy is based on the magnetostriction. The magnetostriction describes the magnetization induced elastic deformation of the crystal structure. The other way round, a manipulation of the domain size by mechanical forces is possible.

In opposite to ferri- and ferromagnetic materials, antiferromagnets possess no magnetization and thus the magnetostatic field energy vanishes. Since the magnetostatic field energy is important for the formation of (small) domains, the explanation of antiferromagnetic domains is more complicated. Some reasons for the formation of antiferromagnetic domains are given in the following:

- The free enthalpy $G \propto -TS$ also depends on the entropy S. A motivating for the formation of small domains is evident for a temperature $T \neq 0$, since an increase of the entropy, which strongly depends on the domain structure, leads

to a decrease of the free enthalpy. The single domain state is most unfavorable from the entropy point of view.

- The formation of antiferromagnetic domains can be explained by the influence of impurities and surface effects on the domain structure. Such pinning effects are expected to be independent of the temperature.

In this work only antiferromagnetic domains are investigated and thus the following discussion is restricted to the distinction and characterization of antiferromagnetic domains [69]. Depending on the material, especially its symmetry, different types of domains, for which the free enthalpy is minimized, have to be considered. From the symmetry point of view, the total number of domains is given by the ratio of the order of the symmetry group of the paramagnetic crystal to that of the antiferromagnetic crystal. Furthermore the domain structure depends on external parameters as temperature or pressure. Also a coexistence of different domain types is possible. In the following different types of domains are distinguished:

- 180° domains always exist paired. The application of the time-inversion transforms both domains into each other. The spins are reversed since time-inversion reverses the spin direction. 180° domains are observed e.g. on chromium oxide [70].

- Orientation domains can exist, if the magnetic group is a subgroup of the crystallographic point group combined with the time-inversion symmetry. The domains are transformed into each other by the symmetry elements of the crystallographic point group, which are not present in the magnetic point group combined with the time-inversion symmetry. Orientation domains are found e.g. in the spin-flop phase in chromium oxide [71].

- Configuration domains can be present, if the magnetic symmetry group is no subgroup of the crystallographic symmetry group.

- Helix domains are given, if the spins are arranged forming a spiral staircase. Helix domains can be distinguished due to the left-handed or right-handed chirality.

- The incommensurate ordering describes a spin order, where the periodicity of the spin lattice does not match with a multiple integer of the crystallographic lattice constant. The spins are not aligned parallel to the lattice vectors. An arrangement of the spins comparable to the structure of the helix domains is possible, where a spiral staircase oriented along the optical axis of the crystal is formed. Incommensurate ordering is found e.g. in copper borate (below 10 K) [72].

1.1.2.5 Experimental techniques to visualize domains

In this section some experimental methods to investigate the domain structure are discussed. Ferromagnetic (and also ferrimagnetic) domains can be visualized e.g. by the

Faraday effect [73]. Different domains can be distinguished due to different orientations of the magnetization by means of the Faraday rotation. Since the Faraday rotation depends on the orientation of the magnetization, the polarization dependence of the transmitted light can be used to identify the domains. If the magnetization is reversed as in the case of 180° domains, the direction of the Faraday rotation is also reverted. In the case of non-transparent materials the Kerr effect can be used.

Due to the absence of a magnetization in antiferromagnetic domains, methods, which couple to the magnetization, are not suitable. An alternative method is the neutron scattering [74, 75]. The neutron scattering is the only method, which provides a direct coupling to the magnetic moments of the spins, since neutrons possess a magnetic moment, but no charge and thus no perturbing Coulomb interaction as in the case of the electron scattering. Disadvantages of the neutron scattering are the low spatial resolution (of domains), which is typically about 100 μm, and the long exposure times, which are required, whereby dynamical effects can not be studied. Alternatively linear optical techniques as the polarization microscopy [76] can be used, but optical techniques do not provide a direct coupling to the magnetic moments. A distinction of antiferromagnetic domains is only possible due to the magnetostrictive deformation of the crystal lattice causing linear birefringence. However, the birefringence can be rather small, which limits the detection and the resolution. The first application of this method was the distinction of the orientation domains in nickel oxide [65, 66]. Another method is the X-ray diffraction technique, which was also applied to nickel oxide [77, 78].

Nonlinear optical techniques, e.g. the polarization dependent second harmonic generation (SHG), are also suitable to distinguish between different domains. The principle of the distinction of different domains is based on the magnetic symmetry of the domains. A macroscopic approach leads to special selection rules, e.g. for the polarization. In Ch. 5 a detailed description of this method is given. An advantage of the nonlinear optical techniques is the high spatial resolution, which is in the order of a few μm and therefore 1 - 2 orders of magnitude higher compared to the technique of neutron diffraction. Also in opposite to neutron diffraction methods, which require high exposure times, the investigation of dynamical properties is possible with nonlinear optical methods. The possibility to distinguish 180° domains is given using phase sensitive nonlinear optical techniques [79, 80]. The basic principle is the interference of the time-noninvariant SHG signal with an external reference (see Ch. 4). Only in the case of a linear coupling of the nonlinear polarization to the antiferromagnetic order parameter, which means that the SHG intensity depends quadratically on the order parameter, 180° domains can not be distinguished according to their definition (see Ch. 5).

1.1.3 Magnetic symmetry

In this section a classification of the symmetry groups, which describe the investigated (magnetic) system, is given. First, point groups and space groups are distinguished [81]. Point groups consider only symmetry operations, which leave one point fixed. Such

symmetry operations are the spatial rotations $SO(3)$, the spatial inversion $\hat{I}$ as well as a combination of both. Space groups additionally include nontrivial spatial translations $T_{3\infty}$, whereas these translations can not be described by a linear combination of the lattice vectors. If the crystallographic symmetries are classified only by spatial rotations, the 11 Laue groups result. With additional inversions, 32 crystallographic point groups have to be considered. Taking into account also non-trivial translations, the 230 crystallographic space groups (Federov groups) are needed to classify the symmetries. In the case of the magnetic symmetries the crystallographic symmetry is broken by the magnetic ordering of the spins. A consideration of three dimensional space is not sufficient. The magnetic moments are classically described by the model of a circular current. The circular motion is described on the basis of the four dimensional space-time model. Thus also the time-inversion operation $\hat{T}$ has to considered. With regard to the time-inversion symmetry, instead of 32 crystallographic point groups one has to distinguish 122 magnetic point groups (Shubnikov groups [82]). Taking into account additionally the nontrivial translations, 1651 magnetic space groups have to be considered. A detailed description of these classifications is given in Refs. [83, 84, 85].

In the majority of cases the symmetries of the optical properties of a crystal are determined by the point group symmetry only. This results from the fact that the dimension of the unit cell is negligible compared to the optical wavelength. Thus the macroscopic properties are invariant with respect to nontrivial translations [86]. For the macroscopic description of the magnetic properties the magnetic point groups are of big importance. The magnetic point groups are divided into uncolored, gray and black-white groups on the basis of the time-inversion symmetry $\hat{T}$, which allow different forms of magnetic ordering:

- The 32 uncolored groups contain all elements of the crystallographic points groups without the time-inversion symmetry. A description of forms of ferri-, ferro- and antiferromagnetic ordering is possible

- The 32 grey groups possess the same symmetry properties as the uncolored groups in combination with the time-inversion symmetry. Due to the time-inversion symmetry, dia- and paramagnetism are allowed for these groups. Ferromagnetism is forbidden since ferromagnetic materials do not possess time-inversion symmetry. Antiferromagnetism is allowed, if a combination of the time-inversion operation with a nontrivial translation is a symmetry element of the magnetic system.

- The 58 black-white groups have to be considered, if only a part of the crystallographic symmetry elements combined with the time-inversion operation is a symmetry operation of the magnetic system. These groups allow ferri-, ferro- and antiferromagnetism.

1.2   Semiconductors

In this section some properties of semiconductors, which are important for this work, will be discussed. First, a general consideration of the electronic band structure will

be given.

In Ch.1.1 the magnetism resulting from electrons, which occupy atomic orbitals according to Hund's rules, is discussed. This model is sufficient to describe magnetism, which results from electrons of inner shells, e.g. for d-electrons of magnetic ions as Cu^{2+} and Ni^{2+} in insulating CuB_2O_4 and NiO, respectively. These atomic states possess discrete energy levels.

In opposite, the discrete atomic energy levels of electrons of outer shells (e.g. the $4s$- and $4p$-states of Ga and As in GaAs) are split in solids, leading to the formation of broad energy bands. Theoretically the band structure can be calculated by different methods as e.g. the pseudo-potential, the tight binding (LCAO) or the $k \cdot p$ method. Taking into account the Pauli principle, the bands are filled with electrons up to the Fermi level. The electronic, magnetic and optical properties of a material depend strongly on this band structure.

1.2.1   Band structure

According to the conductivity, isolators, semiconductors and metals can be distinguished. Isolators possess electronic bands, which are whether completely filled or empty. In addition the energy distance E_g between the uppermost filled band (valence band) and the lowest empty band (conduction band) is large ($E_g \gtrsim 10 \ eV$) and so the electrons cannot be thermally excited from the valence to the conduction band. Due to the Pauli principle, the electrons of the completely filled valence band cannot contribute to the conductivity and a high resistance of $R > 10^{14} \ \Omega \ cm$ results. In metals the bands are partly filled leading to a high number of electrons, which can contribute to the conductivity, and so the resistance $R << 10^{-2} \ \Omega \ cm$ is very low. In semiconductors for T=0 the bands are whether filled or empty as in the case of isolators. In opposite to isolators, the energy gap is in the order of a few eV. Due to the thermal energy, electrons can be excited from the valence to the conduction band and thus the energy bands are whether nearly filled or nearly empty for T$\neq$ 0 and so the resistance $10^{-2} \ \Omega \ cm < R < 10^9 \ \Omega \ cm$ depends strongly on the temperature and possesses values between that of metals and isolators [30].

Semiconductors can possess whether a direct or an indirect band gap. Examples for semiconductor with an indirect band gap are Si and Ge, where the maximum of the valence and the minimum of the conduction band of the band structure $E(k)$ are located at different k values. Thus only phonon assisted optical excitations from the valence to the conduction band are possible with $\hbar\omega_\gamma \approx E_g$, since the impulse conservation law cannot be fulfilled with the (small) photon impulse only. In opposite, direct semiconductors as GaAs and CdTe reveal a maximum of the valence and the minimum of the conduction band of the band structure $E(k)$ at the same k value (Γ point). Thus optical excitations are possible for $\hbar\omega_\gamma \approx E_g$. In this work only direct semiconductors are considered.

Fig. 1.2(a) shows the band structure of GaAs calculated by an empirical tight binding method [87]. A good description of the band structure near the Γ point can
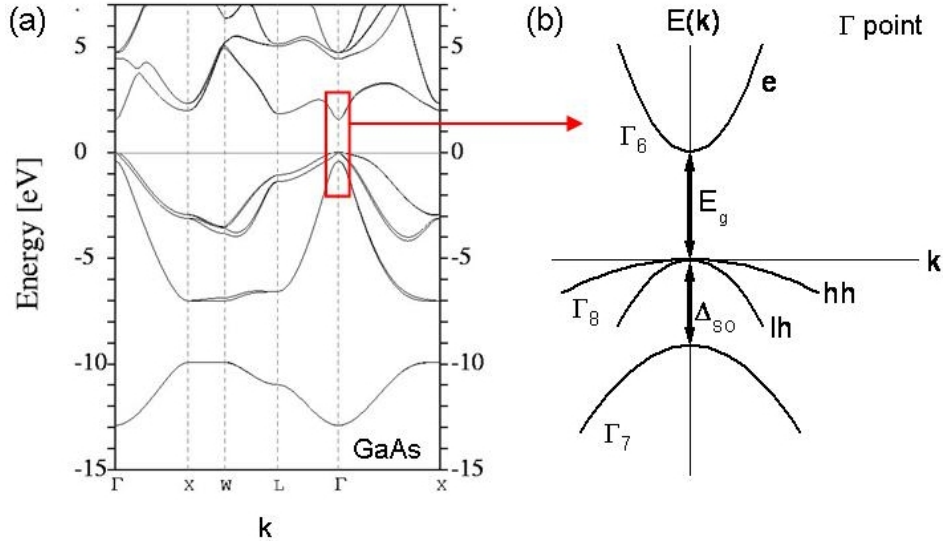
Figure 1.2: *Band structures: (a) Empirical tight binding calculation for GaAs taken from Ref. [87], (b) Parabolic approximation for direct band gap semiconductors in the vicinity of the Γ point.*

be also given by the model of free electrons with effective masses (Fig. 1.2(b)). The dispersion of free electrons is $E(k) = \frac{\hbar^2 k^2}{2m}$. A substitution of the mass m by an effective mass m^* takes into account the influence of the periodic lattice potential on the carriers. The anisotropic effective masses can be determined by the slope of the parabolically approximated bands in the vicinity of the Γ point with

$$\left(\frac{1}{m^*} \right)_{i,j} = \frac{1}{\hbar^2} \frac{d^2 E(k)}{dk_i dk_j} \ , \tag{1.9}$$

where i and j denote cartesian coordinates. In Fig. 1.2(b) the parabolically approximated conduction and valence bands are shown. The conduction band, labelled with e, is mainly formed by the s-type wave functions of the atomic orbitals with $L = 0$ and $S = \frac{1}{2}$ leading to the angular momentum $J = \frac{1}{2}$. The symmetry of the conduction band is Γ_6. The valence bands mainly display the p-type wave functions of the atomic orbitals with $L = 1$ and $S = \frac{1}{2}$ leading to the angular momentums $J = \frac{3}{2}$ for the heavy ($J_z = \pm\frac{3}{2}$) and light ($J_z = \pm\frac{1}{2}$) hole bands and $J = \frac{1}{2}$ for the so-called split-off band. The heavy and light hole bands, labelled with hh and lh, respectively, are described by the symmetry Γ_8, whereas the split-off band has the symmetry Γ_7. Due to the higher mass of the heavy holes, the slope of the heavy hole band is smoother than the slope of the light hole band. The split-off band is separated energetically by Δ_{SO} from the heavy and light hole bands due to the spin-orbit coupling. In the case of large spin-orbit splitting, the Γ_7 band is fully occupied and does not influence the optical properties. Also a wide band gap results in a weak coupling between the conduction and the valence bands. This simplified band structure model provides a basis for understanding the electronic and magnetic properties discussed below.

In this work, on the one hand the magnetic properties of the *insulators* CuB_2O_4 and NiO are investigated. For these insulators, mostly the (inner) 4d-electrons of Cu and Ni reflect the magnetic properties of the material. A consideration of the magnetic moments of the magnetic ions (see Ch.1.1) is sufficient and the band structure of the insulators can be neglected. However, on the other hand the magnetic properties of dia- (GaAs, CdTe) and paramagnetic ($Cd_{1-x}Mn_xTe$) *semiconductors* are studied. Here the consideration of the band electrons is indispensable. Thus in the following free carrier induced magnetic properties as the Landau diamagnetism (Ch. 1.2.3.2) and the $sp-d$ exchange interaction (Ch. 1.2.4) are considered.

1.2.2 Excitons

The excitation of an electron from the completely filled valence band to the empty conduction band of a semiconductor creates an electron-hole pair. If this pair is not separated, then due to Coulomb interaction the quasi-particle known as exciton is formed. Bound electron-hole pairs can propagate within the crystal lattice. The Coulomb interaction between the electron and the hole leads to the exciton binding energy E_{ex}=1..1000 meV, which depends strongly on the material. Exciton energies are below the energy necessary for inter-band excitations. The optical creation of an exciton requires photon energies $\hbar\omega >E_g-E_{ex}$. Two types of excitons can be distinguished. Mott-Wannier excitons possess a low binding energy and thus the averaged distance between the electron and the hole d_{e-h} is large compared to the lattice constant a ($d_{e-h} >> a$). In opposite Frenkel excitons have a large exciton binding energy leading to $d_{e-h} \approx a$.

The two particle problem of the Frenkel excitons in the effective mass approximation can be described by the Schrödinger equation

$$\left[\frac{\mathbf{p}_e^2}{2m_e^*} + \frac{\mathbf{p}_h^2}{2m_h^*} - \frac{e^2}{4\pi\varepsilon_0\varepsilon_r|\mathbf{r}_e - \mathbf{r}_h|}\right] \Psi(\mathbf{r}_e, \mathbf{r}_h) = E\ \Psi(\mathbf{r}_e, \mathbf{r}_h)\,, \qquad (1.10)$$

where the indices e and h denote electrons and holes and ε_r is the static dielectric constant. The dielectric constant takes into account the electrostatic shielding due to the polarizability of the lattice. Analogue to the hydrogen problem a transformation to the relative ($\mathbf{r}$) and the center of gravity ($\mathbf{R}$) coordinates can be performed. Using a separation approach the eigenfunctions can be obtained:

$$\Psi(\mathbf{r}, \mathbf{R}) = \frac{1}{\sqrt{V}} \exp(i\mathbf{K}\mathbf{R})\phi_{nlm}(\mathbf{r})\,, \qquad (1.11)$$

where V is the crystal volume and normalizes the wave functions. The motion of the center of gravity is described by plane waves with the wave vector $\mathbf{K}$. The energy of the center of gravity is given by $\hbar^2\mathbf{K}^2/(2M)$. Analogue to the hydrogen atom the relative motion of the electron and the hole is specified using the relative coordinate $\mathbf{r}$. This leads to the eigenfunctions of the hydrogen atom $\phi_{nlm}(\mathbf{r})$, where $n = 1, 2, 3..$ is the main quantum number, $l = 0, 1, 2, .., n-1$ is the orbital quantum number and
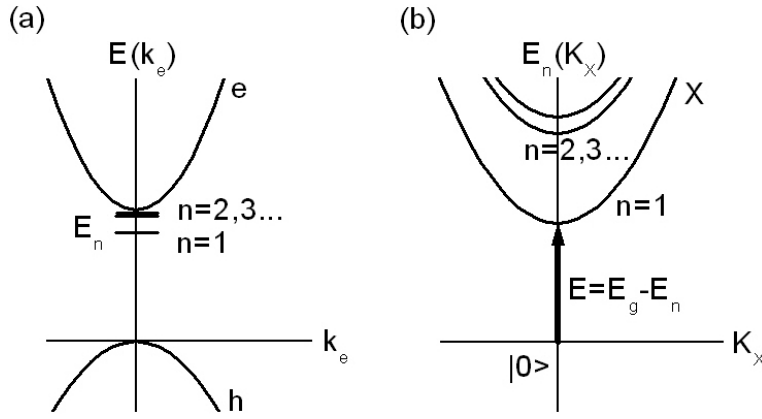
Figure 1.3: *Exciton energy levels at E_g-E_n. (a) Two particle picture (electron, hole): Band structure $E(k_e)$ vs. electron wave vector k_e. Exciton energy levels are schematically shown below the conduction band. (b) One (quasi-)particle picture (exciton): Exciton dispersion $E_n(K_X)$ with exciton wave vector K_X.*

$m = -l, -(l-1), .., 0, .., l-1, l$ is the magnetic quantum number. Thus the eigenvalues of the exciton are given by

$$E_n = E_g - \frac{\mu}{m_e \varepsilon_r^2} \frac{Ryd}{n^2} + \frac{\hbar^2 \mathbf{K}^2}{2M}, \qquad n = 1, 2, 3.., \qquad (1.12)$$

where $Ryd = e^4 m_e / [32(\pi \varepsilon_0 \hbar)^2] = 13.6\ eV$ is the Rydberg constant and $\mu = (1/m_e^* + 1/m_h^*)^{-1}$ is the reduced mass. Only excitons with $\mathbf{K} = 0$ can be excited optically or recombine emitting a photon, which results from the impulse conservation law and the low photon impulse compared to the high impulse of the center of mass of the exciton. Thus the term $\hbar^2 \mathbf{K}^2/(2M)$ in Eq. 1.12 can be neglected.

Fig. 1.3 shows schematically the exciton energy levels and the band structure. The energy distance between the exciton energy levels and the lowest conduction band depends on the main quantum number $n = 1, 2, 3..$. A creation or an annihilation of an exciton is only possible, if the electron and the hole are at the same position ($\mathbf{r}$=0). Therefore only s-like excitons (l=0), which have a non-vanishing probability density at $\mathbf{r}$=0, will be considered here. The exciton binding energy E_{ex} is 4.2 meV in GaAs and 10 meV in CdTe. An observation of the $1s$, $2s$, $3s$.. excitons is possible in absorption and luminescence spectra. From the symmetry point of view, a one-photon transition between the p-like Γ_8 valence band and the s-like Γ_6 conduction band is allowed in the electric-dipole approximation. In opposite this transition is not electric-dipole allowed for a two-photon excitation as e.g. is required for the SHG process investigated in this work. Thus without an external perturbation, s-like excitons can not be probed with two-photon excitations. However, p and d excitons are not accessible by one-photon experiments, but can be visualized in two-photon experiments.

1.2.3   Dia- and paramagnetism of free carriers

Application of a magnetic field to a semiconductor gives rise to various magnetic effects caused by band electrons. In semiconductors as GaAs and CdTe, where no magnetic

Figure 1.4: *Pauli param-agnetism: Sub-bands with spins parallel and antipar-allel to the quantization axis (a) without magnetic field and (b) with mag-netic field. The splitting of the sub-bands leads to a majority of electrons with spins parallel to the direc-tion of the magnetic field (hatched area).*
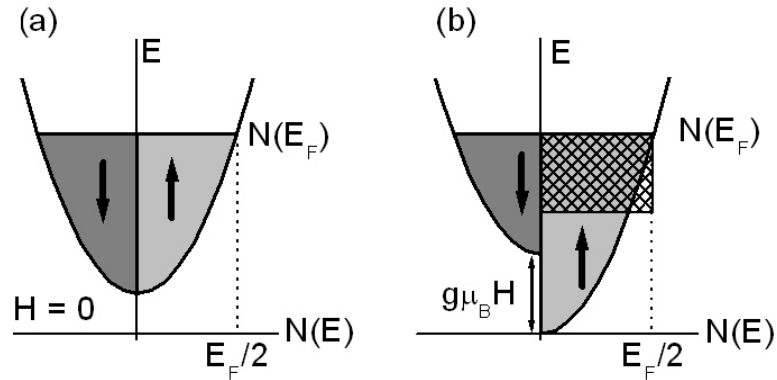
ions are implanted, the free carriers cause Pauli paramagnetism and Landau diamag-netism. A model to describe both effects is the model of the free electron gas. The magnetic moment of a free electron is $\mu_e = \mu_B(g_e S + l)$, where $g_e = 2$ and $S = \pm 1/2$ are the electron g-factor and spin, respectively, and l is the orbital momentum of the free electron. The effect of the orbital momentum of the band electrons will be discussed in Ch.1.2.3.2. First, the spin of the free electrons is considered.

1.2.3.1 Pauli paramagnetism

Pauli paramagnetism results from the spin of the band electrons. Fig. 1.4 shows the electronic density of states $N(E) \propto \sqrt{E}$ with and without magnetic field. Without magnetic field the energy parabola $E \propto N(E)^2$ for spin up and spin down are not shifted against each other, since no spin direction is preferential (Fig. 1.4(a)). In a magnetic field the energy of the electrons with spin parallel to the direction of the magnetic field is decreased in opposite to electrons with antiparallel spin alignment, which is a result of the Zeeman splitting

$$\Delta E_z = g_e \mu_B S H \,. \tag{1.13}$$

A distinction between the sub-bands with electrons possessing spin parallel or antipar-allel to the quantization axis, which is given by the direction of the magnetic field, is necessary (Fig. 1.4(b)). The splitting between the sub-bands is $2\mu_B H$. In the case of a small splitting $2\mu_B H << E_F$ the macroscopic magnetization is proportional to the hatched area shown in Fig. 1.4(b). The Pauli susceptibility is given by

$$\chi_{para}^{Pauli} = \mu_0 \mu_B^2 N(E_F) \,, \tag{1.14}$$

where $N(E_F)$ is the density of states at the Fermi level E_F. A weak temperature dependence of the Pauli paramagnetism results from the temperature dependence of the chemical potential $\mu(T) = E_F(1 - O(T^2))$, which influences the density of states $N(E, \mu(T))$. At high temperature the Fermi statistic passes into the Boltzmann statis-tic leading to the typical temperature dependence of the magnetic susceptibility of free spins (see Eq. (1.5)).
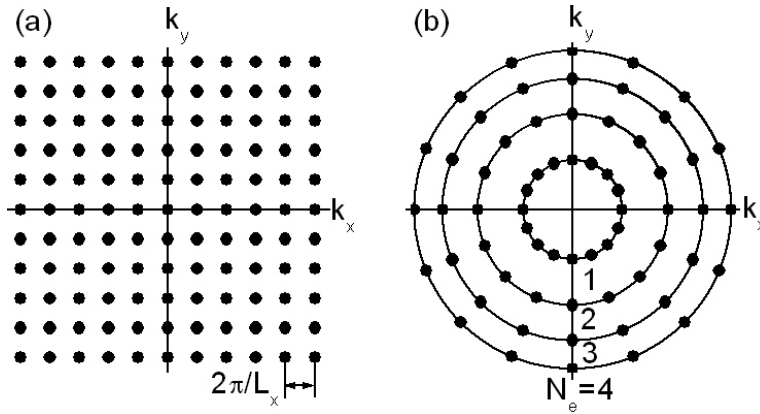
Figure 1.5: *(a) Allowed electronic states in k-space without magnetic field. (b) In an applied magnetic field H_z an additional quantization of the states appears. The electronic states condensate at the Landau cylinders.*

In opposite to metals and strongly doped semiconductors, Pauli paramagnetism in undoped semiconductors (and insulators) is weak. This results from the fact that at low temperature nearly no free carriers are present in undoped semiconductors. As is known, for T=0 the density of states at the Fermi level, which is between the conduction and the valence band for T=0, vanishes and therefore the Pauli paramagnetism disappears at low temperature.

1.2.3.2 Landau diamagnetism and Landau-levels

In opposite to the atomic diamagnetism discussed in Ch. 1.1, where the orbital momentum L of the atomic electrons is considered, here the circular motion of the free electrons (with angular momentum l) caused by an external magnetic field will be considered.

In the following a description of the motion of non-interacting electrons in a static homogeneous magnetic field B_z is given in the effective mass approximation. Here the vector potential $\mathbf{A} = (0, B_z x, 0)$ and the Landau gauge $div\mathbf{A} = 0$ are chosen. The minimal substitution of the momentum operator $\mathbf{p} \to \mathbf{p} - e\mathbf{A}$ leads to the Schrödinger equation

$$\left[\frac{(\mathbf{p}_e - e\mathbf{A})^2}{2m_e^*} \right] \Psi(\mathbf{r}_e) = E\Psi(\mathbf{r}_e) \,. \tag{1.15}$$

Here the Zeeman term, which induces the electron spin splitting $2\mu_B B_z$, is neglected. A separation approach for the wave function $\Psi(\mathbf{r}_e) = \chi(x) \exp(ik_y y) \exp(ik_z z)$ enables to write the Schrödinger equation in the form

$$\left[-\frac{\hbar^2}{2m_e^*} \frac{d^2}{d\widetilde{x}^2} + \frac{1}{2} m_e^* (\omega_c^e)^2 \widetilde{x}^2 \right] \chi(\widetilde{x}) = \left(E - \frac{\hbar^2 k_z^2}{2m_e^*} \right) \chi(\widetilde{x}) \,, \tag{1.16}$$

where $\omega_c^e = \frac{eB}{m_e^*}$ is the electron cyclotron frequency and $\widetilde{x} = x - \hbar k_y/(eB_z)$. This is the Schrödinger equation of an one-dimensional harmonic oscillator, which possesses the eigenvalues

$$E = \hbar\omega_c^e \left(N_e + \frac{1}{2} \right) + \frac{\hbar^2 k_z^2}{2m_e^*} \,, \tag{1.17}$$
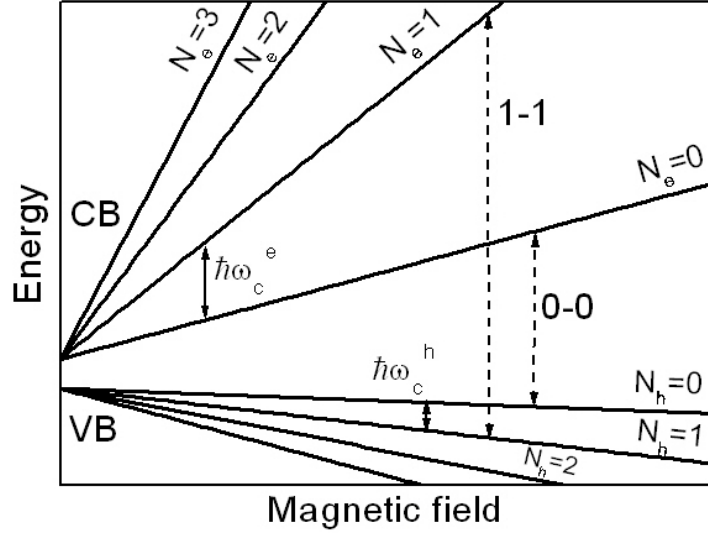
Figure 1.6: *Landau-levels of the valence and conduction band states (solid lines). Inter-Landau-level transitions (dashed lines) are determined by the selection rules $\Delta N = 0$.*

where $\hbar\omega_c^e/2$ is the zero point motion of the harmonic oscillator. The eigenfunctions are given by the product of plane waves in $y-$ and $z-$direction and the one-dimensional wave functions of the harmonic oscillator in $x-$direction, which are described on the basis of the Hermite polynomials H_{N_e}

$$\chi_{N_e}(\widetilde{x}) = \frac{1}{\sqrt{2^{N_e} N_e!}} \left(\frac{m_e^* \omega_c^e}{\pi\hbar} \right)^{1/4} \exp\left(\frac{m_e^* \omega_c^e \widetilde{x}^2}{2\hbar} \right) H_{N_e} \left(\sqrt{\frac{m_e^* \omega_c^e}{\hbar}} \widetilde{x} \right) . \tag{1.18}$$

The formation of the Landau-levels labeled with $N_e = 0, 1, 2, ..$ corresponds to a quantization of the motion of the electrons in the plane perpendicular to the direction of the magnetic field with equidistant, discrete energy levels. The free motion along the direction of the magnetic field with quasi-continuous eigenenergies leads to a formation of one-dimensional sub-bands. A quantization constraint is that the relaxation time τ between electron scattering processes is larger than the period of the circulation of the electrons $T = 2\pi/\omega_c^e$ ($\omega_c^e \tau > 1$). At low temperature, high magnetic fields and a large mean free path, which requires a high crystal quality, the electrons rotate with the cyclotron frequency ω_c^e. Then the states of the Fermi sphere (Fig. 1.5(a)) condensate on the Landau cylinders or Landau-levels (Fig. 1.5(b)). For a non-interacting free electron gas, and a possible occupation of the Landau-levels with electrons with spin up and spin down (Zeeman splitting is neglected), the degeneracy of the Landau-levels is given by

$$g = \frac{L^2 e B_z}{\pi\hbar} , \tag{1.19}$$

where L is the length of the crystal.

Analogous to the formation of the Landau-levels from the electronic states of the conduction bands, which is discussed above, the hole states are quantized in the magnetic field and form Landau-levels with the quantum numbers $N_h = 0, 1, 2, ..$. Due to the different mass of the holes m_h^*, the hole cyclotron frequency is ω_c^h and differs from that of the electrons. The orbital quantized valence bands are described by Eq. (1.17)

by replacing the index e by h. The Landau-levels of the conduction and the valence band are shown schematically in Fig. 1.6 by solid lines. Optical transitions between the Landau-levels of the electron and hole states are so-called inter-Landau-level transitions (dashed lines). E.g. an electron can be excited from the quantized valence to the quantized conduction band, similar to the creation of an exciton described above. Here the spin splitting is neglected. The selection rules for an one-photon excitation or recombination of an electron-hole pair are $\Delta N = N_e - N_h = 0$.

Beside the optical properties determined by the inter-Landau-level transitions, diamagnetism arises from the Landau-level formation. A calculation of the magnetic susceptibility considering the energy levels of the Landau-levels and their occupation based on the Fermi statistic, reveals the temperature independent Landau susceptibility

$$\chi_{dia}^{Landau} = \frac{1}{3}\left(\frac{m_e}{m_e^*}\right)^2 \mu_0 \mu_B^2 N(E_F) = -\frac{1}{3}\left(\frac{m_e}{m_e^*}\right)^2 \chi_{para}^{Pauli}, \qquad (1.20)$$

where the effective mass takes into account the mobility of the electrons.

Note that at low temperature the magnetism of undoped semiconductors is based on the atomic magnetism described in Ch. 1.1. However, the optical probe of the carriers around the band gap can reveal the magnetism displayed by the free carriers.

1.2.4 Diluted magnetic semiconductors (DMS)

In the following the magnetic properties of diluted magnetic semiconductors will be considered. Well known examples for this group of magnetic materials are the II-VI semiconductors with magnetic ions as Mn^{2+}. In this work, among other material systems, $Cd_{1-x}Mn_xTe$ is studied and thus in the following important properties of diluted II-VI semiconductors are discussed on the basis of $Cd_{1-x}Mn_xTe$, where two interacting sub-systems are of importance. On the one hand there are delocalized electrons of the conduction and valence band of the host material (II-VI compound). The electronic and magnetic properties of sp band electrons are discussed above. On the other hand the random dilution with magnetic impurity ions introduces localized magnetic moments. The magnetic properties of localized non-interacting spins are discussed in Ch. 1.1. New properties arise from the interaction between the spins of the sp band carriers and the localized spins of the d-electrons of the magnetic ions, which leads to effects as paramagnetism, ferromagnetism, antiferromagnetism, the formation of the spin-glass phase, the magnetic-field-induced metal-insulator transition or the formation of the bound magnetic polaron. Also wide gap semiconductors as (Cd,Mn)Te feature e.g. giant Zeeman splitting and giant Faraday rotation.

In diluted magnetic semiconductors it is possible to tune the band gap energy and the magnetic properties by the choice of the host material and the concentration of the magnetic ions and so provides an opportunity to engineer the electronic and magnetic properties of a system.
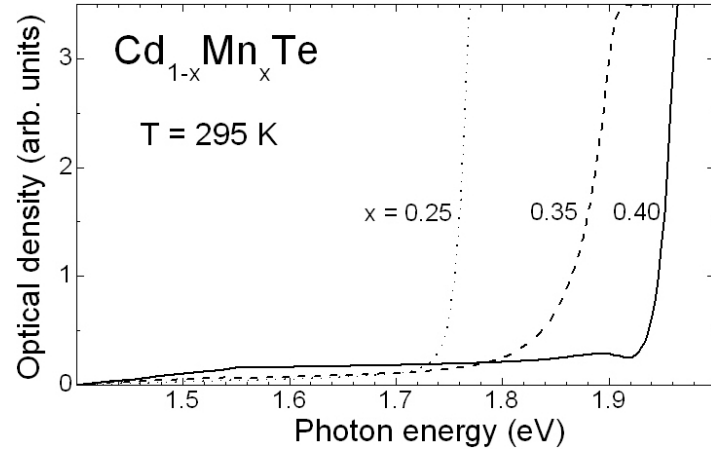
Figure 1.7: *Linear absorption in $Cd_{1-x}Mn_xTe$ at 295 K [45]. The band gap absorption for different values x displays the dependence of the band gap energy on the manganese concentration.*

1.2.4.1 Band gap shift

Systems like (Cd,Mn)Te, where one of the components (cations or anions or both) is substituted iso-electronically by other ions, are called "alloys" or "solid solutions". Substituting ions have the same number of valence electrons and therefore they do not serve as donors or acceptors. In the case of low Mn^{2+} content x, the band structure of the diluted material system resembles qualitatively that of the constituent material shown in Fig. 1.2(b). Since the diluted system possesses the same crystal structure and the *sp* bands originate from the electrons of the constituent atoms, only quantitative changes are induces by the presence of the magnetic ions. An important point is that the band gap energy E_g can change strongly with the Mn^{2+} content. E.g. for $Cd_{1-x}Mn_xTe$ the shift of the band gap energy was found to depend linearly on the manganese concentration x [88, 31]

$$
\begin{aligned}
E_g(T = 300K) &= (1.528 + 1.316x)eV, \\
E_g(T = \ 80K) &= (1.586 + 1.501x)eV, \\
E_g(T = \ 10K) &= (1.595 + 1.592x)eV, \\
E_g(T = 4.2K) &= (1.606 + 1.592x)eV,
\end{aligned}
$$

$$(1.21)$$

which is predicted by the virtual crystal approximation (VCA). This result is valid only for $x < 0.77$. For higher concentrations the crystallographic structure of zinc-blende-type changes to the NiAs-type, which results in strong changes of the electronic structure.

The shift of the band gap can be e.g. observed in absorption spectra, where band gap absorption strongly suppresses the intensity of the transmitted light. Fig. 1.7 shows linear absorption spectra for bulk $Cd_{1-x}Mn_xTe$ crystals with $x = 0.25$, 0.35 and 0.4 at room temperature, where the variation of the band gap energy is described by Eq. (1.21).
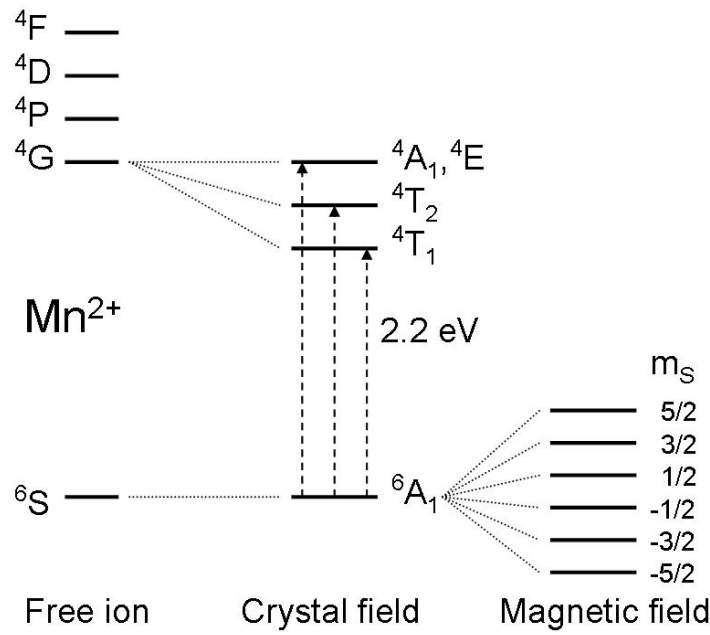
Figure 1.8: *Schematic energy level diagram of the 3d electron states of Mn^{2+}. In the crystal field the free ion states are split. Dashed arrows correspond to intra-Mn^{2+} transitions. An applied magnetic field leads to additional Zeeman splitting.*

1.2.4.2 *d* states in crystal and magnetic field

Beside the influence of the magnetic ions on the electronic band structure, also the magnetic properties of the host material are strongly changed by the magnetic moments of the impurity ions. The magnetic ions introduce magnetic moments to the (dia)magnetic host system. In the following, first the optical properties resulting from intra-Mn^{2+} electronic transitions are discussed and subsequently the magnetic properties caused by the electronic d states of the Mn^{2+} ions are considered.

Fig. 1.8 shows the electronic d states of the manganese ions for the free ion, in the crystal field and in an applied magnetic field. The free Mn atom has the electronic configuration $(Ar)3d^54s^2$. According to Hund's rules, the $3d$ electrons form the ground state ^6S with $S=5/2$ and $L=-2-1+0+1+2=0$. The excited states ^4P, ^4D, ^4F and ^4G with $L=1,2,3$ and 4 are obtained by one spin flip leading to $S=3/2$, where ^4G is the energetically lowest excited state.

In the crystal the Mn^{2+} d levels hybridize with the sp bands of the host material leading to broadened d bands. The crystal field is mainly induced by the four next neighboring Te anions and lifts the (2L+1)-fold degeneracy. Since the ground state is not degenerated, no splitting occurs and the resultant state in the crystal field is labeled $^6A_1$ according to the group theoretical transformation properties. The degenerated excited states ^4G are split by the crystal field into the energy levels labeled with $^4T_1$, $^4T_2$, ^4E and $^4A_1$ [89]. In the case of the free ion, transitions between the ground state ^6S and the excited states ^4G are forbidden by the parity and by the selection rule $\Delta S = 0$. In the crystal field the parity is broken since no local inversion symmetry is given. Also the selection rule $\Delta S = 0$ is not strictly valid because of spin-orbit coupling. Thus the transition $^6A_1 \rightarrow^4 T_1$ becomes allowed and plays an important role for the optical properties. The transition energy is about 2.2 eV. At high Mn concentration $x \gtrsim 0.4$ around and above 2.2 eV the optical properties are dominated

by the transition $^6A_1 \rightarrow ^4T_1$ and transitions from the valence to the conduction band can be suppressed. The temperature dependence of the band gap energy and the intra-Mn^{2+} transitions have the same qualitative character [31]. Unexpectedly the transitions $^6A_1 \rightarrow ^4T_1, ^4T_2, ^4E, ^4A_1$ have been found to be broadened about 100 meV even for very low concentration x [31, 90], although they should reflect narrow atomic-like states/transitions.

In an external magnetic field B_z, the ground state $^6A_1$ splits due to the spin $S = 5/2$ into six energy levels labeled with $m_S = -5/2, -3/2, -1/2, 1/2, 3/2, 5/2$. The Zeeman splitting is given by $\Delta E_z[meV] = 0.116 g_{Mn} m_S B[T]$, where $g_{Mn} = 2$ is the Landé factor according to Eq. (1.3), and thus is on the order of a few meV below 10 T. Spin paramagnetism arises with a magnetization given by Eq. (1.2), where $J = S$ and non-interacting free magnetic moments are assumed.

1.2.4.3 $d - d$ exchange interaction

In real systems the exchange interaction between localized magnetic moments of the magnetic ions can be of big importance. The exchange interaction is based on the Coulomb repulsion and the Pauli principle and can lead to long-range magnetic ordering. Note that collective phenomena are not induced by magnetic dipole-dipole interaction, since the interaction energy is too low to explain e.g. the presence of ferromagnetism at room temperature. Magnetic dipole-dipole interaction is only important for magnetic properties at temperatures below a few Kelvin. Here magnetic dipole-dipole interaction will be neglected.

Different forms of exchange interaction can be distinguished:

1. Direct exchange between magnetic ions

2. Indirect exchange via nonmagnetic ions

3. Indirect exchange via free carriers

In opposite to some magnetic materials as e.g. Fe or Cu, where the distance between the magnetic ions is small and the d orbitals can partially overlap leading to direct exchange interaction, in diluted magnetic semiconductors the magnetic ions are separated by a relatively large distance and the exchange interaction is mediated by nonmagnetic ions or carriers. First, the indirect exchange via nonmagnetic ions will be discussed.

The Hamiltonian to describe the exchange interaction includes an isotropic and an anisotropic contribution. The isotropic contribution is the Heisenberg Hamilton operator, which is given by Eq. (1.6). Here only two Mn ion spins at the lattice sites i and j are considered and the Hamiltonian can be described by [91]

$$\hat{H}_{d-d\ exchange} = \hat{H}_{isotropic} + \hat{H}_{anisotropic}, \tag{1.22}$$

$$\hat{H}_{isotropic} = -J_{ij}\mathbf{S}_i \cdot \mathbf{S}_j, \tag{1.23}$$

$$\hat{H}_{anisotropic} = -\mathbf{D}_{ij} \cdot (\mathbf{S}_i \times \mathbf{S}_j), \tag{1.24}$$
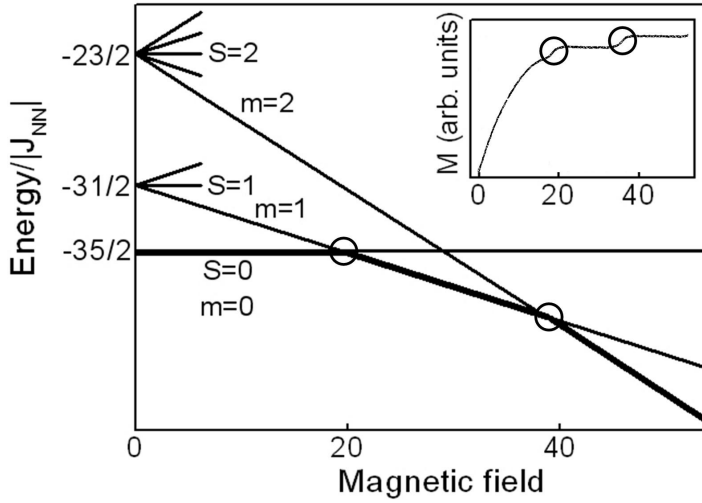
Figure 1.9: *Energy levels of two antiferromagnetically coupled Mn ions in a magnetic field (calculated by Eq. 1.26). At low magnetic fields the antiferromagnetic ground state S=0, m=0 is the lowest state. Due to the Zeeman splitting with raising magnetic field successive the states S=1, m=1 and S=2, m=2 become the lowest states. The inset shows the step-like increase of the magnetization [94].*

where J_{ij} is the isotropic and $\mathbf{D}_{ij}$ is the anisotropic exchange constant. The vector $\mathbf{D}_{ij}$ of the anisotropic Dzyaloshinskii-Moria exchange interaction [53] is perpendicular to the plane of the two Mn ions and the intermediate Te ion. The coupling of the Mn ions is mediated via virtual hopping processes of the $5p$ electrons of the Te ion (superexchange interaction). This effect is correlated to the pd hybridization. The mediation of the exchange interaction by anions [92] leads to antiferromagnetic exchange interaction for nearest-neighbors J_{NN} and next-nearest-neighbors J_{NNN}. In $Cd_{1-x}Mn_xTe$ the nearest-neighbors exchange integral J_{NN}=-6.3 K is found to be about five times larger than J_{NNN} [93].

The Hamiltonian to describe the nearest-neighbors exchange interaction in a magnetic field is given by [95]

$$\hat{H} = -2J_{NN}\mathbf{S}_1 \cdot \mathbf{S}_2 - g_{Mn}\mu_B(m_1 + m_2)B \,, \tag{1.25}$$

where the product of the spin operators $\mathbf{S}_1$ and $\mathbf{S}_2$ can be calculated by

$$2\mathbf{S}_1 \cdot \mathbf{S}_2 = \mathbf{S}^2 - \mathbf{S}_1^2 - \mathbf{S}_2^2 \,.$$

The eigenvalues of the spin operators $\mathbf{S}_i^2$ are $S_i(S_i + 1)$ with $S_1 = S_2 = 5/2$. Then the eigenvalues of the Hamiltonian are given by

$$E = -J_{NN}\left(S(S+1) - \frac{35}{2}\right) - g_{Mn}\mu_B m_S B \,, \tag{1.26}$$

where $S = 0, 1, .., 5$ is the total spin of the two Mn ion system and $m_S = -5, -4, .., 4, 5$ is the magnetic quantum number. The energy levels are shown in Fig. 1.9. At low magnetic fields the total spin of the ground state of two antiferromagnetically coupled Mn ions is zero (S=0). The antiferromagnetically coupled ions do not contribute to the magnetization M. At high magnetic fields (>10 T) the antiferromagnetic exchange interaction between nearest-neighbors can be overcome leading to a steplike raise of the magnetization. Considering only nearest-neighbors, steps in the magnetization

Figure 1.10: *Effective parameters $S_0(x)$ and $T_0(x)$ to calculate the magnetization in $Cd_{1-x}Mn_xTe$ according to Eq. (1.2) with the substitutions $S \to S_0(x)$ and $T \to T + T_0(x)$ [96].*
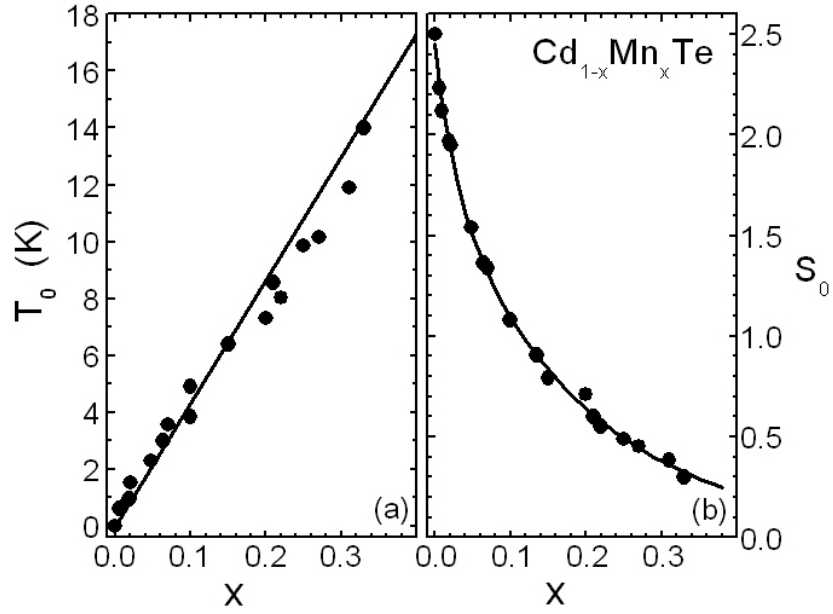
appear if $g_{Mn}\mu_B m_S B = 2J_{NN}S(S+1)$ is fulfilled. For $g_{Mn}\mu_B m_S B > 2J_{NN}S(S+1)$, the two Mn ion states with $S = 1, 2, 3, 4, 5$ ($m_S < 0$) are energetically below the antiferromagnetic ground state $S = 0$ ($m_S = 0$) of two nearest-neighbors. In Fig. 1.9 the lowest state is shown by the bold line and changes of the lowest state are marked by circles. The experimental determination of the magnetic field strengths, at which the steps in the magnetization occur, enable to calculate the nearest-neighbors exchange integral J_{NN}.

In a more complicated way, antiferromagnetic clusters, which include more than two antiferromagnetically coupled Mn ions, lead to such a steplike behavior, but the steps are considerable smaller and appear at lower magnetic fields, since $J_{NN} > J_{NNN} > J_{NNNN} > ...$. Thus a linear increase of the magnetization can be observed at high magnetic fields. Furthermore the exchange constants J_{NN} and J_{NNN} are given for averaged Mn distances. This averaging leads also to a broadening of the steps and thus a nearly linear increase of the magnetization.

So the antiferromagnetic d-d exchange interaction leads to a reduction of the magnetization in a magnetic field. For high Mn concentration the magnetization of the Mn system cannot be described by the Brillouin function given by Eq. (1.2) However, an empirical expression with phenomenological fitting parameters [97] was found to describe the magnetization sufficiently. This requires the substitutions $S \to S_0(x)$ and $T \to T + T_0(x)$ in Eq. (1.2), where the effective temperature $T_0(x)$ influences the shape of the Brillouin function and the effective spin $S_0(x)$ corrects the magnitude of M. Fig. 1.10 shows the effective parameters, which will be used to calculate the magnetization in $Cd_{1-x}Mn_xTe$ in Ch. 3.
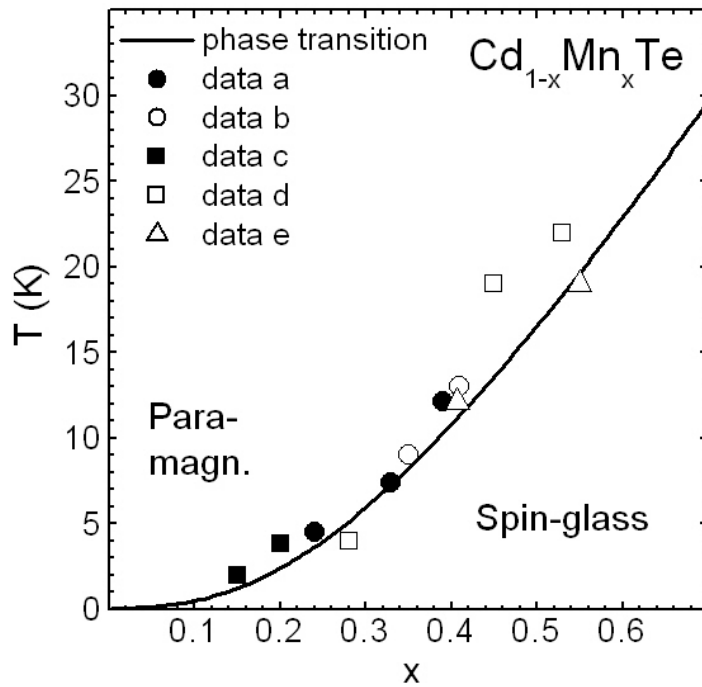
Figure 1.11: *Magnetic phase diagram of $Cd_{1-x}Mn_x Te$. At high temperature and low Mn concentration x the paramagnetic phase is present. Due to the Mn-Mn interaction at low temperature a short-range antiferromagnetic ordering (spin-glass phase) is observed. Data are taken from: phase transition [100], data a and b [101], data c [102], data d [103] and data e [104].*

1.2.4.4 Spin glass phase

Beside the paramagnetic phase at high temperature, also a spin-glass phase at low temperature exists in $Cd_{1-x}Mn_x Te$ [98]. The phase transition between the paramagnetic and the spin-glass phase is revealed e.g. by a cusp in the temperature dependence of the static magnetic susceptibility measured at low magnetic fields, especially an irreversible remanent magnetization [99] is observed, but no anomaly of the specific heat is found at the critical temperature T_a. The magnetic phase diagram of $Cd_{1-x}Mn_x Te$ is shown in Fig. 1.11.

In the spin-glass phase no long-range magnetic ordering [97] is present and the spins are macroscopically disordered. Differences are observed between experimental data obtained using field-cooled and zero-field-cooled sample preparation. The formation of the spin-glass phase is attributed to the magnetic dipole-dipole and the $d-d$ exchange interaction [100], which results in a possible frustration of the antiferromagnetic spin alignment. Since the antiferromagnetic exchange raises with Mn concentration, it is obvious that the spin-glass behavior is closely related to the presence of clusters.

1.2.4.5 $sp-d$ exchange interaction

Beside the $d-d$ interaction between the magnetic ions also $sp-d$ interaction between the delocalized s and p band electrons and the localized d electrons of the magnetic ions is of importance for the magneto-optical properties in diluted magnetic semiconductors. Here the Zeeman splitting (Eq. (1.13)) and the Landau-level quantization (Eq. (1.17)) in a magnetic field will not be considered, since in wide-gap diluted magnetic semiconductors in many cases these effects can be neglected compared to the giant Zeeman

splitting discussed below. The fact that the Zeeman and the Landau-level splitting can be neglected results from the large effective masses $m_{e,h}^*$ and the g-factors $g_{e,h}$, which are in the order of magnitude of one, of the sp band carriers.

The $sp - d$ exchange interaction can be described by the Kondo-like exchange Hamiltonian [105]

$$\hat{H}_{sp-d\ exchange} = -\sum_i J(\mathbf{r} - \mathbf{R}_i)\mathbf{S}_i \cdot \sigma \,, \tag{1.27}$$

where $\mathbf{S}_i$ and $\mathbf{R}_i$ are the spin operator and the coordinates of the i-th Mn ion and $\mathbf{r}$ and σ denote the spin operator and the coordinates of the band electron. $J(\mathbf{r} - \mathbf{R}_i)$ is the $sp - d$ exchange integral and the summation over all Mn ions in the crystal has to be considered. Since the wave functions of the s and p electrons are extended compared to the dimension of the unit cell, the following approximations can be used:

- In the molecular field approximation instead of the Mn spins $\mathbf{S}_i$ the thermally averaged spin $< \mathbf{S} >$ is used.

- In the virtual crystal approximation the summation over all Mn ion sites i is substituted by a summation over all cation sites j weighted with the Mn concentration x.

If the magnetic field is applied along the z axis of the paramagnetic system, the averaged localized spin $< \mathbf{S} > = < S_z >$ and the delocalized spin $\sigma = \sigma_z$ can be substituted by their z components. Then the Hamiltonian is given by

$$\hat{H}_{sp-d\ exchange} = -x\sigma_z < S_z > \sum_j J(\mathbf{r} - \mathbf{R}_j) \tag{1.28}$$

and has the periodicity of the lattice. This enables to use the eigenfunctions of the undiluted crystal to determine the eigenvalues of $\hat{H}_{sp-d\ exchange}$. The eigenvalues of $\hat{H}_{sp-d\ exchange}$ can be calculated using first order perturbation theory. Then the energy variations of the conduction and valence bands are given by

$$\Delta E_{\Gamma_6} = xN_0\alpha < S_z > m_S, \qquad m_S = \pm\frac{1}{2}, \tag{1.29}$$

$$\Delta E_{\Gamma_8} = \frac{1}{3}xN_0\beta < S_z > m_J, \qquad m_J = \pm\frac{1}{2}, \pm\frac{3}{2}, \tag{1.30}$$

where

$$N_0\alpha = < S|J|S > = 220\ meV, \tag{1.31}$$
$$N_0\beta = < P|J|P > = -880\ meV, \tag{1.32}$$

are the exchange integrals of the conduction and the valence band using s-like and p-like eigenfunctions S and P, respectively. The values of the exchange integrals are given for $Cd_{1-x}Mn_xTe$ [31]. The averaged localized spin value is given by

$$< S_z > = S_0 B_{\frac{5}{2}}\left(\frac{5g_{Mn}\mu_B B}{2k_B(T + T_0)}\right). \tag{1.33}$$

A systematic behavior of the exchange constants α and β is found for all Mn, Fe or Co-based diluted magnetic II-VI semiconductors:
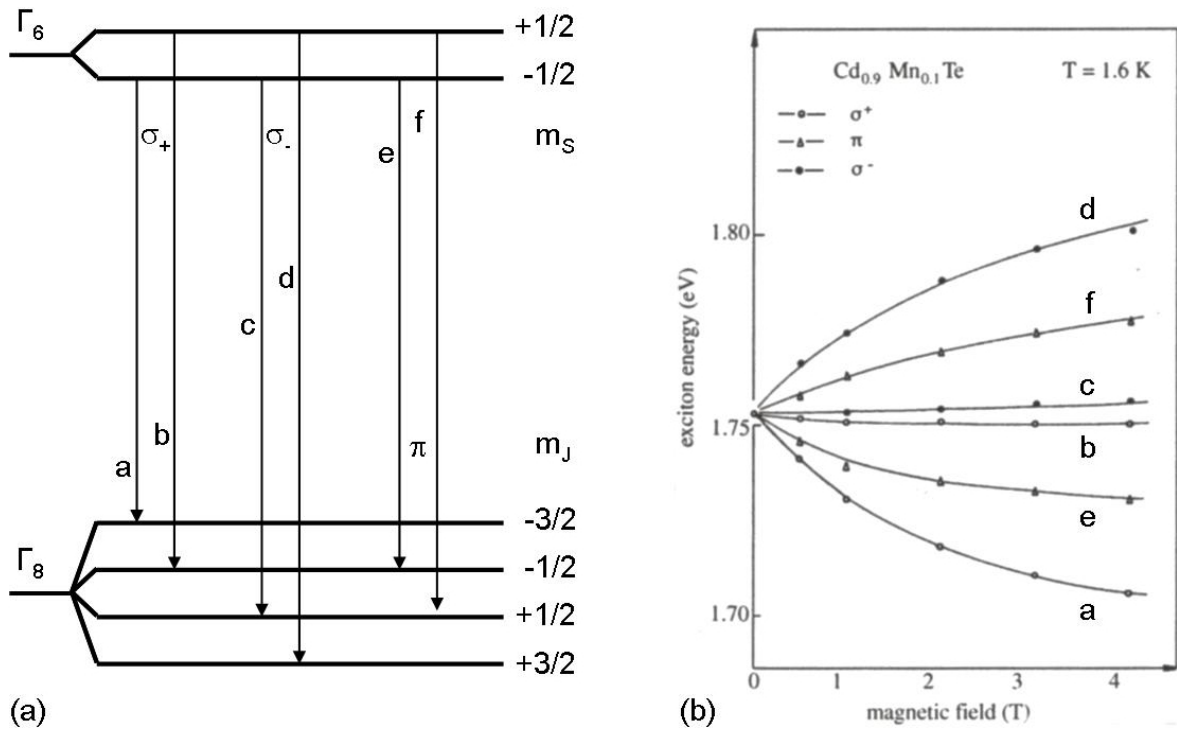
Figure 1.12: *(a) Giant Zeeman splitting of the conduction (Γ_6) and valence (Γ_8) band at the Γ point. Electric-dipole allowed one-photon transitions with $\Delta m_J = 0, \pm 1$ are shown by arrows. In the Faraday geometry ($\mathbf{H} \parallel \mathbf{k}$) the optical transitions labeled with a,b and c,d are allowed in combination with the emission of σ_+ and σ_- circular polarized light, respectively. The transitions e and f are excitable with linear polarized light in the Voigt geometry ($\mathbf{H} \perp \mathbf{k}$). (b) Giant Zeeman splitting of the exciton of $Cd_{0.9}Mn_{0.1}Te$ as a function of the magnetic field in the Faraday configuration [106].*

- The exchange constants have opposite sign: $\alpha > 0$ and $\beta < 0$.

- The absolute value of β is larger than that of α: $|\beta| > |\alpha|$.

- The Mn concentration does not influence the exchange constants: $\alpha \neq \alpha(x)$ and $\beta \neq \beta(x)$.

The physical explanation for this behavior is given by two competing mechanisms [107]:

- The 1/r-Coulomb potential leads to an exchange interaction between the s and p band carriers and the d electrons and gives a positive contribution to the exchange integrals $\alpha_{pot} > 0$ and $\beta_{pot} > 0$. Thus the Coulomb interaction favors a ferromagnetic alignment of the band carriers and the localized electrons.

- The hybridization of the wave functions of the p band electrons and the d electrons gives a negative contribution to the exchange integral $\beta_{hybrid} > 0$ and so favors an antiferromagnetic alignment of the p band electrons and the localized d electrons.

From the symmetry point of view, the $s-d$ hybridization is forbidden at the Γ point and thus $\alpha_{hybrid} = 0$ vanishes and is determined only by the Coulomb interaction $\alpha = \alpha_{pot} > 0$.

Furthermore the contribution of the $p-d$ hybridization is found to be stronger than the contribution of the Coulomb potential, which explains the relation $|\beta| > |\alpha|$ and the absolute value of $\beta = \beta_{pot} + \beta_{hybrid} < 0$. Concluding, α and β are dominated by $s-d$ and $p-d$ interaction and thus correlated to the conduction and valence bands, respectively.

Fig. 1.12(a) shows schematically the giant Zeeman splitting of the valence and the conduction bands. Electric-dipole allowed one-photon transitions with $\Delta m_J = 0, \pm 1$ are shown by arrows. In the Faraday geometry ($\mathbf{H} \parallel \mathbf{k}$) the optical transitions labeled with a,b and c,d are allowed in combination with the emission of σ_+ and σ_- circular polarized light, respectively. The transitions e and f are excitable with linear polarized light in the Voigt geometry ($\mathbf{H} \perp \mathbf{k}$). The optical transitions shown by arrows display the exchange splitting of the free-exciton ground state (to be compared to two-photon transitions discussed in Ch. 3). Fig. 1.12(b) shows this exchange splitting of the exciton [106]. Typical values of ΔE_{GZ} are on the order of 10-100 meV at low temperature and high magnetic field and depend strongly on the concentration of the magnetic ions. In $Cd_{1-x}Mn_xTe$, ΔE_{GZ} varies up to about 120 meV.

The magneto-optical properties are strongly influenced by this giant Zeeman splitting. Moreover a wide spectrum of features is induced by the $sp-d$ exchange interaction. Giant Faraday rotation is due to a large difference in dispersion for opposite circular polarizations of light in the Faraday geometry, which is also induced by the giant Zeeman splitting. Another example is the magnetically induced semiconductor-semimetal transition in narrow-gap DMS [31]. Furthermore magnetic ordering phenomena as the magnetic polarons as well as antiferro- and ferromagnetic coupling can be induced by the $sp-d$ exchange interaction.

1.3 Nonlinear magneto-optics

1.3.1 Nonlinear optics

The development of the laser in 1960 by Maiman [108] based on the theoretical considerations by Schawlow and Townes [109] provided a basis for experimental nonlinear optics. By means of lasers, the generation of light fields with a field strength of $>10^6$ V/m became possible. Such high field strengths enable to excite electronic transitions by multiple photons. The excitation leads to a nonlinear polarization $\mathbf{P}$ describing the amplitude of the dipole moment in the material. The polarization is Taylor expanded in ascending powers of the electric field $\mathbf{E}$

$$P_i = \varepsilon_0 \sum_{j=1}^{3} \chi_{ij}^{(1)} E_j + \varepsilon_0 \sum_{j,k=1}^{3} \chi_{ijk}^{(2)} E_j E_k + \varepsilon_0 \sum_{j,k,l=1}^{3} \chi_{ijkl}^{(3)} E_j E_k E_l + \dots , \qquad (1.34)$$

where $\chi^{(m)}$ is the electric susceptibility of m-th order and ε_0 is the dielectric constant. At low field strengths the higher order terms are negligible compared to the linear term $\chi^{(1)}$ representing the linear response of the material to the electric field. However the nonlinear response of the material to the electric field becomes important for high field strengths. The second term of the Taylor expansion describes different nonlinear processes explained in the following. Solving the equation $P_{nl} = \varepsilon_0 \chi^{(2)} E_1 E_2$ with the approach $E_i \sim e^{i\omega_i t} + e^{-i\omega_i t}$ leads to the nonlinear polarization $P_{nl} \sim e^{i(\omega_1+\omega_2)t} + e^{i(\omega_1-\omega_2)t} + \ldots$, where ω_1 and ω_2 are the frequencies of the incident light waves. The first term describes the sum frequency generation (SFG), whereas photons with the frequency $\omega_3^{SFG} = \omega_1 + \omega_2$ are generated. The special case $\omega_1 = \omega_2$ represents the second harmonic generation (SHG), which is used as a tool to investigate the magnetic properties of different materials in this work. SHG was studied first by Franken using a ruby laser to generate SHG in quartz [1]. The second term reproduces the difference frequency generation (DFG), whereas photons with the frequency $\omega_3^{DFG} = \omega_1 - \omega_2$ are generated. Another process described by $\chi^{(2)}$ is the optical parametric amplification (OPA). Thereby a weak signal can be amplified by means of the optical parametric amplification. The optical parametric oscillation explains the effect that an incident light wave (P) is split into two light waves, the signal (S) and the idler (I) light wave, whereas the photon energies are correlated by $\omega_P = \omega_S + \omega_I$. This effect is used to realize the optical parametric oscillator (OPO), which is explained in more detail in Chapter 1.3.4.2. The third and also higher terms of the Taylor expansion describe multiple photon processes, where more than three photons are involved (e.g. the third-harmonic generation (THG)). Nonlinear processes offer a higher degree of freedom compared to linear optical processes. The increased degree of freedom derives from the possibility to chose the propagation direction as well as the polarization of each involved photon independently. Due to different selection rules, some transitions can be excited with nonlinear processes, which are forbidden for linear optical processes. This enables to use nonlinear optical techniques to obtain complementary or hardly accessible information about the properties of the investigated system. In the following the nonlinear polarization will be used as a source in the inhomogeneous wave equation in Chapter 1.3.1.1.

1.3.1.1   Nonlinear wave equation

The self-contained electromagnetic theory is based on the Maxwell equations and the Lorentz force [110]. The propagation of electromagnetic waves can be derived from the Maxwell equations

$$\operatorname{div} \mathbf{E} = \frac{\rho}{\varepsilon_0}\,, \tag{1.35}$$

$$\operatorname{div} \mathbf{B} = 0\,, \tag{1.36}$$

$$\operatorname{rot} \mathbf{E} = -\frac{\partial \mathbf{B}}{\partial t}\,, \tag{1.37}$$

$$\operatorname{rot} \mathbf{B} = \varepsilon_0 \mu_0 \frac{\partial \mathbf{E}}{\partial t} + \mu_0 \mathbf{j}\,, \tag{1.38}$$

whereas $\mathbf{E}$ and $\mathbf{B}$ are the electric and the magnetic field, ρ and $\mathbf{j}$ are the electric charge density and the electric current, and ε_0 and μ_0 are the permittivity and the permeability, respectively. Thereby the electric charge density ρ and the electric current $\mathbf{j}$ can be described by means of a multipole expansion [111]

$$\rho = \rho_0 - \operatorname{div}\mathbf{P} - \operatorname{grad}(\operatorname{div}\widehat{Q}) + \dots \tag{1.39}$$

$$\mathbf{j} = \mathbf{j}_0 + \operatorname{rot}\mathbf{M} - \frac{\partial}{\partial t}\operatorname{div}\widehat{Q} + \dots \tag{1.40}$$

where $\mathbf{P}$ is the electric dipole moment, $\mathbf{M}$ is the magnetic dipole moment and $\widehat{Q}$ is the electric quadrupole moment.

In the case that no free carriers and currents are present in the material, the terms ρ_0 and $\mathbf{j}_0$ vanish. Applying the operation $\triangledown \times$ to Eq. 1.37 and using the Eqs. 1.35 and 1.38, the inhomogeneous nonlinear wave equation

$$\operatorname{rot}(\operatorname{rot}\mathbf{E}) + \varepsilon_0\mu_0\frac{\partial^2\mathbf{E}}{\partial t^2} = -\mu_0\frac{\partial^2\mathbf{P}}{\partial t^2} - \mu_0\operatorname{rot}\frac{\partial\mathbf{M}}{\partial t} + \mu_0\operatorname{div}\frac{\partial^2\widehat{Q}}{\partial t^2} \tag{1.41}$$

can be obtained. The nonlinear sources are given by terms of the electric dipole, the magnetic dipole and the electric quadrupole. Considering the SHG, the terms can be written as follows:

$$\text{electric dipole moment} \quad : \quad P_i(2\omega) = \varepsilon_0\chi^{(ED)}_{ijk}E_j(\omega)E_k(\omega)\,, \tag{1.42}$$

$$\text{magnetic dipole moment} \quad : \quad M_i(2\omega) = \frac{c}{\varepsilon_0 n(\omega)}\chi^{(MD)}_{ijk}E_j(\omega)E_k(\omega)\,, \tag{1.43}$$

$$\text{electric quadrupole moment} \quad : \quad Q_{ij}(2\omega) = \frac{\varepsilon_0 c}{2i\omega n(\omega)}\chi^{(EQ)}_{ijkl}E_k(\omega)E_l(\omega)\,. \tag{1.44}$$

The leading order term is given by the electric dipole moment. Higher order terms contribute significantly to the SHG signal if whether the electric dipole term is forbidden (see Ch. 5.2.2) or the higher order terms are enhanced (see Ch. 2.6).

1.3.1.2 Second harmonic generation (SHG)

The process of the second harmonic generation is shown schematically in Fig. 1.13. Two photons of the light field $E(\omega)$ excite the ground state. The first photon creates an excitation from the ground state $|g>$ to an intermediate state $|i>$. The intermediate state can be a virtual state or a real eigenstate, which is excited during a short time range Δt obeying the Heisenberg uncertainty principle $\Delta E \cdot \Delta t \geq \hbar$. Here ΔE is the energy difference between the energy of the exciting photon and the difference between the energies of the excited state and the ground state. The second photon can generate the transition from the intermediate state to the final state during the time Δt. The final state decays by coherent emission of a photon creating the light field $E(2\omega)$.

The quantum mechanical description of the process of second harmonic generation is given by means of the transition probability [112]

$$\omega_{fg} \propto \sum_i \frac{<g|\hat{H}_{WW}(2\hbar\omega)|f><f|\hat{H}_{WW}(\hbar\omega)|i><i|\hat{H}_{WW}(\hbar\omega)|g>}{(E_f - E_g - 2\hbar\omega)(E_i - E_g - \hbar\omega)}\,, \tag{1.45}$$
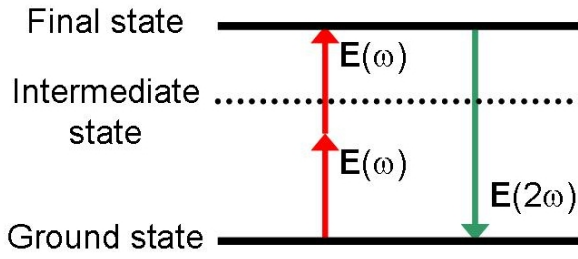
Figure 1.13:   *Illustration of the SHG process. Two photons of the light field $E(\omega)$ generate an excitation from the ground state to the final state. In a coherent process the SHG light field $E(2\omega)$ is generated. The intermediate states can be real or virtual states.*

where E_g, E_i and E_f are the energies of the states $|g>$, $|i>$ and $|f>$, respectively, and $\hat{H}_{WW}(\hbar\omega)$ and $\hat{H}_{WW}(2\hbar\omega)$ are the operators specifying the interaction. The summation takes into account all possible intermediate states. The interaction between light and matter is described by the interaction Hamilton operators considered in Ch. 1.3.1.3, which are given by the electric dipole operator, the magnetic dipole operator, the electric quadrupole operator or higher order terms. The denominator of Eq. 1.45 reveals resonances in the cases that the energy of the first exciting photon is close to the energy difference between the intermediate state and the ground state or the energy of the emitted photon is close to the energy difference between the final state and the ground state. Close to resonances the transition probability increases strongly. This effect leads to very strong and spectrally narrow SHG signals.

1.3.1.3   Light-matter interaction

The interaction between light and matter is described by the Hamiltonian discussed in the following. In the case of non-interacting electrons the Hamilton operator depends on the properties of the particles, which are given by the mass m, the charge $q = -e$ and the momentum p. The influence of the periodic structure of the crystal is taken into account by the potential V. In an electromagnetic field the minimum substitution of the momentum operator $\hat{p} \rightarrow \hat{p} - e\hat{A}$, where $\hat{A}$ is the vector potential, and the consideration of the energy contribution of the electric field $\mathbf{E}$ and the magnetic field $\mathbf{B}$ leads to the Hamiltonian

$$\hat{H} = \sum_{e^-}[\frac{1}{2m}(\hat{p}-e\hat{A})^2 - eV] \quad + \frac{\varepsilon_0}{2}\int(E^2 + c^2 B^2)d^3r \qquad (1.46)$$

$$= \sum_{e^-}(\frac{\hat{p}^2}{2m} - eV) + (\frac{e^2}{2m}\hat{A}^2 - \frac{e}{m}\hat{p}\hat{A}) + \frac{\varepsilon_0}{2}\int(E^2 + c^2 B^2)d^3r \qquad (1.47)$$

$$= \hat{H}_{Electrons} \quad + \quad \hat{H}_{Interaction} \quad + \quad \hat{H}_{Fields}. \qquad (1.48)$$

Thereby the transformation of the Hamiltonian enables to separate the contributions $\hat{H}_{Electrons}$, $\hat{H}_{Interaction}$ and $\hat{H}_{Fields}$. $\hat{H}_{Electrons}$ is a contribution which reflects the motion of non-interacting electrons in the potential V. $\hat{H}_{Fields}$ describes the energy contribution originating from the electric and magnetic fields. The interaction between the applied fields (e.g. the light fields) and the charged particles is described by $\hat{H}_{Interaction}$. The nonlinear part $\hat{H}'_{Interaction} = \frac{e^2}{2m}\hat{A}^2$ explains the diamagnetic properties of the material. For example the diamagnetic shift of the exciton energy in semiconductors,

which is proportional to H^2, can be described with this term. In the following the linear part $\hat{H}''_{Interaction} = \frac{-e}{m}\hat{p}\hat{A}$, which describes the interaction between light and matter and explains transitions between the eigenstates $|g>$, $|i>$ and $|f>$, is considered. Using a multipole expansion of the vector potential

$$\hat{A} = A_0\hat{e}e^{\pm i\mathbf{k}(\omega)\mathbf{r}} \approx A_0\hat{e}(1 \pm i\mathbf{k}(\omega)\mathbf{r}), \tag{1.49}$$

it is possible to distinguish different transitions. Here $\hat{e}$ is the unit vector and A_0 is the amplitude of the vector potential. The first term of the multipole expansion in Eq. (1.49) leads to the electric dipole term $\hat{H}_{ED} = e\mathbf{E}\mathbf{r}$. The second term reveals the magnetic dipole term $\hat{H}_{MD} \sim \mathbf{k} \times \mu$, where μ is the magnetic moment, as well as the electric quadrupole term $\hat{H}_{EQ} \sim (\mathbf{k}\mathbf{r})(e\mathbf{E}\mathbf{r})$. These operators can be inserted into Eq. (1.45) to calculate the transition probability for each process. Thereby the magnetic dipole and electric quadrupole processes are weaker by a factor of the fine structure constant $\alpha \simeq \frac{1}{137}$ compared to the electric dipole process [112]. In many cases the optical approach $\mathbf{k}\mathbf{r} << 1$ is suitable, since $\lambda = \frac{2\pi}{k}$ is much larger than the lattice constant $a \sim |\mathbf{r}|$. Therefore usually only the electric dipole term is considered. It will be shown in Ch. 2.6, that this is not always sufficient, especially for the case of magnetic-field-induced SHG in semiconductors.

1.3.2 Magnetic second harmonic generation (SHG) contributions

Beside the "crystallographic" SHG contribution $\chi^{(2)}_{ijk}$ different SHG contributions reflecting the magnetic properties of the material can occur. One example is the magnetic SHG contribution which is observed in NiO and will be discussed in Ch. 5. This contribution displays the long-range ordering of the magnetic moments. Another example is the magnetic-field-induced SHG contribution, e.g. observed in semiconductors (Ch. 2). In this case the magnetic SHG contribution can be only observed in an applied magnetic field. In opposite to the crystallographic SHG contribution the magnetic SHG contribution allows the investigation of the magnetic properties determined by the spins within the material. The spins are magnetic moments, which can be described by a current density $\mathbf{j}(\mathbf{r})$. Since the current density changes its direction under time-inversion, also the magnetic moments and therefore the spins are inverted. Thus the magnetic SHG contribution in magnetically ordered materials behaves as a c-tensor in many cases. An exception is e.g. NiO, since the magnetic SHG contribution depends quadratically on the antiferromagnetic order parameter and therefore is described by an i-tensor [113]. In opposite the crystallographic SHG contribution is always time-invariant and characterized by an i-tensor.

In the case that the system is magnetically ordered and the magnetic SHG contribution is time-noninvariant another restriction for the magnetic SHG results. The application of the time-inversion leads to a change of the sign of the nonlinear susceptibility in the magnetically ordered phase, whereas in the magnetically disordered phase, reflecting only the crystallographic symmetry, the sign of the susceptibility does not change. Therefore the magnetic SHG contribution must vanish in the magnetically

disordered phase and only the crystallographic contribution is observable. This effect is observed e.g. in CuB_2O_4.

In the case of magnetically disordered materials, e.g. diamagnetic or (diluted) paramagnetic semiconductors, the nonlinear susceptibility is time-invariant and therefore described by an i-tensor. The application of a magnetic field induces the magnetic SHG.

Due to the fact that the magnetic SHG contribution is, according to experience, orders of magnitude weaker than the crystallographic contribution [114], the determination of the non-vanishing tensor components is necessary to separate the crystallographic and the magnetic contribution by means of polarization selection rules. This concept is used for the detection of the magnetic SHG contribution in this work.

1.3.3 Symmetry of tensors

The symmetry is of particular importance in physics. The consideration of symmetry allows to determine fundamental laws. For example the conservation laws of energy, momentum and angular momentum are based on the homogeneity of time and space and the isotropy of space, respectively [115]. The symmetry of a system allows to determine symmetry constraints of physical properties, e.g. whether a physical process is allowed and which tensor components are involved. Therefore the basic is given by the Neumann principle [83, 85]. The Neumann principle reveals that the physical properties of a system possess at least the same symmetry properties as the system itself. Therefore the application of each symmetry operation of the system to the tensors describing its physical properties should display the invariance of the tensors. This leads to a set of linear equations, which has to be solved to obtain constraints for the vanishing of tensor components. Thus the description of the physical property is simplified.

The optical properties of solid states considered in this work are described by the optical nonlinear susceptibilities. These susceptibilities are characterized by a tensor of rank n. The general transformation of a tensor $\hat{\chi}$ is given by

$$\chi'_{ijk...n} = \sum_p \sum_q \sum_r \ldots \sum_u l_{ip} l_{jq} l_{kr} \ldots l_{nu} \chi_{pqr...u} \,, \tag{1.50}$$

where the transformation matrix is composed by the tensor components l_{xy}. By means of Eq. 1.50, transformations of the coordinate system of the tensor can be performed using rotation matrices. Such transformations are used in this work to calculate the rotational anisotropy of the SHG signal. A detailed description of the calculation of the rotational anisotropy is given in Ch. 5.

Tensors can be classified by means of their transformation properties. The inversion operator $\hat{I}$ transforms the spatial coordinates $\mathbf{r} \to -\mathbf{r}$. This leads to an inversion of the chirality of the coordinate system. Tensors can be classified to be polar or axial tensors depending on their properties with respect to the inversion operation:

$$\text{polar tensor} \quad : \quad \chi'_{ijk...n} = l_{ip} l_{jq} l_{kr} \cdot \ldots \cdot l_{nu} \cdot \chi_{pq...u} \,, \tag{1.51}$$

$$\text{axial tensor} \quad : \quad \chi'_{ijk...n} = -l_{ip} l_{jq} l_{kr} \cdot \ldots \cdot l_{nu} \cdot \chi_{pq...u} \,, \tag{1.52}$$

where Einstein's sum convention has to be considered. The components of the inversion matrix (l_{ij}) are given by $l_{ij} = -\delta_{ij}$ using the Dirac's delta function. The eigenvalues of the parity operator are $P_{\hat{I}} = \pm 1$, since twice application of the operator should re-establish the primary handedness.

The theoretical consideration of the time-inversion operation $\hat{T}$ is based on the formal substitution $t \rightarrow -t$. Similar to the inversion operation, the eigenvalues of the time-inversion operation are $P_{\hat{T}} = \pm 1$. Twice application leads to the primary "direction of time". Tensors, which change sign under time-inversion, are called c-tensors (change tensor), whereas tensor, which are invariant under time-inversion, are called i-tensors. The consideration of the time-inversion operation is only reasonable, if no direction of time is preferential. Considering macroscopic systems, which maximize their entropy in order to achieve a thermodynamical state of equilibrium, the time-inversion operation is not suitable. This is the case if dissipative processes (e.g. absorption effects or transport properties) are involved. In the case of dynamical effects, e.g. propagating electromagnetic waves exciting a crystal, the time-inversion of such dynamical effects has to be considered as well. Often the terminology of reciprocal and non-reciprocal effects is used instead of i- and c-tensors. In this work the terminology of i- and c-tensors is chosen.

The classification of a tensor using space inversion as well as time inversion and the symmetry of the system enables to determine its non-vanishing tensor components. These non-vanishing tensor components can be determined by means of books discussing group theory [83, 84]. Note that tensor components, which are allowed by symmetry, might be weak or forbidden by another reason. The other way round the vanishing of forbidden tensor components is unconditional.

The determination of the selection rules for the SHG process enables to simulate the SHG anisotropy. This is a powerful tool to get insight into the involved SHG mechanisms as will be shown in Ch. 2. Another possibility is to determine the symmetry of a system by means of the observed non-vanishing tensor components (see Ch. 4.3.5).

1.3.4 Experimental setup

In order to generate a detectable SHG intensity in the sample, a high intensity of the incident light is required. Additionally, for SHG spectroscopy a tunable light source is indispensable. Therefore a laser system consisting of a Nd:YAG laser and a BBO-based optical parametric oscillator (OPO) is used. The magnetic properties of the investigated materials are studied at low temperatures and in high magnetic fields generated by a split-coil cryostat.

1.3.4.1 Nd:YAG-laser

As a light source a solid-state Nd:YAG laser pumped by flash lamps is used. The optically active material consists of a yttrium aluminium garnet crystal doped with neodymium. The Nd:YAG laser is operated at a fixed repetition rate of 10 Hz with
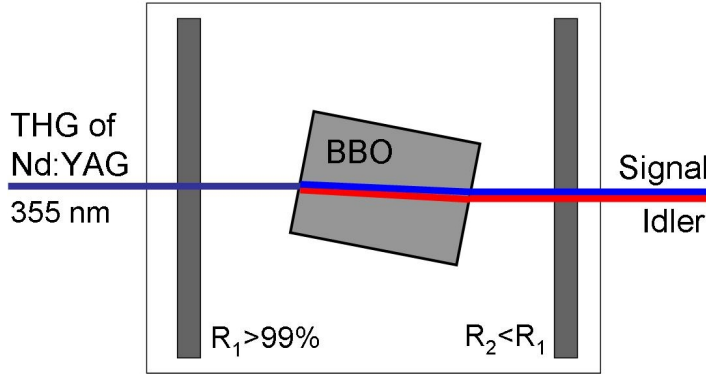
Figure 1.14: *Optical compo-nents of an OPO: The OPO consists of a pivoted BBO crys-tal and a resonator with di-electric mirrors (reflection co-efficients R_i). The third har-monic of the light emitted by a Nd:YAG laser generates two light waves with different fre-quencies, the so-called signal and idler light waves, in the BBO crystal.*

a pulse duration of 7 ns. A maximum pulse energy of 850 mJ at 1.17 eV (1064 nm) can be reached. The laser is Q-switched by a Pockels cell and generates light with a spectral line width of about 0.1 meV. Two KD*P (KH_2PO_4) crystals stabilized in temperature serve to generate the second and, subsequently, the third harmonic of the fundamental light wave at 2.33 eV (532 nm) and 3.49 eV (355 nm), respectively. The efficiency of the generation of the third harmonic is about 20 % with respect to the energy of the fundamental light wave. The third harmonic, which is separated from the second harmonic and the fundamental light wave by dielectric mirrors and a Pellin-Broca prism, is used to pump the OPO.

1.3.4.2 Optical parametric oscillator (OPO)

The optical parametric oscillator consists of a nonlinear crystal in an optical resonator. Fig. 1.14 shows schematically the operating mode of an OPO. The OPO is pumped by the third harmonic of the Nd:YAG laser. In a nonlinear process the incident light field (P) induces two light fields, the so-called idler (I) and signal (S) beams, where conventionally the light wave with the higher energy is termed signal. This process corresponds to the reversed sum-frequency generation. The special case, that the energies of the idler and the signal light wave are equal, represents the reversed SHG process.

Conservation of energy and momentum for the nonlinear process of the parametric oscillation are given by

$$Conservation\ of\ energy: \qquad \omega_P \;=\; \omega_S + \omega_I, \qquad (1.53)$$
$$Conservation\ of\ momentum: \qquad n_P\omega_P \;=\; n_S\omega_S + n_I\omega_I, \qquad (1.54)$$
$$with \;\; k_i \;=\; n_i\omega_i/c,$$

where ω_i is the frequency, k_i is the wave number and n_i is the refraction index of the light wave i. The energy of the idler and signal light wave are tuned using the phase matching condition given by Eq. 1.54, which is satisfied using the birefringence in anisotropic crystals. Thereby the ordinary incident third harmonic of the Nd:YAG

Figure 1.15: *Dispersion relation of a BBO crystal calculated by the Sellmeier formula. The energies of the idler and signal light waves are given as a function of the tuning angle between the propagation direction of the incident light wave and the optical z axis of the BBO crystal. For the experiments the idler light wave is used in the energy range from 0.6-1.6 eV (emphasized line).*
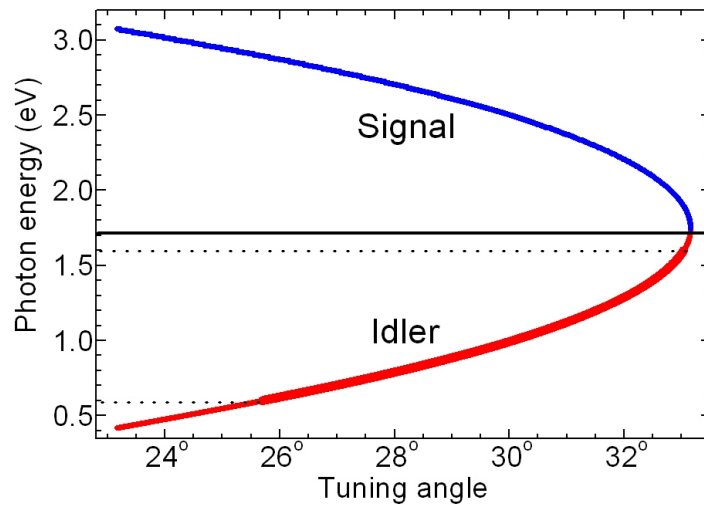
laser is polarized perpendicular to the extraordinary idler and signal light waves. The phase matching condition is fulfilled by a rotation of the BBO crystal (as shown in the following) and so varying the extraordinary refraction indices n_S and n_I (so-called type-I OPO). This leads to a tuning of the respective energies.

The OPO resonator consists of two dielectric mirrors. These mirrors are arranged in the plan-parallel Fabry-Perot configuration [116]. The third harmonic of the Nd:YAG laser is injected through the first mirror. The idler and signal light wave are extracted by means of the second mirror. Specific wideband mirrors, which are suitable for the full spectral range of 0.4-3.1 eV, are used and possess a reflectivity of 99 % and 70 %, respectively, with respect to the signal energy.

The nonlinear crystal beta barium borate β-BaB$_2$O$_4$ (BBO) with a special antireflection coating for the third harmonic (355 nm) of the Nd:YAG laser is used. The crystal possesses the symmetry C_{3v} and features strong birefringence. This enables to tune the phase matching condition in a large idler and signal energy range using only small angles of rotation of the crystal [117]. Due to the low dispersion and the high transmission in the energy range 0.4-6.5 eV, a large spectral range is accessible [118]. In the case that the BBO crystal is pumped by the third harmonic of the Nd:YAG laser, the OPO can be in principle used as a light source in the spectral range of 0.5-3 eV. In this study only the idler light wave is used, permitting spectroscopic experiments in the range of 0.6-1.6 eV and thus allowing measurement of SHG spectra from 1.2 to 3.2 eV. The intrinsic line width of an BBO-based OPO varies from ~1 meV at $\hbar\omega_I = 0.6$ eV to $\gtrsim 30$ meV at $\hbar\omega_I = 1.75$ meV. Injection seeding is a possibility to reduce the line width to ~0.01 meV. In this work a monochromator is used to improve the spectral resolution of the SHG signal. The used type-I OPO features an angle of 30 % between the surface normal and the optical axis. Fig. 1.15 shows the dispersion relation of such a type-I BBO crystal given by the Sellmeier formula. Thereby refraction indices are calculated analytically [118]. Only relative small tuning angles of 25-33° are necessary to tune the idler and signal energies in the wide range aforementioned. The maximum conversion efficiency $\frac{I_S+I_I}{I_P}$ of a BBO crystal with a length of 15 cm is about 30 %. For the SHG experiments the idler light wave is used and the signal light wave and

the third harmonic of the Nd:YAG laser are suppressed by optical filters. A maximum pulse energy of the idler light wave of 10 mJ at 2.3 eV can be reached, where the pulse duration is about 5 ns.

A detailed study of the spectral properties of optical parametric oscillators using BBO is given in Ref. [119].

1.3.4.3 Experimental configuration

The idler light wave of the OPO is used to investigate the SHG signal in transmission and reflection geometry. Proper polarizations of the fundamental (idler) light wave are chosen by the use of a Glan-Thompson prism and a computer-controlled rotatable achromatic half-wave plate (application range: 0.5-1.77 eV). In some experiments, the SHG signal is exited by circularly polarized light and circularly polarized light (SHG) are detected, which is achieved by using achromatic quarter-wave plates. The incident light is focussed onto the sample mounted inside of a superconducting split coil cryostat. External magnetic fields up to 11 T are applied in the Voigt geometry perpendicular to the direction of the light propagation or in the Faraday geometry parallel to the direction of light propagation. In the Voigt geometry the magnetic field is aligned exactly perpendicular to the direction of light propagation in order to avoid Faraday rotation of both, the fundamental and the SHG light polarization within the sample and the windows of the cryostat. The sample temperature is varied from 1.6 up to 300 K. The observed SHG intensities are normalized by the squared pulse energy of the light transmitted through the sample using a quartz plate and a joule meter. A computer-controlled rotatable polymer polarizing foil is used to investigate the SHG polarization. Optical filters are used to separate the fundamental and SHG light behind the sample. In order to suppress scattered light as well as two-photon luminescence, which is strong in semiconductors at low temperatures, a double pass prism monochromator with a resolution of 0.5-10 meV is used. Finally the transmitted SHG light is focussed onto a liquid nitrogen-cooled charge-coupled-device camera (CCD). The CCD chip possesses a resolution of 1024×256 pixel elements with a pixel size of $(25 \ \mu m)^2$ and provides sensitivity in the spectral range of 1.1-4 eV (Si chip). However, high sensitivity is only given in the range 1.2-3.5 eV, which fortunately coincides with the spectral SHG range accessible with the idler beam of the OPO. The integrated SHG signal is transmitted to a computer. A special computer program controls the OPO and the simultaneously driven monochromator, the polarizing components, the strength of the magnetic field as well as the temperature within the cryostat and the CCD camera. Fig. 1.16 shows the experimental setup.

Rotational anisotropy of the SHG signal can be measured by rotating the polarization planes of the incident and SHG light wave simultaneously. The polarization plane of the incident beam is controlled by a rotation of the achromatic half-wave plate, and the polarization plane of the detected SHG light wave is chosen by a proper orientation of the polymer polarizing foil.
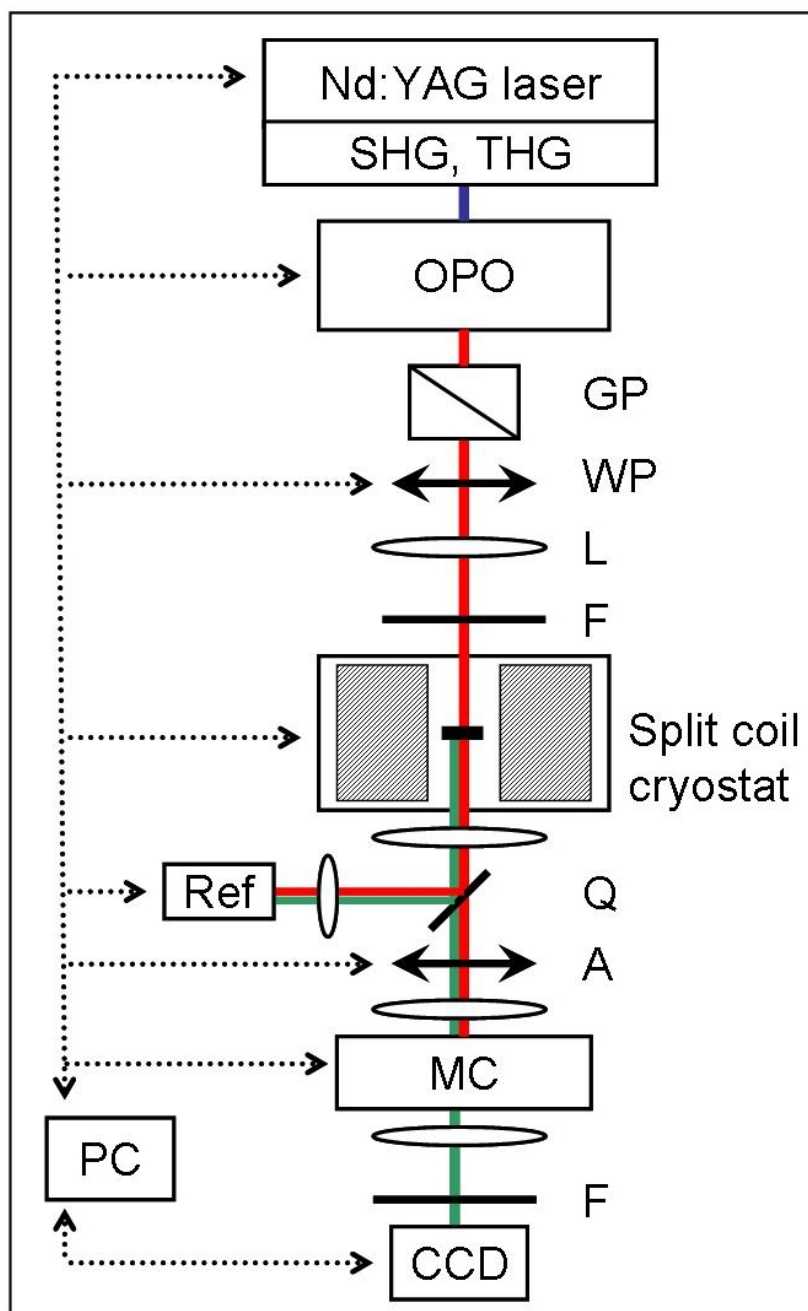
Figure 1.16: *Experimental Setup: SHG/THG: second/third harmonic, OPO: optical parametric oscillator, GP: Glan prism, WP: $\lambda/2$ wave plate, L: quartz lens, F: optical filter, Ref: reference (joule meter), Q: fused quartz plate, A: analyzer foil, MC: monochromator, PC: computer, CCD: charged-coupled-device camera.*

Chapter 2

Diamagnetic semiconductors

Most of the undoped semiconductors such as Si, Ge, GaAs, CdTe are diamagnets. Their atomic or ionic structure is spin-compensated and therefore the interaction with an applied magnetic field occurs mainly via orbital degree of freedom. Thus the interaction with an applied magnetic field is very weak and characterized by a negative magnetic susceptibility with a negligible temperature dependence [30].

In this section second harmonic generation (SHG) in diamagnetic semiconductors will be discussed. GaAs has been chosen for the present study since it is one of the most important semiconductors both for fundamental physics and for technological applications. Recent publications show the continuing interest to the nonlinear optical properties of this material [24, 120, 121, 122].

In this work, second harmonic generation is studied in the semiconductor gallium arsenide (GaAs) in a broad spectral and temperature range. Magnetic-field-induced SHG (MFISH) in the spectral range near the band gap in GaAs is observed. MFISH spectra reveal well-defined polarization properties and characteristic magnetic-field and temperature dependencies. The polarization properties investigated by rotational anisotropy are explained by model calculations based on a phenomenological analysis. The rotational anisotropy of the MFISH signal distinctly differs from that obtained in the electric-dipole approximation. Therefore nonlocal contributions in the nonlinear optical susceptibility, indicating that nonlinear magneto-optical spatial-dispersion comes together with the electric-dipole term, must be involved in order to explain the MFISH signal. Optical transitions between Landau-levels are found to be responsible for the observed MFISH spectra. Therefore orbital quantization is the source of magnetic-field-induced SHG in diamagnetic III-V semiconductors such as GaAs. These mechanisms of magnetic-field-induced SHG are also important for other semiconductors. Cadmium telluride (CdTe) serves as an example for a II-VI semiconductor. Furthermore the influence of the sample quality on the MFISH signal is discussed for GaAs and (Cd,Mg)Te. For this study only semiconductors possessing zinc-blende structure are chosen. Their advantage is the possibility to suppress fully the crystallographic SHG by a proper sample orientation and, thus, MFISH can be studied without perturbing crystallographic SHG contribution.

2.1   Crystal structure

GaAs crystallizes in the cubic space group $P\bar{4}3m$. The corresponding point group symmetry is $\bar{4}3m$. Fig.2.1 shows the unit cell, where the lattice constant is a = 5.65 Å.
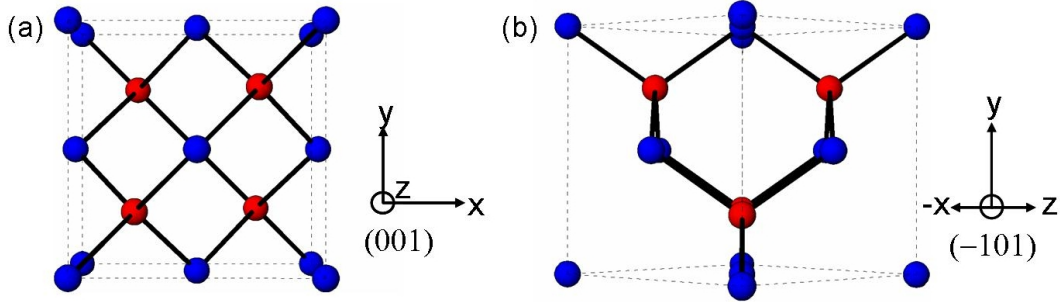
Figure 2.1: *Crystal Structure of GaAs. Ga^{3+} and As^{3-} ions occupy two fcc lattices shifted by a quarter of the diagonal along a $\langle 111 \rangle$ axis. The unit cell is shown along $\langle 001 \rangle$ (a) and $\langle 110 \rangle$ (b) direction.*

Two fcc lattices which are shifted by a quarter of the diagonal along a $\langle 111 \rangle$ axis and occupied by Ga^{3+} and As^{3-} ions, respectively, build up the crystal.

The symmetry group $\bar{4}3m$, describing the investigated semiconductors GaAs, CdTe as well as $Cd_{1-x}Mg_x$Te and $Cd_{1-x}Mn_x$Te, contains the symmetry elements

$$1\,,3(2)\,,6(\bar{2})\,,4(\pm 3)\,,3(\pm\bar{4})\,, \tag{2.1}$$

where e.g. $3(\pm\bar{4})$ denotes a fourfold rotation around one of the three symmetry axes followed by an inversion operation [83].

2.2   Polarization selection rules for SHG

Based on the crystallographic symmetry discussed above, the selection rules for different SHG processes will be determined and used as a basis for the analysis of the rotational anisotropy of SHG signal. Since the crystallographic electric-dipole SHG process is the simplest process, which in most cases provides the strongest SHG contribution, it will be discussed first. However, this work is focussed on SHG processes induced by the application of an external magnetic field, i.e. on magnetic-field-induced SHG (MFISH). In order to detect the MFISH contributions, experiments are performed for specific crystal orientations, where the crystallographic SHG is fully suppressed due to symmetry reasons.

Since the crystal is non-centrosymmetric, SHG is allowed in the electric-dipole (ED) approximation. Then the leading order SHG polarization $\mathbf{P}(2\omega)$ can be written as [3, 4]

$$P_i(2\omega) = \epsilon_0 \chi_{ijk} E_j(\omega) E_k(\omega), \tag{2.2}$$

where $\mathbf{E}(\omega)$ is the electric field at the fundamental frequency. This equation defines the crystallographic contribution to SHG. The nonlinear SHG susceptibility χ_{ijk} has been investigated in several works [24, 123]. Microscopically, χ_{ijk} is given by the non-centrosymmetric part of the electric charge density. It is a polar third-rank tensor with non-vanishing components [83]

$$\chi_{xyz} = \chi_{xzy} = \chi_{yxz} = \chi_{yzx} = \chi_{zxy} = \chi_{zyx},\tag{2.3}$$

where x, y and z denote the crystallographic axes.

In the following the polarization dependence of the SHG signal, namely its rotational anisotropy, will be calculated for different experimental geometries. For that purpose the tensor components given by Eq. (2.3) with respect to the crystal coordinate system will be first transformed into the coordinate system of the laser light beam, which depends on the experimental geometry, and then will be inserted into Eq. (2.2).

The coordinate system of the light waves is given by the wave vectors $\mathbf{k}(\omega) \parallel \mathbf{k}(2\omega)$ and the electric field vectors $\mathbf{E}(\omega)$ and $\mathbf{E}(2\omega)$ of the fundamental and the second harmonic (SH) light wave, respectively. The crystallographic coordinate system is defined by the crystallographic axes $\mathbf{x}$, $\mathbf{y}$ and $\mathbf{z}$.

First the rotational anisotropy for (110) crystal orientation and normal light incidence with $\mathbf{k} \parallel [110]$ will be calculated. The results are given in Fig. 2.2(a). For convenience in presentation of the calculated rotational anisotropy, light propagating along the $[10\bar{1}]$ axis, which is an equivalent axis to [110], will be considered. For the polarization geometry $\mathbf{E}(2\omega) \parallel \mathbf{E}(\omega)$, the SHG anisotropy is given by

$$I(2\omega)_{\parallel}^{SHG} \propto |\chi_{xyz}[\cos(\vartheta) - \cos(3\vartheta)]|^2.\tag{2.4}$$

For $\mathbf{E}(2\omega) \perp \mathbf{E}(\omega)$

$$I(2\omega)_{\perp}^{SHG} \propto |\chi_{xyz}[-\frac{1}{3}\sin(\vartheta) + \sin(3\vartheta)]|^2\tag{2.5}$$

is derived. In Eqs. (2.4) and (2.5) the rotational anisotropy is given as function of the angle ϑ between the polarization plane of the fundamental light and the crystallographic axis [010].

For another geometry, considering (111) crystal orientation, with light propagating along the [111] axis the SHG anisotropy is described by

$$I(2\omega)_{\parallel}^{SHG} \propto |\chi_{xyz}\cos(3\theta)|^2\tag{2.6}$$

in the case of $\mathbf{E}(2\omega) \parallel \mathbf{E}(\omega)$, and

$$I(2\omega)_{\parallel}^{SHG} \propto |\chi_{xyz}\sin(3\theta)|^2\tag{2.7}$$

is obtained for $\mathbf{E}(2\omega) \perp \mathbf{E}(\omega)$. Here the rotational anisotropy is given as a function of the angle θ between the polarization plane of the fundamental light and the crystallographic axis $[11\bar{2}]$. Figure 2.2 shows simulations of the crystallographic SHG anisotropy using Eqs. (2.4)-(2.7).
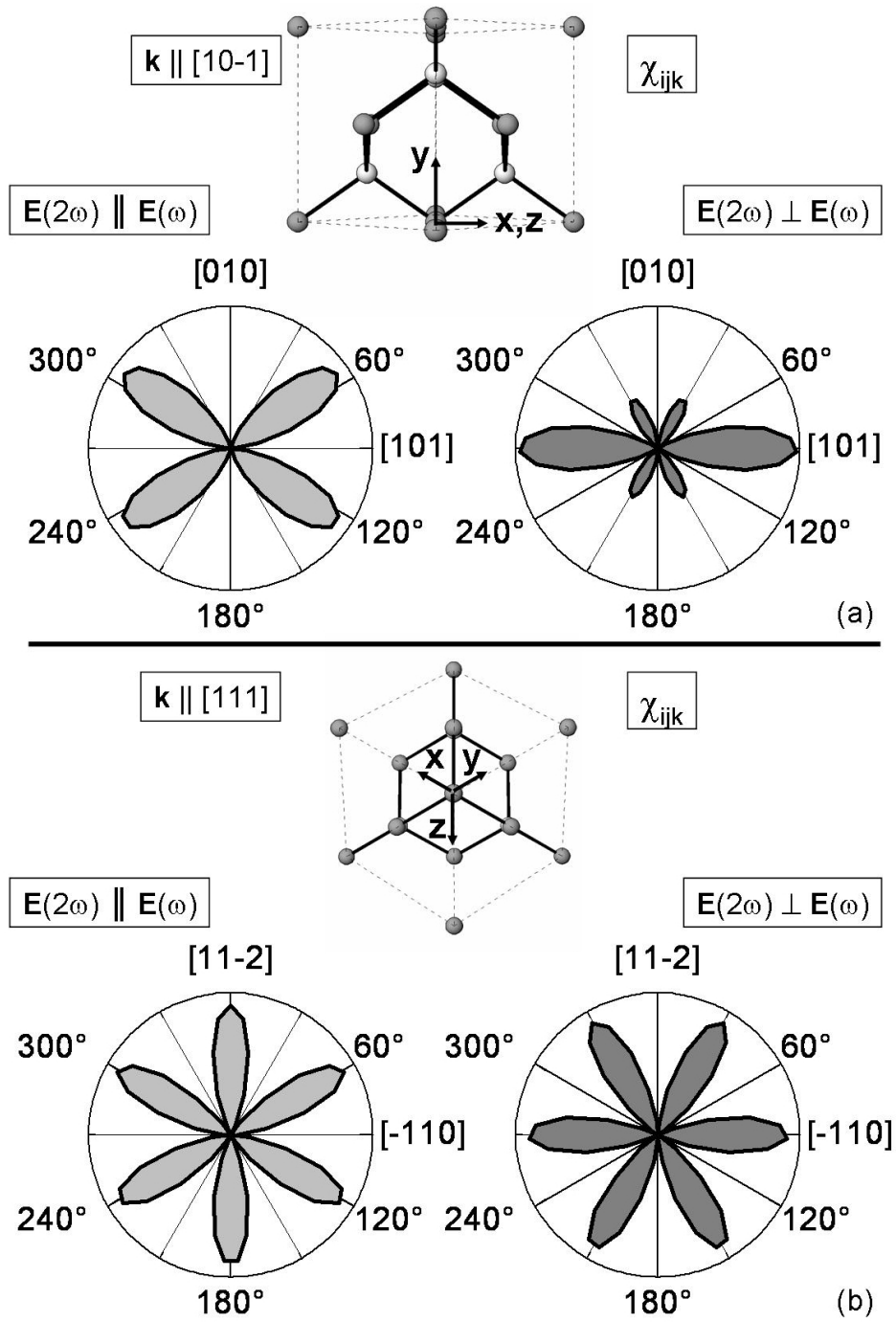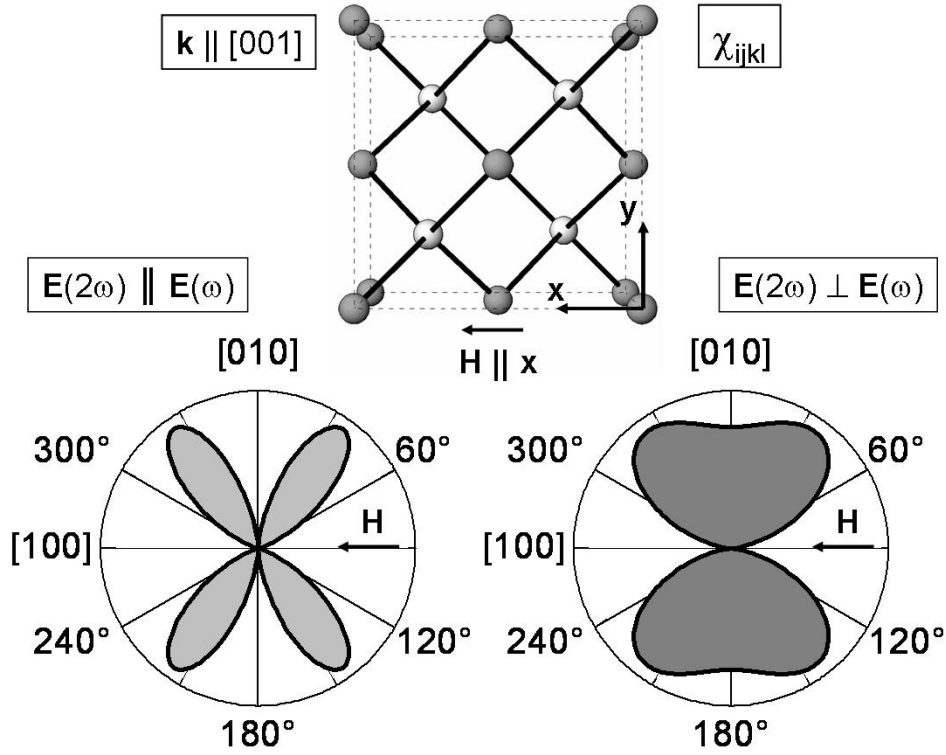
Figure 2.2: Simulations of crystallographic SHG rotational anisotropy for the geometries $\mathbf{E}(2\omega) \parallel \mathbf{E}(\omega)$ and $\mathbf{E}(2\omega) \perp \mathbf{E}(\omega)$ for (110)≡(10$\bar{1}$) and (111) crystal orientations, based on Eqs. (2.4)-(2.7). In this presentation $\mathbf{k}$ is oriented perpendicular to the figure plane along crystallographic axes [10$\bar{1}$] and [111] in panels (a) and (b), respectively.

For (001)-oriented samples χ_{ijk} does not provide crystallographic SHG for normal light incidence. This is remarkable, as it allows to study MFISH signals without their

interference with crystallographic signals.

In the following the MFISH signal will be discussed for (001) crystal orientation and normal light incidence with $\mathbf{k} \parallel [001]$. The leading order SHG contribution in a static magnetic field $\mathbf{H}(\equiv \mathbf{H}(0))$, which has to be distinguished from $\mathbf{H}(\omega)$ of the light field, can be described by

$$P_i(2\omega) = \epsilon_0 \mathrm{i} \chi_{ijkl} E_j(\omega) E_k(\omega) H_l. \tag{2.8}$$

This contribution is related to perturbations of the charge and spin distribution by the external magnetic field. The magnetic-field-induced nonlinear susceptibility χ_{ijkl} is an axial fourth-rank i-tensor with non-vanishing components [83]

$$
\begin{aligned}
-\chi_{xyyx} &= \chi_{xzzx} = \chi_{yxxy} = -\chi_{yzzy} = -\chi_{zxxz} = \chi_{zyyz}, \\
-\chi_{xyxy} &= \chi_{xzxz} = \underline{\chi_{yxyx}} = -\chi_{yzyz} = -\chi_{zxzx} = \chi_{zyzy}, \\
-\chi_{xxyy} &= \chi_{xxzz} = \underline{\chi_{yyxx}} = -\chi_{yyzz} = -\chi_{zzxx} = \chi_{zzyy}.
\end{aligned}
\tag{2.9}
$$

The analysis of the tensor components χ_{ijkl} in Eq. (2.9) shows that MFISH described by Eq. (2.8) is forbidden in the Faraday geometry ($\mathbf{k} \parallel \mathbf{H}$) [124]. Without loss of generality one can select the magnetic field direction along the z-axis ($\mathbf{H} \parallel \mathbf{z}$). In this case only tensor components with the last index $l = z$ contribute. On the other hand, due to ($\mathbf{k} \parallel \mathbf{z}$) the first three indices cannot be equal to z ($i, j, k \neq z$). No components fulfilling these conditions can be found in Eq. (2.9).

For the Voigt geometry ($\mathbf{k} \perp \mathbf{H}$), especially with $\mathbf{k} \parallel \mathbf{z}$ and $\mathbf{H} \parallel \mathbf{x}$, only the underlined tensor components in Eq. (2.9) contribute to the SHG signal. Due to the permutability of the two exciting photons at the fundamental frequency, the components $\chi_{yxyx} = \chi_{yyxx}$ cannot be distinguished. Therefore only two tensor components, χ_{xyyx} and χ_{yxyx}, are independent. Using Eq. (2.8) for the MFISH polarization and applying a transformation of the coordinate system, the MFISH rotational anisotropy can be calculated. In the case of $\mathbf{E}(2\omega) \parallel \mathbf{E}(\omega)$, the anisotropy in electric-dipole approximation is given by

$$I(2\omega)_\parallel^{MFISH} \propto |-(\chi_{xyyx} + 2\chi_{yxyx})[\sin(\varphi) + \sin(3\varphi)]|^2, \tag{2.10}$$

and for $\mathbf{E}(2\omega) \perp \mathbf{E}(\omega)$

$$
\begin{aligned}
I(2\omega)_\perp^{MFISH} \propto |\chi_{xyyx}[3\cos(\varphi) + \cos(3\varphi)] \\
+ \chi_{yxyx}[-2\cos(\varphi) + 2\cos(3\varphi)]|^2
\end{aligned}
\tag{2.11}
$$

is derived for light propagating along the [001] axis. Here the MFISH intensity is given as a function of the angle φ between the polarization plane of the fundamental light and the crystallographic axis [010]. Fig. 2.3 shows the rotational anisotropy for the specific choice of tensor components $-\chi_{xyyx} = \chi_{yxyx}$. Note that the shape of the anisotropy pattern given by $I(2\omega)_\parallel^{MFISH}$ in Eq. (2.10) does not depend on the choice of values for χ_{xyyx} and χ_{yxyx}. In contrast, the shape of the anisotropy pattern given by $I(2\omega)_\perp^{MFISH}$ in Eq. (2.11) varies strongly with the choice of values for χ_{xyyx} and χ_{yxyx}.
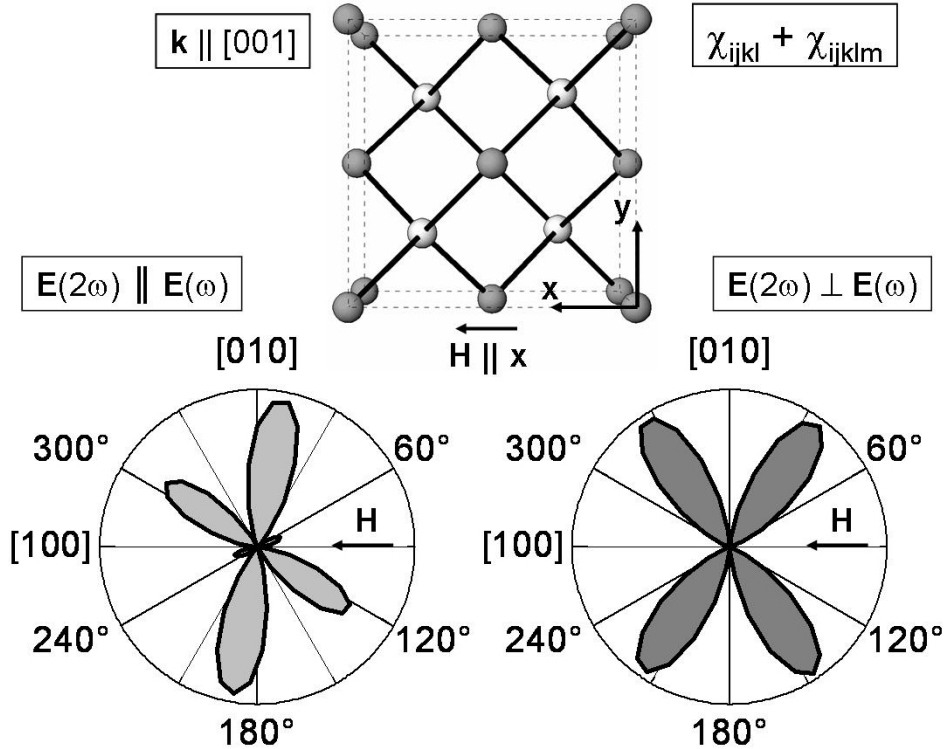
Figure 2.3: Simulations of MFISH rotational anisotropy for the geometries $\mathbf{E}(2\omega) \parallel \mathbf{E}(\omega)$ and $\mathbf{E}(2\omega) \perp \mathbf{E}(\omega)$ for (001) crystal orientation based on Eqs. (2.10)-(2.11) taking into account the electric-dipole approximation with light wave vector $\mathbf{k} \parallel [001]$ and external magnetic field $\mathbf{H} \parallel [100]$.

It will be shown in Ch. 2.6, that the electric-dipole approximation is not sufficient to model the rotational anisotropy of the MFISH signal in semiconductors with zinc-blende structure like GaAs, CdTe, (Cd,Mg)Te and (Cd,Mn)Te. To solve this problem, higher nonlinear susceptibility terms have to be taken into account.

MFISH contributions can be generally described by

$$\begin{pmatrix} \mathbf{P}^{2\omega} \\ \mathbf{M}^{2\omega} \\ \mathbf{Q}^{2\omega} \end{pmatrix} \propto \begin{pmatrix} \chi^{eeem} & \chi^{eemm} & \chi^{emmm} \\ \chi^{meem} & \chi^{memm} & \chi^{mmmm} \\ \chi^{qeem} & \chi^{qemm} & \chi^{qmmm} \end{pmatrix} \begin{pmatrix} \mathbf{E}^{\omega}\mathbf{E}^{\omega}\mathbf{H} \\ \mathbf{E}^{\omega}\mathbf{H}^{\omega}\mathbf{H} \\ \mathbf{H}^{\omega}\mathbf{H}^{\omega}\mathbf{H} \end{pmatrix}, \qquad (2.12)$$

where $\mathbf{H}^{\omega} \equiv \mathbf{H}(\omega)$ is the magnetic field at the fundamental frequency and $\mathbf{M}^{2\omega} \equiv \mathbf{M}(2\omega)$ and $\mathbf{Q}^{2\omega} \equiv \mathbf{Q}(2\omega)$ are the magnetization and electric-quadrupole polarization at the MFISH frequency, respectively. All nonlinear susceptibilities contributing to Eq. (2.12) are symmetry-allowed for the point group $\bar{4}3m$ [83]. However, nonlinear processes, which include more than two magnetic quantities, such as χ^{emmm}, χ^{memm}, χ^{mmmm} and χ^{qmmm} or involving both, an electric-quadrupole polarization and a magnetic quantity, such as χ^{qemm}, will be neglected, since they are believed to be small. The remaining contributions χ^{eemm}, χ^{meem} and χ^{qeem}, which involve either two magnetic

quantities or an electric-quadrupole polarization, can be rewritten as

$$P_i(2\omega) = \epsilon_0 \chi_{ijklm} E_j(\omega) E_k(\omega) k_l(\omega) H_m, \tag{2.13}$$

so that nonlinear magneto-optical spatial-dispersion is taken into account. The appearance of the wave vector $\mathbf{k}(\omega)$ arises from the multipole expansion of the vector potential up to the first order, which is given by

$$\mathbf{A} = A_0 \mathbf{e} \cdot \exp(\pm i\mathbf{k}(\omega)\mathbf{r}) \approx A_0 \mathbf{e}(1 \pm i\mathbf{k}(\omega)\mathbf{r}), \tag{2.14}$$

where $\mathbf{e}$ is the unit vector and A_0 is the amplitude of the vector potential. The term $A_0\mathbf{e}$ leads to the electric-dipole SHG contribution considered in Eqs. (2.2) and (2.8). The next order term $A_0\mathbf{e}\,i\mathbf{k}(\omega)\mathbf{r}$ represents both, the magnetic-dipole and the electric-quadrupole approximation, leading to the $i\mathbf{k}$-dependence of the MFISH contributions described by Eq. (2.13).

The nonlinear susceptibility tensor χ_{ijklm} is an axial time-invariant fifth-rank tensor. The full set of non-vanishing tensor components is given by [125, 83]

$$-\chi_{xyzxx} = \chi_{xzyxx} = \chi_{yxzyy} = -\chi_{yzxyy} = -\chi_{zxyzz} = \chi_{zyxzz}$$
$$-\chi_{xyzzz} = \chi_{xzyyy} = \chi_{yxzzz} = -\chi_{yzxxx} = -\chi_{zxyyy} = \chi_{zyxxx}$$
$$-\chi_{xzyzz} = \chi_{xyzyy} = \chi_{yzxzz} = -\chi_{yxzxx} = -\chi_{zyxyy} = \chi_{zxyxx},$$
$$-\underline{\chi_{xyxzx}} = \chi_{xzxyx} = \chi_{yxyzy} = -\chi_{yzyxy} = -\chi_{zxzyz} = \chi_{zyzxz}$$
$$-\underline{\chi_{xxyzx}} = \chi_{xxzyx} = \chi_{yyxzy} = -\chi_{yyzxy} = -\chi_{zzxyz} = \chi_{zzyxz}$$
$$-\chi_{xyxxz} = \chi_{xzxxy} = \chi_{yxyyz} = -\chi_{yzyyx} = -\chi_{zxzzy} = \chi_{zyzzx}$$
$$-\chi_{xxyxz} = \chi_{xxzxy} = \chi_{yyxyz} = -\chi_{yyzyx} = -\chi_{zzxzy} = \chi_{zzyzx}$$
$$-\chi_{xyyzy} = \chi_{xzzyz} = \underline{\chi_{yxxzx}} = -\chi_{yzzxz} = -\chi_{zxxyx} = \chi_{zyyxy}$$
$$-\chi_{xyyyz} = \chi_{xzzzy} = \chi_{yxxxz} = -\chi_{yzzzx} = -\chi_{zxxxy} = \chi_{zyyyx}$$
$$-\chi_{xxxyz} = \chi_{xxxzy} = \chi_{yyyxz} = -\underline{\chi_{yyyzx}} = -\chi_{zzzxy} = \chi_{zzzyx}.$$

$$\tag{2.15}$$

Due to the permutability of the two exciting photons, the components $-\chi_{xyzxx} = \chi_{xzyxx}$ of the first set of tensor components cannot be distinguished and therefore must vanish. For the same reason, the second and third ($\chi_{xyzzz} = \chi_{xzyzz}$), fourth and fifth ($\chi_{xyxzx} = \chi_{xxyzx}$) and sixth and seventh ($\chi_{xyxxz} = \chi_{xxyxz}$) set of tensor components are equal.

The analysis of the tensor components shows that MFISH described by Eq. (2.13) is forbidden in the Faraday geometry ($\mathbf{k} \parallel \mathbf{H} \parallel \mathbf{z}$), since tensor components of type χ_{ijklm} with $i, j, k \neq z$ and $l, m = z$ are not allowed.

Underlined tensor components denote MFISH contributions, which can be excited in the Voigt geometry with $\mathbf{k} \parallel \mathbf{z}$ and $\mathbf{H}^0 \parallel \mathbf{x}$. In this geometry, the tensor components

$$\chi_{yxxzx}, \ \chi_{yyyzx}, \ \chi_{xxyzx} = \chi_{xyxzx} \tag{2.16}$$

provide MFISH. Thus only the tensor components χ_{yxxzx}, χ_{xxyzx} and χ_{yyyzx} are independent. Using Eqs. (2.8) and (2.13) for the MFISH polarization and applying a

transformation of the coordinate system, the MFISH rotational anisotropy can be calculated for the case that electric-dipole and spatial-dispersion MFISH are induced. For $\mathbf{E}(2\omega) \parallel \mathbf{E}(\omega)$, the anisotropy is given by

$$
\begin{aligned}
I(2\omega)_{\parallel}^{MFISH} \propto \big| &- (\chi_{xyyx} + 2\chi_{yxyx})[\sin(\varphi) + \sin(3\varphi)] \\
&+ (\chi_{yxxzx} + 2\chi_{xxyzx})[\cos(\varphi) - \cos(3\varphi)] \\
&+ \chi_{yyyzx}[3\cos(\varphi) + \cos(3\varphi)]\big|^2,
\end{aligned} \tag{2.17}
$$

and for $\mathbf{E}(2\omega) \perp \mathbf{E}(\omega)$

$$
\begin{aligned}
I(2\omega)_{\perp}^{MFISH} \propto \big| &\chi_{xyyx}[3\cos(\varphi) + \cos(3\varphi)] \\
&+ \chi_{yxyx}[-2\cos(\varphi) + 2\cos(3\varphi)] \\
&+ \chi_{yxxzx}[3\sin(\varphi) - \sin(3\varphi)] \\
&- \chi_{xxyzx}[2\sin(\varphi) + 2\sin(3\varphi)] \\
&+ \chi_{yyyzx}[\sin(\varphi) + \sin(3\varphi)]\big|^2
\end{aligned} \tag{2.18}
$$

is derived for light propagating along the [001] axis. The MFISH intensities shown in

Figure 2.4: Simulations of MFISH rotational anisotropy for the geometries $\mathbf{E}(2\omega) \parallel \mathbf{E}(\omega)$ and $\mathbf{E}(2\omega) \perp \mathbf{E}(\omega)$ for (001) crystal orientation based on Eqs. (2.17)-(2.18) taking into account the electric-dipole terms as well as the spatial dispersion terms ($\mathbf{k} \parallel$ [001]). The following parameters have been chosen based on the results of Ref. [16]: $\chi_{xyyx}=3$, $\chi_{yxyx}=3$, $\chi_{yxxzx}=8$, $\chi_{xxyzx}=1$ and $\chi_{yyyzx}=170$.

Fig. 2.4 are given as a function of the angle φ between the polarization plane of the fundamental light and the crystallographic axis [010]. Specific values for the tensor components chosen to simulate the rotational anisotropy are given in the caption.

The MFISH rotational anisotropy in Fig. 2.4 is calculated for (001) crystal orientation, where the crystallographic SHG does not provide any contribution. In case of (110) or (111) crystal orientations, MFISH can be also observed, but it comes together with the crystallographic SHG, which is about an order of magnitude stronger than MFISH. In order to avoid possible interference effects between MFISH and crystallographic SHG, for the following experimental studies of MFISH an exact (001) crystal orientation will be used.

Above, the theoretical macroscopic model on the basis of symmetry analysis is given. In the following experimental part, the effect of magnetic field, temperature, SHG energy and polarization angle φ on the MFISH intensity will be studied. E.g. at a fixed temperature and for a fixed electronic transition, the rotational anisotropy will be investigated as a function of the magnetic field. In general, a variation of the experimental conditions can lead to strong changes of the shape of the rotational anisotropy pattern. For an arbitrary angle φ the MFISH intensity $I(2\omega)_{\parallel,\perp}^{MFISH}(\varphi)$ displays a superposition of all five tensor components, which is described by Eqs. (2.17) and (2.18). Special cases are

$$I(2\omega)_{\parallel}^{MFISH}(\varphi = 0°) \propto |\chi_{yyyzx}|^2 \qquad (2.19)$$

$$I(2\omega)_{\perp}^{MFISH}(\varphi = 90°) \propto |\chi_{yxxzx}|^2 \qquad (2.20)$$

$$I(2\omega)_{\perp}^{MFISH}(\varphi = 0°) \propto |\chi_{xyyx}|^2, \qquad (2.21)$$

where the MFISH intensity is not given by a superposition of several tensor components, but is proportional to a single tensor component.

2.3 Description of GaAs, CdTe and Cd$_{1-x}$Mg$_x$Te samples

The investigated III-V semiconductor GaAs samples have been fabricated by three different methods: (i) 10 μm gas-phase-epitaxy layer grown on a semi-insulating GaAs (001) substrate [126] (no. F-239(2)), (ii) 2 μm epilayer grown by molecular-beam epitaxy on (001) GaAs substrate (no. p338) and (iii) (001)-oriented 0.5 mm thick platelet of bulk GaAs grown by the Bridgman method. The sample of type (i) has a very low defect density of 10^{14} cm^{-3} and most of the experimental data shown below are obtained with this sample. The samples of types (ii) and (iii) have a defect density of about 10^{15} cm^{-3}. They show very similar experimental features compared to the sample (i), but with weaker and broader spectral lines. The comparative study of these samples is given in Ch. 2.9.

II-VI semiconductor samples have been fabricated in the Institute of Physics, Warsaw, by molecular-beam epitaxy on (001) GaAs/Cd$_{0.72}$Mg$_{0.28}$Te hybrid substrates.

1 μm thick epilayers have been grown on top of a $Cd_{0.8}Mg_{0.2}Te$ buffer layer and have been overgrown by a 50 nm $Cd_{0.8}Mg_{0.2}Te$ cap layer to reduce undesired surface effects. Three samples are studied with epilayers of CdTe (no. 121304D), $Cd_{0.99}Mg_{0.01}Te$ (no. 102805C) and $Cd_{0.92}Mg_{0.08}Te$ (no. 102805A). The band gap E_g of $Cd_{1-x}Mg_xTe$ increases with raising Mg content and is described by the dependence $E_g = (1.606 + 1.755x)$ eV. Therefore, the buffer, cap and hybrid substrate layers of $Cd_{1-x}Mg_xTe$ are transparent at energies of the fundamental light and SHG signals of the examined materials.

2.4   Crystallographic SHG in GaAs

It has been shown in Ch. 2.2, that in (001)-oriented GaAs samples the crystallographic SHG is absent for normal light incidence. Therefore, for measuring the crystallographic SHG, the GaAs samples are tilted by 45° around the [010] axis. Note, that the internal angle is significantly less than 45° due to the refractive index of GaAs, which varies strongly with the wave length [127]. However, a variation of the internal angle does not change the shape of the rotational anisotropy pattern, but influences only the SHG intensity. Crystallographic SHG measured over a wide spectral range below and above the fundamental band gap $E_g = 1.519$ eV is shown in Fig. 2.5. The vanishing of the signals for specific polarizations, which can be clearly seen from the rotational anisotropy diagram, confirms that the signal is solely formed by the SHG process and has no luminescence contribution. Luminescence is an optical process of lower order as compared to SHG and it is expected to display isotropic signals in cubic materials.

In the allowed geometry $[\mathbf{E}(2\omega) \perp \mathbf{E}(\omega) \parallel [101]]$ a strong decrease of the SHG intensity is found around the band gap energy. This decrease does not display the pure spectral dependence of the squared nonlinear optical susceptibility given by Eq. (2.2). One of the reasons for that can be the reabsorption of the SHG light with energies exceeding the GaAs band gap energy. Another reason can be given due to the energy dependence of the SHG coherence length. It decreases continuously with raising energy, both below and above the band gap. Below the band gap, the coherence length at normal incidence can be calculated as [128]

$$l_{coh} = \frac{\lambda}{4 \mid n(\omega) - n(2\omega) \mid},$$ (2.22)

where λ is the fundamental wavelength and $n(\omega)$ and $n(2\omega)$ are the refractive indices at the fundamental and second harmonic frequencies, respectively. Estimated values for the refractive index at 6 K show, that the coherence length decreases from $\sim$2 μm at 1.3 eV to $\sim$1 μm at 1.5 eV [16]. Above the band gap, the coherence length is reduced to the value of the attenuation length given by [3]

$$l_{coh} = \frac{1}{\beta} = \frac{\lambda_F}{2\pi k},$$ (2.23)

where β is the imaginary part of the wave vector above the band gap, and k is the absorption coefficient. Estimated values show that the coherence length decreases from $\sim$1 μm at 1.6 eV to $\sim$0.7 μm at 2 eV [16].
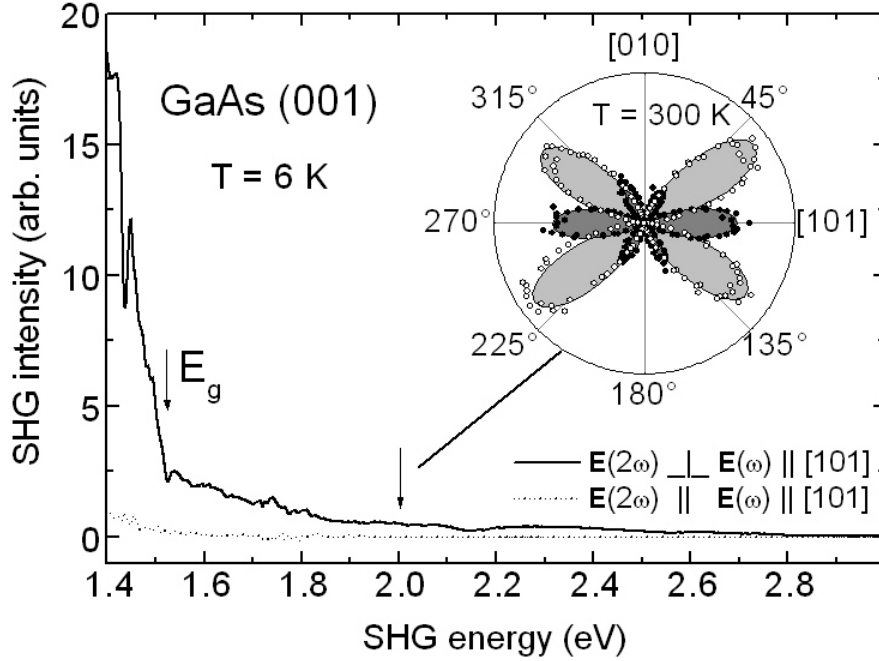
Figure 2.5: Spectral dependence of crystallographic SHG in a GaAs sample of type (i) tilted by 45°. SHG spectra measured at T=6 K are shown for the electric-dipole allowed [$\mathbf{E}(2\omega) \perp \mathbf{E}(\omega) \parallel [101]$] and forbidden [$\mathbf{E}(2\omega) \parallel \mathbf{E}(\omega) \parallel [101]$] polarization geometries. The inset shows the rotational anisotropy detected at 2.0 eV and T=300 K in two geometries: $\mathbf{E}(2\omega) \parallel \mathbf{E}(\omega)$ (light grey shaded area and open dots) and $\mathbf{E}(2\omega) \perp \mathbf{E}(\omega)$ (grey shaded area and filled dots).

A fit of the experimental SHG anisotropy using Eqs. (2.4) and (2.5) is shown in the inset of Fig. 2.5. Note that the shape of the crystallographic anisotropy does not vary with the SHG energy and the temperature. Good agreement between experimental data and simulations (shaded areas) is received confirming a high structural and optical quality of the sample as well as its proper orientation. A misalignment larger than 1° between the crystallographic axes and the laboratory coordinate system would cause an observable distortion of the SHG rotational anisotropy patterns. Therefore, rotational anisotropy of the SHG signal is used to control the proper orientation of the samples.

2.5 Magnetic-field-induced SHG (MFISH) in GaAs

In the following the crystallographic contribution to the SHG signal due to χ_{ijk} will be suppressed using normal light incidence in (001)-oriented samples. This enables the detection of pure MFISH signals.

Figure 2.6: (a) MFISH spectra in GaAs for Faraday geometry ($\mathbf{H} \parallel \mathbf{k}(\omega) \parallel \mathbf{z}$) at different magnetic fields. Circularly (σ^-) polarized light is chosen for excitation and detection. (b) Landau-level fan diagram of MFISH peak energies. Circles are experimental data with symbol sizes scaled by the MFISH intensity. Good agreement is found between peak energies and optical transition energies between Landau-levels calculated from Eq. (2.24) for $N_e = N_h$ (solid lines). The dashed line gives the literature data for the diamagnetic shift of the 1s-exciton state.
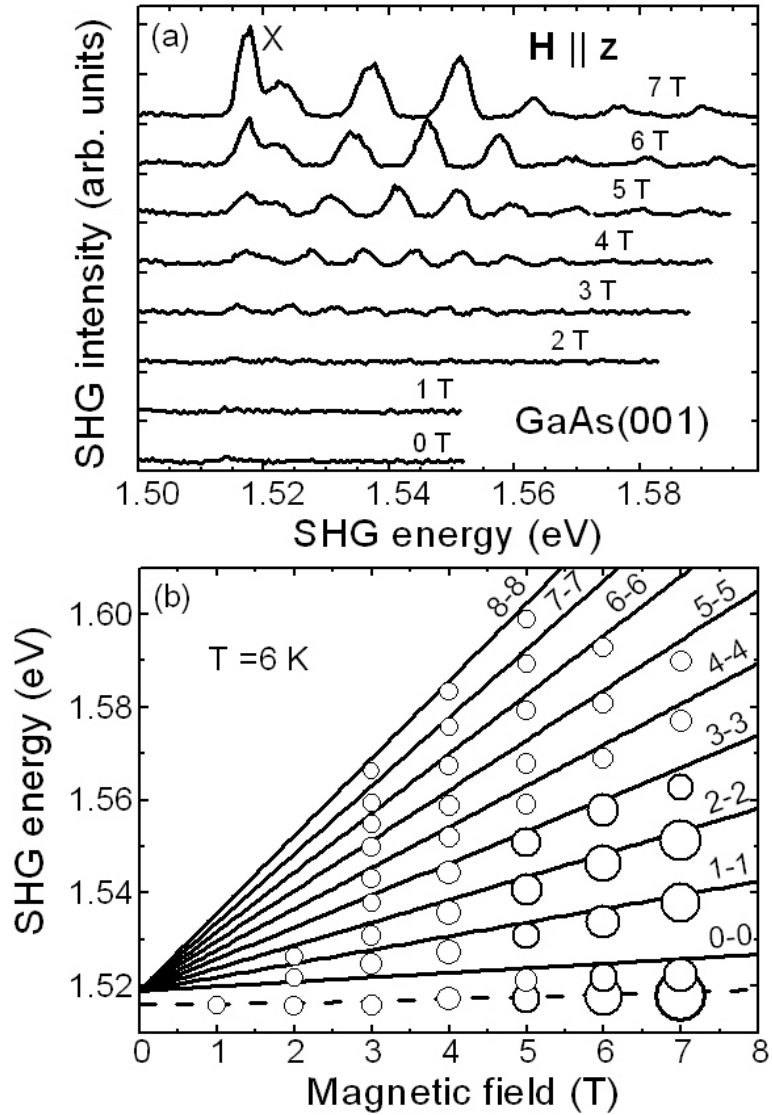
2.5.1 Faraday geometry

First, MFISH experimental data measured in the Faraday geometry ($\mathbf{H} \parallel \mathbf{k}(\omega) \parallel \mathbf{z}$) will be presented. The symmetry considerations based on Eqs. (2.8) and (2.13) suggest, that in this case MFISH is not allowed. However, a set of narrow SHG transitions induced by the external magnetic field is observed. The peak energies of these lines shift with high accuracy according to the known spectrum of magneto-excitons in GaAs [129, 130]. MFISH spectra measured with circularly polarized excitation and detection photons are shown in Fig. 2.6(a) for different magnetic fields. No signal is detected at zero magnetic field. With increasing magnetic field a set of narrow lines shifting to higher energies appears and gains in intensity. The strongest peak is observed at the lowest SHG energy. This line is labelled as X-line and is associated with the 1s-exciton state, as will be show below.

The magnetic field dependence of the peak energies is plotted in Fig. 2.6(b), where the symbol sizes are scaled by the MFISH intensity. Such a presentation of the results is

typical for the fan-chart diagram of magneto-excitons measured by linear spectroscopy methods like absorptions, reflection and photoluminescence excitation spectroscopy. The shift of the lowest line shows a very good coincidence with the diamagnetic shift of the 1s-exciton state in GaAs [129, 130], which is traced by a dashed line. It starts from 1.516 eV, which is the 1s-exciton energy at zero magnetic field. The exciton binding energy in GaAs is 4.2 meV and the band gap, which corresponds to the optical transition from the top of the valence band to the bottom of the conduction band, has an energy of 1.519 eV at a temperature of 6 K. A calculation of the magneto-exciton spectrum is beyond the scope of this work. Instead, the solid lines in Fig. 2.6(b) display optical transitions between Landau-levels of free electrons and holes, whose orbital motion is quantized by the magnetic field [131]. The magneto-exciton states are expected to be a few meV below the Landau-levels due to Coulomb effects.

The Landau-level transitions are calculated by

$$E = E_g + \frac{e\hbar}{c}\left[\frac{1/2 + N_e}{m_e^*} + \frac{1/2 + N_h}{m_h^*}\right]H, \qquad (2.24)$$

where $E_g = 1.519$ eV is the GaAs band gap energy, $m_e^* = 0.067m_e$ and $m_{hh}^* = 0.51m_e$ are the electron and heavy-hole effective masses [132] and $N_e = N_h = 0, 1, 2, ...$ are the Landau-level quantum numbers. Here the Zeeman splitting of Landau-levels is not taken into account since it does not exceed 1 meV below 7 T, which is below the experimental resolution of the setup.

A comparison between the experimental data and the calculated lines reveals, that the MFISH transitions, which are located 2-5 meV below the calculated Landau-level energies, can be indeed assigned to the magneto-exciton states. It will be show below (see Fig. 2.12), that the MFISH lines in the Faraday geometry are observable even in a larger spectral range up to 1.70 eV.

2.5.2 Voigt geometry

According to the analysis provided in Ch. 2.2, MFISH in the Voigt geometry ($\mathbf{H} \parallel$ $\mathbf{x}$, $\mathbf{k}(\omega) \parallel \mathbf{z}$) is allowed in both, the electric-dipole and the magneto-optical spatial-dispersion, approximations given by Eqs. (2.8) and (2.13), respectively. This prediction is in good agreement with the experimental data shown in Fig. 2.7. The observed MFISH signal originates from the strongest component χ_{yyyzx}. It is measured for $\mathbf{E}(2\omega) \parallel \mathbf{E}(\omega) \parallel \mathbf{y}$ in magnetic fields up to 11 T and is about five times stronger than the MFISH in the Faraday geometry (for details see Fig. 2.12). Other experimental features are qualitatively similar to what has been found for the Faraday geometry. A set of narrow lines appears with increasing magnetic field. The lines gain in intensity and shift to higher energies. Their energies, which are compared with the calculated Landau-level energies in Fig. 2.7(b), demonstrate good coincidence. The main difference is the rich structure of peaks related to each Landau-level transition. It originates from the field-induced mixing of magneto-exciton states due to the complex energy and spin structure of the valence band. This phenomenon is well established for the linear
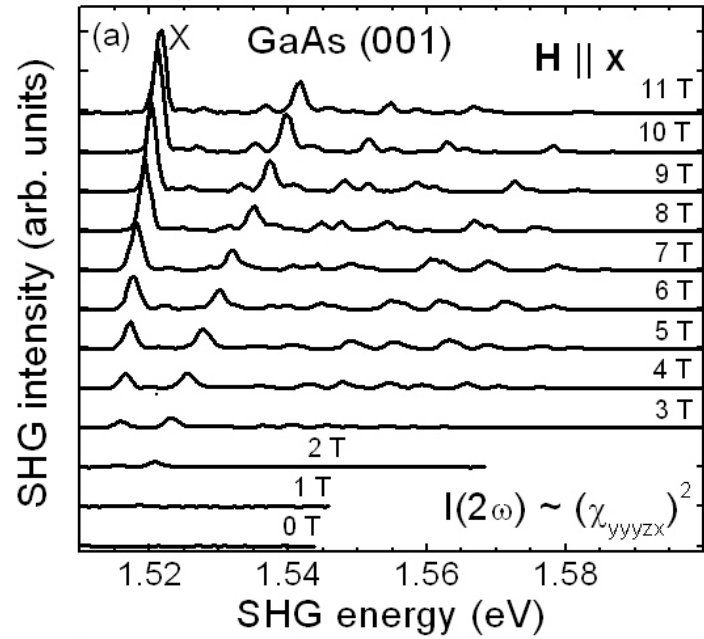
Figure 2.7: (a) MFISH spectra at different magnetic fields in GaAs (Voigt geometry). (b) Landau-level fan diagram of MFISH peak energies. Circles are experimental data with symbol sizes scaled by the MFISH intensity. Solid lines present optical transitions between Landau-levels calculated from Eq. (2.24) for $N_e = N_h$. The dashed line gives the literature data for the diamagnetic shift of 1s-exciton state.
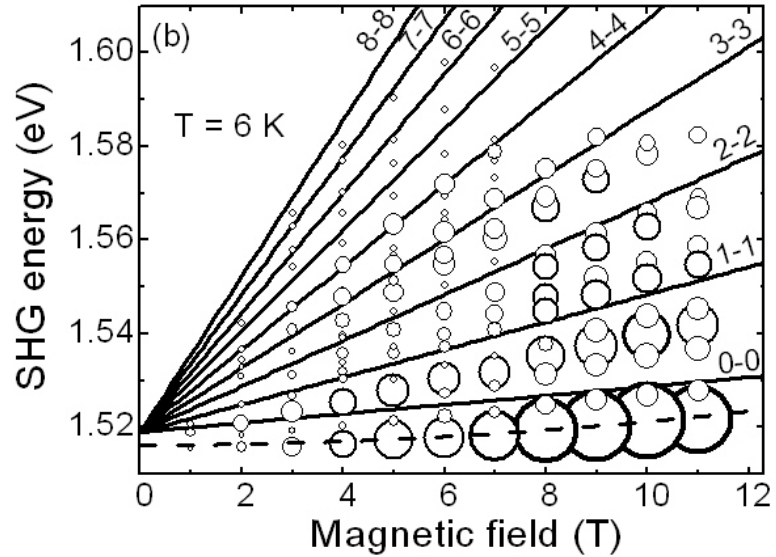
spectra of magneto-excitons in GaAs and other semiconductors with zinc-blende crystal structure.

In the following the dependence of the MFISH intensity will be studied as a function of the magnetic field.

2.5.3 Magnetic field dependence of MFISH intensity

An increase of the MFISH intensity of the strongest X-line is shown in Fig. 2.8 for the Faraday (filled circles) and the Voigt (open circles) geometry. For both geometries a quadratic dependence of the MFISH intensity on the magnetic field strength is found. The H^2-fit to the experimental data is given by a solid line. The intensity of the MFISH signal is proportional to the square of the nonlinear polarization, i.e. $I(2\omega) \propto |\mathbf{P}(2\omega)|^2$.
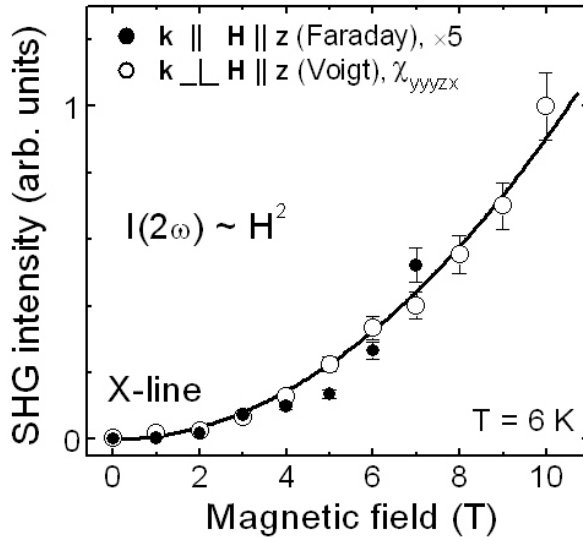
Figure 2.8: *MFISH intensity of the X-line as a function of magnetic field in Faraday and Voigt geometry in GaAs. Experimental data are shown by symbols. Intensities are normalized to the signal in the Voigt geometry, which is stronger by a factor of five compared to that in the Faraday geometry. The solid line is a H^2-fit to the data.*

Therefore it can be concluded, that the nonlinear polarization $P(2\omega)$ depends linearly on H. This result is in full agreement with the conclusions of the phenomenological approach given by Eqs. (2.8) and (2.13). Such a dependence is characteristic for the MFISH signals due to the orbital quantization of the electronic states, which is contrary to the MFISH based on the spin quantization (see Ch. 3). This quadratic dependence of the MFISH intensity on the magnetic field will be discussed below in more detail in combination with the rotational anisotropy for all nonlinear tensor components in the Voigt geometry.
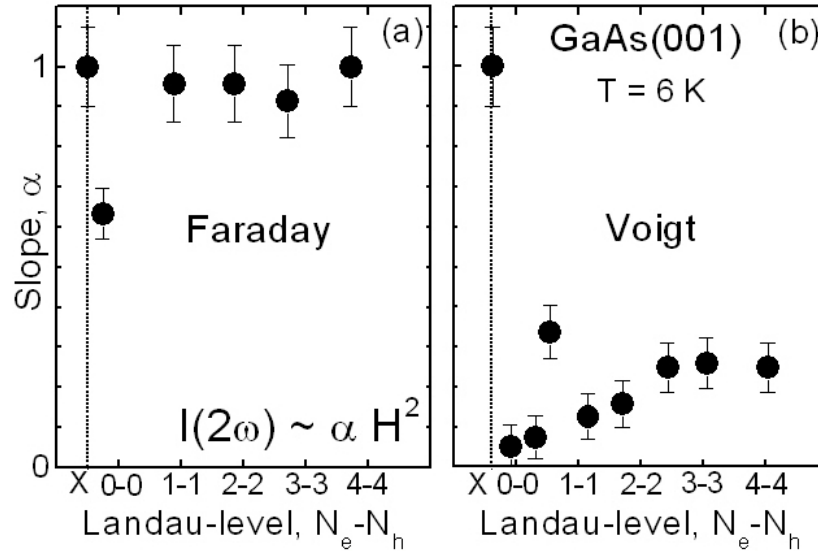
Figure 2.9: Slope α of the quadratic dependence of the MFISH intensity on the magnetic field $I(2\omega) \sim \alpha H^2$ vs. Landau-level quantum numbers $N_e - N_h$. Results are based on the experimental data for (a) Faraday geometry given in Fig. 2.6 and (b) Voigt geometry given in Fig. 2.7.

Fig. 2.9 shows the slope α of the quadratic dependence of the MFISH intensity on the magnetic field $I(2\omega) \sim \alpha H^2$ for the transitions X, $0-0$, $1-1$, $2-2$, $3-3$ and $4-4$ in the Faraday and Voigt geometries. The results are obtained from a fit to the experimental data presented in Figs. 2.6 and 2.7. In the Faraday geometry with exception of the first Landau-level transition $(0-0)$, the slope does not vary significantly with the Landau-level quantum number and even reveals the same value for the X-line. In opposite, in the Voigt geometry the α value for the X-line exceeds significantly the slopes of all other transitions. One can see an increasing tendency for the slope values with raising Landau-level quantum number. In the following the X-line will be studied as an example for the set of observed lines.

2.5.4 Temperature dependence of MFISH signal

The MFISH signal is rather robust against an increase of temperature and it can be detected up to 200 K as is shown in Fig. 2.10(a). With increasing temperature the MFISH lines lose intensity and shift to lower energies. Surprisingly, the thermal broadening of these lines is very weak as it is illustrated by the inset. The dominant mechanism responsible for the shift of the MFISH lines is the decrease of the GaAs band gap energy with decreasing temperatures. This is confirmed by Fig. 2.10(b) where the MFISH peak positions are compared with the expected temperature shifts for the $1s$-exciton and Landau-level transitions [132].

The dependence of the integrated intensity of the $1s$-exciton (X-line) on the temperature is given in the inset of Fig. 2.10(b). The decrease of the MFISH intensity cannot be described by a mono-exponential form and therefore no specific activation energy can be assigned. One of the possible mechanisms for the temperature dependence of the MFISH intensity is carrier-phonon scattering, which perturbs the cyclotron motion of the free carriers and therefore violates the orbital quantization. For excitonic lines in linear optical spectra, the scattering causes a broadening of the lines. This is definitely not the case for MFISH spectra as is shown by the inset of Fig. 2.10(a). It can be suggested, that the difference comes from the coherent origin of the SHG process. The temperature stability of the MFISH line width may be explained in analogy to X-ray Bragg scattering on the crystal lattice. Thermal motion of atoms leads to a decrease of the X-ray signal intensity, which is described by the Debye-Waller factor in the case of the Bragg scattering [30]. The line width, however, remains constant due to the fact, that signal contributions of many unit cells interfere constructively only, if the interference constraint is fulfilled.
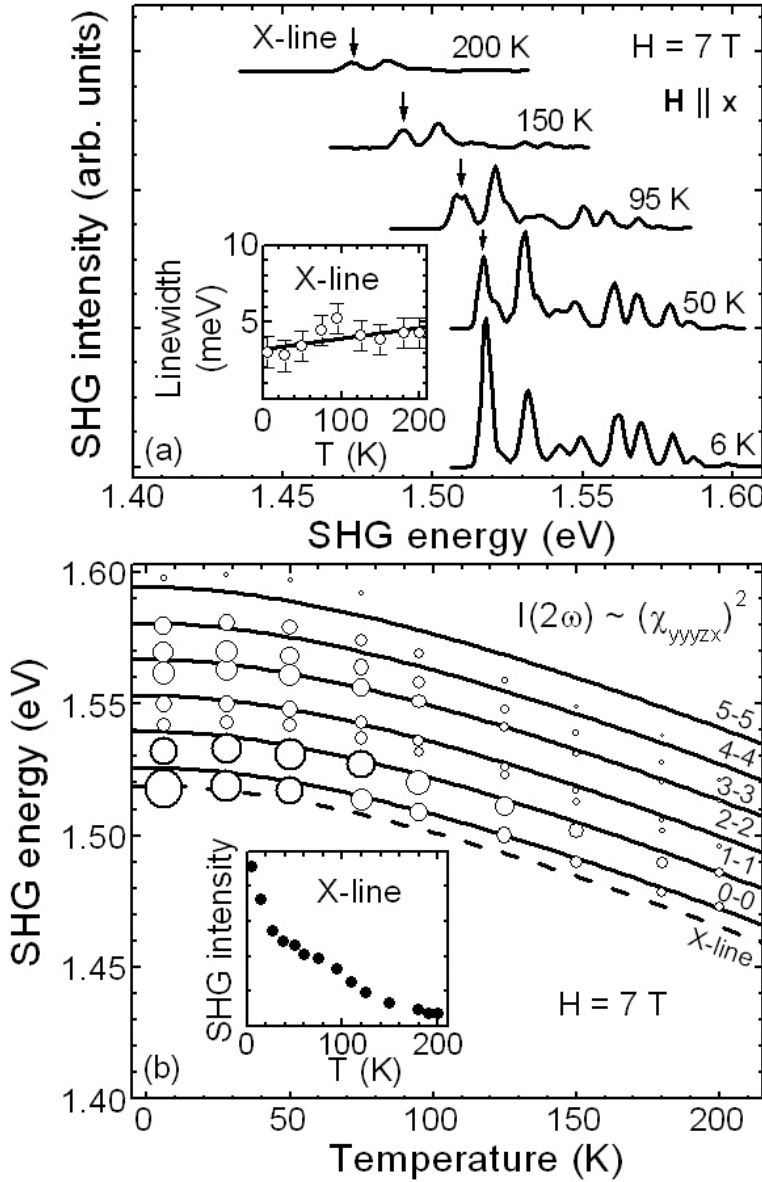
Figure 2.10: (a) MFISH spectra at different temperatures in GaAs (Voigt geometry). (b) MFISH peak energies vs. temperature. Circles are experimental data with symbol sizes scaled by the MFISH intensity. Solid lines present optical transition energies between Landau-levels calculated from Eq. (2.24) for $N_e = N_h$ at $B = 7$ T combined with the temperature dependence of the GaAs band gap [132]. The integrated MFISH intensity of the X-line is given in the inset.

2.5.5 Transmission vs. reflection geometry

Due to the fact, that GaAs is transparent at the fundamental frequency ($\hbar\omega < E_g$), absorption only appears for the SHG light above the band gap ($2\hbar\omega > E_g$). In this case the transmission geometry ($\mathbf{k}(\omega) \parallel \mathbf{k}(2\omega) \parallel \mathbf{z}$) can be used. Nevertheless, for materials, which possess absorption even at the fundamental frequency, the reflection geometry ($-\mathbf{k}(\omega) \parallel \mathbf{k}(2\omega) \parallel \mathbf{z}$) is an alternative. In this case the same selection rules as for transmission geometry are valid and thus the same rotational anisotropy, which is calculated above, is expected.

Fig. 2.11 shows MFISH spectra for the transmission and reflection geometry. In both cases the MFISH spectra are found to be very similar with respect to the spectral position of the observed peak energies as well as their relative peak intensities. The only difference is that the MFISH intensity is found to be about one order of magnitude
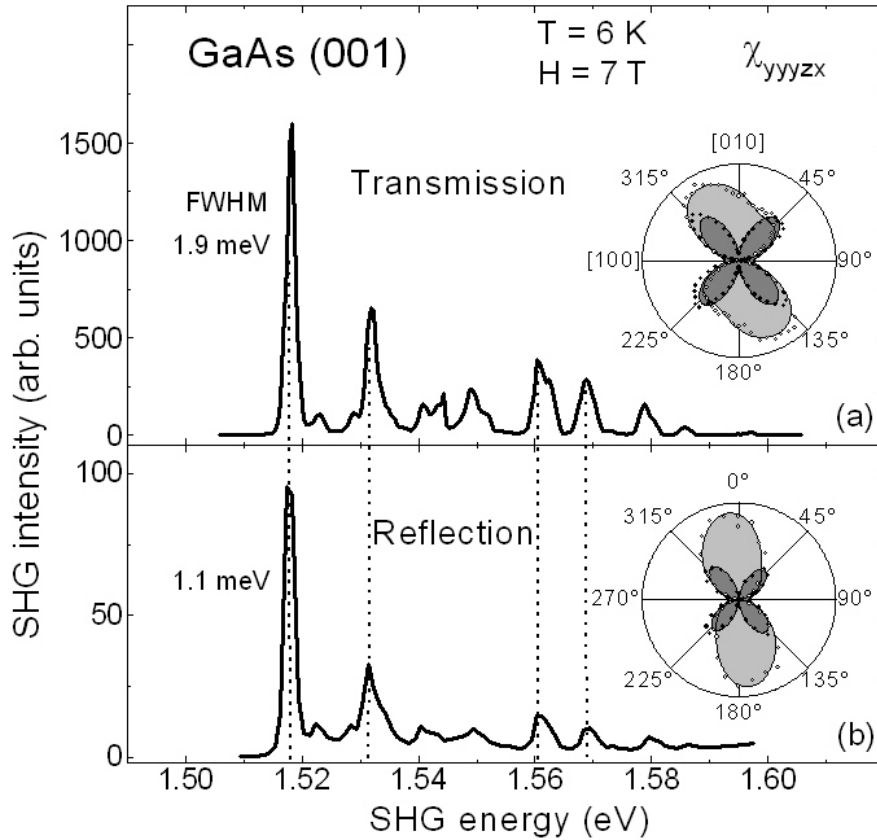
Figure 2.11: MFISH spectra in (a) transmission geometry ($\mathbf{k}(\omega) \parallel \mathbf{k}(2\omega) \parallel \mathbf{z}$) and (b) reflection geometry ($-\mathbf{k}(\omega) \parallel \mathbf{k}(2\omega) \parallel \mathbf{z}$). In both cases the polarization geometry is $\mathbf{E}(2\omega) \parallel \mathbf{E}(\omega) \parallel y$ (χ_{yyyzx}). The ordinate scale shows MFISH intensity in arbitrary units, but the ratio between intensities for different geometries is relevant. The insets show the rotational anisotropy.

weaker in the reflection geometry. A possible explanation might be, that MFISH is generated mainly by the reflected beam at the fundamental frequency and thus the pump power to induce the MFISH is drastically reduced. The observed line widths of the X-line are of comparable magnitude (1-2 meV) and close to the experimental resolution limit. The rotational anisotropy for the transmission and reflection geometry does not differ significantly and is shown in the insets of Fig. 2.11. In the following only the transmission geometry will be considered due to the higher MFISH intensity.

2.6 Rotational anisotropy and magneto-spatial dispersion

In this chapter, experimental data of the characteristic polarization dependence of the MFISH signal are discussed. It will be shown, that the electric-dipole approximation
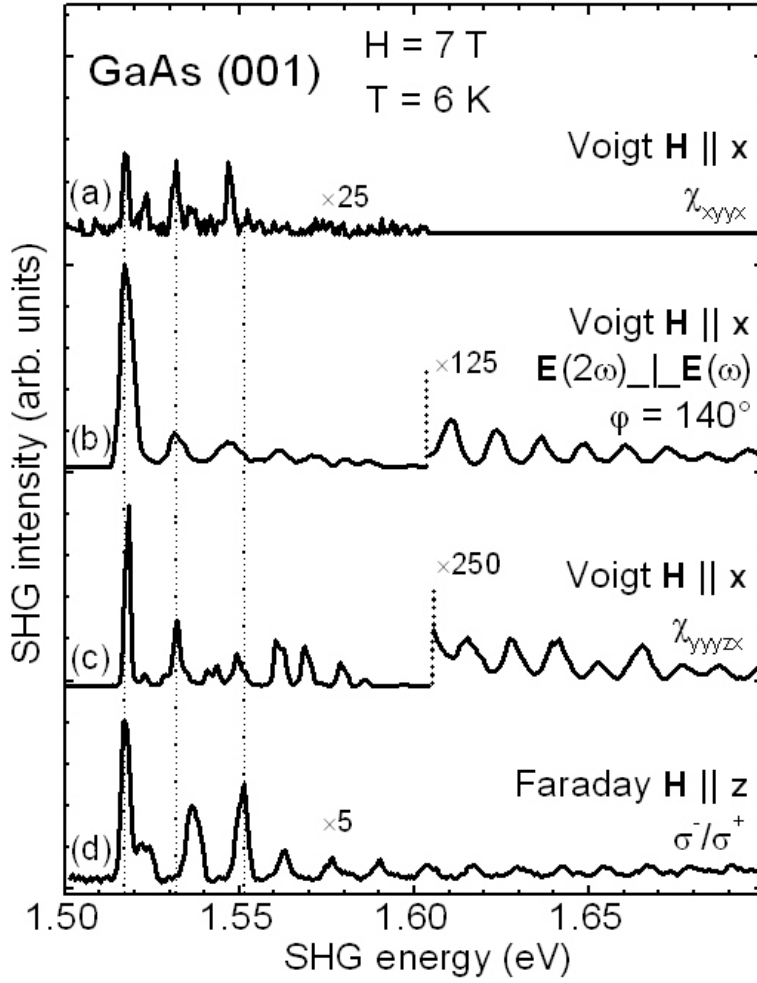
Figure 2.12: *MFISH spectra in GaAs for $\mathbf{k}(\omega)$ $\parallel$ $\mathbf{z}$ and different magnetic field orientations. In the Voigt geometry the light is linearly polarized: (a) Electric-dipole component χ_{xyyx} [$\mathbf{E}(2\omega)$ $\perp$ $\mathbf{E}(\omega)$ $\parallel$ $\mathbf{y}$], (b) Polarization geometry $\mathbf{E}(2\omega)$ $\perp$ $\mathbf{E}(\omega)$ with φ = 140° displaying an interference of all five tensor components, (c) Spatial-dispersion component χ_{yyyzx} [$\mathbf{E}(2\omega)$ $\parallel$ $\mathbf{E}(\omega)$ $\parallel$ $\mathbf{y}$], (d) In the Faraday geometry σ^- circularly polarized light is used for excitation and σ^+ polarized MFISH is detected. The ordinate scale shows MFISH intensity in arbitrary units, but the ratio between intensities for different geometries is relevant.*

is not sufficient for modeling the rotational anisotropy, and further terms have to be considered. Also the spectral and magnetic field dependencies of the different tensor components will be analyzed.

MFISH spectra, measured in different polarization configurations and magnetic field geometries at normal light incidence, are shown in Fig. 2.12. The applied magnetic field induces SHG signals consisting of a set of narrow lines in the spectral range of 1.51-1.70 eV. Here the extended energy range is displayed compared to the data given in Figs. 2.6 and 2.7.

In this Chapter, only the Voigt geometry spectra [Figs. 2.12(a)-(c))] are discussed. Their comparison with the Faraday geometry data is given in Ch. 2.7.

High spectral resolution (<1 meV) is reached by using a narrow monochromator slit leading to a lower MFISH intensity and therefore the signal-to-noise ratio decreased. MFISH signals measured for $\mathbf{E}(2\omega) \perp \mathbf{E}(\omega)$ and shown in Figs. 2.12(a) and (b) are allowed in the electric-dipole approximation described by Eq. (2.8). In the case of (a) it is given by the pure fourth-rank tensor component χ_{xyyx}. For (b) it could be explained by a contribution of the tensor components χ_{xyyx} and χ_{yxyx}. The signal measured in $\mathbf{E}(2\omega) \parallel \mathbf{E}(\omega)$ and shown in Fig. 2.12(c) corresponds to the χ_{yyyx} electric-dipole

Figure 2.13: *MFISH rotational anisotropy in GaAs for geometries* $\mathbf{E}(2\omega) \parallel \mathbf{E}(\omega)$ *(light shaded areas and open circles) and* $\mathbf{E}(2\omega) \perp \mathbf{E}(\omega)$ *(dark shaded areas and filled circles) measured at $T = 6$ K and $H = 7$ T. The experimental data are given by circles and the shaded areas represent simulations using Eqs. (2.17) and (2.18). Note that a proper description cannot be given in the electric-dipole approximation based on Eqs. (2.10) and (2.11) and displayed in panel (e). Panel (f) shows the crystal orientation in the experiment.*
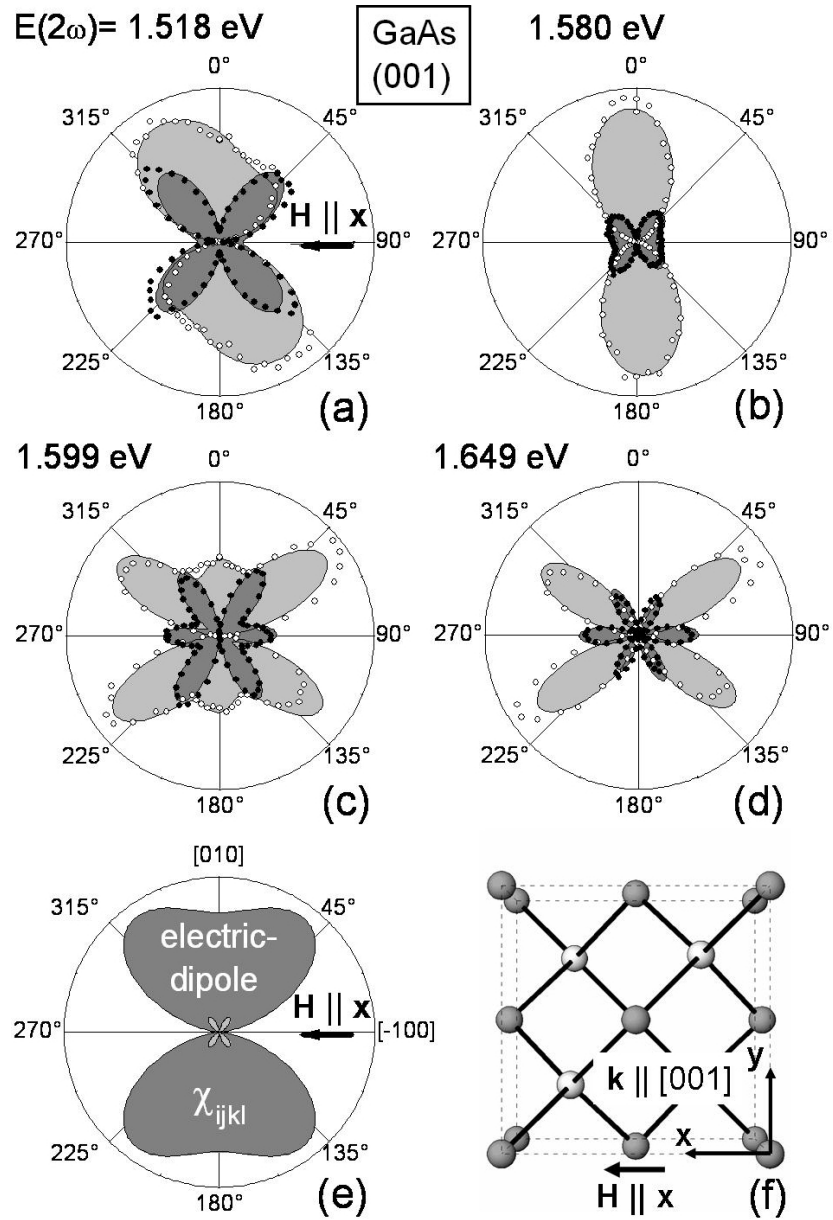
component, which, however, is forbidden. It becomes allowed taking into account the spatial-dispersion mechanism, which gives an MFISH contribution χ_{yyyzx} (fifth-rank tensor). Surprisingly, the MFISH intensity in the case of the χ_{yyyzx} component is 50 times larger than that for the electric-dipole allowed χ_{xyyx} component. It confirms, that the electric-dipole approximation is not sufficient and the magneto-spatial dispersion mechanism given by Eq. (2.13) is required for an adequate description of MFISH signals.

In the following the characteristic rotational anisotropy for different MFISH lines is considered. Thereby information about the underlying nonlinear optical processes is received. The MFISH intensities shown in Fig. 2.13 are given as a function of the angle φ between the polarization plane of the fundamental light and the crystallographic axis [010] for the $\mathbf{E}(2\omega) \parallel \mathbf{E}(\omega)$ and $\mathbf{E}(2\omega) \perp \mathbf{E}(\omega)$ geometries.

The rotational anisotropy of the MFISH signal features diverse twofold patterns which cannot be explained using only the electric-dipole approximation leading to a rotational anisotropy given by Eqs. (2.10) and (2.11) and shown exemplarily by Fig. 2.13(e). In conclusion, the magneto-spatial dispersion mechanisms, allowing e.g. the fifth-rank tensor component χ_{yyyzx}, is of big importance for the MFISH signals in GaAs.

The experimental data from Fig. 2.13 are fitted using Eqs. (2.17) and (2.18) and by taking into account, that the nonlinear optical susceptibilities are represented by complex numbers. Note that the real and imaginary parts of the nonlinear susceptibility, which are correlated to each other by the Kramers-Kronig equation, can vary strongly with the parameters of the experiment (e.g. the magnetic field strength, photon energy and temperature). This would lead in turn to strong changes in the shape of the rotational anisotropy. A Fortran program based on a modified Marquardt procedure [133] is used to fit the experimental data at each photon energy. The results of this computation are displayed in Fig. 2.13(a)-(d) by shaded areas. Good agreement between experimental and calculated MFISH intensities is found for all rotational anisotropies. This indicates that an approach, which includes both, electric-dipole and magneto-spatial dispersion, contributions is sufficient to describe the whole variety of observed MFISH signals.

2.6.1   Spectral dependence

In this part, the fitting procedure as well as the physical meaning of the fitting parameters will be discussed in more detail.

Considering the fact, that the tensor components of the nonlinear susceptibilities χ_{xyyx}, χ_{yxyx}, χ_{yxxzx}, χ_{yyyzx} and χ_{xxyzx} are represented by complex numbers, a set of ten fitting parameters is involved. One of the parameters [here: $\text{Im}(\chi_{xxyzx})=0$] can be fixed, which means a certain choice for the phase of the set of complex parameters. Unfortunately, the remaining set of nine parameters depends on the starting values used for the fitting procedure. Thus the set of fitting parameters is not unique and cannot be attributed to the real and imaginary parts of the nonlinear susceptibility. However, the absolute values of three tensor components $|\chi_{xyyx}|$, $|\chi_{yxxzx}|$ and $|\chi_{yyyzx}|$ are determined uniquely by this fitting procedure. An alternative possibility is to measure these values directly from the MFISH intensity for $\varphi = 0°$, $90°$ as can be seen from Eqs. (2.19)-(2.21). It leads to the same values of the tensor components as determined with the fitting procedure. No direct access to the absolute values of the tensor components $|\chi_{yxyx}|$ and $|\chi_{xxyzx}|$ can be obtained, since these components cannot be probed separately, because $\varphi \neq 0°$, $90°$ is required to obtain their contributions. But for $\varphi \neq 0°$, $90°$ all tensor components contribute and an interference of the imaginary and real parts of all components occurs [Eqs. (2.17) and (2.18)].

The set of absolute values of the tensor components obtained by the fitting procedure is given in Fig. 2.14 as function of the SHG energy. Fig. 2.14(a) shows the electric-dipole components described by a fourth-rank tensor, whereas Fig. 2.14(b) reveals the magneto-spatial dispersion components described by a fifth-rank tensor.
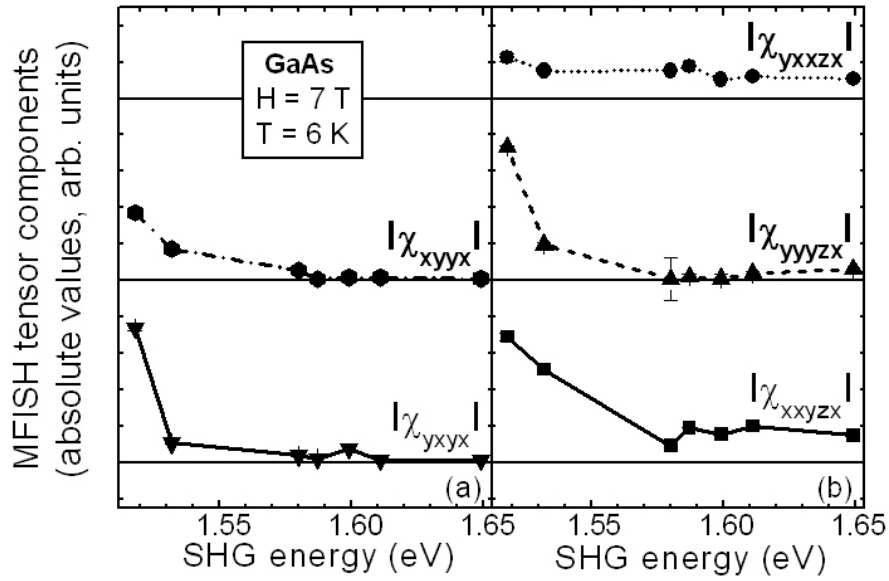
Figure 2.14: Spectral dependence of the absolute values of the MFISH tensor components in GaAs (a) electric-dipole components of χ_{ijkl}-type, (b) magneto-spatial dispersion components of χ_{ijklm}-type.

Strong changes of the slopes close to the GaAs band gap at 1.519 eV and a continuous decrease with increasing MFISH energy are confirmed. The reasonable magnitude of the error bars indicates a high reliability of the tensor component values found by the fitting procedure.

2.6.2 Magnetic field dependence

The magnetic field dependence of the tensor component χ_{yyyzx} shown in Fig. 2.8 is discussed above. Here the magnetic field dependence of the MFISH signal for different polarization geometries is discussed. Fig. 2.15(a)-(c) shows rotational anisotropy patterns for different magnetic fields. In the following specific polarizations are considered in order to explain the complex polarization dependence of the MFISH signal. In panels (a)-(c) triangles give the MFISH contribution of $I(2\omega)_{\parallel}^{MFISH}(\varphi = 0°) \propto |\chi_{yyyzx}|^2$, whereas data given by squares display the result of interference of all five tensor components $I(2\omega)_{\parallel}^{MFISH}(\varphi = 30°)$ according to Eq. (2.17). Panel (d) gives the magnetic field dependence of the MFISH intensity for these polarization geometries. In the case of $\varphi = 0°$, a quadratic dependence on the magnetic field is found for the MFISH intensity, whereas for $\varphi = 30°$, surprisingly, a linear dependence is revealed. In order to explain this linear dependence, the absolute values of the tensor components obtained by the fitting procedure are considered. They are shown in Fig. 2.16.

The component $|\chi_{yxxzx}|$ is rather weak and thus can be neglected. The specific field dependence found for $|\chi_{yxyx}|^2$ as well as the linear dependence for $|\chi_{xxyzx}|^2$ can be explained as follows. For $\varphi \neq 0°, 90°$, the MFISH intensity is given by a complex
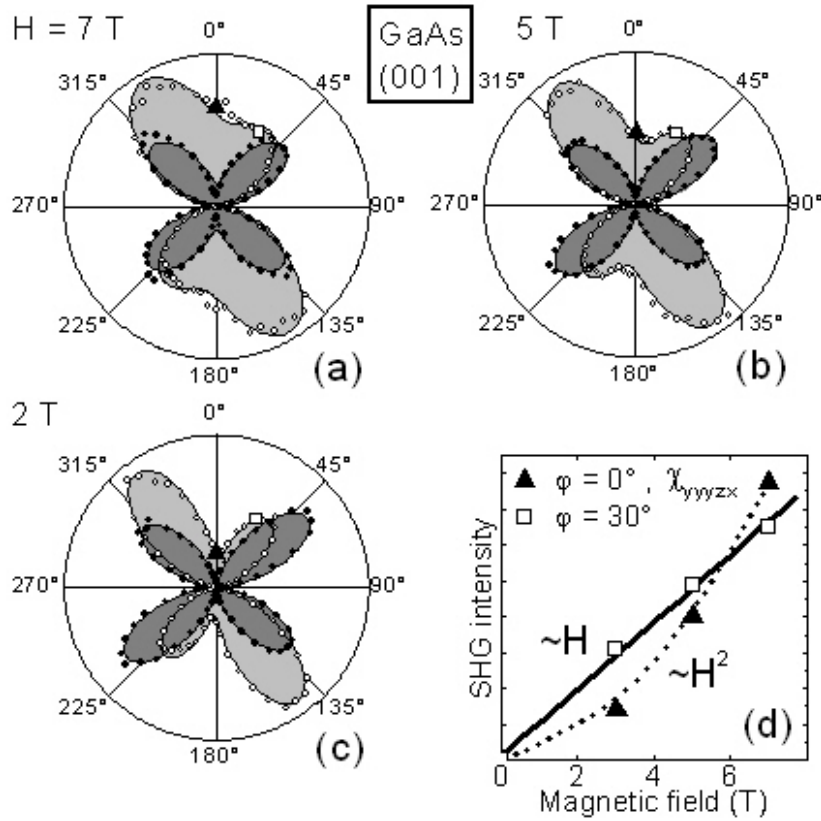
Figure 2.15: *MFISH rotational anisotropy of the X-line in GaAs measured at $T = 6$ K. In panel (d) specific polarization geometries are chosen to determine the MFISH intensity dependence of $I(2\omega)_\parallel^{MFISH}(\varphi = 0°) \propto |\chi_{yyyzx}|^2$ (triangles) and $I(2\omega)_\parallel^{MFISH}(\varphi = 30°)$ (squares) on magnetic field.*
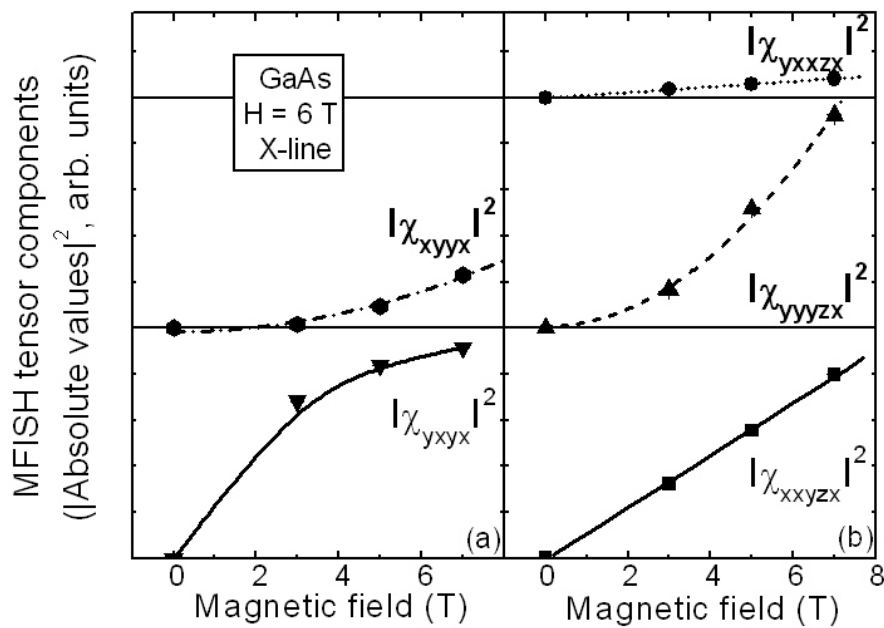
Figure 2.16: *Magnetic field dependence of the absolute values of the MFISH tensor components in GaAs for the X-line at $T = 6$ K obtained by the fitting procedure. (a) electric-dipole components of χ_{ijkl}-type, (b) magneto-spatial dispersion components of χ_{ijklm}-type.*

interference of all tensor components. This leads to the fact that the fitting procedure does not result in an unique set of parameters. Therefore the tensor components χ_{yxyx} and χ_{xxyzx} cannot be determined. One of the combinations for these components, that allows to describe the rotational anisotropies from Fig. 2.15, is given in Fig. 2.16. In contrast, the squared tensor components $|\chi_{xyyx}|$ and $|\chi_{yyyzx}|$ can be determined uniquely, as can be seen from Eqs. (2.21) and (2.19), respectively. Both components display a quadratic behavior on the magnetic field, which is in full accordance with Eqs. (2.8) and (2.13) and thus with the macroscopic model, since $I(2\omega)^{MFISH} \propto H^2$.

2.7 Comparison of Faraday and Voigt geometries

2.7.1 MFISH spectra

MFISH spectra obtained in the Faraday geometry with circularly polarized light (line) and the Voigt geometry with linearly polarized light (shaded area) are compared in Fig. 2.17. This comparison reveals some important differences.

The MFISH intensity in the Voigt geometry is found to be about five times stronger. This is not very surprising, as the nonlinear susceptibility tensor components are symmetry forbidden for the Faraday geometry (see Ch. 2.2) and cannot be described on the basis of Eqs. (2.8) and (2.13).

One of the explanations for the observation of the relatively strong MFISH signal in the Faraday geometry is based on a possible contribution of the crystallographic SHG mechanism. One can clearly see in Fig. 2.17 the existence of a background signal in the Faraday geometry, while it is not observed in the Voigt geometry. It is attributed to residual crystallographic SHG. Its interference with the magnetic SHG may explain the experimentally observed MFISH for the Faraday geometry.

Another possible explanation is the following: The magnetic field lifts the spin degeneracy of the Landau-levels and induces a spin quantization, which is characterized by the spin splitting $\mu_B (g_e + g_h) H$. Here μ_B is the Bohr magneton and $g_{e(h)}$ are the g-factors of conduction band electrons and valence band holes. Even though the spin splitting is small (it does not exceed one meV below 10 T), it might influence the MFISH process in the Faraday geometry, since the spin inversion symmetry is broken. This mechanism is similar to the MFISH process, which will be discussed for diluted magnetic semiconductors featuring giant Zeeman splitting in Ch. 3. For a description of the MFISH process in the Faraday geometry the additional spin degree of freedom would have to be taken into account.

Spectra in the Voigt geometry feature more lines and peak energies differ from those in the Faraday geometry. This originates from the symmetry of the conduction and valence band states and its modification for different configurations of the applied magnetic field and light wave vector. A detailed discussion will be given below.

The amplitude of the MFISH lines decreases with increasing energy for both field orientations, but the character of the decrease differs qualitatively for the two geometries. It can be seen from Fig. 2.12, where MFISH spectra in an extended energy
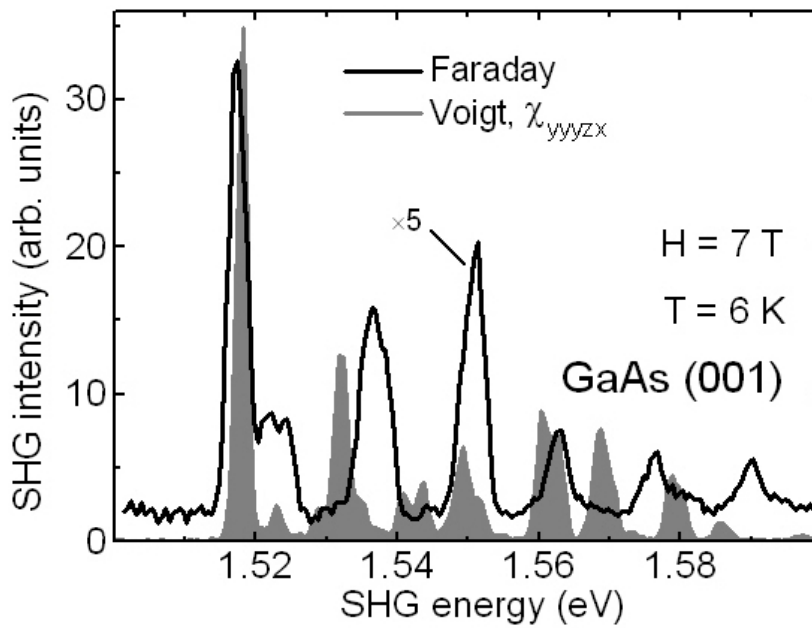
Figure 2.17: *MFISH spectra in GaAs. In the Faraday geometry circular σ^- polarized light is chosen for excitation and σ^+ polarized MFISH is detected (intensity is multiplied by a factor of 5). For comparison, the MFISH contribution χ_{yyyzx} (Voigt geometry) using linear polarizations is given by the shaded area.*
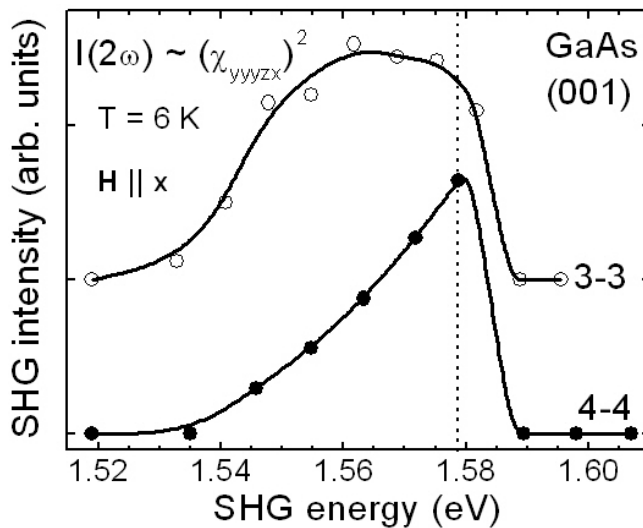
Figure 2.18: *Spectral dependence of the MFISH intensity described by χ_{yyyzx} for different Landau-levels in the Voigt geometry. The MFISH signal increases with the MFISH energy of the corresponding Landau-level transition $N_e - N_h$ (e.g. 3-3, 4-4), which is tuned by varying the magnetic field. Above 1.58 eV the MFISH intensity decreases rapidly.*

range up to 1.70 eV are displayed. The MFISH spectrum (d) for the Faraday geometry demonstrates a smooth intensity decrease within the whole energy range.

A remarkable feature of the spectra in the Voigt geometry is the abrupt decrease of intensity between 1.58 and 1.59 eV. In Fig. 2.12(a)-(c) it is shown for $H = 7$ T, and it can be followed on the fan chart of Fig. 2.7(b). It is indeed linked to a certain spectral energy and not to the Landau-levels, which pass this energy with increasing magnetic field. To illustrate that, the intensities of the 3-3 and 4-4 MFISH lines in the Voigt geometry are plotted in Fig. 2.18. The strong decrease above 1.58 eV has been established for all MFISH tensor components. A possible explanation for this cut-off energy at 1.59 eV might be the optical-phonon scattering. Note that the energy difference between this cut-off energy and the GaAs band gap (or $1s$-exciton ground state) is about 70 meV, which is rather close to the energy of two optical phonons of

$2\times\hbar\omega_{LO}=2\times36.6$ meV in GaAs.

2.7.2 Fan charts

In contrast to the good description of the MFISH signal in the Faraday geometry by the model of Landau-levels [see Fig. 2.6(b)], this model is not sufficient to explain the MFISH signal in the Voigt geometry [see Fig. 2.7(b)]. In general, the Coulomb interaction between electrons and holes has to be taken into account, which complicates the Landau-level diagram leading to a rich fan chart of magneto-excitons [130]. In opposite to the Coulomb interaction, which possesses a spherical symmetry, the Landau-level quantization features a cylindrical symmetry with an symmetry axis defined by the magnetic field. Consequently, no exact mathematical solution including both interactions can be formulated for the exciton. Instead, approximations for the limits of low and high magnetic fields have to be considered. In the case of low magnetic fields $\hbar\omega_c \ll R$, where ω_c is the cyclotron frequency and R is the exciton binding energy (exciton Rydberg), the Coulomb interaction dominates over the magnetic confinement, and gives $R \geq$4.2 meV for the 1s-exciton and $\geq$1 meV for the binding energy of the 2s-exciton in GaAs. The magnetic field is considered by perturbation theory, leading to a diamagnetic shift $\propto H^2$. In the case of high magnetic fields $\hbar\omega_c \gg R$ the Landau-level quantization, which is characterized by the cyclotron energy given by $\hbar\omega_c^e \approx 1.75$ meV/T for the electron states, prevails. Then the Coulomb interaction is treated by perturbation theory. Both descriptions are not suitable in the magnetic field range of a few Tesla, where $\hbar\omega_c \sim R$. In this case the magneto-excitons reveal a complicated spectrum already in linear absorption experiments [130]. Even richer spectra are expected for MFISH induced by two photons, which gives a higher flexibility to fulfill the angular momentum conservation. Therefore additional optical transitions, which are inactive for linear spectroscopy, might become allowed.

A possible explanation for the different fan charts in the Voigt and the Faraday geometry is the following: The bulk crystal has no intrinsic preferential direction. Such directions are introduced by experimental conditions: (a) by the magnetic field orientation, and (b) by the propagation direction of the fundamental light. In the Faraday geometry, these two directions coincide and only one preferential direction is present. The Landau-level orbital movement of the carriers is perpendicular to $\mathbf{k}(\omega)$ and therefore is in-plane of the light polarizations. In contrast, in the case of the Voigt geometry two such axes, which are perpendicular to each other, $\mathbf{H} \parallel \mathbf{x}$ and $\mathbf{k}(\omega) \parallel \mathbf{z}$, exist. Therefore the Landau orbital movement occurs in a plane, in which also the light propagation is located, which represents a geometry with lowered symmetry, so that more complex SHG selection rules are expected, leading to a richer magneto-exciton spectrum [see Fig. 2.7(b)].

Note that the strongest observed component in the Voigt geometry is χ_{yyyzx} (Fig. 2.16), where the polarizations of all light waves are parallel to the y axis, which is in the plane of the orbital movement caused by $\mathbf{H} \parallel \mathbf{x}$. In this case the polarizations can only couple to the movement of the carriers along the y axis but not along the z axis since $\mathbf{k}(\omega) \parallel \mathbf{z}$. In accordance with the previous argumentation, no χ_{xxxzx} MFISH

signal is observed, where polarizations of the light waves are parallel to the magnetic field $\mathbf{H} \parallel \mathbf{x}$ [see $I(2\omega)_{\parallel}^{MFISH}(\varphi = 90°)$ in Fig. 2.13(a)-(d)]. Strong MFISH contributions are also found, if the polarization of either the MFISH or the fundamental light wave has a component in the plane of the orbital movement ([see $I(2\omega)_{\parallel}^{MFISH}(\varphi = 0°)$, $I(2\omega)_{\perp}^{MFISH}(\varphi = 0°)$ or $I(2\omega)_{\perp}^{MFISH}(\varphi = 90°)$ in Fig. 2.13(a)-(d)]. This indicates, that the MFISH couples to the orbital movement of the carriers and therefore the orbital quantization plays a key role.

2.8 Magnetic-field-induced SHG in CdTe

So far the MFISH process is discussed for the III-V semiconductor GaAs. In order to prove the general nature of the observed phenomena, the II-VI semiconductor CdTe is chosen for further studies. The MFISH data are found to be very similar to the features observed in GaAs.

Fig. 2.19(a) shows MFISH spectra of CdTe in the Voigt geometry. In an applied magnetic field, a SHG signal appears consisting of a set of narrow lines in the spectral range from 1.59 to 1.67 eV. With increasing magnetic field, these lines shift to higher energies and gain in intensity. The intensity increase is proportional to H^2 as can be seen from the corresponding fit to the data for the strongest X-line (1s-exciton) in the inset, which is similar to GaAs (see Fig. 2.8). The X-line width is found to be less than 4 meV.

The fan chart of the MFISH lines is given in Fig. 2.19(b). Similarly to GaAs, these lines can be assigned to magneto-exciton states. The diamagnetic shift of the 1s-exciton state [134] given by the dashed line follows well the X-line. At zero magnetic field it starts from 1.596 eV, which is the 1s-exciton energy in CdTe at $T = 6$ K. The solid lines in Fig. 2.19(b), which trace optical transitions between Landau-levels, are calculated using Eq. (2.24) with the following parameters for CdTe at $T = 6$ K: $E_g = 1.606$ eV, $m_e^* = 0.096 \, m_0$ and $m_{hh}^* = 0.674 \, m_0$ [134]. Here the exciton spin splitting, which does not exceed 0.1 meV below 10 T, is not taken into account.

The MFISH intensities shown in Fig. 2.20 are given as a function of the angle φ between the polarization plane of the fundamental light and the crystallographic axis [010] for the $\mathbf{E}(2\omega) \parallel \mathbf{E}(\omega)$ and $\mathbf{E}(2\omega) \perp \mathbf{E}(\omega)$ geometries. Similar to GaAs, the rotational anisotropy of the MFISH signal features complicated twofold patterns. The MFISH rotational anisotropy is simulated by means of Eqs. (2.17) and (2.18). Good agreement between experimental and calculated MFISH intensities is found for all rotational anisotropies.

Fig. 2.21 shows the spectral dependence of the absolute values of the tensor components obtained from the fit of the rotational anisotropy data. As in GaAs (compare with Fig. 2.14), strong changes of the slope close to the band gap and a continuous decrease with increasing MFISH energy are observed.

Concerning the magnetic field dependence of the MFISH signal, an important difference to GaAs appears. Fig. 2.22 shows rotational anisotropy of the X-line for different

Figure 2.19: (a) MFISH spectra of CdTe at different magnetic fields in Voigt geometry and at $T = 6$ K. The inset shows the integrated intensity of the strongest X-line vs. magnetic field. The solid line is a H^2-fit to the data. (b) Landau-level fan chart diagram of the MFISH peak positions: circles are experimental data with intensities given by the symbol size. Solid lines give optical transitions between Landau-levels calculated from Eq. (2.24) for $N_e = N_h$. The dashed line gives literature data for the diamagnetic shift of 1s-exciton state [134].
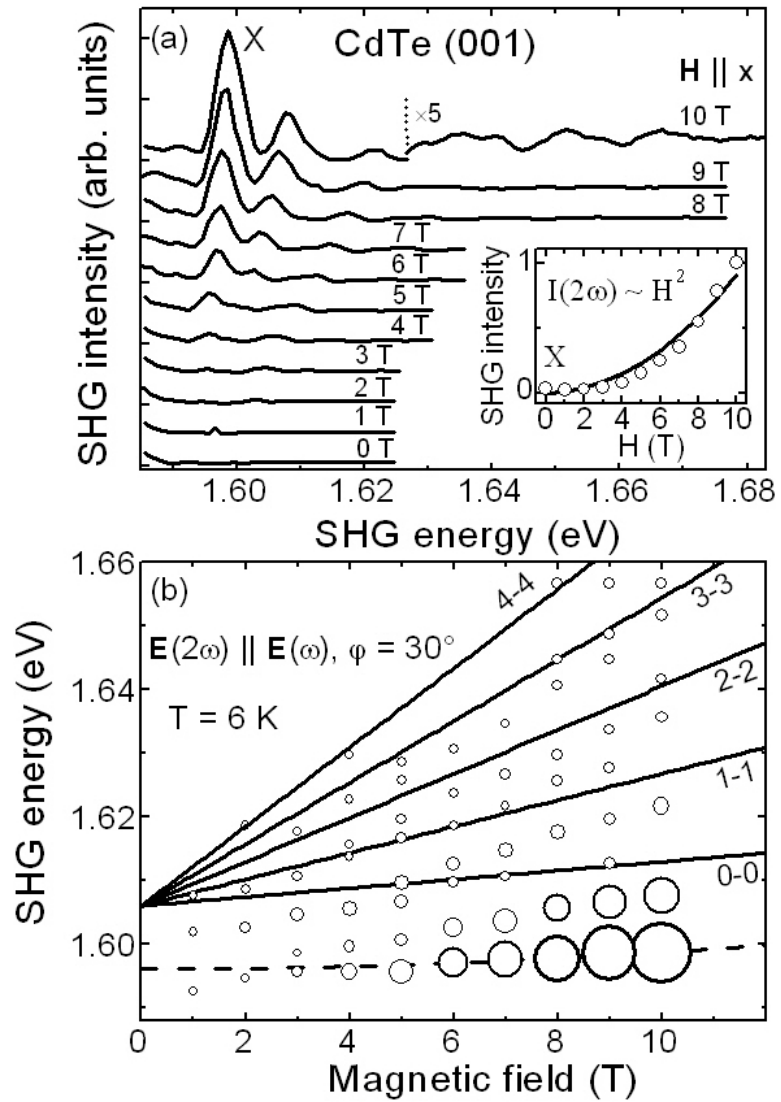
magnetic fields. The magnetic field dependence of $I(2\omega)_{\parallel}^{MFISH}(\varphi = 0°) \propto |\chi_{yyyzx}|^2$ and $I(2\omega)_{\parallel}^{MFISH}(\varphi = 30°)$ is given in panel (d). For both cases a quadratic magnetic field dependence of MFISH intensity is found. This is in partial contrast to GaAs [Fig. 2.15(d)], where a linear field dependence is observed for $I(2\omega)_{\parallel}^{MFISH}(\varphi = 30°)$.

Fig. 2.23 shows that also the absolute values of all five MFISH tensor components increase quadratically with the magnetic field, which is in opposite to the observation in GaAs (Fig. 2.16). Thus, in CdTe the experimental data are in full accordance with the macroscopic model described by Eqs. (2.8) and (2.13), which leads to $I(2\omega)^{MFISH} \propto H^2$.

The entirety of these findings shows that the MFISH phenomena in CdTe manifest themselves in a very similar fashion as in GaAs. This leads to the conclusion that very similar MFISH properties can be expected for the wide class of semiconductor and insulator materials with zinc-blende crystal structure.
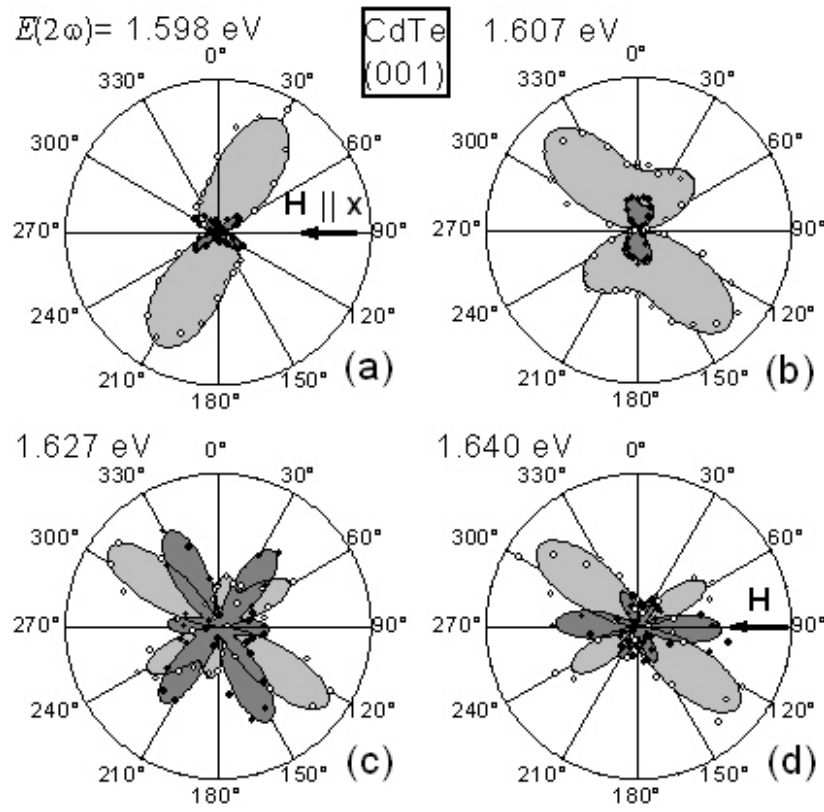
Figure 2.20: *MFISH rotational anisotropy in CdTe for the geometries* $\mathbf{E}(2\omega) \parallel \mathbf{E}(\omega)$ *(light shaded areas and open circles) and* $\mathbf{E}(2\omega) \perp \mathbf{E}(\omega)$ *(dark shaded areas and filled circles) at* $T = 6$ K *and* $H = 10$ T. *Experimental data are given by circles and shaded areas represent simulations using Eqs. (2.17) and (2.18).*
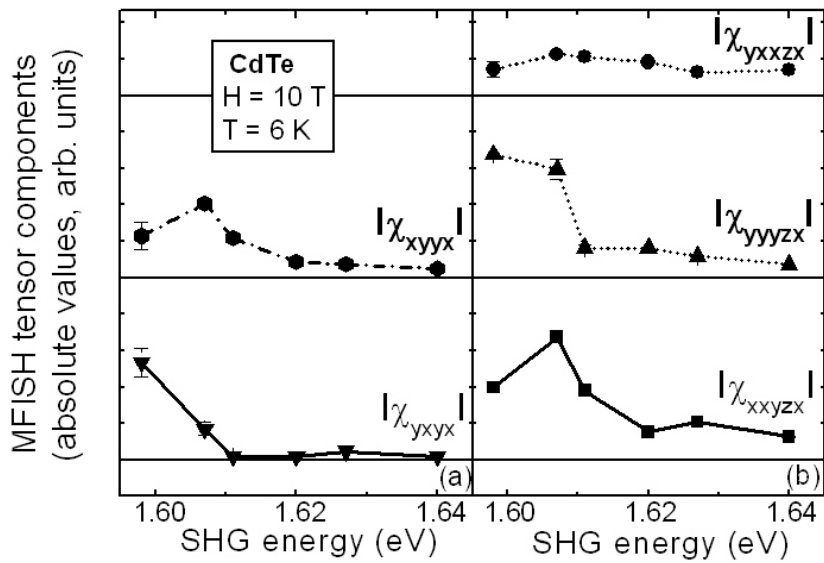
Figure 2.21: *Spectral dependence of the absolute values of the MFISH tensor components in CdTe obtained from simulation of the rotational anisotropies shown in Fig. 2.20: (a) electric-dipole components of* χ_{ijkl}-*type, (b) magneto-spatial dispersion components of* χ_{ijklm}-*type.*

Figure 2.22: (a)-(c): MFISH rotational anisotropy of the X-line in the geometries $\mathbf{E}(2\omega) \parallel \mathbf{E}(\omega)$ (light shaded areas and open circles) and $\mathbf{E}(2\omega) \perp \mathbf{E}(\omega)$ (dark shaded areas and filled circles) in CdTe at $T = 6$ K. (d): Specific polarization geometries are chosen to determine the MFISH intensity dependence of $I(2\omega)_{\parallel}^{MFISH}(\varphi = 0°) \propto |\chi_{yyyzx}|^2$ (triangles) and $I(2\omega)_{\parallel}^{MFISH}(\varphi = 30°)$ (squares) on the magnetic field.
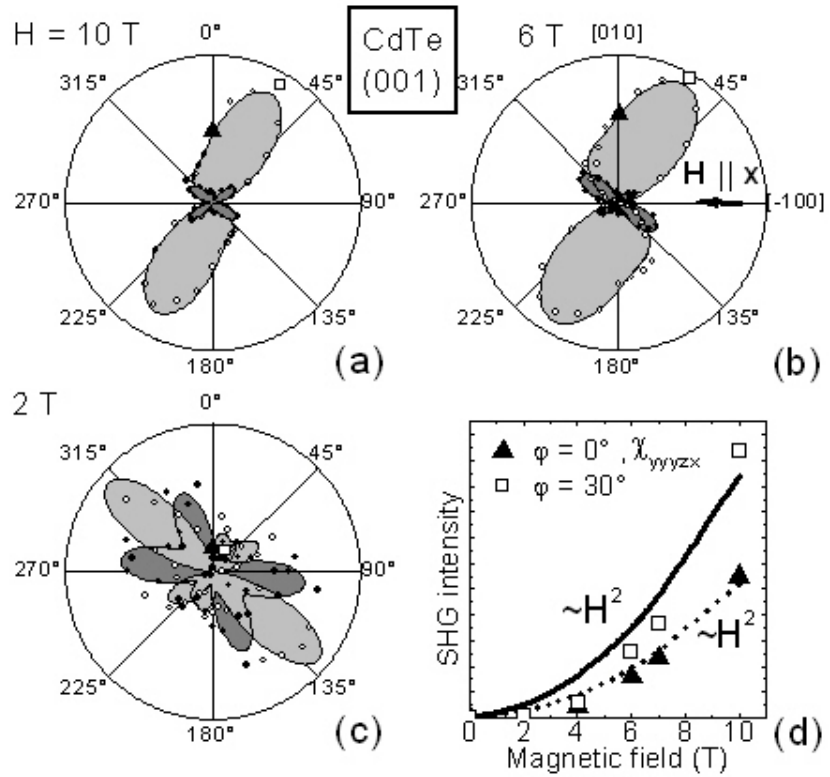
Figure 2.23: Magnetic field dependence of the absolute values of the MFISH tensor components in CdTe for the X-line at $T = 6$ K obtained by the simulation of the rotational anisotropies shown in Fig. 2.22. (a) electric-dipole components of χ_{ijkl}-type, (b) magneto-spatial dispersion components of χ_{ijklm}-type.
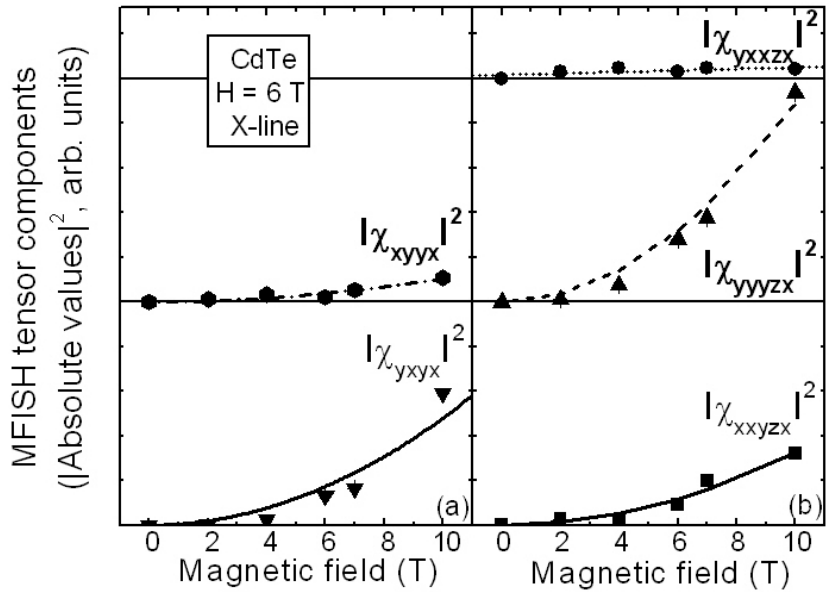
2.9 Crystal quality

It is well-known, that the structural quality of the crystal is of big importance for achieving an efficient SHG signal. This results from the coherent nature of the SHG process, where the coherence length is an important parameter. The same is expected for MFISH signals. Indeed, a strong correlation of the MFISH efficiency with the structural quality of the studied samples is found. In this part, two sets of samples with different approaches for the manipulation of the structural quality are examined. The first approach deals with the binary GaAs semiconductor grown by various technological procedures. Here the main difference comes from the density of the defects (see Ch. 2.3). The second approach exploits the concept of ternary alloys. It is examined for the $Cd_{1-x}Mg_xTe$ alloy, which is extended from the binary CdTe alloy by an isoelectronic substitution of Cd^{2+} cations by Mg^{2+} cations. This causes structural imperfections due to an inhomogeneous distribution of Mg^{2+} ions in the cation sublattice. Also the optical properties are influenced, e.g. the absorption edge is shifted to higher energies and broadened due to the alloy fluctuations.

2.9.1 GaAs

MFISH spectra for three different GaAs samples are shown in Fig. 2.24. For all samples the spectra are found to be similar with respect to the spectral peak positions, although the peak intensities vary significantly. Also the width of the MFISH lines differs from sample to sample. E.g. the width of the X-line is 1.9 meV, 6.3 meV and 5.1 meV for samples of type (i), (ii) and (iii), respectively. This is in good agreement with the higher density of defects in samples (ii) and (iii). As one can see in Fig. 2.24, with increasing line width the SHG intensity decreases about two orders of magnitude. Therefore, both criteria indicate that the sample (i) possesses the highest quality and the most efficient MFISH signal.

The rotational anisotropy of the X-line for different types of GaAs samples is shown in the insets of Fig. 2.24. All anisotropy patterns reveal roughly a similar shape for each sample compared to the strong changes for different energies in Fig. 2.13(a)-(d). Differences are attributed to the influence of the crystal quality on the nonlinear susceptibility tensor components.
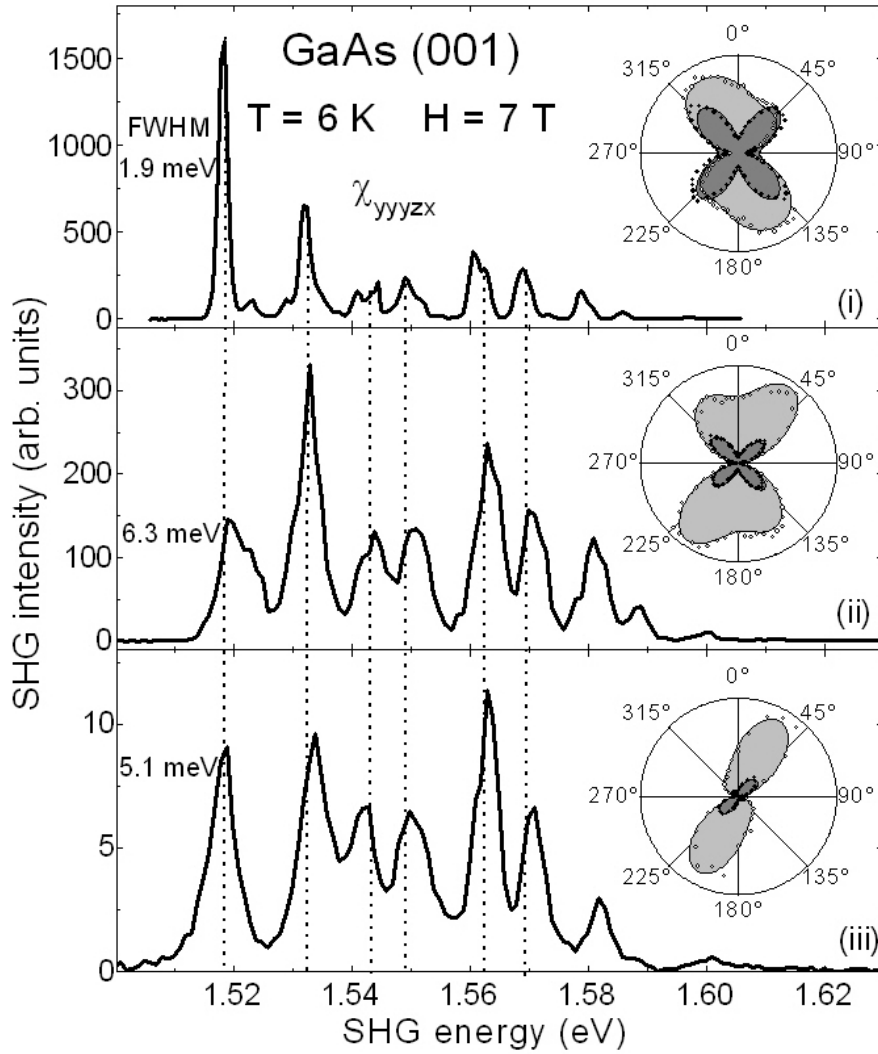
Figure 2.24: Influence of the sample quality on the MFISH spectra in GaAs. (i) 10 μm gas-phase-epitaxy layer, (ii) 2 μm epilayer grown by molecular-beam epitaxy, (iii) 0.5 mm platelet of bulk GaAs grown by the Bridgman method.

2.9.2 (Cd,Mg)Te

For the ternary alloy (Cd,Mg)Te, the structural quality is influenced by the Mg^{2+} content. Fig. 2.25 shows MFISH spectra for $Cd_{1-x}Mg_x$Te samples with magnesium concentrations of $x = 0$, 0.01 and 0.08. In comparison to the spectra shown for GaAs in Fig. 2.24, the magneto-exciton structure is less pronounced. In the case of $x = 0.01$ the exciton states related to the $0 - 0$, $1 - 1$ and $2 - 2$ Landau-level transition can be traced. However, for $x = 0.08$ only lines associated with the $0 - 0$ and $1 - 1$ transitions are observable and higher transitions are broadened and not distinguishable. In this case the number of observed magneto-exciton transitions can serve as a criterium for
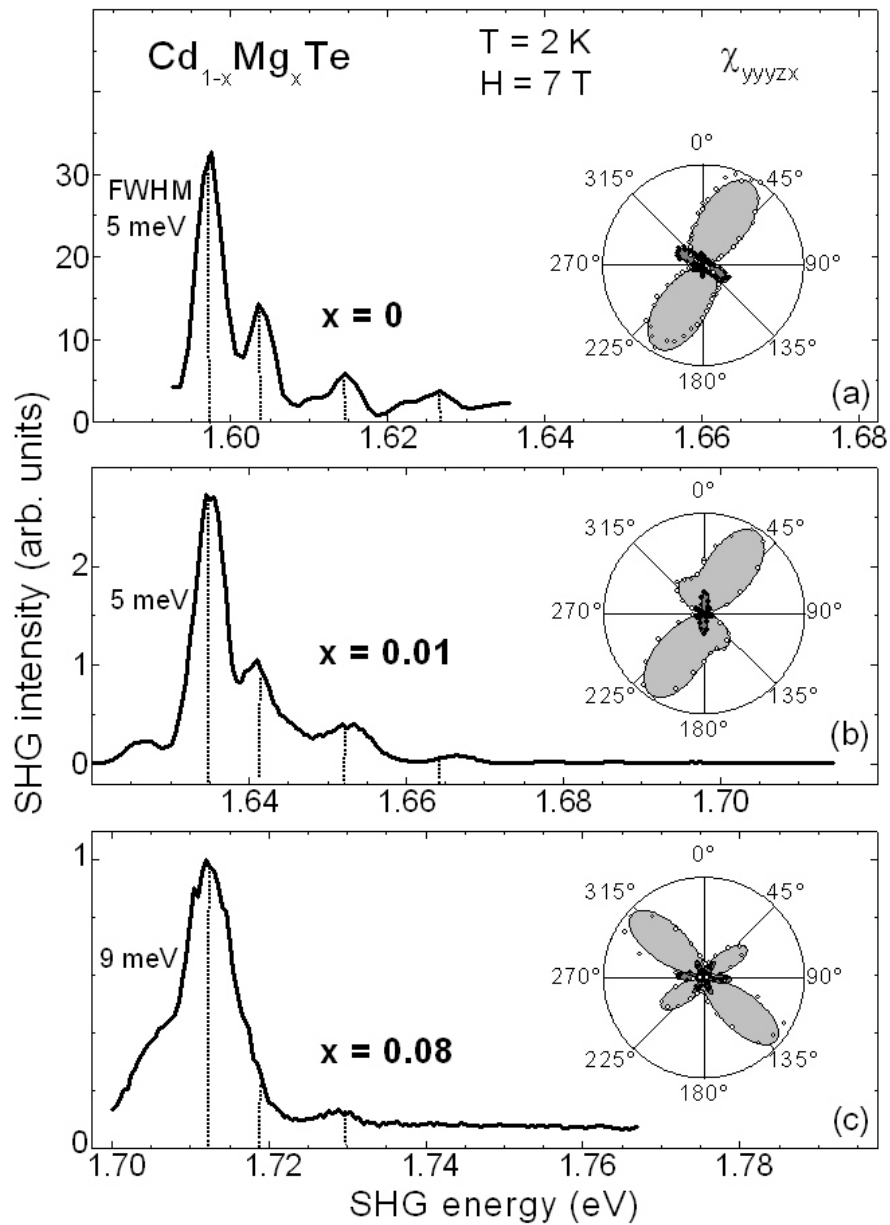
Figure 2.25: Influence of the magnesium concentration on the MFISH spectra and the rotational anisotropy in $Cd_{1-x}Mg_xTe$. (a) $x = 0$, (b) $x = 0.01$ (c) $x = 0.08$. Magnetic field is applied in the Voigt geometry.

the crystal quality. With increasing Mg concentration the MFISH intensity decreases by an order of magnitude and the X-line broadens from about 5 up to 9 meV.

Note that in $Cd_{1-x}Mg_xTe$ also a quadratic magnetic field dependence of the MFISH intensity corresponding to the χ_{yyyzx} component is found, which is presented for the Mg concentrations $x = 0.01$ and 0.08 in Fig. 2.26 and is similar to the results for $x=0$ shown in the inset of Fig. 2.19(a).

Figure 2.26: *MFISH intensity vs. magnetic field (Voigt geometry) in $Cd_{1-x}Mg_xTe$ with $x = 0.01$ and 0.08 for the component χ_{yyyzx}. Experimental data are shown by symbols. Solid lines are H^2-fits to the data.*
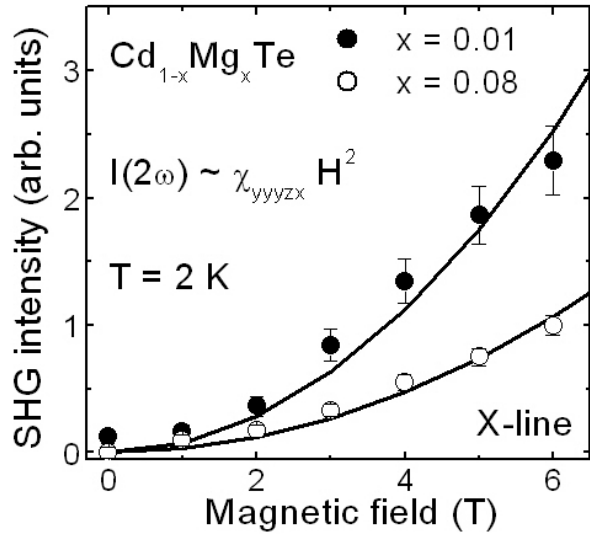
The insets of Fig. 2.25 display the rotational anisotropy of the X-line. Strong changes of the shape of the anisotropy patterns are observed indicating strong changes of the structural quality. Thus the quality of the crystal, which decreases with increasing Mg concentration, strongly influences the MFISH signal.

In this Chapter it is demonstrated that the various parameters of MFISH like the signal intensity, line broadening, number of distinguishable lines, as well as rotational anisotropy patterns are very sensitive to the structural quality of the materials. This may serve as a basis for optical methods for material characterization.

2.10 Summary

Magnetic-field-induced SHG is investigated in the diamagnetic semiconductors GaAs, CdTe and (Cd,Mg)Te possessing a direct band gap. Magneto-exciton states are found to be the basis for the MFISH process. Therefore orbital quantization of electronic states is the major source of MFISH in diamagnetic semiconductors. MFISH intensity is shown to depend quadratically on the strength of the magnetic field. Nonlinear magneto-optical spatial-dispersion is revealed to be necessary for explaining the MFISH process. The macroscopic analysis is based on symmetry considerations. Simulations of rotational anisotropy taking into account electric-dipole and magneto-spatial dispersion contributions show a good agreement with the experimental data.

A possible explanation of the involvement of higher order processes to the SHG by the application of a magnetic field is the following. The field induces an orbital quantization of free carrier states in conduction and valence bands. This leads to a strong increase of the density of states at the discrete Landau-level energies. Potentially this might cause the enhancement of higher order contributions. These magneto-spatial dispersion contributions show a characteristic length scale on the order of the light wave vector $\mathbf{k}(\omega)$.

MFISH spectroscopy beyond the electric-dipole approach combined with the application of external magnetic fields leads to new possibilities to study electronic and spin structures of semiconductors and their heterostructures. MFISH spectroscopy is a supplementary method and an alternative to linear optical methods. Exemplarily, the rotational anisotropy of the MFISH intensity varying with the MFISH energy might reflect the Bloch-function contributions to the Landau-levels. This might enable to obtain experimental information about the Bloch-function, which is hardly accessible by other optical methods.

The general nature of the observed MFISH phenomena is proved since the same MFISH process is found in III-V and II-VI semiconductors. Hopefully, the experiments will motivate the development of a microscopic theory, which is required for getting a better understanding of the involved physical mechanisms.

Chapter 3

Diluted magnetic semiconductors

Diluted magnetic semiconductors (DMS) are a large group of materials featuring plenty of various electronic, magnetic, optical and magneto-optical properties. In this group, diamagnetic ions at cation positions in the crystal structure of alloys on the basis of II-VI (e.g. CdTe, ZnSe, ZnO) or III-V (GaAs, GaN) semiconductors are partially replaced by paramagnetic ions as Mn, Ni, Fe, etc. [31, 106, 134]. Due to these magnetic ions with partially filled $(3d)^n$ or $(4f)^n$ shells, spin-dependent coupling between localized d- or f-states and s- and p-band-states occurs. This coupling mechanism based on the exchange interaction between carriers and localized ions can lead to magnetic ordering. A well known example is the $Ga_{1-x}Mn_xAs$ system with $x \sim 0.05 - 0.06$, where the ferromagnetic Curie temperature raises up to 100-150 K and even higher [135, 136]. The exchange interaction between holes and localized spins leads to phenomena as the magnetic-field-induced metal-insulator transition, the formation of the bound magnetic polarons etc. Moreover, this interaction leads to the giant Zeeman splitting of valence and conduction bands and impurity levels and therefore to giant Faraday rotation [137] and nonreciprocal linear birefringence in the Voigt configuration [32]. This gives rise to important practical applications of magnetic semiconductors as nonreciprocal devices in optical telecommunication systems.

Application of a magnetic field to a DMS medium leads to magnetic-field-induced symmetry breaking and can cause new optical nonlinearities. Different types of magnetic-field-induced SHG can be distinguished. In magnetically ordered materials phase transitions can be induced by a magnetic field leading to new allowed tensor components or single domains can be created which increases the existing SHG signal [25, 7]. In ferri- and ferromagnetic materials a spontaneous magnetization can be controlled by the magnetic field and magnetization-induced SHG is observed [138, 7]. Recently magnetization-induced SHG was observed in ferromagnetic $Ga_{1-x}Mn_xAs$ [139]. Applying a magnetic field to para- or diamagnetic materials reduces the symmetry and therefore new SHG contributions are induced. Magnetic-field-induced SHG in diamagnetic semiconductors is discussed in Ch. 2.

In this chapter, orbital and spin quantization of electronic states as a driven mechanism of magnetic-field-induced SHG in the semiconductor $Cd_{1-x}Mn_xTe$ ($x = 0 - 0.64$) will be discussed. SHG spectra with well-defined polarization properties and character-

istic magnetic-field and temperature dependencies are observed around the band gap in $Cd_{1-x}Mn_xTe$. These phenomena are explained by specific nonlinear processes for the interaction of light with the magnetized medium, taking into account Landau-orbital and Zeeman-spin quantization of semiconductor bands. Subsequently, MFISH will be used to study spin glass phase magnetic properties.

$Cd_{1-x}Mn_xTe$ is chosen for the present study as being one of the most studied DMS. It is a model material for fundamental physics and is also used for technological purposes. It was found as a very good magneto-optical medium for non-reciprocal devices and high-resolution Faraday microscopy at low temperatures [140]. Strong thermally induced self-focussing of a laser beam near the band-edge was observed in $Cd_{1-x}Mn_xTe$ ($0 < x < 0.6$) at room temperature [141]. Measurements of the absolute values of the SHG coefficient d_{41} in the transparency region at $\lambda = 1.5$ μm using bulk $Cd_{1-x}Mn_xTe$ characterize it as a promising nonlinear-optical material [142].

3.1 Macroscopic description of SHG

Similar to GaAs and CdTe, (Cd,Mn)Te crystallizes in the zinc-blende structure described by the non-centrosymmetric point group $\overline{4}3m$. From the symmetry point of view in the electric-dipole approximation [2, 3, 4] the leading order SHG polarization $\mathbf{P}(2\omega)$ is given by Eq. (2.2) and is discussed in Ch. 2.2. For (001)-oriented samples, the crystallographic SHG vanishes for normal light incidence. Then the MFISH contribution is assumed to be be described by

$$
\begin{aligned}
P_i(2\omega) &= \epsilon_0 i \chi_{ijkl} E_j(\omega) E_k(\omega) B_l(0) \\
&+ \epsilon_0 \chi_{ijklm} E_j(\omega) E_k(\omega) k_l(\omega) B_m(0),
\end{aligned} \tag{3.1}
$$

according to Ch. 2.2. Here $\mathbf{B}(0) = \mu_0[\mathbf{H}(0) + \mathbf{M}(0)]$ is the magnetic induction, $\mathbf{H}(0)$ is the static external magnetic field and $\mathbf{M}(0)$ is the magnetization of the medium. The magnetic-field-induced nonlinear susceptibilities χ_{ijkl} and χ_{ijklm} as well as the resulting rotational anisotropy are discussed in detail in Ch. 2.2.

3.2 Band structure in magnetic field

The process of SHG in the vicinity of the semiconductor band gap involves electronic states from the bottom of the conduction band and the top of the valence band. Application of a magnetic field gives rise to Landau-level (LL) orbital quantization [131] and to spin splitting due to the Zeeman effect. For the sake of simplicity, the Coulomb attraction between electrons and holes will not be considered. For modeling the optical spectrum, here only transitions between LLs with equal quantum numbers $N = 0, 1, 2, ..$ for electron and hole are considered, since they have the largest oscillator strength and therefore dominate in the spectra as is shown above. With these approximations, the energy spectrum near the band gap can be described by:

$$
E = E_g + E_{LL}(N) + E_Z(S, J) + E_{GZ}(S, J). \tag{3.2}
$$
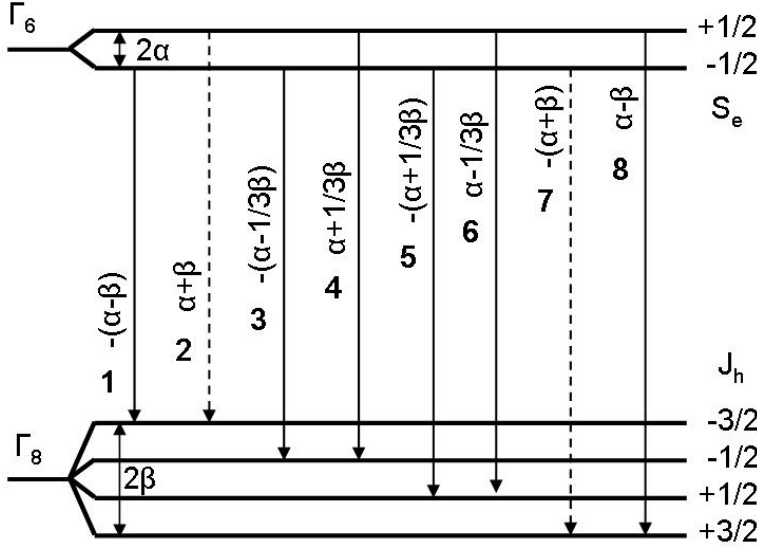
Figure 3.1: *Giant Zeeman splitting diagram: In a magnetic field the conduction (Γ_6) and valence (Γ_8) bands split according to Eq. (3.4). The optical transitions between the electronic states are labeled by **1-8**. Transitions **2** and **7** are forbidden for single-photon processes, as they require a change of the spin by ± 2.*

Here E_{LL} describes the LL quantization. The third term in Eq. (3.2) accounts for the spin splitting due to the Zeeman effect:

$$E_Z(S_e, J_h) = (S_e g_e + J_h g_h)\mu_B H, \tag{3.3}$$

with projections on the field direction of the electron spin $S_e = \pm\frac{1}{2}$ and the hole total angular momentum $J_h = \pm\frac{3}{2}, \pm\frac{1}{2}$. $g_{e(h)}$ are the g-factors of electrons (holes). μ_B is the Bohr magneton. The last term in Eq. (3.2) is the giant Zeeman splitting in diluted magnetic semiconductors [31]:

$$E_{GZ}(S, J) = x S_0 N_0 (\frac{\beta}{3}J - \alpha S) B_{\frac{5}{2}} \left[\frac{5\mu_B g_{Mn} H}{2 k_B (T_{Mn} + T_0)} \right], \tag{3.4}$$

where $g_{Mn}=2$. k_B is the Boltzmann constant, and T_{Mn} is the temperature of the Mn-spin system (in the experiment $T_{Mn} = T$). S_0 and T_0 are phenomenological parameters describing the Mn-Mn antiferromagnetic interactions. $B_{\frac{5}{2}}$ is the modified Brillouin function. $N_0\alpha$=220 meV and $N_0\beta$=-880 meV are the exchange integrals for the conduction and valence band states, interacting with the localized magnetic moments of the Mn^{2+} ions [31]. Fig. 3.1 shows schematically the giant Zeeman splitting described by Eq. (3.4). The possible transitions between the electronic states are labeled by **1-8**. These labels of the electronic transitions will be used in the following. ΔE_{GZ}, which is defined by

$$\Delta E_{GZ} = E_{GZ}(+\frac{1}{2}, +\frac{3}{2}) - E_{GZ}(-\frac{1}{2}, -\frac{3}{2}), \tag{3.5}$$

gives the energy splitting of the exciton states in a magnetic field.

The competition between the terms $E_{LL}(N)$ and $E_{GZ}(S, J)$ is shown in Fig. 3.2. The energy level diagrams are calculated for different Mn concentrations. Spin and orbital quantization have different functional dependencies on the magnetic field. E_{GZ} saturates with increasing field, whereas E_{LL} and E_Z increase linearly. In diamagnetic wide band gap semiconductors E_Z is one or two orders of magnitude smaller than E_{LL}.
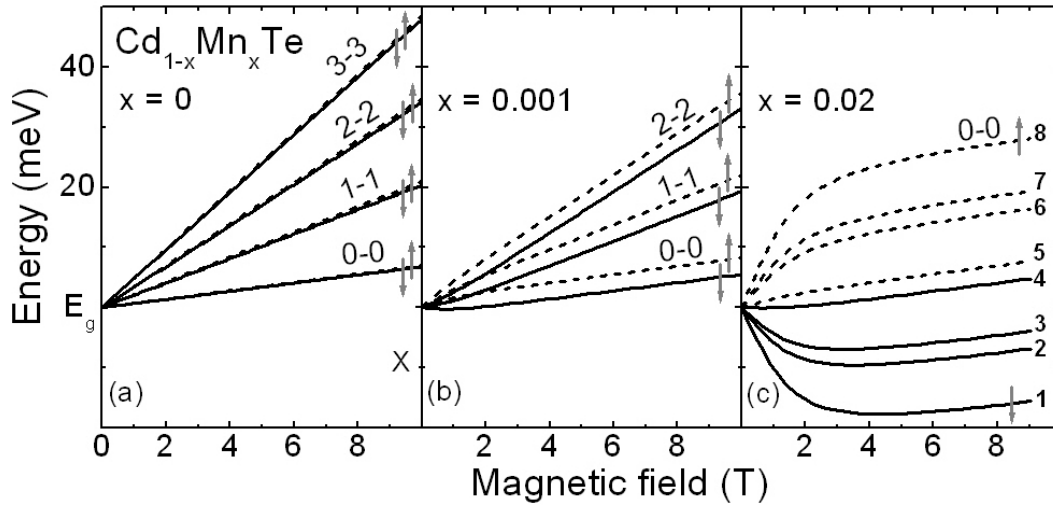
Figure 3.2: *Influence of the Mn concentration x on the band structure of $Cd_{1-x}Mn_xTe$ in a magnetic field: (a) $x=0$: the Landau-level contribution $E_{LL}(N)$ dominates the band structure, (b) $x=0.001$: the Landau-level contribution $E_{LL}(N)$ and the giant Zeeman splitting $E_{GZ}(S,J)$ influence the band structure significantly, (c) $x=0.02$: the giant Zeeman splitting $E_{GZ}(S,J)$ dominates. Modeling is done for $T = 2$ K.*

For example, in CdTe at $H=10$ T the exciton Zeeman splitting does not exceed 0.1 meV, while the cyclotron energy amounts to 10 meV (see Fig. 3.2(a)). By contrast, in diluted magnetic semiconductors E_{GZ} varies up to 100 meV, and can become considerably larger than E_{LL} (see Figs. 3.2(c)). Therefore in (Cd,Mn)Te one can realize situations in which either orbital or spin quantization dominates. The investigation of their interplay becomes possible, if E_{GZ} is on the order of E_{LL} (see Figs. 3.2(b)).

3.3 Description of $Cd_{1-x}Mn_xTe$ samples

Three different types of $Cd_{1-x}Mn_xTe$ samples are investigated:

(A) $Cd_{1-x}Mn_xTe$ epilayers with concentrations $x > 0.1$ are grown by molecular beam epitaxy on (001)-oriented GaAs substrates. CdTe is used as a buffer layer on which a 10 μm epitaxy layer of $Cd_{1-x}Mn_xTe$ is grown. Samples with $x = 0.04$ (no. 121404A), 0.08 (no. 52505D), 0.12 (no. 052505C), 0.16 (no. 121404B), 0.18 (no. 52505A), 0.22 (no. CT485), 0.36 (no. 121404C) and 0.64 (no. 121504B) are investigated. For these samples, E_g varies from 1.67 eV to 2.62 eV.

(B) $Cd_{1-x}Mn_xTe$ epilayers with concentrations $x < 0.1$ are grown by molecular beam epitaxy on (001)-oriented GaAs substrates. $Cd_{0.8}Mg_{0.2}Te$ (E_g=1.96 eV) is used as a buffer layer on which a 1 μm epitaxy layer of $Cd_{1-x}Mn_xTe$ is grown. On top, a 50 μm $Cd_{0.8}Mg_{0.2}Te$ layer is grown to prevent surface effects. Experimental results for $x = 0.001$ (E_g=1.61 eV) (no. 052705A) are presented here.
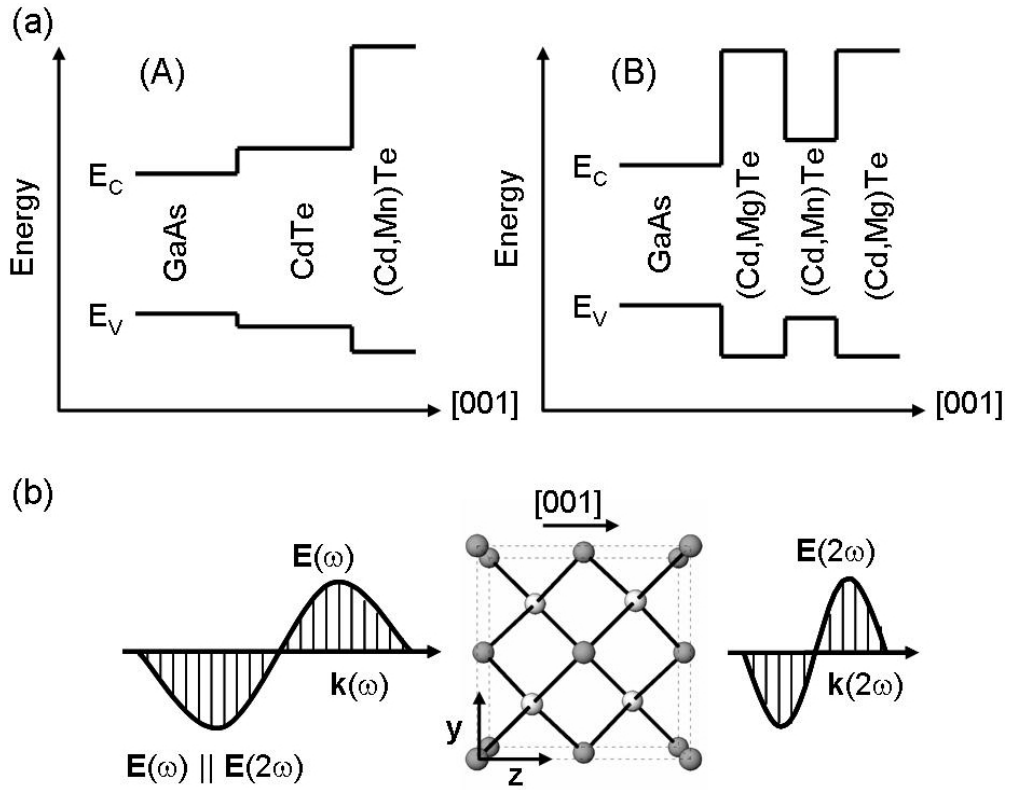
Figure 3.3: *(a) Band structure of samples of type (A) and (B). (b) Experimental geometry with $\mathbf{k}(\omega)$ $\parallel$ $\mathbf{z}$ for (001)-oriented samples. Exemplarily polarizations $\mathbf{E}(2\omega) \parallel \mathbf{E}(\omega) \parallel \mathbf{y}$ are shown.*

(C) Cd$_{1-x}$Mn$_x$Te bulk single crystals are grown by the Bridgman method. The orientation of the crystals is checked by X-ray technique. The thickness of the coplanar (110) and (100) platelets vary in the range of $0.2 - 0.9$ μm. The samples are characterized by optical absorption and photoluminescence (PL) spectra given in Ref. [45]. Samples with $x = 0.24$, $x = 0.35$ and $x = 0.40$ are investigated. Only experimental results for $x = 0.24$ are presented here.

Fig. 3.3(a) shows the band structures of samples of type (A) and (B).

Fig. 3.3(b) shows schematically the experimental geometry. The coordinate system of the light waves is given by the wave vectors $\mathbf{k}(\omega) \parallel \mathbf{k}(2\omega)$ and the polarizations $\mathbf{E}(\omega)$ and $\mathbf{E}(2\omega)$ of the fundamental and the SHG light wave, whereas the crystallographic coordinate system is defined by the crystallographic axes $\mathbf{x}$, $\mathbf{y}$ and $\mathbf{z}$. Exemplarily, the figure shows the polarizations geometry $\mathbf{E}(2\omega) \parallel \mathbf{E}(\omega) \parallel \mathbf{y}$ with $\mathbf{k}(\omega) \parallel \mathbf{k}(2\omega) \parallel \mathbf{z}$. Applying a static magnetic field $\mathbf{H} \parallel \mathbf{x}$, this geometry is described by the tensor component χ_{yyyzx} in Eq. (2.13). Exact 90° angle between light propagation $\mathbf{k} \parallel \mathbf{z}$ and magnetic field direction $\mathbf{H} \parallel \mathbf{x}$ is very important in order to avoid any Faraday rotation of the fundamental and SHG light polarization in the sample.

3.4 Crystallographic SHG

The crystallographic SHG contribution has been investigated in several works [45, 123]. In order to measure the crystallographic SHG, the (001)-oriented $Cd_{0.84}Mn_{0.16}Te$ sam-
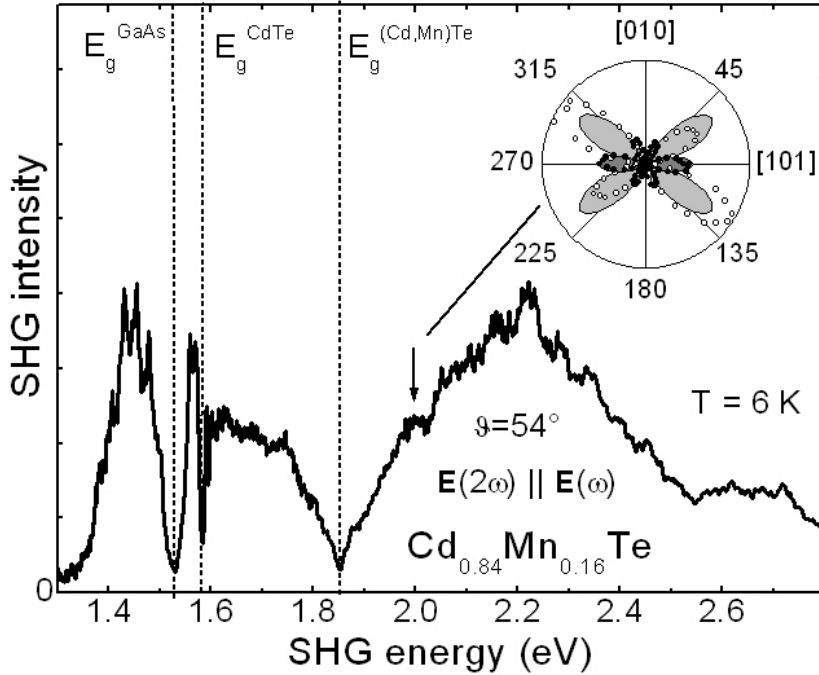
Figure 3.4: *Crystallographic SHG spectrum and rotational anisotropy in a $Cd_{0.84}Mn_{0.16}Te$ sample of type (A) for the geometry $\mathbf{E}(2\omega) \parallel \mathbf{E}(\omega)$ with $\vartheta = 54°$ according to Eq. (2.4). The inset shows the rotational anisotropy for the geometries $\mathbf{E}(2\omega) \parallel \mathbf{E}(\omega)$ (light grey shaded area and open dots) and $\mathbf{E}(2\omega) \perp \mathbf{E}(\omega)$ (grey shaded area and filled dots).*

ple is tilted by 45° around the [010] axis (see Ch. 2.4). Crystallographic SHG in transmission geometry in a wide spectral range is shown in Fig. 3.4 for $Cd_{0.84}Mn_{0.16}Te$ of type (A). A strong decrease of the SHG intensity is found close to the band gaps of GaAs (1.519 eV), CdTe ($\sim$1.596 eV) and $Cd_{0.84}Mn_{0.16}Te$ ($\sim$1.861 eV). This decrease does not display the pure spectral dependence of the squared nonlinear optical susceptibility given by Eq. (2.2). Note that reabsorption of the SHG light reduces the SHG intensity strongly around each band gap. In the following the continuous decrease of the coherence length will be considered below and above the band gaps influencing the SHG spectrum. Similar to GaAs, below the band gap the coherence length for the SHG light at normal incidence can be calculated by Eq. (2.22). Above the band gap the coherence length is reduced to the value of attenuation length given by Eq. (2.23). Both mechanisms explain the strong decrease of the SHG intensity close to each band gap. SHG below each band gap is believed to be generated in the accordant layer of the sample (see also Fig. 3.24 and the detailed discussion in Ref. [45]), and reabsorption leads to a vanishing of the SHG signal above each band gap. Note that the excitation

of the exciton is parity forbidden for the SHG process described by Eq. (2.2). For this reason no X-line is observed in the crystallographic SHG spectrum.

The angular dependence of the rotational anisotropy of the SHG signal can be calculated on the basis of Eqs. (2.4) and (2.5). A fit on the experimental data is shown by the inset of Fig. 3.4 for $Cd_{0.84}Mn_{0.16}Te$. Relatively good agreement between experimental data and simulations (shaded areas) is observed confirming a proper orientation of the sample. The distortion of the anisotropy (open data points) indicates, that the structural and optical quality is not very good compared to that of the GaAs and CdTe epilayers investigated in Ch. 2. Probably, strain between different layers of the heterostructure or inhomogeneity cause this distortion. Furthermore the strong rotational anisotropy evidences, that no two-photon luminescence is detected and the signal is fully contributed by SHG. In the case of two-photon luminescence, an isotropic signal is expected since it is a lower order process.

3.5 Magnetic-field-induced SHG

In the following the crystallographic SHG contribution χ_{ijk} will not be considered since it is suppressed by a proper choice of the experimental geometry. (001)-oriented $Cd_{1-x}Mn_xTe$ samples and normal light incidence are used allowing no generation of crystallographic SHG.

The MFISH contribution is studied as a function of the photon energy, magnetic field, temperature and azimuthal orientation of light polarizations in the following. First, wide range MFISH spectra will be discussed for a $Cd_{0.84}Mn_{0.16}Te$ sample of type (A). Then the spin quantization induced MFISH contribution around the band gap of $Cd_{0.96}Mn_{0.04}Te$ is considered. Subsequently, the influence of the Mn concentration on the observed features will be shown.

3.5.1 Wide range spectra

Fig. 3.5(a) shows typical MFISH spectra of a $Cd_{1-x}Mn_xTe$ sample of type (A). A sketch of the band gap structure is given in Fig. 3.5(b). Since the hole crystal is transparent for the fundamental light at the frequency ω ($\hbar\omega < 1.5\ eV$) and the band gap energies of the stacked layers GaAs, CdTe and $Cd_{1-x}Mn_xTe$ increase along the direction of the light propagation, MFISH from all layers is observable and no band gap absorption of the MFISH in the following layer(s) appears. Above 1.5 eV and 1.6 eV the MFISH signals generated in the GaAs and CdTe layers, respectively, can be observed and are spectrally well separated due to the different band gap energies. Depending on the concentration x, the MFISH signal induced in $Cd_{1-x}Mn_xTe$ is also separated spectrally ($E_g(x) > 1.6$ eV).

MFISH spectra for a specific polarization at T=5 K for normal light incidence are shown by Fig. 3.5(a) for H=0 T and H=9 T. Note that at zero magnetic field only a weak signal (gray area) is observed below 1.6 eV, which might be attributed to residual

Figure 3.5: *(a) MFISH spectrum for $\mathbf{k}(\omega) \parallel z$ and $\mathbf{H}(0) \parallel x$ in GaAs/CdTe/ $Cd_{0.84}Mn_{0.16}Te$. Due to the difference in the band gap energies of GaAs, CdTe and $Cd_{1-x}Mn_xTe$, the MFISH contributions are spectrally well separated. (b) Band structure of samples of type (A): GaAs (001) substrate is used to grow a CdTe buffer layer and, on top, a $Cd_{1-x}Mn_xTe$ epilayer. The sketch shows the energy gap of the different layers in combination with the SHG processes.*
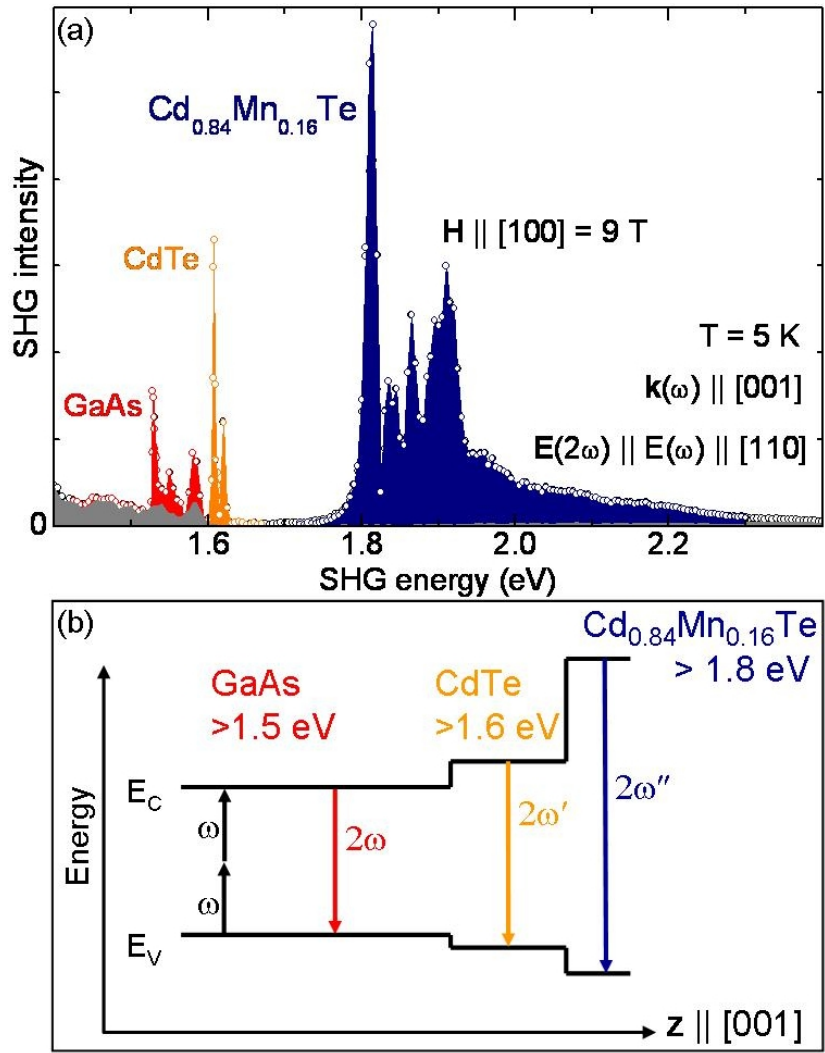
photoluminescence. The absence of the signal above 1.6 eV confirms the proper suppression of the crystallographic SHG contribution. The applied magnetic field induces a SHG signal consisting of a set of narrow lines in the spectral ranges 1.52-1.59 eV and 1.60-1.68 eV. These MFISH contributions, which are generated in the diamagnetic semiconductor layers GaAs and CdTe, are discussed in Ch. 2. Another MFISH contribution consisting of a set of narrow lines as well as a spectrally broad background is present in the spectral range 1.75-2.40 eV which is related to the $Cd_{0.84}Mn_{0.16}Te$ layer. The center of the set of narrow lines found in the spectral range 1.80-1.95 eV coincides with the band gap energy $E_{gap} = 1.86$ eV of $Cd_{0.84}Mn_{0.16}Te$ at 4.2 K. The line width of the narrowest line at 1.8 eV is (20±3) meV. A maximum splitting between the lines of about 120 meV is observed. The exact spectral positions of the lines depend on the polarizations of the light waves, which will be discussed in the following.
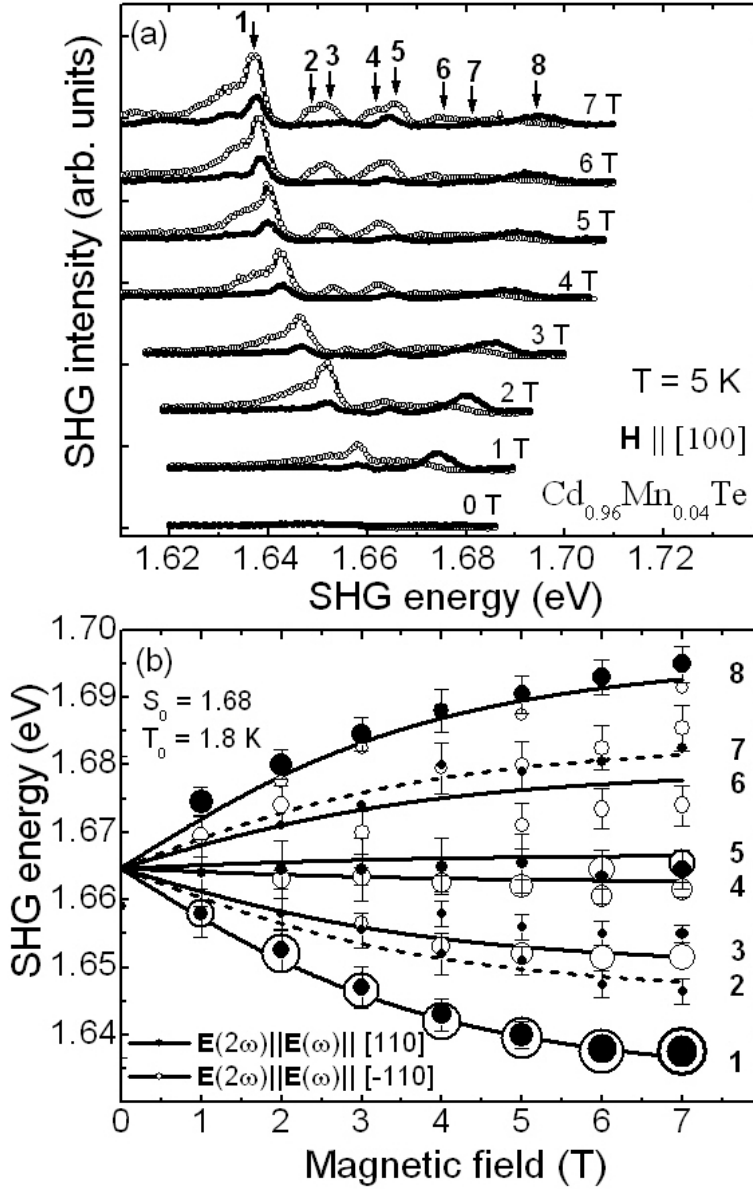
Figure 3.6: (a) MFISH spectra of $Cd_{0.96}Mn_{0.04}Te$ measured for $\mathbf{k}(\omega)\|\mathbf{z}$ and $\mathbf{H}\|\mathbf{x}$ for two polarization combinations. (b) Peak positions of the MFISH lines vs. magnetic field. Dots are experimental data with relative intensities given by the symbol sizes. Lines give the energies of optical transitions calculated according to Eqs. (3.2) and (3.4) with S_0=1.68 and T_0=1.8 K.

3.6   Spin quantization induced SHG

In this section, the MFISH contribution near the band gap of $Cd_{1-x}Mn_x Te$ will be considered more detailed by variation of the magnetic field and the temperature.

3.6.1   Field dependence

Fig. 3.6(a) shows SHG spectra obtained near the band gap of $Cd_{0.96}Mn_{0.04}Te$ ($E_g = 1.67$ eV) at different magnetic fields (T=5 K). The spectra radically differ from those of GaAs or CdTe. They feature eight lines, which shift and gain intensity with increasing magnetic field. The energy splitting ΔE_{GZ} between the strongest peaks labelled 1 and 8 amounts to 57 meV > $E_{LL} = 10$ meV at H=7 T, which is a typical value for the giant
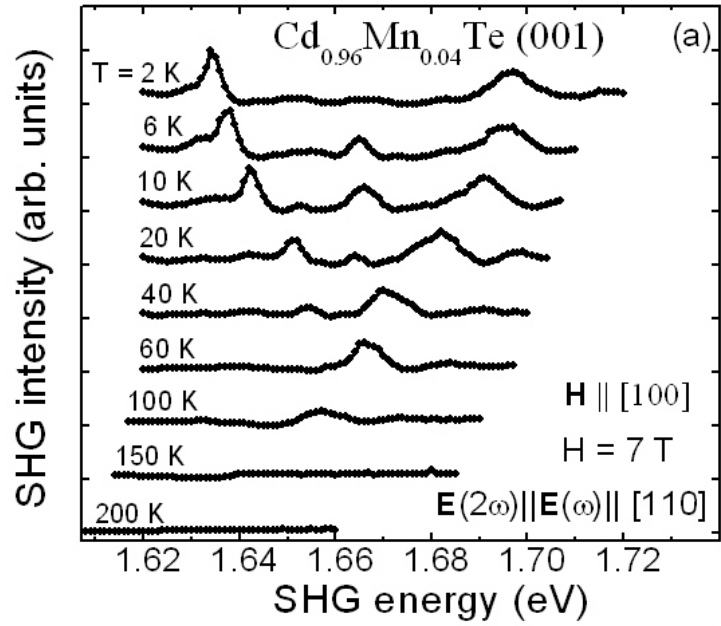
Figure 3.7: *(a) Temperature dependence of MFISH spectra of $Cd_{0.96}Mn_{0.04}Te$ measured for $\mathbf{k}(\omega)\|\mathbf{z}$ and $\mathbf{H}\|\mathbf{x}$ for two polarization combinations. (b) MFISH peak energies in $Cd_{0.96}Mn_{0.04}Te$ vs. temperature at $H{=}7$ T. Dots are experimental data with intensities given by the symbol sizes. Solid lines are calculations accounting for the temperature dependencies of the giant Zeeman splitting and of the band gap [88].*
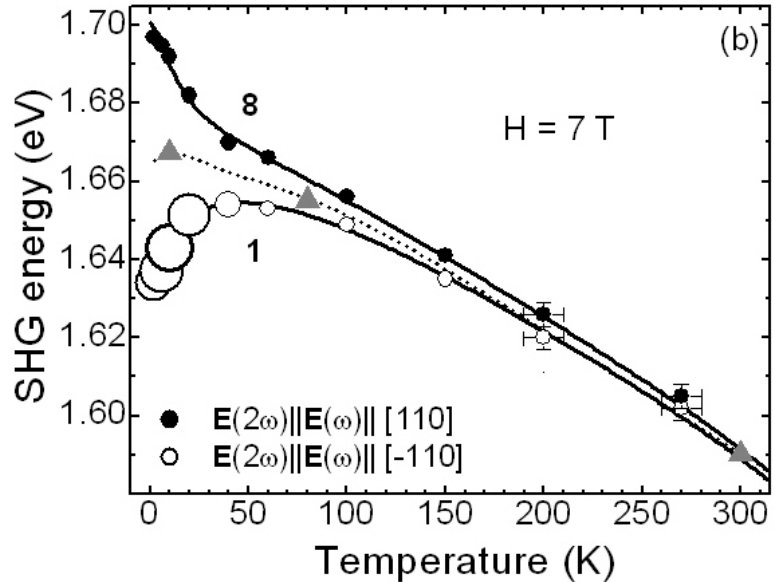
Zeeman splitting of heavy-hole exciton states in $Cd_{0.96}Mn_{0.04}Te$, as measured, e.g., in reflectivity [31]. Note that as compared to the diamagnetic GaAs and CdTe, MFISH signal appears in (Cd,Mn)Te at the energies of the spin-split optical transitions. The line width is about 4 meV and is independent of H, which is similar to the MFISH line width for CdTe (see Ch. 2).

The energy shifts of the eight lines in magnetic field are given in Fig. 3.6(b) by symbols. Lines indicate the energies calculated according to Eqs. (3.2) and (3.4) for the optical transitions between the spin-split conduction and valence bands in $Cd_{0.96}Mn_{0.04}Te$. A very good agreement is achieved between experimental results and calculations, confirming the assignment of the optical transitions, which is shown more detailed by the scheme in Fig. 3.1. Note, that the transitions **2** and **7**, highlighted by the dashed

lines, require a change of angular momentum by ± 2 and therefore cannot be excited by one-photon processes (compare to Fig. 1.12(b)). However, it is possible to address them by SHG, since two photons are involved in the excitation process.

3.6.2 Temperature dependence

In order to prove unambiguously, that the mechanism of MFISH generation originates from spin quantization, the specific temperature dependence of the spin splitting in diluted magnetic semiconductors is exploited. ΔE_{GZ} depends strongly on the polarization of the Mn spins and therefore on the temperature T_{Mn} of the Mn-ions. The energy shifts of the two strongest MFISH lines **1** and **8** in the temperature range from 2 to 270 K are given in Fig. 3.7. With increasing temperature the giant Zeeman splitting decreases continuously, and this is accompanied by a strong reduction of the SHG intensity. The peak energies can be well reproduced by Eqs. (3.2) and (3.4) plus the known dependence for the temperature shift of the band gap in (Cd,Mn)Te at H=0 T [88]. The results of this modeling are shown by the solid lines. The line width increases from $\sim$4 meV at 2 K up to $\sim$7 meV at 100 K due to carrier-Mn spin exchange scattering.

3.6.3 Spin quantization

From the data in Figs. 3.6 and 3.7 it is obvious, that the MFISH in (Cd,Mn)Te is controlled by the giant Zeeman splitting. In the following the MFISH intensity integrated over the strongest line **1** as well as the giant Zeeman splitting will be discussed as functions of the magnetic field and the temperature. The variation of ΔE_{GZ} shown in Figs. 3.8(c) and (d) is in good agreement with the calculations based on Eqs. (3.2) and (3.4) (solid line). In addition the MFISH intensity dependence on the magnetic field as well as on the temperature is described by the same modified Brillouin function, which is shown in Figs. 3.8(a) and (b). Therefore, an important experimental finding is, that the SHG intensity in $Cd_{0.96}Mn_{0.04}Te$ is proportional to the spin splitting.

   For deeper insight, in Fig. 3.9 the experimentally obtained dependence of the MFISH intensity on ΔE_{GZ}, which is tuned by a variation of either the magnetic field or the temperature, are plotted. One data set is measured at T=5 K for H varied in the range $0-7$ T (closed circles), and another set is taken at H=7 T for temperatures ranging between $6-200$ K (open circles). The data sets are in close coincidence and can be well described by a linear dependence. The dependence $I(2\omega) \propto \Delta E_{GZ}$ additionally confirms, that the MFISH in paramagnetic (Cd,Mn)Te is determined by the spin-splitting.

3.6.3.1 Spin-splitting as a source of MFISH

In the following a possible explanation of the vanishing of the MFISH signal in zero magnetic field is given. If the electronic states involved in the SHG process are spin-degenerated in zero magnetic field, the spin-contribution to SHG might vanish, because
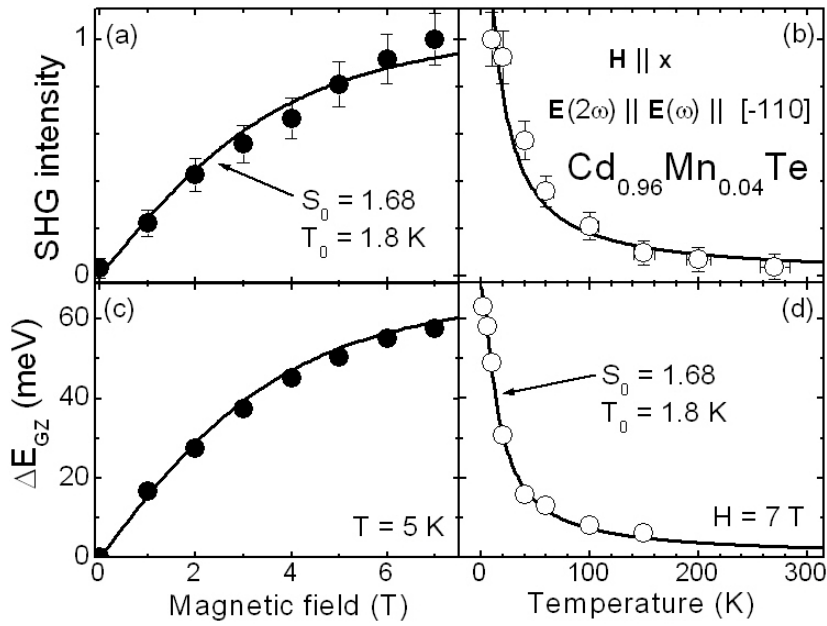
Figure 3.8: *Integrated MFISH intensity vs. magnetic field (a)and temperature (b) and giant Zeeman splitting vs. magnetic field (c) and temperature (d) in $Cd_{0.96}Mn_{0.04}Te$. Solid lines are fits to the data using the Brillouin function of Eq. (3.4).*

the spins possess a randomly distributed phase and therefore the SHG contributions annihilate each other. When the magnetic field is applied, the degeneracy is lifted, since the wave functions of different spin states have different phases. With increasing field the mixing of states with different phases decreases and thus the MFISH intensity might increase. It may be expected, that the phase of the MFISH signal from spin states with opposite spin directions lead to a phase difference of 180° of the according MFISH
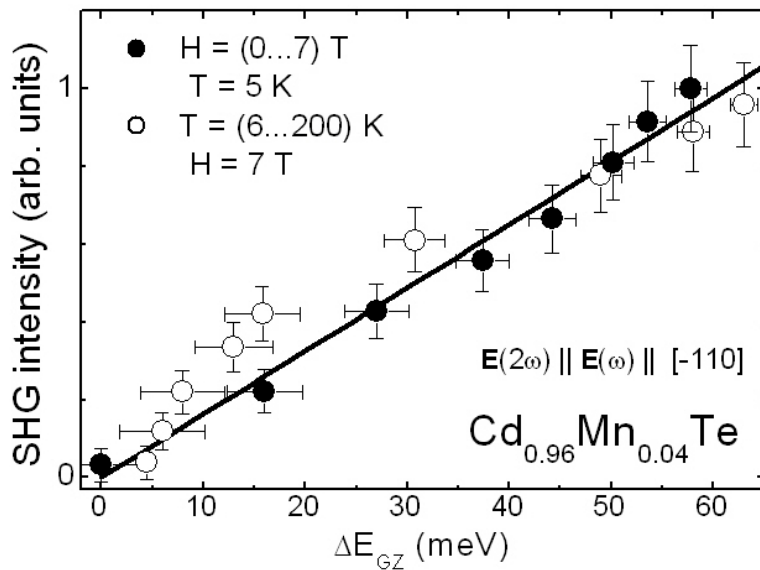
Figure 3.9: *Integrated SHG intensity as a function of the giant Zeeman splitting ΔE_{GZ}, which is controlled either by the magnetic field at a fixed temperature (closed circles) or by the temperature at a fixed magnetic field (open circles). The line is a linear interpolation of the experimental data.*
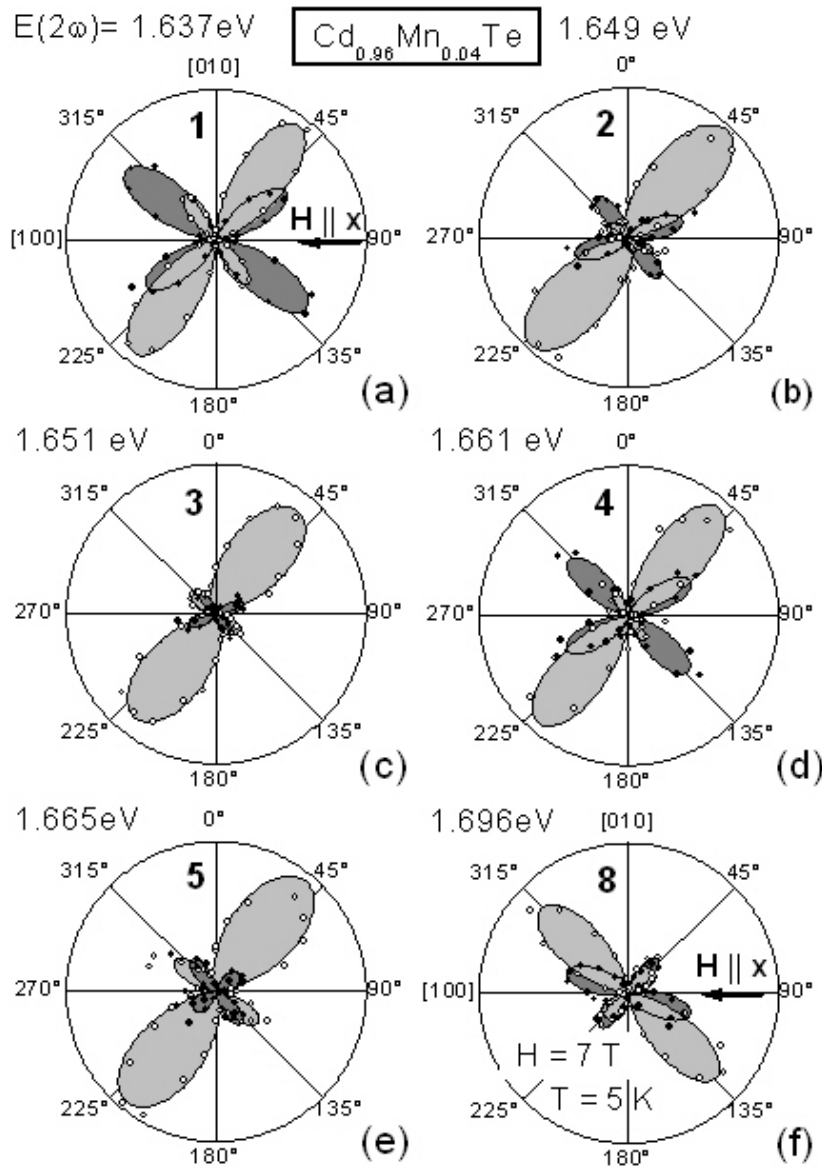
Figure 3.10:
Rotational anisotropy of the MFISH signals for the optical transitions **1-5** and **8** in $Cd_{0.96}Mn_{0.04}Te$. The anisotropy is given for geometries $\mathbf{E}(2\omega) \parallel \mathbf{E}(\omega)$ (light shaded areas and open circles) and $\mathbf{E}(2\omega) \perp \mathbf{E}(\omega)$ (dark shaded areas and filled circles) at 5 K and 7 T. The experimental data are given by circles and shaded areas present simulations.

signals. Hints for such an interference are observed in MFISH spectra in positive and negative magnetic fields [143].

In comparison, the orbital quantization induced MFISH can be explained by an increasing density of states at the Landau-levels, which leads to a resonance enhancement of the SHG process and thus to the observed intensity increase. In opposite, spin splitting lifts the degeneracy of the spin states and might increase the degree of coherence of the spin states contributing to the spin-induced SHG process.

3.6.4   Rotational anisotropy

The MFISH rotational anisotropies shown by Fig. 3.10 are recorded as a function of the azimuthal angle φ between the crystallographic [010] axis and the fundamental MFISH polarization $\mathbf{E}(\omega)$ for the $\mathbf{E}(2\omega) \parallel \mathbf{E}(\omega)$ and $\mathbf{E}(2\omega) \perp \mathbf{E}(\omega)$ geometries.

The rotational anisotropy of the MFISH signal features diverse twofold patterns which cannot be explained using only the electric-dipole approximation described by the nonlinear susceptibility χ_{ijkl} in Eq. (3.1). The experimental data for the rotational anisotropy have been fitted simultaneously for both geometries taking into account the complexity of the nonlinear optical susceptibilities χ_{ijkl} and χ_{ijklm} in Eqs. (3.1). The fitting procedure is described in more detail in Ch. 2.6.1. The calculated curves are shown by lines with shaded areas. Similar to the results for diamagnetic semi-conductors, a good agreement between experimental and calculated MFISH intensities is found for the rotational anisotropy, indicating that a combination of electric-dipole and spatial-dispersion mechanisms is responsible for the observed nonlinear optical phenomena in diluted paramagnetic semiconductors.

3.6.4.1   Spectral dependence
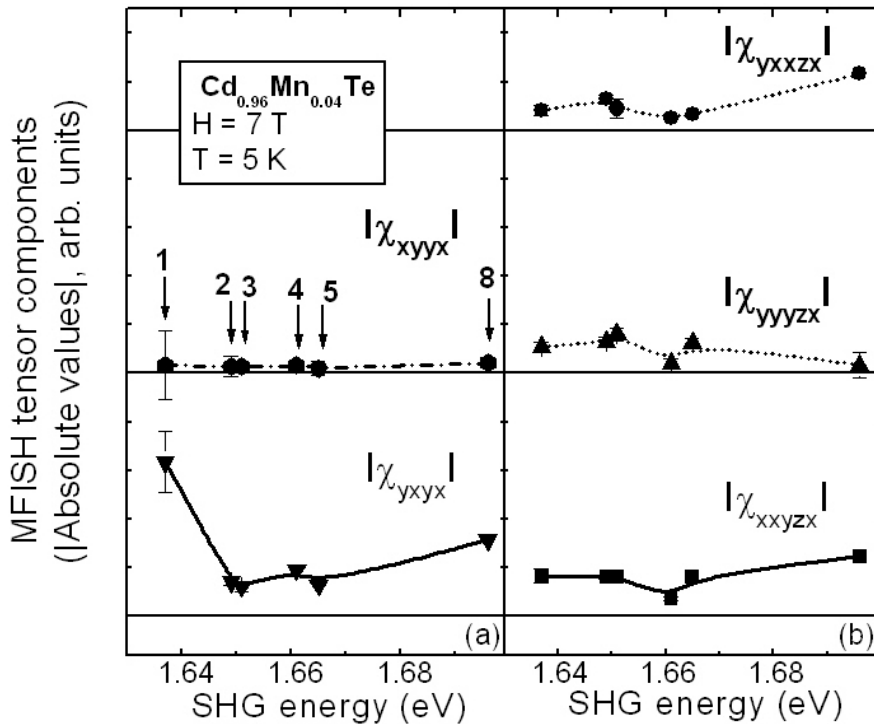
Figure 3.11: Spectral dependence of the absolute values of the MFISH tensor components in Cd$_{0.96}$Mn$_{0.04}$Te: (a) electric-dipole components of χ_{ijkl}-type, (b) magneto-spatial dispersion components of χ_{ijklm}-type.

The set of absolute values of the tensor components obtained by fitting the rotational anisotropies, which are shown in Fig. 3.10, is given in Fig. 3.11 as a function of the SHG energy at 7 T and 5 K. Note that values for $|\chi_{yxyx}|$ and $|\chi_{xxyzx}|$ are not unique and thus no physical meaning can be attributed, but values for $|\chi_{xyyx}|$, $|\chi_{yxxzx}|$ and $|\chi_{yyyzx}|$ can unambiguously be determined and thus reveal the absolute values of the nonlinear susceptibility tensor components (see detailed discussion in Ch. 2.6.1).
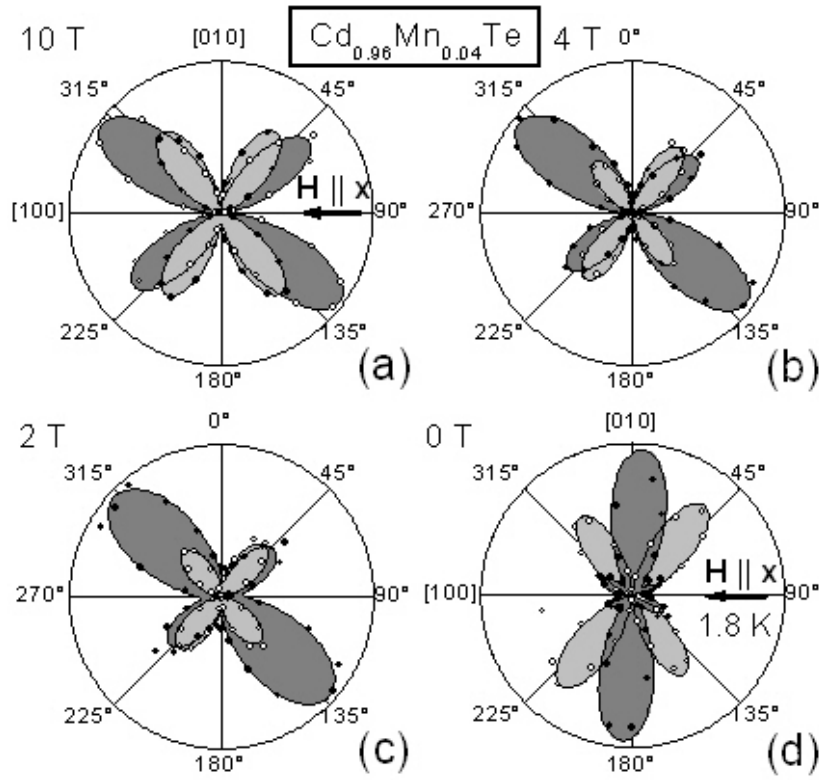
Figure 3.12:
*Rotational anisotropy of the MFISH signals in $Cd_{0.96}Mn_{0.04}Te$ for geometries $\mathbf{E}(2\omega) \parallel \mathbf{E}(\omega)$ (light shaded areas and open circles) and $\mathbf{E}(2\omega) \perp \mathbf{E}(\omega)$ (dark shaded areas and filled circles) for the transition **1**. The experimental data are given by circles and shaded areas present simulations.*

Fig. 3.11(a) shows the electric-dipole components described by a fourth-rank tensor, whereas Fig. 3.11(b) reveals the magneto-spatial dispersion components described by a fifth-rank tensor. Significant changes of the absolute values are found for the transition **1** and **8**, which reveal the highest MFISH intensity. Absolute values for the transitions **2**-**5** feature only minor differences. The reasonable magnitude of the error bars indicates a high reliability of the tensor component values found by the fits.

3.6.4.2   Magnetic field dependence

In Ch. 3.6.3, the magnetic field dependence of $I(2\omega)_{\parallel}^{MFISH}(\varphi = 45°)$, which is equivalent to the geometry $\mathbf{E}(2\omega) \parallel \mathbf{E}(\omega) \parallel [\bar{1}10]$ and shown in Fig. 3.8(a), is found to be described by the modified Brillouin function.

Here the magnetic field dependence of the MFISH signal for other polarization geometries will be considered. Fig. 3.12(a)-(d) shows rotational anisotropy patterns for different magnetic fields for the transition **1**. Only minor changes of the shape of the patterns are observed between 10 T and 0.5 T. The very low MFISH intensity at 0 T shown in Fig. 3.12(d) can be attributed to residual crystallographic SHG due to its characteristic rotational anisotropy (compare to the rotational anisotropy shown in Fig. 3.4, note that the axes of the polar diagrams do not coincide). On the basis of these rotational anisotropy data the absolute values of the tensor components are calculated by the fitting procedure.

Fig. 3.13 shows the squared absolute values of the MFISH tensor components obtained by the fitting procedure. In full accordance to the data presented in Fig. 3.8(a),

Figure 3.13: *Magnetic field dependence of the squared absolute values of the MFISH tensor components in $Cd_{0.96}Mn_{0.04}Te$ for the transition **1** at 1.8 K obtained by the fitting procedure. (a) electric-dipole components of χ_{ijkl}-type, (b) magneto-spatial dispersion components of χ_{ijklm}-type.*
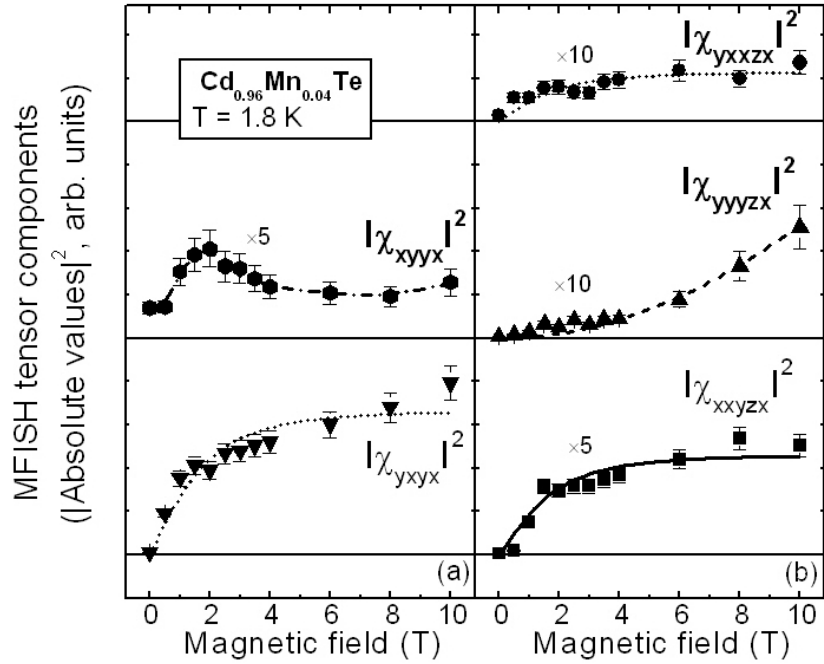
the fitted tensor components $|\chi_{yxxzx}|$, $|\chi_{xxyzx}|$ and $|\chi_{yxyx}|$ reveal a magnetic field dependence, which can be described by the modified Brillouin function (solid lines) leading to the conclusion that pure spin quantization induced MFISH is observed for these components. In contrast, the tensor component $|\chi_{yyyzx}|$ displays a quadratic magnetic field dependence (solid line) as observed for diamagnetic semiconductors shown in Fig. 2.23. Thus this contribution is attributed to orbital quantization induced MFISH. The component $|\chi_{xyyx}|$ reveals a strange magnetic field dependence, which might be explained by an interference between spin and orbital quantization induced contributions.

Recapitulating, the squared absolute value of the unambiguously determined tensor component $|\chi_{yxxzx}|$ displays a MFISH intensity, which is described by the modified Brillouin function and thus the nonlinear polarization $P_i(2\omega)$ is found to be linear proportional to the magnetization. Note that the macroscopic model would lead to a quadratic dependence of the nonlinear polarization $P_i(2\omega)$ on the magnetization. This discrepancy might be solved by adding an factor $1/|\mathbf{M}(0)|$ to the magnetization term in Eq. (3.1). In opposite, the squared absolute value of the unambiguously determined tensor component $|\chi_{yyyzx}|$, which is attributed to the orbital quantization induced MFISH contribution, is found to depend quadratically on the external magnetic field, which is in full accordance with the macroscopic model.

3.7   Interplay of spin and orbital quantization

Above a detailed discussion of the spin quantization induced SHG in paramagnetic $Cd_{0.96}Mg_{0.04}Te$ is given. In Ch. 2, orbital quantization induced SHG in diamagnetic semiconductors is discussed, e.g. for CdTe. Next, the interplay of both MFISH mechanisms, the orbital and the spin quantization, will be investigated. With decreasing
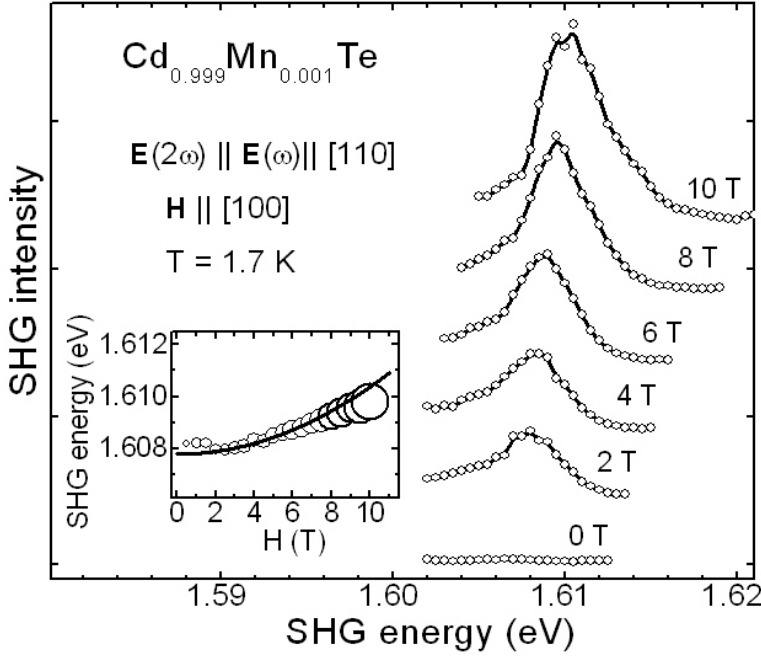
Figure 3.14: *MFISH spectra of $Cd_{0.999}Mn_{0.001}Te$ as a function of the magnetic field for $\mathbf{k}(\omega)\|\mathbf{z}$ and $\mathbf{H}(0)\|\mathbf{x}$. The inset shows the SHG peak energy vs. magnetic field.*

Mn concentration x, the giant Zeeman splitting and therefore the MFISH intensity originated by spin quantization of the electronic states decreases. On the other hand with increasing Mn concentration the crystal quality gets worse and thus the orbital quantization induced SHG intensity decreases. For a proper concentration value x, both contributions, the orbital and spin quantization SHG, are of the same order of magnitude. This allows the investigation of orbital and spin quantization contributions simultaneously. For this purpose, samples with low Mn concentration of type (B) are chosen, where $Cd_{0.8}Mg_{0.2}Te$ instead of CdTe is used as a buffer layer in order to avoid MFISH contributions of CdTe which could not be separated spectrally from MFISH contributions of $Cd_{1-x}Mn_xTe$ with very low Mn concentrations.

Fig. 3.14 shows the magnetic field dependence of the MFISH signal, which features a narrow line near the band gap of $Cd_{0.999}Mn_{0.001}Te$ (E_{gap}=1.608 eV), at 1.7 K for normal light incidence. With increasing magnetic field, this line shifts from the extrapolated value of 1.608 eV at zero magnetic field to higher energies and gains in intensity. The line width is less than 4 meV as in the case of CdTe. Neither crystallographic SHG nor PL signal is detected at zero field, confirming the proper suppression of both signals. The magnetic field dependence of the MFISH peak energy as a function of the magnetic field displays the diamagnetic shift of the $1s$ exciton, which is shown in the inset where the peak intensities are represented by the symbol sizes. Note that the maximum giant Zeeman splitting is only on the order of 1 meV at 10 T and therefore below the experimental resolution limit.

Fig. 3.15 shows the magnetic field dependence of the MFISH peak intensity at 1.7 K. Below 4 T, the dominant mechanism contributing to the MFISH intensity is the giant Zeeman splitting. In this range, the magnetic field dependence is well described by the dotted line, which is derived by the modified Brillouin function given by Eq. (3.4) using the literature values S_0=2.5 and T_0=0 (taken from Fig. 1.10). Thus the MFISH

Figure 3.15: *MFISH intensity of $Cd_{0.999}Mn_{0.001}Te$ vs. magnetic field: dots are experimental data while lines represent calculations. Below 4 T the SHG intensity depends linear on the magnetization M described by the giant zeeman splitting given by Eq. (3.4) (dotted line). Above 4 T the MFISH intensity is proportional to the squared magnetic field H^2 (dashed line). A fit to the data including both dependencies is shown by the solid line.*
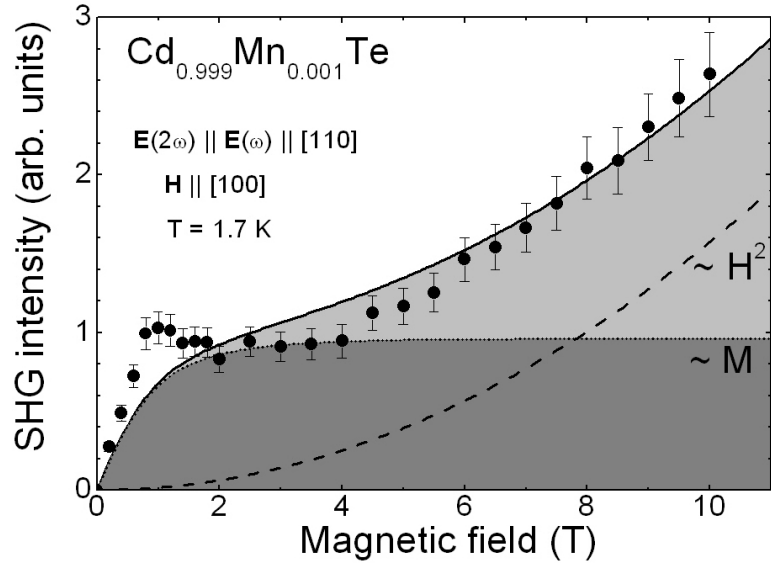
intensity is found to be linear proportional to the magnetization. Above 2 T, the contribution from giant Zeeman splitting is saturated. With increasing field ($H >4$ T), the MFISH intensity increases quadratically with the magnetic field as can be seen from the corresponding fit to the data (dashed line). This quadratic dependence of the MFISH intensity on the magnetic field is discussed in detail for diamagnetic CdTe in Ch. 2. A fit to the data, including both dependencies, is shown by the solid line. A good agreement between the experimental data and the simulation is found. Thus both mechanisms, the spin and the orbital quantization, contribute to the MFISH signal.

Figs. 3.16(a) and (b) show the temperature dependence of the MFISH signal at 2 T and 10 T, respectively, in the temperature range between 1.7 to 50 K. In both cases the energy shift of the spectral lines follows the temperature decrease of the $Cd_{0.999}Mn_{0.001}Te$ band gap energy and the giant Zeeman splitting $\Delta E_{GZ} \sim 1$ meV can be neglected. For magnetic fields below 4 T (see Fig. 3.16c), the decrease of the MFISH intensity is linear proportional to the magnetization indicating, that the decrease of the magnetization is the dominant mechanism. The solid line (dark grey area) is derived from the modified Brillouin function given by Eq. 3.4. The estimated orbital quantization induced contribution at 2 T (light grey area) can be neglected. Above 4 T both effects, spin splitting and orbital quantization, contribute to the MFISH signal. Fig. 3.16(d) presents the MFISH intensity as a function of the temperature at 10 T. The dotted line (dark grey area) is calculated by the modified Brillouin function for 10 T using the same parameters as chosen for the calculation of the modified Brillouin function for 2 T. This Brillouin function displays the MFISH contribution induced by the giant Zeeman splitting. Additionally, an orbital quantization induced SHG contribution is present at high magnetic fields shown by the light grey area.

This demonstrates, that both effects, the orbital and the spin quantization of electronic states, induce MFISH in $Cd_{0.999}Mn_{0.001}Te$. The magnetic field leads to giant
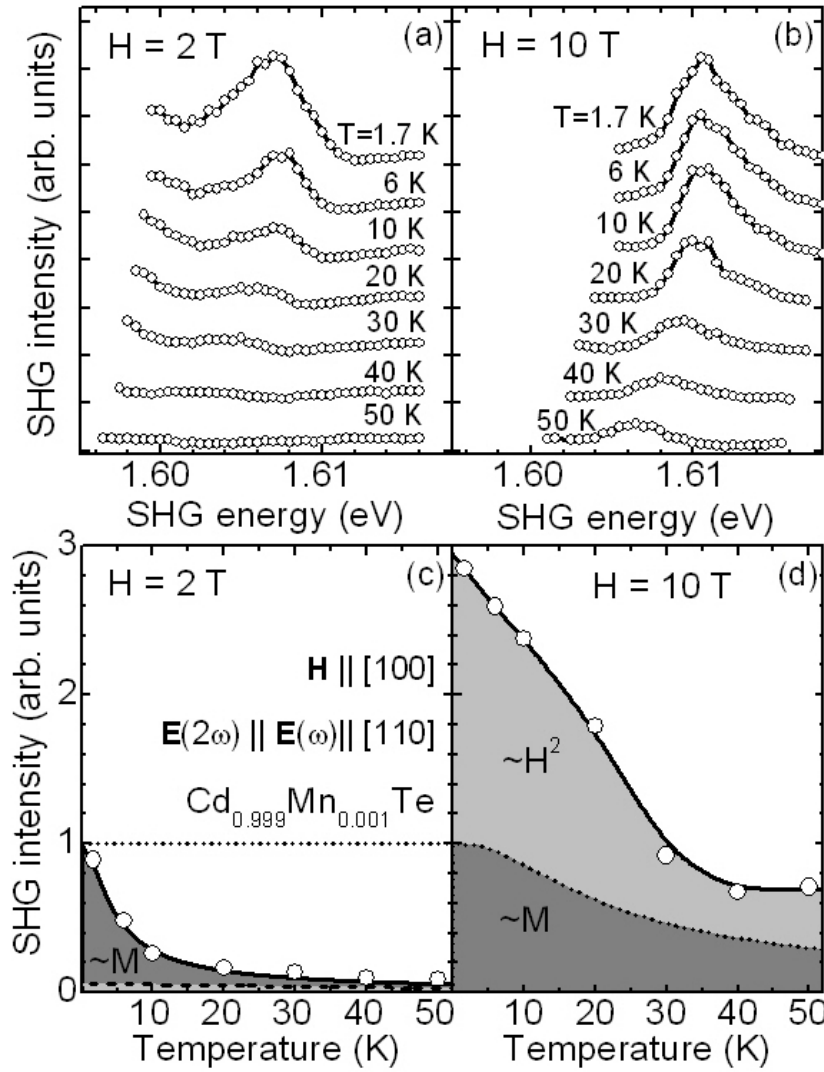
Figure 3.16:
MFISH spectra of $Cd_{0.999}Mn_{0.001}Te$ as a function of the temperature: (a) H = 2 T, (b) H = 10 T. MFISH intensity vs. temperature: (c) H = 2 T, only spin quantization induced SHG (d) H = 10 T, spin and orbital quantization induced SHG.

Zeeman splitting, which clearly dominates the MFISH mechanism at low magnetic fields. The magnetic field and temperature dependence of the MFISH intensity is described by the modified Brillouin function. Another dominant process is that the magnetic field induces Landau-level quantization. Thereby the Zeeman splitting of the Landau-levels is much smaller than the giant Zeeman splitting in $Cd_{1-x}Mn_xTe$ and does not contribute significantly to the MFISH mechanism. In the case of the orbital quantization induced contribution, the MFISH intensity depends quadratically on the strength of the magnetic field.

3.8 MFISH dependence on the Mn concentration

In this section, the influence of the Mn concentration on the MFISH signal will be discussed.

Figure 3.17: (a) MFISH spectra of $Cd_{0.64}Mn_{0.36}Te$ as a function of magnetic field for $\mathbf{k}(\omega)\|\mathbf{z}$ and $\mathbf{H}\|\mathbf{x}$. The spectral dependence of the MFISH signal can be modeled by a Gauß fit of two superposed curves with a line width >48 meV (solid lines). (b) Giant Zeeman splitting diagram of the MFISH peak positions: dots are experimental data with relative intensities given by the symbol sizes. Solid lines give optical transition energies between giant Zeeman split bands calculated from Eq. (3.4).
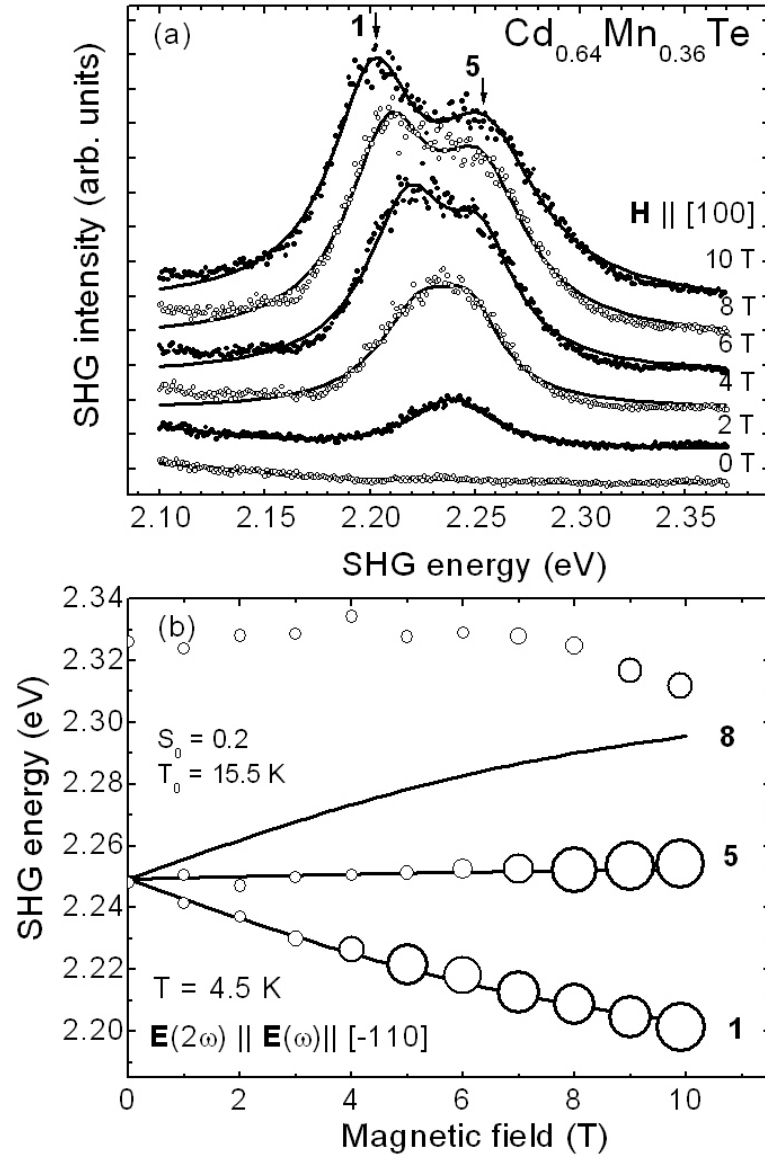
3.8.1 High Mn concentration

Above, $Cd_{1-x}Mn_xTe$ with low manganese concentration is investigated in order to specify the interplay between spin and orbital quantization induced MFISH. Here $Cd_{1-x}Mn_xTe$ with high manganese concentration will be considered.

Fig. 3.17(a) shows the magnetic field dependence of the MFISH spectra near the band gap of $Cd_{0.64}Mn_{0.36}Te$ (type (A) sample with $E_{gap} = 2.05$ eV) at 4.5 K. At zero magnetic field a weak signal is observed. Possible explanations are, that whether the crystallographic SHG contribution is not fully suppressed or SHG induced by strain, e.g. between different layers, appears. In an applied magnetic field, the observed MFISH signal consists of two overlapping lines. The splitting between these lines arises from the magnetic field. The observed spectral dependence of the MFISH signal can be modeled by a Gauß fit to the data revealing, that two broad lines with a line width
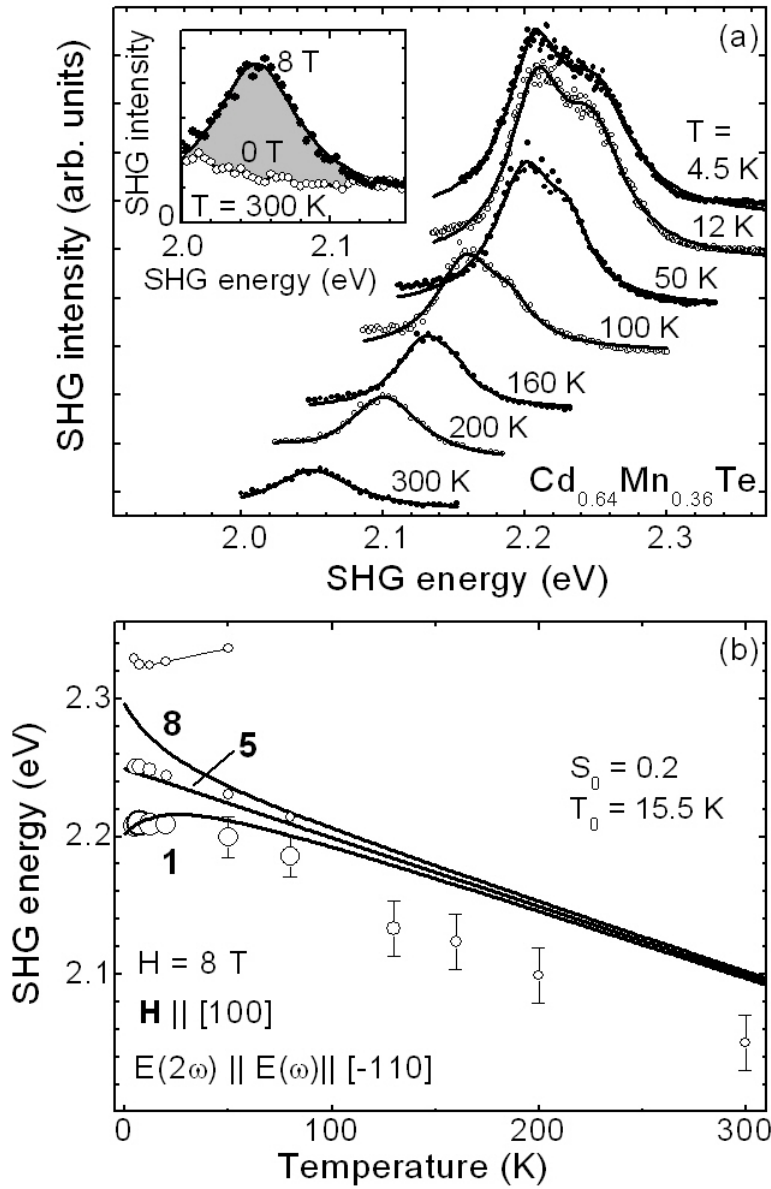
Figure 3.18: (a) MFISH spectra at different temperatures in $Cd_{0.64}Mn_{0.36}Te$ at $H = 8$ T. Note that MFISH is found even at 300 K (inset). (b) MFISH peak energies vs. temperature. Dots are experimental data with intensities given by the symbol sizes. Solid lines are calculations accounting for the temperature dependencies of the giant Zeeman splitting and of the band gap.

>48 meV are superposed. For the following analysis of the spectra, these two lines are fitted by superposed Gauß curves plotted as lines in Fig. 3.17(a).

Fig. 3.17(b) shows the magnetic field dependence of the MFISH energies of the two electronic transitions **1** and **5**. The parameters S_0=0.2 and T_0=15.5 K are used to calculate the modified Brillouin function given by Eq. (3.4). Note that for a high manganese concentration of $x = 0.36$ only the transitions **1** and **5** are observed, whereas for $x = 0.04$ the full set of eight transitions is observed (Fig. 3.6). However, good agreement between experimental data for the MFISH peak energies vs. magnetic field and the giant Zeeman splitting calculated by Eq. 3.4 is observed for the transitions **1** and **5**. This indicates that spin quantization is also the origin of MFISH in strongly doped diluted paramagnetic semiconductors. A possible explanation of the absence of the other MFISH lines in the spectra in $Cd_{0.64}Mn_{0.36}Te$ can be given by the inhomo-

geneous distribution of the manganese ions leading to an inhomogeneous broadening of the lines. Therefore the MFISH peak intensity decreases with increasing Mn concentration. Furthermore a distinction between the lines becomes impossible due to the large line width.

The temperature dependence of the MFISH spectra for $Cd_{0.64}Mn_{0.36}Te$ at 8 T is shown by Fig. 3.18(a) in the temperature range of 4.5-300 K. Due to the inhomogeneous broadening, the distinction of the two observed lines is difficult and so the dominant mechanism to describe the temperature behavior of the peak energies is the shift of the band gap energy. Because of inhomogeneous broadening due to the Mn distribution, the line width is about 50 meV. The line width does not vary significantly with the temperature. Note that the MFISH signal can be observed even at room temperature, as shown in the inset of Fig. 3.18(a). The MFISH intensity at room temperature is about one order of magnitude smaller compared to the signal at 4.5 K

MFISH peak energies obtained by Gauß fits on the spectral data are presented in Fig. 3.18(b). Below 80 K, a good description of the SHG peak energies can be given by the modified Brillouin function (solid lines) combined with the dependence for the temperature shift of the band gap energy [88]. Above 80 K, a distinction between the transitions **1** and **5** is not possible.
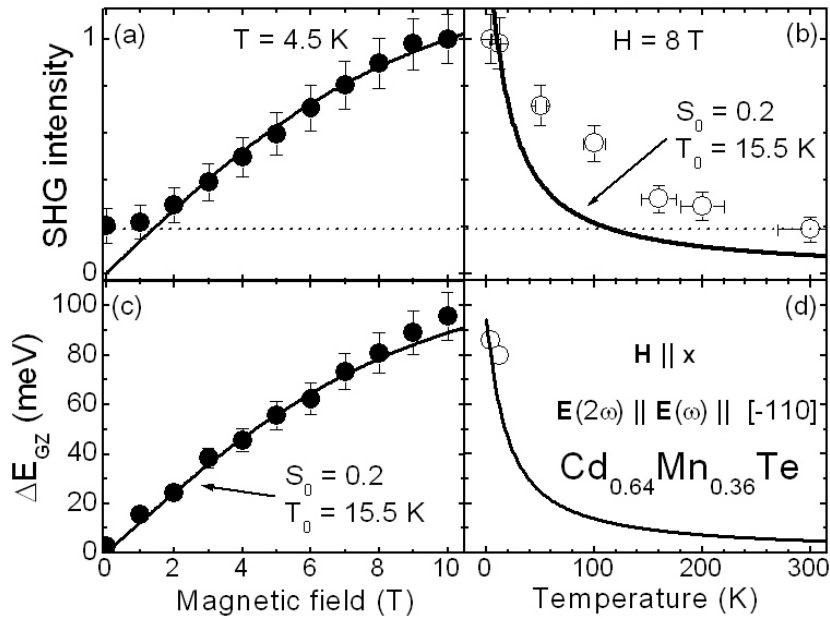
Figure 3.19: *Integrated MFISH intensity vs. magnetic field (a)and temperature (b) and giant Zeeman splitting vs. magnetic field (c) and temperature (d) in $Cd_{0.96}Mn_{0.04}Te$. Solid lines are fits to the data using the Brillouin function of Eq. (3.4).*

On the basis of the data shown in Figs. 3.17 and 3.18, the magnetic field and temperature dependence of the MFISH intensity as well as the giant Zeeman splitting can be determined. Figs. 3.19(a) and (c) show the magnetic field dependence of the integrated MFISH intensity and the giant Zeeman splitting, respectively. Good agree-

ment between the experimental data and the calculations using Eq. (3.4) (solid lines) is found. Figs. 3.19(b) and (d) show the temperature dependence of the integrated MFISH intensity and the giant Zeeman splitting. It is not possible to calculate the giant Zeeman splitting from the experimental data presented in Fig. 3.18 at high temperatures, which results from the broadening of the lines and the strong decrease of the MFISH intensity. The experimental data for the MFISH intensity deviate from the calculated modified Brillouin function (solid line in Fig. 3.19(b)). Note that at zero magnetic field (see Fig. 3.19(a)) and high temperature (see Fig. 3.19(b)) a residual SHG intensity is observed. This deviation from the modified Brillouin function might be partly explained by a crystallographic SHG contribution. However, a possible influence of the Mn-Mn interaction and/or clusters [31] to the MFISH signal at high Mn concentration cannot be excluded so far.

In conclusion, due to inhomogeneous broadening of the lines in the MFISH spectra in $Cd_{1-x}Mn_xTe$ with high Mn concentration , the spectral distinction between different MFISH lines becomes impossible. Thus the complete set of eight possible transitions cannot be observed.

3.8.2   Comparison for different Mn concentrations

Above, the MFISH mechanisms in $Cd_{1-x}Mn_xTe$ are discussed exemplarily on the basis of experimental data for the specific concentrations $x = 0.001$ (low concentration), $x = 0.04$ (intermediate concentration) and $x = 0.36$ (high concentration). In this section the properties of the MFISH signal will be investigated as a function of the manganese concentration.

MFISH spectra for $Cd_{1-x}Mn_xTe$ with x=0.64, 0.36, 0.22, 0.18, 0.16, 0.12, 0.08, 0.04, 0.001 and 0 are shown in Fig. 3.20(a)-(j). Starting from binary CdTe (see Fig. 3.20(i)), the MFISH signal is induced by orbital quantization and the MFISH process is shown to be described on the basis of the Landau-level model (see Ch. 2). With increasing Mn concentration in CdTe, the orbital quantization induced MFISH intensity decreases rapidly. This phenomenon is discussed in Ch. 2.9.2 for $Cd_{1-x}Mg_xTe$, where the influence of the presence of nonmagnetic magnesium ions on the MFISH intensity is shown. Thus with increasing Mn concentration the orbital quantization induced MFISH contribution becomes weaker. Additionally, with increasing concentration of magnetic ions (e.g. Mn^{2+}), a spin-quantization induced MFISH contribution appears gaining in intensity. For very low manganese concentration x (see Fig. 3.20(h)) the giant Zeeman splitting is below the resolution limit and a single line is observed close to the band gap energy. Above x=0.001 the giant Zeeman splitting becomes observable and amounts to a value of about 120 meV for x=0.16 (Fig. 3.20(d)), where the spectral separation of the lines **1**-**8** is maximal. For x >0.18 the inhomogeneous broadening rules out the possibility to distinguish between all eight lines. In particular, for x=0.36 only two transitions (lines **1** and **5**) are distinguishable (Fig. 3.20(a)). Also the observed giant Zeeman splitting decreases, which is attributed to the creation of clusters limiting the applicability of the model of free spins from which the (unmodified) Brillouin function is derived (see Ch. 1.2.4.3).
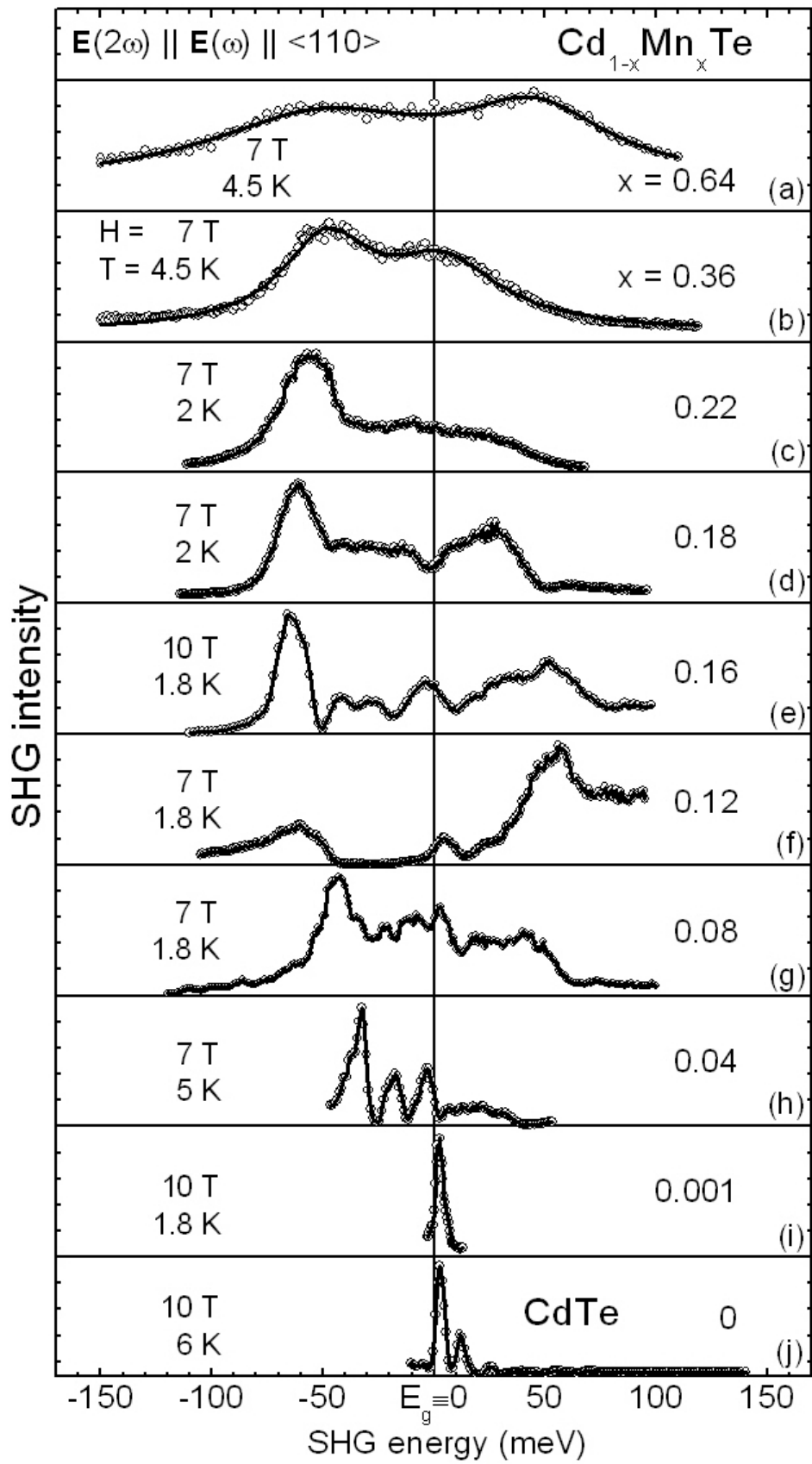
Figure 3.20: *Dependence of the spectral features of the MFISH signal of $Cd_{1-x}Mn_xTe$ on the manganese concentration x=0.64..0 (a)-(j). The MFISH spectra are measured for $\mathbf{k}(\omega)\|\mathbf{z}$ and $\mathbf{H}\|\mathbf{x}$ under comparable conditions (H=7..10 T, T=1.7..6 K, $\mathbf{E}(2\omega) \| \mathbf{E}(\omega) \| <110>$).*
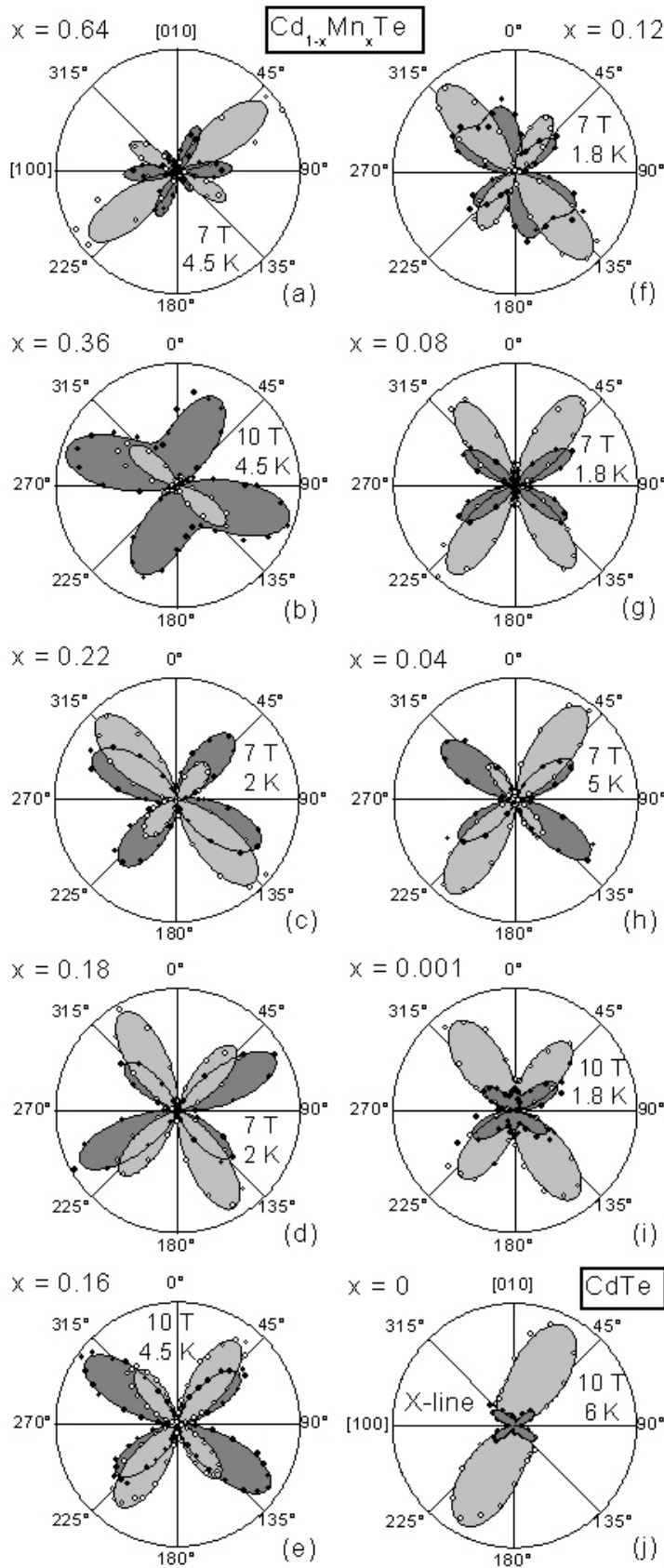
Figure 3.21: (a)-(j): Rotational anisotropy of the MFISH signals in $Cd_{1-x}Mn_x Te$ for geometries $\mathbf{E}(2\omega) \parallel \mathbf{E}(\omega)$ (light shaded areas and open circles) and $\mathbf{E}(2\omega) \perp \mathbf{E}(\omega)$ (dark shaded areas and filled circles). The experimental data are given by circles and shaded areas present simulations. Comparable conditions (H=7..10 T, T=1.7..5 K, line **1**) are used to compare the anisotropy for different Mn concentrations x.

The rotational anisotropies of the line **1** for different Mn concentrations x under comparable conditions (H=7..10 T, T=1.7..6 K) are shown in Fig. 3.21. The rotational anisotropies of the MFISH signal feature a rich variety of twofold patterns. The experimental data for the rotational anisotropy have been fitted by the same procedure discussed above. The calculated curves are shown by lines with shaded areas. Good agreement between experimental and calculated MFISH intensities is found for the rotational anisotropy for all Mn concentrations x.
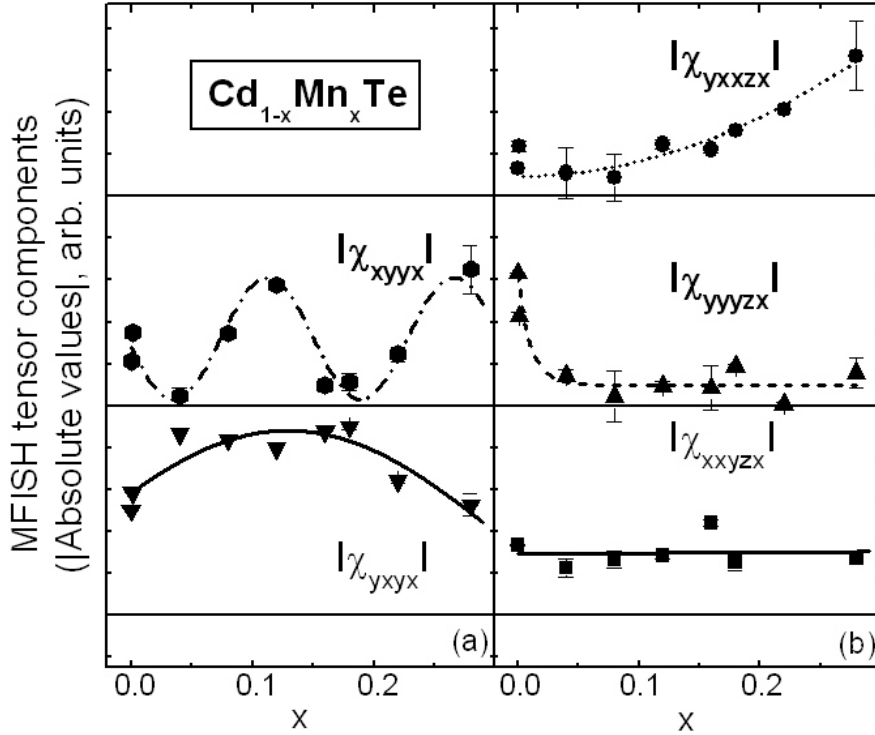
Figure 3.22: *Dependence of the absolute values of the MFISH tensor components on the manganese concentration x in $Cd_{1-x}Mn_xTe$ for line **1**: (a) electric-dipole components of χ_{ijkl}-type, (b) magneto-spatial dispersion components of χ_{ijklm}-type.*

The set of absolute values of the tensor components obtained by the fitting procedure are shown in Fig. 3.22 as a function of the Mn concentration x. Fig. 3.22(a) shows the electric-dipole components described by a fourth-rank tensor, whereas Fig. 3.22(b) reveals the magneto-spatial dispersion components described by a fifth-rank tensor.

The absolute value of the tensor component $|\chi_{yyyzx}|$, which is attributed to the orbital MFISH contribution (see discussion of Fig. 3.13(b)), decreases exponentially with increasing Mn concentration. This is reasonable since with increasing concentration of impurity ions the orbital MFISH contribution decreases strongly. In contrast, the absolute value of the tensor component $|\chi_{yxxzx}|$ increases quadratically with increasing x, which is in accordance with an expected increase of the spin quantization induced MFISH contribution with raising Mn concentration. The tensor component $|\chi_{xyyx}|$ reveals an oscillatory behavior $[|\chi_{xyyx}| \sim \cos(c \cdot x + \alpha)]$. This might be explained by
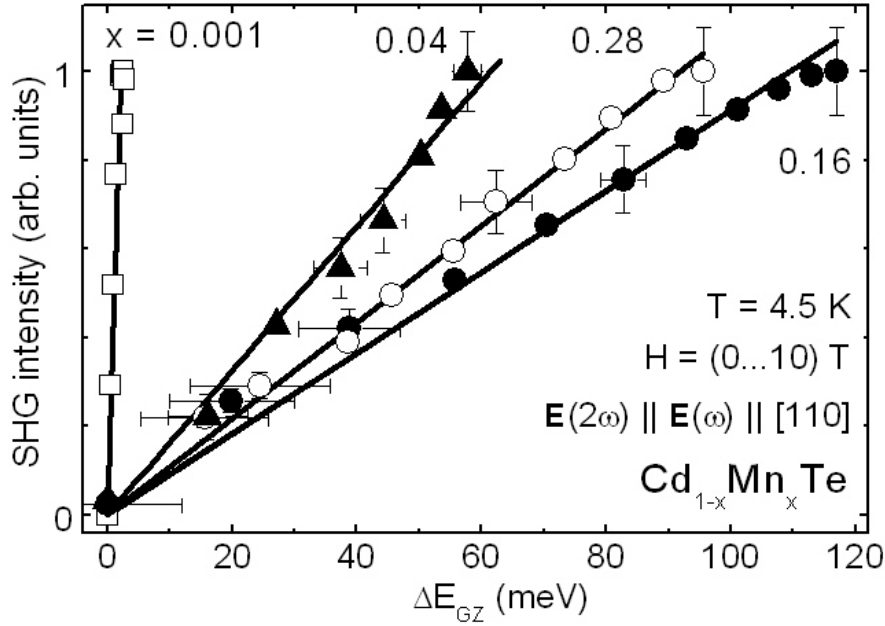
Figure 3.23: *Integrated SHG intensities for different Mn concentrations x as functions of the giant Zeeman splitting ΔE_{GZ}, which is controlled by the magnetic field at 4.5 K. The lines are linear interpolations of the experimental data. Saturated MFISH intensities are normalized to 1.*

an interference between the spin and the orbital induced MFISH contributions, which would be in accordance with the data for $|\chi_{xyyx}|^2$ for $x=0.04$ shown in Fig. 3.13(a), where also an interference is observed. Since $|\chi_{yxyx}|$ and $|\chi_{xxyzx}|$ are not determined unique, their behavior will not be discusses here.

Fig. 3.23 shows the dependence of the MFISH intensity on the giant Zeeman splitting for different Mn concentrations x. The data sets are measured at T=4.5 K for H varied in the range $0-10$ T and can be well described by a linear dependence. The dependence $I(2\omega) \propto \Delta E_{GZ}$ confirms, that the MFISH in paramagnetic (Cd,Mn)Te is determined by the spin splitting for Mn concentration in the range $0.001 < x < 0.36$.

3.9   Spin glass phase

In this section, the spin glass-like magnetic properties in $Cd_{1-x}Mn_xTe$ will be investigated. Therefore a bulk $Cd_{0.76}Mn_{0.24}Te$ sample of type (C) is used. Note that a remanent magnetization, which is a characteristic property of the spin glass phase and will be discussed below, is only observed in this sample.

3.9.1   Wide range spectra

Fig. 3.24 shows crystallographic (grey line) and magnetic (black area) SHG spectra in the large spectral range of 1.6-3.2 eV for a (110)-oriented $Cd_{0.76}Mn_{0.24}Te$ sample of type (C) at 6 K. Note that for normal light incidence the crystallographic contribution, which is discussed in Ch. 3.4, is allowed for (110)-oriented $Cd_{1-x}Mn_xTe$. The SHG and MFISH intensities are given in arbitrary units, but the relative values for SHG and MFISH are of importance. Note that the crystallographic SHG contribution is about
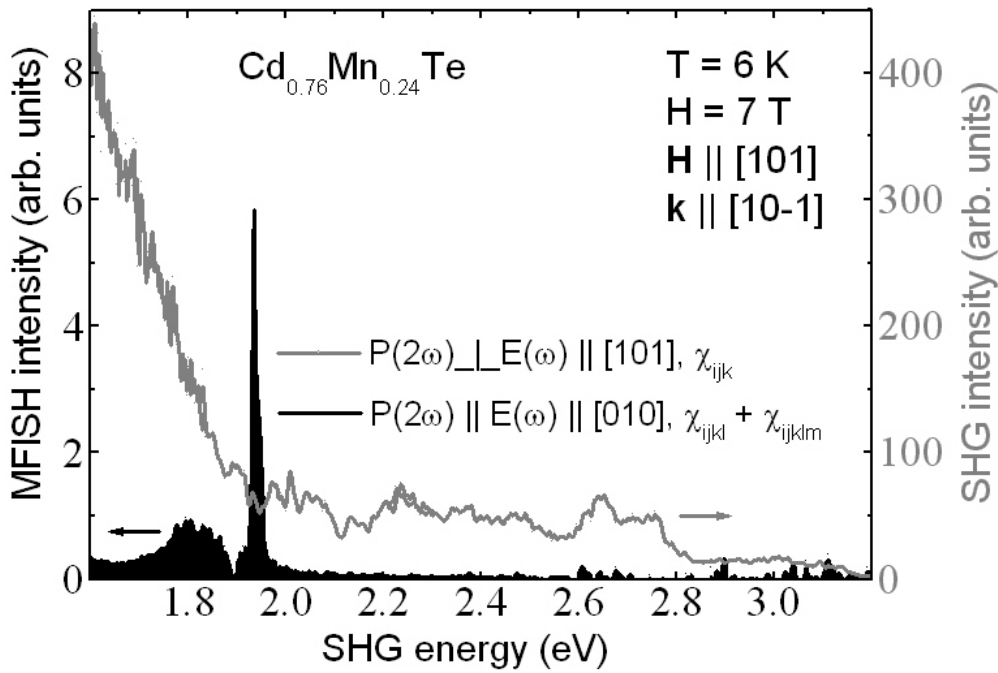
Figure 3.24: *Spectral dependence of the crystallographic (grey line) and magnetic (black area) SHG contribution in $(110) \equiv (10\bar{1})$ oriented $Cd_{0.76}Mn_{0.24}Te$ of type (C). The intensities are given in arbitrary units, but the relative values for SHG and MFISH are of importance.*

two orders of magnitude stronger than the MFISH contribution. In the following the strong crystallographic SHG contribution is suppressed using the polarization geometry $\mathbf{E}(2\omega) \parallel \mathbf{E}(\omega) \parallel [010]$. Thereby the detection of the weaker magnetic SHG contribution becomes possible. In a magnetic field, a MFISH signal consisting of a ∼100 meV broad band at 1.8 eV and a narrow line with a line width of ∼15 meV at about 1.93 eV appears. The magnetic field and temperature behavior of this narrow line, which is close to the band gap $E_{gap} = 1.99$ eV of $Cd_{0.76}Mn_{0.24}Te$, will be investigated below.

3.9.2   SHG signal coupled to spin glass phase

MFISH spectra for different magnetic fields are shown by Fig. 3.25(a). With decreasing magnetic field, the MFISH lines shift from ∼1.94 eV at 7 T to ∼1.98 eV at 0 T proving their magnetic origin. An important finding is, that the MFISH intensity is not influenced by the magnetic field as shown by the inset of Fig. 3.25(a) (filled dots). This is in contrast to the linear dependence of the MFISH intensity on the giant Zeeman splitting and thus on the magnetic field as found for $Cd_{1-x}Mn_x$Te samples of type (A) and (B) shown in Fig. 3.23. Therefore the magnetic properties of this sample of type (C) are expected to be very different, which will be considered more detailed below. For magnetic SHG being present also at zero magnetic field, the terminology of MSHG (magnetic SHG) will be used instead of MFISH (magnetic-field-induced SHG).
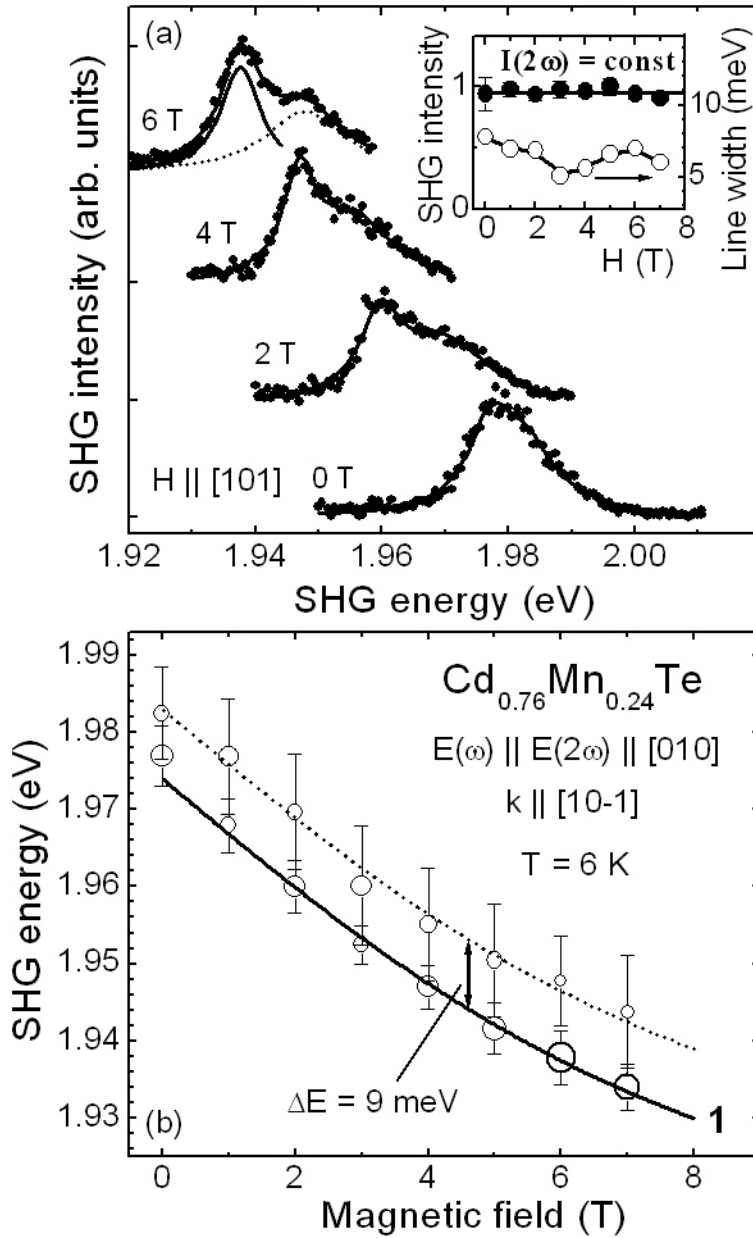
Figure 3.25: (a) Magnetic field dependence of MFISH spectra in $Cd_{0.76}Mn_{0.24}Te$ of type (C). Solid lines correspond to fits on the data using two Gauß functions. MFISH peaks shift with decreasing magnetic field to higher energy. The inset shows the MFISH intensity and the line width vs. the magnetic field. Note that the MFISH intensity does not vary with the applied magnetic field. Thus, below the terminology of MSHG (magnetic SHG) will be used instead of MFISH (magnetic-field-induced SHG). (b) Giant Zeeman splitting diagram of the MFISH peak positions: dots are experimental data with relative intensities given by the symbol sizes. Solid lines give optical transition energies between giant Zeeman split bands calculated from Eq. (3.4) with $S_0=0.5$ and $T_0=8.4$ K.

The line widths found by fitting the spectral dependence of the MFISH intensity using two Gauß functions are 6 meV and 15 meV at 6 T and 6 K. The line width does not vary strongly with the magnetic field as shown by the inset of Fig. 3.25(a) for the energetically lowest line.

The magnetic field dependence of the MFISH peak energies, which are also obtained by fitting the spectral dependence of the MFISH intensity using two Gauß functions, is shown by Fig. 3.25(b). Lines correspond to calculations of the giant Zeeman splitting using Eq. (3.4) with the effective spin $S_0=0.5$ and the effective temperature $T_0=8.4$ K taken from Fig. 1.10. Note that in $Cd_{0.76}Mn_{0.24}Te$ only the transition **1** is observed. Good agreement between experimental data for the MFISH peak energies vs. the magnetic field and calculations (solid line) is revealed. The dashed line, which is
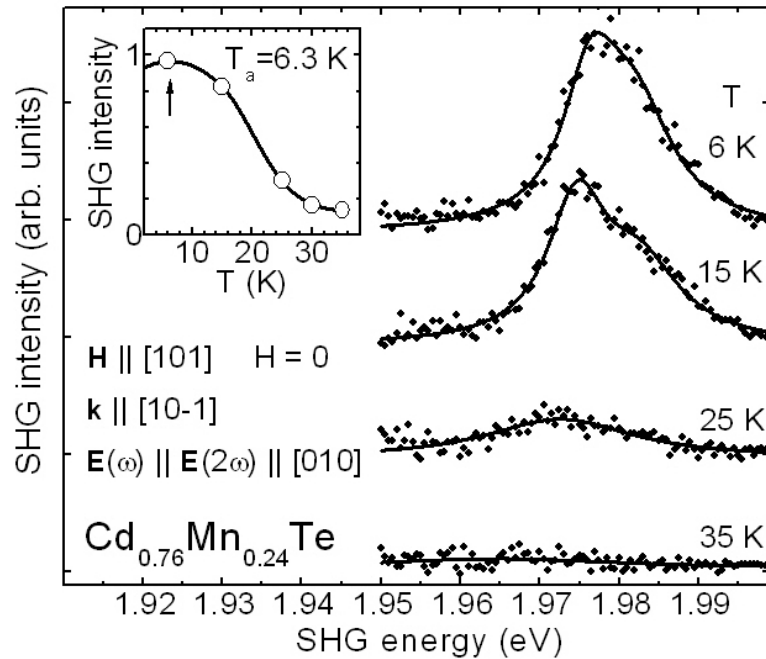
Figure 3.26: *Temperature dependence of the MSHG signal in $Cd_{0.76}Mn_{0.24}Te$ of type (C) at 0 T. Note that the sample was cooled to 6 K in an applied magnetic field of 7 T before. The inset shows the MSHG intensity vs. temperature.*

shifted by 9 meV with respect to the solid line, describes the energetically higher MFISH peak. A possible explanation of this energy shift might be given by strain inside the bulk sample, which influences the energy of the electronic band states.

Fig. 3.26 shows MSHG spectra for different temperatures at zero magnetic field. Before, these MSHG spectra were measured, the sample was cooled to 6 K in an applied magnetic field of 7 T. With decreasing magnetic field (at 6 K) the MSHG peaks shift as shown in Fig. 3.25. However, the MSHG intensity does not vary with the magnetic field. Note that at zero magnetic field the MSHG intensity features the same intensity as found for high magnetic fields. With increasing temperature, the MSHG intensity decreases continuously. The inset of Fig. 3.26 presents the temperature dependence of the integrated MSHG intensity near the band gap, which reveals a cusp at ~6 K and a vanishing of the MSHG signal above 30 K. After raising the temperature and thereby reducing the MSHG signal, a reduction of the temperature is not sufficient to recover the MSHG signal. This indicates, that no long-range magnetic ordering is present. The MSHG signal can only be recovered by applying a magnetic field at low temperature. A similar behavior was reported for the spin glass-like magnetic phase in $Cd_{1-x}Mn_xTe$, which appears at low temperature [31, 144]. The inset of Fig. 3.26 and the previous discussion reveal that the MSHG signal displays such a spin glass behavior. The vanishing of the MSHG signal above 30 K indicates, that short-range ordering vanishes. Note that the MSHG coupled to these spin glass magnetic properties, especially the remanent magnetization, are only observed in one $Cd_{0.76}Mn_{0.24}Te$ sample of type (C).

3.9.3 Mn concentration vs. anomaly temperature

Although the MSHG signal coupled to the remanent magnetization, which is a characteristic spin glass magnetic property, is only observed in $Cd_{0.76}Mn_{0.24}Te$ of type
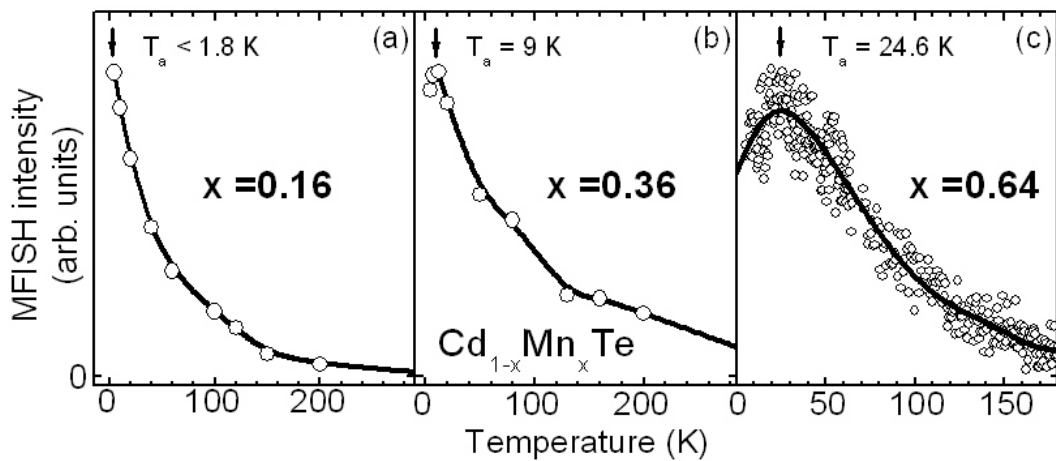
Figure 3.27: *Dependence of the anomaly temperature T_a on the Mn concentration x in $Cd_{1-x}Mn_xTe$: (a) $x = 0.16$, integrated MFISH intensity for $\mathbf{E}(2\omega) \parallel \mathbf{E}(\omega) \parallel [110]$ at $H=7$ T, (b) $x = 0.36$, integrated MFISH intensity for $\mathbf{E}(2\omega) \parallel \mathbf{E}(\omega) \parallel [\bar{1}10]$ at $H=8$ T, (c) $x = 0.64$, SHG peak intensity at $E(2\omega)=2.625$ eV for $\mathbf{E}(2\omega) \parallel \mathbf{E}(\omega) \parallel [\bar{1}10]$ at $H=0$ T, measured after field cooling ($H=8$ T, $T<2$ K).*

(C), anomalous temperature dependencies are also found for $Cd_{1-x}Mn_xTe$ of type (A). Fig. 3.27 shows the temperature dependencies of the MFISH intensity for Mn concentrations $x = 0.16$ (a), $x = 0.36$ (b) and $x = 0.64$ (c). In the case of $x = 0.16$ and $T >1.8$ K, only the normal temperature dependence described by the modified Brillouin function (Eq. (3.4)) is observed (a). Thus $T_a < 1.8$ K is found for $x = 0.16$. For
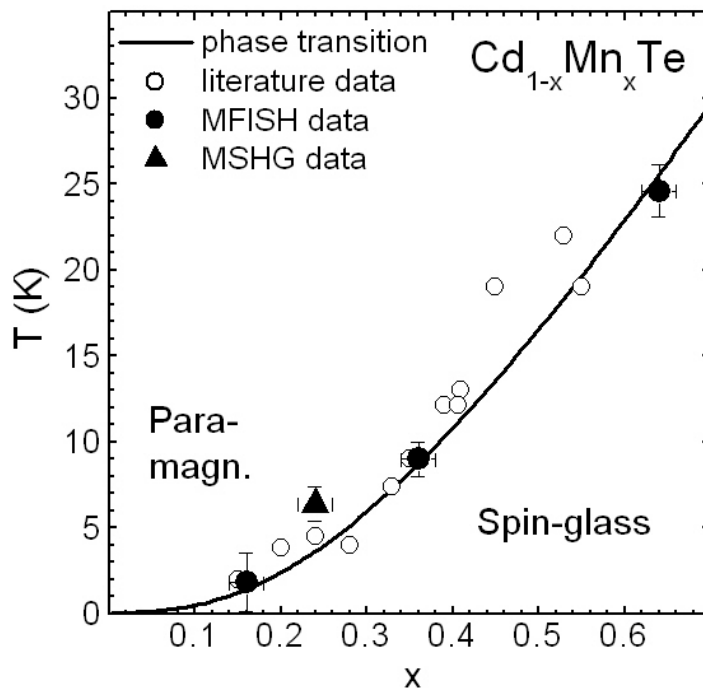
Figure 3.28: *Magnetic phase diagram of $Cd_{1-x}Mn_xTe$. At high temperature and low Mn concentration x the paramagnetic phase is present. Due to the Mn-Mn interaction at low temperature a short-range antiferromagnetic ordering (spin glass phase) is observed. References for literature data (open circles) and phase transition (solid line) are given in the caption of Fig. 1.11. MFISH and MSHG data are shown by filled circles and filled triangle, respectively.*

higher manganese concentrations, anomalies in the temperature dependence appear. For $x = 0.24$, 0.36 and 0.64 the anomaly temperatures $T_a = 6$ K (inset of Fig. 3.26), 9 K (Fig. 3.27(b)) and 24.6 K (Fig. 3.27(c)) are found, respectively. Here the anomaly temperature T_a is defined by a cusp in the temperature dependence of the MFISH intensity.

The anomaly temperature values found by means of MFISH and MSHG are represented by filled circles and filled triangle, respectively, in Fig. 3.28. The observed anomaly temperatures coincide with high accuracy with the spin glass phase transition temperatures reported in literature (open circles in Fig. 3.28) [98]. Therefore MFISH and MSHG can be used as a tool to probe the spin glass magnetic properties.

3.10 Summary

In conclusion, a detailed description of the magnetic properties of $Cd_{1-x}Mn_xTe$ for different Mn concentrations is revealed by magnetic-field-induced SHG. Two important forms of quantization of electronic states, which appear in an applied magnetic field, are found to originate the MFISH signal in $Cd_{1-x}Mn_xTe$. On the one hand, in paramagnetic $Cd_{1-x}Mn_xTe$ the magnetic field induces giant Zeeman splitting. The MFISH intensity is shown to depend linear on the giant Zeeman splitting described by the modified Brillouin function. For high Mn concentrations, this mechanism clearly dominates the MFISH process. By contrast to linear optics, the complete set of eight transitions between the giant Zeeman split valence and conduction bands can be observed in the MFISH data. Furthermore the magnetization-induced SHG is observed even at room temperature. On the other hand, the magnetic field induces Landau-level quantization. This process is present in diamagnetic (e.g. CdTe) as well as the diluted paramagnetic (e.g. $Cd_{1-x}Mn_xTe$) semiconductors. It is shown, that Landau orbital and Zeeman spin quantization of electronic states are driven mechanisms of magnetic-field-induced SHG in the semiconductor $Cd_{1-x}Mn_xTe$. Additionally, the possibility to investigate the magnetic properties of the spin glass phase in $Cd_{1-x}Mn_xTe$ by means of MSHG and MFISH is shown.

The mechanisms of spin and orbital quantization of the valence and conduction bands being the origin of MFISH can be relevant for different types of semiconductors, having various crystallographic and electronic band structures.

For more detailed insight, microscopic model calculations of MFISH accounting for the electronic band structure of specific semiconductors are required. This is underlined by the fact, that the phenomenological analysis cannot fully explain the data, as it would give a MFISH intensity that is proportional to the square of the spin-splitting, which is in contrast to the observations.

Chapter 4

Antiferromagnetic insulators

In this section the power of the SHG technique for the investigation of antiferromagnets will be demonstrated. Copper borate (CuB_2O_4) is chosen since its magnetic structure is rather complicated. CuB_2O_4 is a non-centrosymmetric magnetically ordered material. The unusual coexistence of a 'weak' Dzyaloshinskii-Moria type ferromagnetism and an incommensurate magnetic ordering stimulates interests [145, 146]. Due to the complexity of the magnetic structure, the analysis and interpretation of experimental results is rather complicated. For example, the interpretations of diffraction data lead to contradictory proposals of magnetic structures [146, 147, 148]. Therefore, CuB_2O_4 is a good material for demonstrating the potential of magnetic-field-induced second harmonic generation (MFISH).

A rich spectrum of magnetic effects is observed in CuB_2O_4. Three different types of magnetic-field-induced SHG (MFISH) processes are investigated in the antiferromagnetic two-sublattice compound CuB_2O_4. Giant MFISH intensities, which are already visible to the naked eye, are spectrally studied. The sublattice selective and resonance enhanced contributions are compared to results obtained by linear optical methods measuring linear absorption, photoluminescence and linear birefringence. Since MFISH couples to the magnetic structure, it is possible to distinguish the sublattices and determine the respective order as well as their interaction. Magnetic phase diagrams for both sublattices are constructed for different geometries. The domain structure is investigated by phase-sensitive SHG measurements.

The following types of MFISH can be distinguished:

(A) In magnetically disordered materials (or sublattices) the external magnetic field reduces the symmetry in a perturbative way. Thereby new SHG contributions appear. The only known example is a weak surface induced MFISH signal at fixed frequency from Si [17].

(B) In magnetically ordered materials (or sublattices), where the magnetic field induces a phase transition, new SHG components appear. These new SHG components are only observed in the spin-flop phase of Cr_2O_3 [71] and the system of hexagonal manganites [149].

(C) In magnetically ordered materials (or sublattices), where an existing SHG signal is enhanced by the magnetic field, a single-domain state with maximum magnetization is created. This leads to an increase of the existing SHG contributions. Such processes are given in Ref. [14]. Thereby the source of these SHG contributions is the intrinsic magnetic order and the externally applied magnetic field is only used to manipulate the magnetic order.

As will be shown, all three MFISH mechanisms are observed very clearly and with high MFISH intensities in CuB_2O_4.

4.1 Crystal properties

4.1.1 Crystal structure

CuB_2O_4 crystallizes in the tetragonal space group $I\overline{4}2d$ [150]. The corresponding point group symmetry is $\overline{4}2m$. The unit cell consists of 12 formula units, where the lattice constants are given by a = 11.484 Å and b = 5.620 Å. BO_4 tetrahedrons and two nonequivalent Cu^{2+} sublattices build up the crystal shown in Fig.4.1. Cu^{2+} ions at 4b
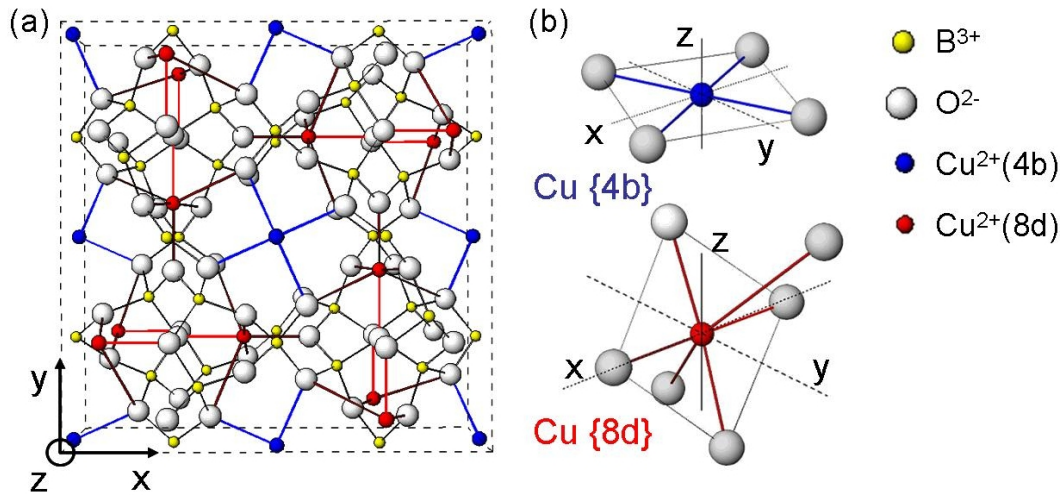
Figure 4.1: *Crystal Structure of CuB_2O_4: (a) Unit cell, (b) Cu^{2+} ions and local surrounding at 4b and 8d sites.*

sites are surrounded by four oxygen atoms in planar quadratic coordination, so that the local symmetry is $\overline{4}$. Cu^{2+} ions at 8d sites occupy distorted octahedral positions with exceptionally large separation of 3.069 Å from the two apical O^{2-} ions [150]. The local symmetry is 2.

The symmetry group $\overline{4}2m$, describing CuB_2O_4, contains the following symmetry operations:

$$1\,,2_x\,,2_y\,,2_z\,,\overline{2}_{xy}\,,\overline{2}_{-xy}\,,\pm\overline{4}_z\,, \tag{4.1}$$

where $\overline{4}_z$ denotes a fourfold rotation around the optical z axis followed by an inversion operation. The symmetry axes $\pm$xy denote the diagonals between the crystallographic axes x and y.

4.1.2   Magnetic structure

Magnetic properties of CuB_2O_4 originate from the Cu^{2+} spin 1/2 and interaction of 4b and 8d sublattices. Above the Néel temperature $T_N = 21$ K, CuB_2O_4 is paramagnetic. Below T_N it is antiferromagnetic. At 10 K $< T < 21$ K the 4b site exhibits commensurate easy-plane antiferromagnetism with weak Dzyaloshinskii-Moria type ferromagnetic component [146, 147, 148]. Thereby the antiferromagnetically ordered spins cause a weak ferromagnetic moment within the tetragonal plane (001), which results from a slight derivation from the ideal antiferromagnetic alignment. The exchange interaction between 4b ions is transferred via boron and oxygen ions (Cu-O-B-O-Cu) [147]. At 10 K the spontaneous magnetic moment is about 0.56 emu/g [147]. The 8d site remains disordered according to contemporary belief [146, 148, 72, 151]. Below $T^* = 10$ K incommensurate antiferromagnetism with possible 8d-site ordering is found. The incommensurate order can be described by a spin density wave with a wave vector, which vanishes at T^* and exceeds the value of the lattice constants below T^*. The spin arrangement is assumed to be described by a spin helix [146]. Another phase transition at $\lesssim 2$ K is reported [152].

4.1.3   Energy level diagram

Starting from the undisturbed atomic $Cu^{2+}(3d^9)$ eigenstates, the energy level diagram is derived for the different Cu^{2+} sites by taking the ligand field into account. The ligand field lowers the symmetry of the free Cu^{2+} ion, which is described by the rotation group D_2^+, and therefore lifts the degeneracy of the $Cu^{2+}(3d^9)$ eigenstates. Considering the local symmetries $\overline{4}$ and 2, the split eigenstates are described by the symmetry representations $\Gamma_1 + 2\Gamma_2 + \Gamma_3 + \Gamma_4$ and $3\Gamma_1 + 2\Gamma_2$, respectively [84]. The sequence of these energy levels is obtained by the following assumptions:

(1) The energy scales with the degree of overlap between the wave function of the Cu^{2+} and O^{2-} ions.

(2) The influence of the remote apical O^{2-} ions in the case of the 8d site is small, since the distance to the Cu^{2+} ion is large compared to the in-plane distance. Therefore on the one hand splitting of xz and yz states will be neglected since the experimental resolution is not sufficient as will be shown. On the other hand, the transition energies between the ground state $x^2 - y^2$ and the excited states xy, yz/xz and $3z^2 - r^2$ are similar in the case of 4b and 8d sites.

(3) The splitting of xz and yz states in the case of the 4b site can be neglected, since it is determined by a variation of the Cu^{2+}-O^{2-} in-plane distance, which is only 2.6% [150].

The obtained energy level diagram is shown by Fig. 4.2. The symmetry representa-
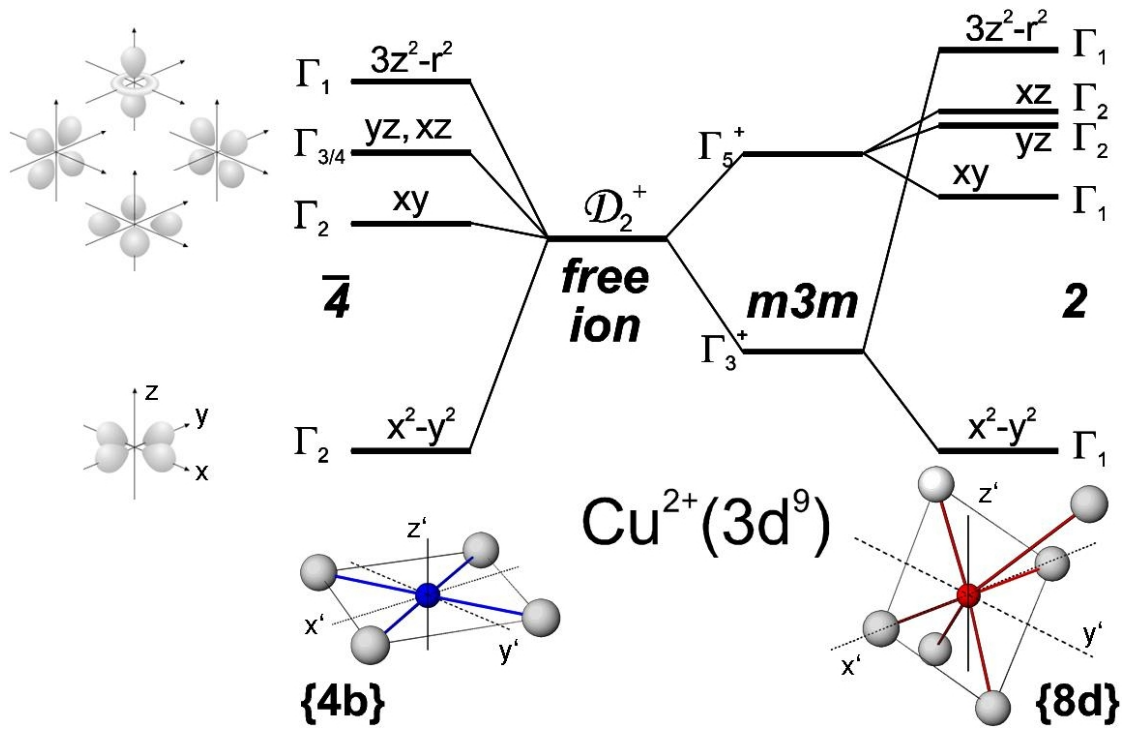
Figure 4.2: *Energy Level Diagram of CuB_2O_4. Electronic states, local symmetry, and coordination of $Cu^{2+}(3d^9)$ ions at 4b and 8d sites in CuB_2O_4. Wave functions (sketches taken from [153]) are given in terms of the local coordinate system (x,y,z) whose axes are defined by the connections between the central Cu^{2+} ion and the square or undistorted octahedron of O^{2-} ligands at the respective sites. Local symmetry is given in bold italics. Sequence of levels is discussed in the text. Coordination is shown for the Cu^{2+} ion (filled spheres) with the nearest O^{2-} ligands (open spheres). Apostrophize axes are those of the global coordinate system (x',y',z').*

tions are linked to the Cu^{2+} d-wave functions by comparison with their eigenfunctions. Note that the Cu^{2+} d-wave functions are mixed with O^{2-} p-wave functions because of the broken centrosymmetry.

Note that CuB_2O_4 is a wide-gap transition-metal oxide with $d-d$ transitions below the band gap E_g = 3.5-4 eV. Therefore, in opposite to the semiconductors discussed in chapters 2 and 3, in CuB_2O_4 electronic states of the valence and conduction bands are of no big importance for the following investigation of the magnetic properties depending on the d states of the Cu^{2+} ions.

4.1.4   Samples

The CuB_2O_4 bulk single crystals are grown by the method of spontaneous crystallization while slowly cooling the melt of the ternary system Li_2O-CuO-B_2O_3 [154]. Using this method, it is possible to grow crystals with a size of $\sim$1 cm^3 and high optical

quality checked by microscope. To obtain the desired crystallographic orientations the crystals are cut and polished into (110), (010) and (001) platelets. The thickness varies in the range of $60 - 100$ μm. Laue diffraction is used in order to orient the samples [155].

4.2 Linear optical methods

In this section the linear optical techniques used in the experiments are introduced. Results obtained by linear birefringence, photoluminescence and linear absorption experiments will be shown.

4.2.1 Linear birefringence

Linear birefringence is an intrinsic material property, which is described by different refraction indices $n_\parallel \neq n_\perp$ for different polarization directions. The indices $\parallel$ and $\perp$ denote polarization directions parallel and perpendicular to the optical axis, respectively. As a consequence, retardation effects appear, since the light speed in a material is given by $c' = c/n$, where c is the light speed in vacuum. The retardation axis is defined to be the axis of fast light propagation. By means of linear birefringence, linearly polarized light can be transformed into elliptically or circularly polarized light and vice versa. In general, beside linear birefringence also dichroism can be present in a material. Dichroism is described by different absorption coefficients $\alpha_\parallel \neq \alpha_\perp$ for different directions of light polarization. Dichroism can result in a rotation of the polarization plane. In the following the experimental setup and the experimental procedure to measure the temperature dependence of the linear birefringence is explained.

In order to measure the linear birefringence of CuB_2O_4, a helium-neon (HeNe) laser is used as a light source. Proper linear polarization of the light wave is chosen by the use of a Glan-Thompson prism and a half-wave plate. The linear polarization axis is oriented at $+45°$ with respect to the retardation axis of the photoelastic modulator (PEM) explained below. Subsequently a quarter-wave plate generates circular polarization. To control the temperature the sample is mounted in a cryostat. The light propagates along the [010] axis through the (010) oriented CuB_2O_4 crystal. Behind the sample a photoelastic modulator (PEM-90 from Hinds Instruments) connected to a lock-in-amplifier is used in order to enhance the signal-to-noise ratio. The PEM retardation axis is aligned parallel to the [101] axis of the (010)-oriented CuB_2O_4 sample. The fused silica bar of the PEM is made to vibrate with a resonant frequency of about 50 kHz and an oscillating birefringence is induced. Afterwards, the light passes an analyzer, which is oriented at $-45°$ with respect to the PEM retardation axis, and is detected by a photodiode. Fig. 4.3 shows the experimental setup and the experimental results for a (010) oriented CuB_2O_4 sample.

In the following the procedure to measure the linear birefringence will be described [156]. Initially the linear polarizer (half-wave plate) and the analyzer are aligned perpendicular to each other in order to suppress the transmitted light, which is detected
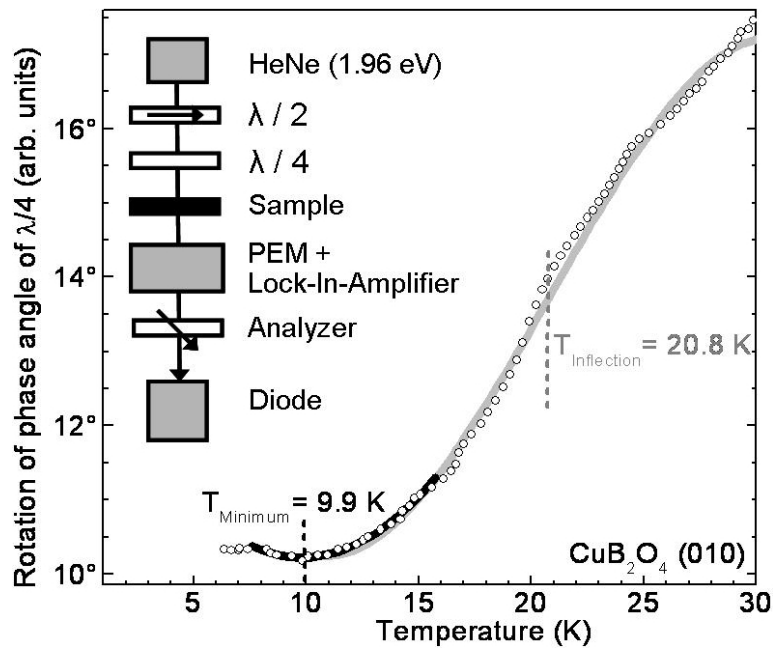
Figure 4.3: *Measurement of the linear birefringence in* CuB_2O_4: *Dichroism* $\alpha_{\parallel} \neq \alpha_{\perp}$ *of the sample is compensated by a proper alignment of the polarizer (half-wave plate) and the analyzer at a fixed temperature (6 K). Linear birefringence* $n_{\parallel} \neq n_{\perp}$ *of the sample is compensated by a computer-controlled quarter-wave plate, whose rotation angle is shown for different temperatures. In order to increase the signal to noise ratio, a photoelastic modulator (PEM) and a lock-in-amplifier are used. The inset shows the experimental setup, which is described in the text.*

by the photo diode. Then the dichroism $\alpha_{[001]} \neq \alpha_{[100]}$ of the sample is compensated by an adjustment of the half-wave plate, which is confirmed by a minimal signal detected by the photo diode, at a fixed temperature (T=6 K). During the measurement the temperature dependent linear birefringence $n_{[001]} \neq n_{[100]}$ of the sample is compensated by a rotation of the computer-controlled quarter-wave plate at each temperature. Assuming that the dichroism only changes negligible with the temperature, the birefringence is measured as a function of the temperature, which is shown in Fig. 4.3.

The experimental curve in Fig. 4.3 shows the arbitrary rotation angle of the quarter-wave plate vs. the temperature and features a local minimum at 9.9 K, which displays the magnetic phase transition at 10 K. Additionally an inflection point at 20.8 K indicates the magnetic phase transition at 21 K. Both features are not well pronounced. Due to the following reasons, this method is not very sensitive. Absorption effects, especially the temperature dependence of the absorption, are neglected. However, CuB_2O_4 is highly absorbing at the wavelength of the HeNe laser (632.8 nm, 1.96 eV). Thus measurements of the linear birefringence in the transparency region of CuB_2O_4 might provide higher sensitivity. A possible improvement might also be the use of a tunable light source in order to exploit the spectral degree of freedom. In addition the measured birefringence includes crystallographic and magnetic contributions, which makes the

detection of the magnetic phase transitions difficult. The crystallographic contribution to the linear birefringence can be suppressed by using (001) oriented CuB_2O_4 samples, where the propagation direction of the light is parallel to the optical axis. However, possible contributions to the linear birefringence caused by strain or defects remain. In conclusion, this method is not very appropriate to obtain access to the magnetic properties of the Cu^{2+} sublattices.

4.2.2 Linear absorption

Linear absorption measurements are carried out in the range of $1.3 - 2.5$ eV using a Cary 2300 spectrophotometer and a 0.85 m SPEX monochromator. The sample is cooled by a closed cycle refrigerator to 20 K. Absorption spectra reveal a strong polarization and light propagation direction dependence, which are shown in Fig. 4.4 for different experimental geometries. Due to the transmission window above 2.5 eV
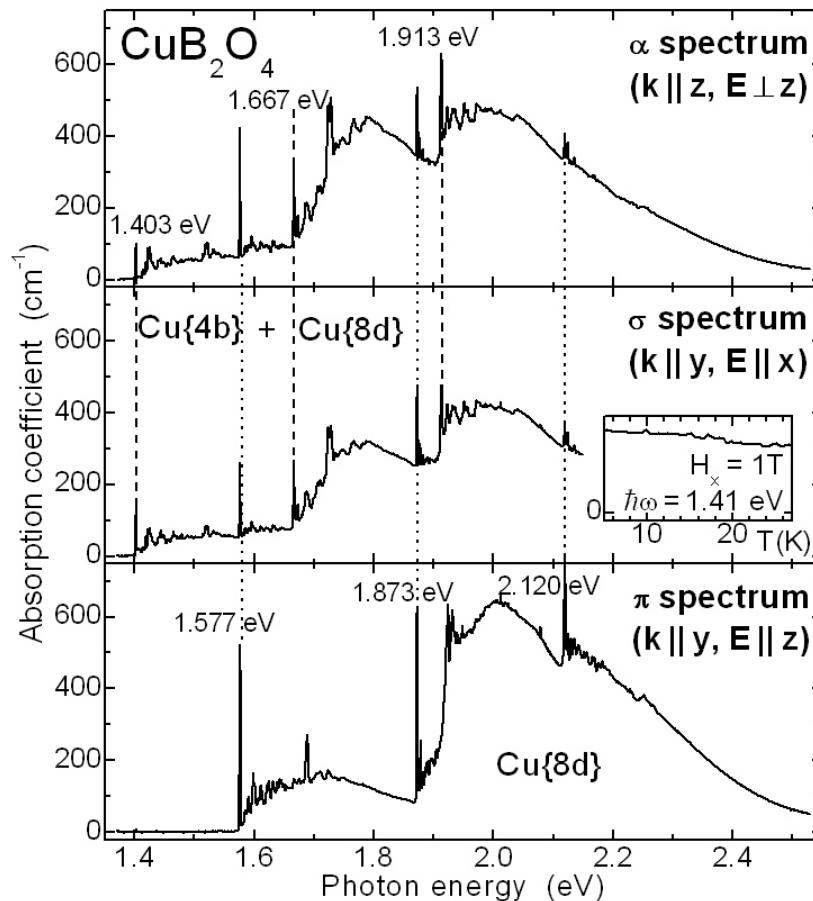
Figure 4.4: *Linear absorption spectra in CuB_2O_4: α spectrum with (001) oriented and σ/π spectra with (010) oriented CuB_2O_4 at $H = 0$, $T = 20$ K. $\mathbf{k}$ and $\mathbf{E}$ denote wave vector and polarization of the incoming light wave at frequency ω. The inset shows exemplarily the temperature dependence of the first line at 1.41 eV in the σ spectrum.*

and below the polarization dependent absorption edge (3.5-4.0 eV [155]), the CuB_2O_4 crystals appear blue.

Narrow and broad transitions in CuB_2O_4 are observed and up to 70 well-resolved phonon sidebands are found. Since most wide-gap transition-metal oxides with $d-d$ transitions below the band gap absorption bands reveal broad and featureless absorption spectra below the band gap [157, 158, 159], different mechanisms should be involved in CuB_2O_4. The well pronounced fine structure in CuB_2O_4 might be explained as follows. The boron ion B^{3+} is very small, since it has the same electron configuration as the helium atom. This might lead to an increased probability density of the outer electrons of the oxygen ions O^{2-} in the vicinity of the boron ions, whereas it is decreased in the vicinity of the copper ions Cu^{2+} [160]. Thus a strong hybridisation of the electronic orbitals of the oxygen ion O^{2-} and the boron ion B^{3+} might be expected, whereas the hybridisation between the Cu^{2+} and O^{2-} ions would be weak. Consequently the Cu^{2+} energy levels would reproduce the sharp atomic Cu^{2+} levels shown in Fig. 4.2. In opposite, in cuprates with large ions as e.g. La_2CuO_4, where lanthanum ions are present instead of boron ions, the large ions occupy more space and the oxygen electrons are shifted more to the copper ions leading to a stronger hybridization and thus to a broadening of the sharp electronic energy levels, which might explain, that no fine structure is observed in cuprates with large ions.

In CuB_2O_4, the α and σ spectra feature six sharp lines at [1.403 eV, 1.667 eV, 1.913 eV] and [1.577 eV, 1.873 eV, 2.120 eV]. These two groups of lines are related to the transitions between the electronic states of the 4b and 8d sites of the Cu^{2+} ions, respectively. In opposite, the π spectrum only reproduces the second group of lines, since the incoming z-polarized light does not couple to the Cu^{2+} 4b site, whose local coordination plane is perpendicular to the z axis (see Fig. 4.1(b)). In the case of the Cu^{2+} 8d site, light with any chosen polarization is absorbed due to its tilted position with respect to the crystallographic axes. Therefore the sublattices can be separated with linear absorption by polarization selection rules.

A critical limitation of linear absorption experiments is revealed by the inset in Fig. 4.4. While absorption displays the lines in Fig. 4.4 as electronic transitions, it is nonetheless insensitive to magnetic ordering, as can be seen from the constant absorption value between 5 K and 25 K. However, it will be shown in section 4.3, that the magnetic structure is revealed by MFISH.

4.2.3   Photoluminescence

Another linear optical technique used in this work to study the magnetic properties of CuB_2O_4 is the photoluminescence (PL). Here an incident light field excites the sample at a fixed wavelength and the photoluminescence light is detected. Thereby the spectral dependence of the PL intensity can be studied. Relaxation processes between the excitation and the photon emission are of big importance. These relaxation processes are mostly based on the phonon scattering. PL spectroscopy enables access to states, which are energetically below the excitation energy and can be excited during the relaxation process. Note that also imperfections (trap states) can provide a strong PL
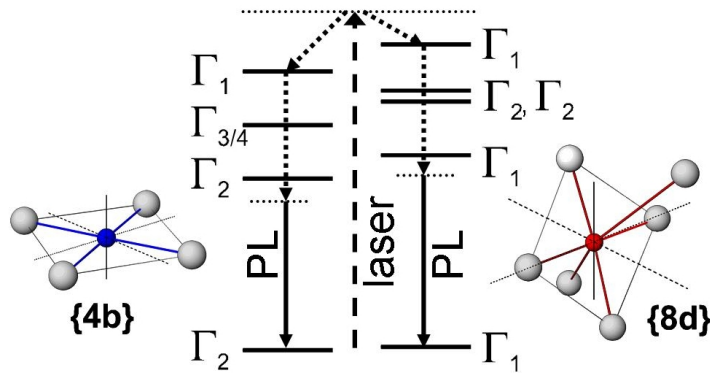
Figure 4.5: *Schematic diagram of the d energy levels of CuB_2O_4 (solid lines) and the PL process. PL excitation at 2.33 eV (dashed arrow) followed by relaxation processes (dotted arrows) leads to the PL signal (solid arrows). Note that trap states (dotted lines below d states) are involved in these processes.*

signal [161]. Fig. 4.5 shows schematically the excitation, possible relaxation and PL emission processes in CuB_2O_4.

For the PL measurements the following experimental setup is used. The photoluminescence is excited by linearly polarized light emitted by a frequency doubled continuous-wave Nd:YAG laser (E_{SH} = 2.33 eV). A split-coil cryostat generates magnetic fields up to 7 T in the Faraday geometry. The photoluminescence signal generated in the (001) oriented CuB_2O_4 sample passes a quarter-wave plate and an analyzer in order to study the polarization dependence of the PL light. The PL signal is also studied spectrally using a 1.5 m triple grating monochromator and a CCD camera.

Photoluminescence spectra are shown in Fig. 4.6. The only observed photoluminescence signal is emitted in the spectral ranges 1.38-1.40 eV and 1.526-1.534 eV, where sets of narrow lines are observed (Fig. 4.6(a), (c)). The line widths of the narrowest lines, e.g. the line at 1.3895 eV at 7 T shown in Fig. 4.6(a), are found to be about 0.1 meV. Thus a lower limit for the life time of the occupied states can be calculated to be 40 ps using the Heisenberg uncertainty principle. Note that inhomogeneous broadening might be involved or lines might be not resolved and therefore the lifetime can be orders of magnitude larger than 40 ps. PL signals nearby 1.39 eV and 1.53 eV are attributed to the lowest transitions of the Cu^{2+} 4b and 8d sites, respectively, since the spectral positions are rather close to the energetically lowest lines found in the absorption spectra. It is shown above, that these lines reveal access to the two sublattices. The PL lines are shifted and enhanced by an applied magnetic field as can be seen from Fig. 4.6(a), (c). Note that no significant difference between the circular polarizations σ^+ and σ^- of the PL light is found in the PL spectra and the PL intensity. However, no shift of the PL peak energies with increasing temperature is observed. The temperature dependence of the integrated PL signals nearby 1.39 eV (Fig. 4.6(b)) reveals an anomaly at 10 K and a strong decrease of the PL signal with increasing temperature below 21 K. This confirms that the Cu^{2+} ions at the 4b sites are magnetically ordered below 21 K and that another phase transition at 10 K is present. In contrast, the integrated PL signals nearby 1.53 eV displays only the anomaly at 10 K but does not show any feature around 21 K. This is also in accordance with the reported property of the magnetic structure, that the Cu^{2+} ions at the 8d sites are magnetically disordered below 21 K, and that a magnetic ordering occurs at 10 K. Thus the magnetic

sublattices can be distinguished by means of PL spectroscopy and different magnetic behavior is found.
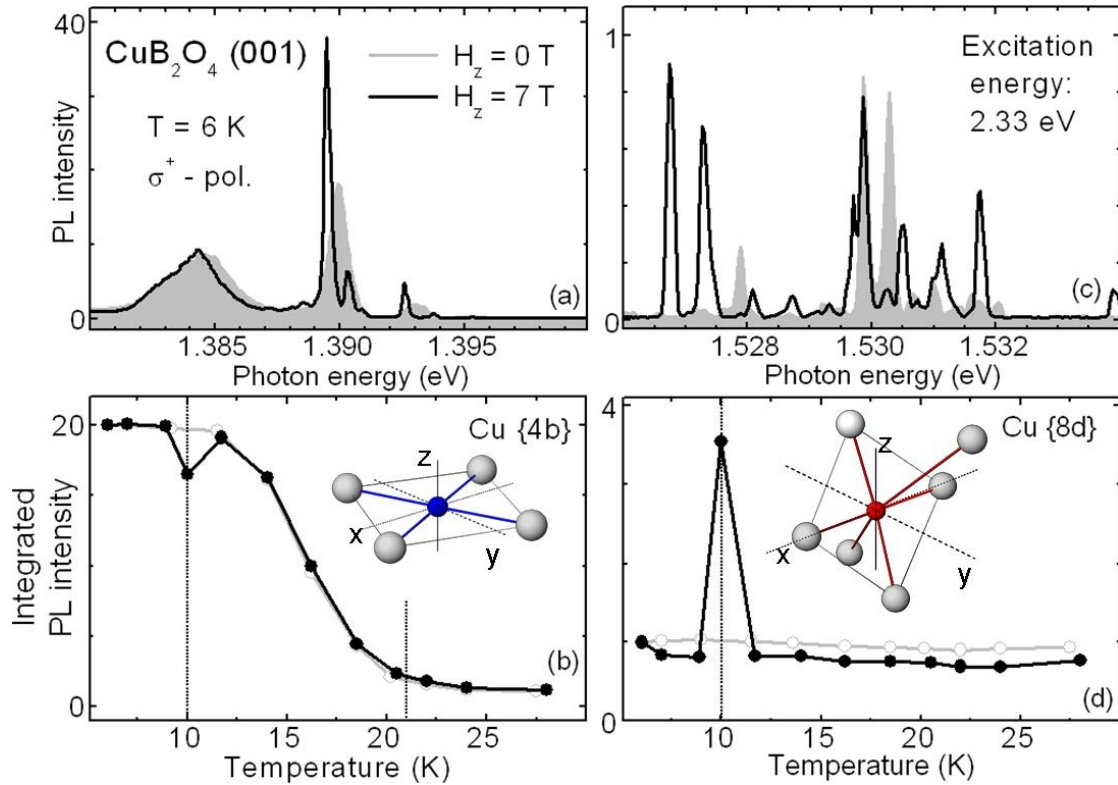
Figure 4.6: *Photoluminescence in CuB_2O_4 in reflection geometry: (a) and (c) show PL spectra at 0 T and 7 T for different spectral ranges. σ^+ polarized PL light is detected in the Faraday geometry ($\mathbf{k} \parallel \mathbf{H} \parallel [001]$) at T = 6 K. The line width of the narrow transitions is about 0.1 meV. (b) and (d) show the temperature dependence of the integrated photoluminescence signal (integrated over the spectral ranges shown in (a) and (c), respectively). Magnetic phase transitions at 10 K and 20 K can be identified.*

However, in opposite to the SHG technique discussed below, PL spectroscopy provides only indirect access to the magnetic sublattices due to the fact, that relaxation processes and traps are involved in the PL process sketched in Fig. 4.5. Furthermore no indication for interaction between sublattices is found.

In conclusion, by means of linear optical techniques it is possible to observe some features caused by the magnetic structure, but no satisfactory access to the Cu^{2+} sublattices using linear optical techniques is reached. In the next chapter the technique of nonlinear magneto-optics will be introduced to obtain new and complementary information about the magnetic structure.

4.3 Nonlinear optical methods (SHG)

4.3.1 SHG processes

The simplest nonlinear optical process is second harmonic generation (SHG). Since CuB_2O_4 possess a non-centrosymmetric crystal structure, the SHG process is allowed in the electric-dipole approximation

$$P_i(2\omega) = \epsilon_0 \chi'_{ijk} E_j(\omega) E_k(\omega), \qquad (4.2)$$

with $\vec{E}(\omega)$ and $\vec{P}(2\omega)$ as electric field of the incident fundamental light and SHG polarization induced in the crystal. Taking into account the crystallographic symmetry $\overline{4}2m$ the nonlinear susceptibility tensor χ'_{ijk} transforms as a polar i-tensor of third-rank. Therefore the allowed tensor components are restricted to have indices xyz and permutations [83]. This crystallographic SHG contribution is investigated in Refs. [47, 155] and will not be considered here. A suitable choice of polarizations for $\vec{E}(\omega)$ and $\vec{P}(2\omega)$ is used to suppress the crystallographic SHG contribution.

SHG in the presence of a static magnetic field $\vec{H}^0$ is described by

$$P_i(2\omega) = \epsilon_0 \mathrm{i} \chi_{ijkl} E_j(\omega) E_k(\omega) H_l^0, \qquad (4.3)$$

where χ_{ijkl} represents the magnetic-field-induced SHG (MFISH) susceptibility which is an axial fourth-rank tensor and time-invariant ($\hat{T}\hat{\chi} = +\hat{\chi}$ with $\hat{T}$ as time reversal) in the case of A-type MFISH and time-noninvariant ($\hat{T}\hat{\chi} = -\hat{\chi}$) in the case of B-type and C-type MFISH respectively.

4.3.2 Spectral separation of Cu^{2+} sublattices

In the following the MFISH process will be used to investigate the magnetic properties of the two Cu^{2+} sublattices. Therefore the spectral, temperature and magnetic field dependence will be investigated. Fig. 4.7 shows polarization dependent MFISH spectra of CuB_2O_4. The inset in Fig. 4.7(b) reveals an increase of the MFISH intensity in the magnetic field by 3 orders of magnitude. Without magnetic field, the MFISH intensity is below the detection limit, and no residual crystallographic SHG is observed confirming its proper suppression.

At $\mu_0 H_x = 7$ T this, according to the following discussion of Fig. 4.9(d), A-type MFISH signal is of the order of magnitude as SHG in crystalline quartz, and thus exceeding the reported effect (see e.g. Ref. [17]) by many orders of magnitude. The MFISH spectrum displays sets of narrow zero-phonon lines (line width < 1 meV) corresponding to $d-d$ transitions of the $Cu^{2+}(3d^9)$ ions. Additionally a spectrally broad background is formed by phonon-assisted transitions (line width > 100 meV). The MFISH signal bears resemblance to the linear absorption by means of spectral features, but the main advantage in the case of the MFISH process is the sensitivity to the magnetic properties of CuB_2O_4.
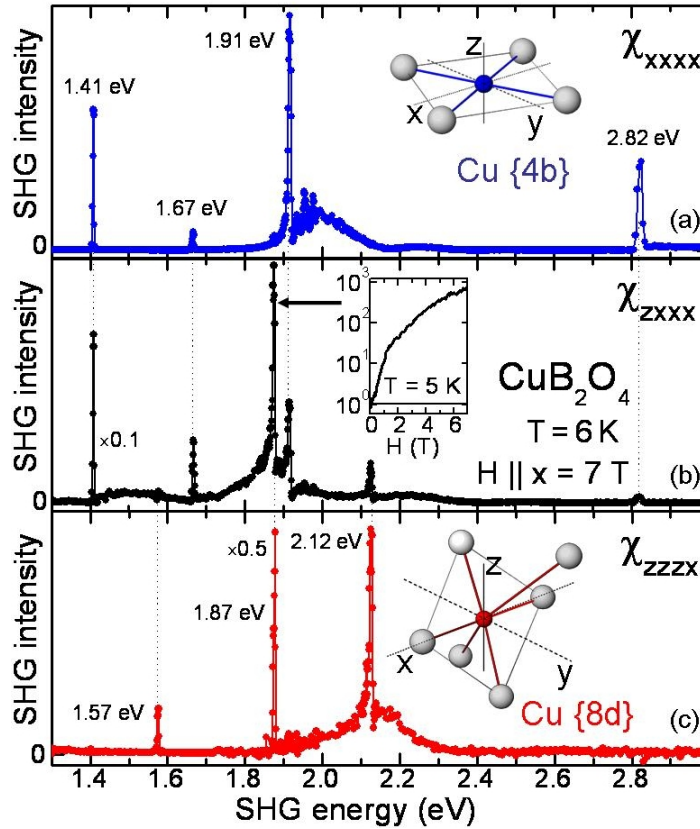
Figure 4.7: *Polarization dependence of sublattice sensitive MFISH in CuB_2O_4. MFISH spectra of (010) oriented CuB_2O_4 in a static magnetic field applied along the x axis. Inset (b) shows the magnetic-field dependence of MFISH. Susceptibilities χ_{ijkl} refer to Eq. (4.3).*

4.3.2.1 Distinction of sublattices by polarization selection rules

Comparing the MFISH spectra for χ_{xxxx}, χ_{zxxx}, and χ_{zzzx} shown in Fig. 4.7(a)-(c), three sets of zero-phonon transitions are observed leading to the following classification:

(1) lines at 1.410 eV, 1.675 eV, 1.910 eV

(2) lines at 1.575 eV, 1.875 eV, 2.120 eV

(3) a line at 2.820 eV.

Lines presented by group (1) are associated to transitions of the $Cu^{2+}\{4b\}$ ion. Those are reproduced by the χ_{xxxx} and χ_{zxxx} components as well as by α and σ polarized light in linear absorption (see Fig. 4.4). However, lines of group (1) are absent in the MFISH spectra showing χ_{zzzx} as well as in π spectrum of linear absorption, because the $Cu^{2+}\{4b\}$ ion and its four O^{2-} ligands form a planar structure in the xy plane, which does not couple to z polarized incident light. Lines presented by group (2) are associated to transitions of the $Cu^{2+}\{8d\}$ ion. They are reproduced by the χ_{zzzx} and χ_{zxxx} components as well as for α, σ and π polarized light in linear absorption. Since

the $Cu^{2+}\{8d\}$ ion and its six O^{2-} ligands form a tilted tetrahedron with respect to the crystallographic axes, light with any polarization is absorbed. Group (3) contains one line at twice the photon energy of the 1.410 eV line from group (1). It does not indicate an electronic state, but a two-photon transition enhanced by a resonant single-photon transition to the intermediate state at 1.410 eV [113].

The spectra shown by Figs. 4.4 and 4.7 are in full agreement with Fig. 4.2. Both Cu^{2+} sites reveal three transitions from the $x^2 - y^2$ ground state to the xy, yz/xz and $3z^2 - r^2$ states. Due to the estimation that the influence of the remote apical O^{2-} ions of the 8d site is small, the transition energies for the 4b and 8d sites are similar.

4.3.2.2 Magnetic ordering of the sublattices

After associating the groups of lines (1)-(3) to the sublattices of CuB_2O_4, their magnetic properties can be investigated. Fig. 4.8 shows MFISH spectra of the component χ_{zxxz}.
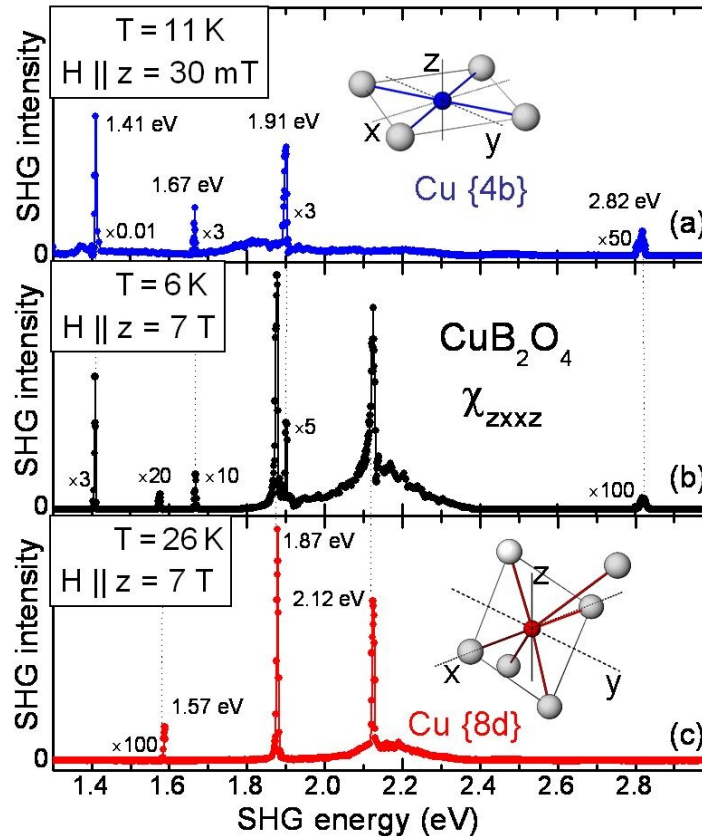
Figure 4.8: *Magnetic phase dependence of sublattice sensitive MFISH in CuB_2O_4. MFISH spectra of component χ_{zxxz} of (010) oriented CuB_2O_4 in a static magnetic field applied along the z axis. Commensurate antiferromagnetic phase: (a) 11 K, 30 mT. (b) 6 K, 7 T. Paramagnetic phase: (c) 26 K, 7 T.*

This component is chosen, since it reproduces both groups of lines and therefore both

sublattices. As shown by the inset of Fig. 4.7(b) no MFISH intensity is generated without externally applied magnetic field. Applying a low magnetic field of 30 mT at 11 K is sufficient to observe the lines of group (1) representing the 4b site (Fig. 4.8(a)). In contradiction to the ordering of the 4b site at low magnetic fields, the 8d site remains disordered since no lines of group (2) are observed. In a high magnetic field of 7 T and at 6 K, additional contributions of lines of group (2) appear (Fig. 4.8(b)) indicating an alignment for the 8d site. Raising the temperature above the Néel temperature to 26 K at 7 T leads to a vanishing of the lines correlated to the 4b site, whereas the lines correlated to the 8d site are still observed (Fig. 4.8c). Therefore the MFISH component χ_{zxxz} of the lines of group (2) indicates the presence of a paramagnetic component of the 8d site.

4.3.3 Coupling between sublattices

In order to have a closer look at the magnetic ordering and coupling of the 4b and 8d sites, the strongest transitions at 1.410 eV and 1.875 eV will be studied using variations of temperature and magnetic field. The dependence of the MFISH signal on the temperature at different magnetic fields is shown in Fig. 4.9. The MFISH
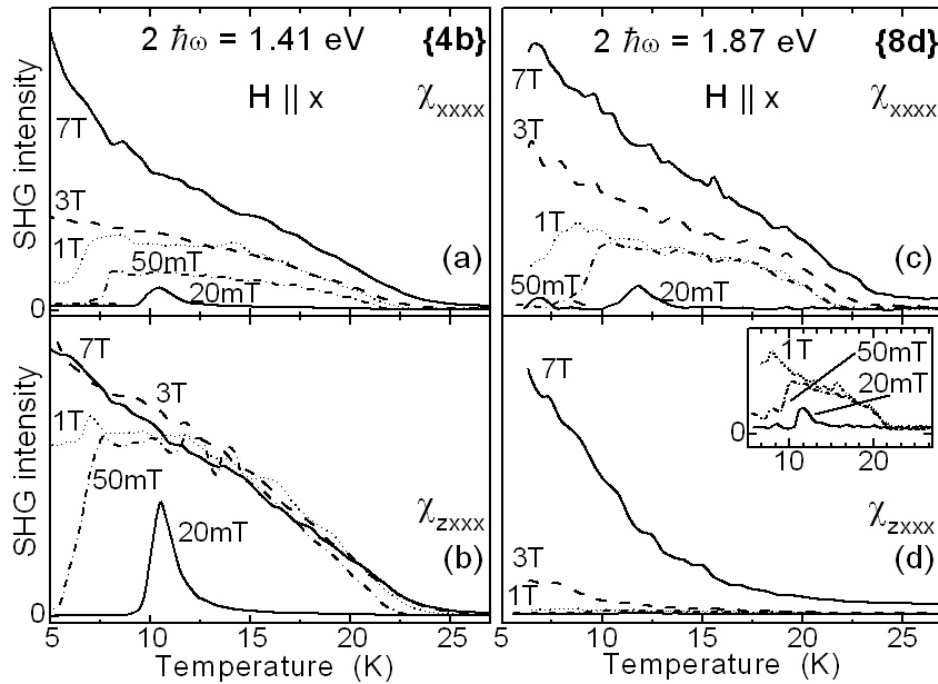
Figure 4.9: *Coupling of sublattices in CuB_2O_4 for H∥x. Temperature dependence of MFISH intensity at (a,b) 4b and (c,d) 8d sites in static magnetic fields applied along the x axis of (010) oriented CuB_2O_4.*

intensity at 1.410 eV reproducing the magnetic ordering of the 4b site (Figs. 4.9(a), (b)) in the range of 10 K $< T <$ 21 K is saturated at 50 mT, which indicates a

saturation of the weak ferromagnetic moment accompanying the antiferromagnetic order. Therefore the temperature and magnetic field dependence of the magnetic order parameter is revealed. In the case of the 8d site, at 1.875 eV both ferromagnetic (Fig. 4.9(c)) and paramagnetic (Fig. 4.9(d)) behavior are observed depending on the detected polarization x or z of the MFISH signal, respectively. Apparently the magnetic ordering of the Cu^{2+} ions at the 4b site is partly transferred to the Cu^{2+} ions at the 8d site, where it coexists with a disordered paramagnetic component.

In opposite to contemporary belief [146, 148, 72, 151], measurements of the MFISH reveal a partial coupling between the 4b and 8d sublattices in the commensurate antiferromagnetic phase in an applied magnetic field.

Similar results are obtained in static magnetic fields applied along the z axis. The
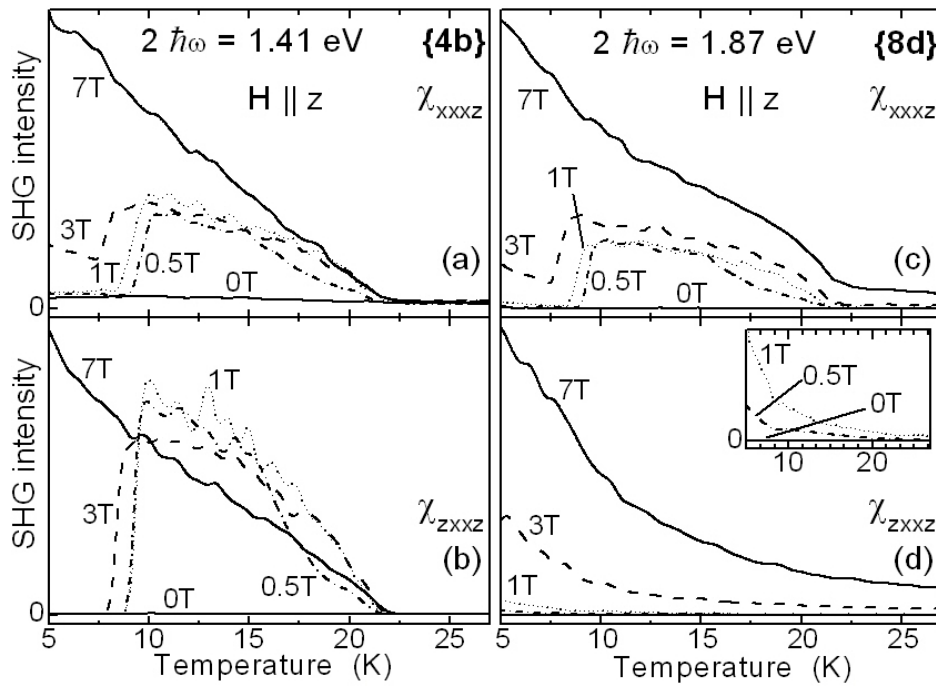
Figure 4.10: *Coupling of sublattices in CuB_2O_4 for H$\|$z. Temperature dependence of MFISH intensity at (a,b) 4b and (c,d) 8d sites in static magnetic fields applied along the z axis of (010) oriented CuB_2O_4.*

temperature dependencies of the MFISH signals at different magnetic field are shown in Fig. 4.10. The weak ferromagnetic moment accompanying the antiferromagnetic order is oriented along the z axis in this case.

The magnetic field dependencies of the MFISH signals at 11 K with magnetic fields applied along the z axis are shown in Fig. 4.11. At 1.410 eV the MFISH signal remains nearly constant at magnetic fields higher than 50 mT reproducing the saturation of the weak ferromagnetic moment. In contrast at 1.875 eV the MFISH signal increases with the magnetic field even above 1 T indicating the alignment of the paramagnetic component. Below 1 T the component χ_{xxxz} (Fig. 4.11(a), (c)) reveals the same slope
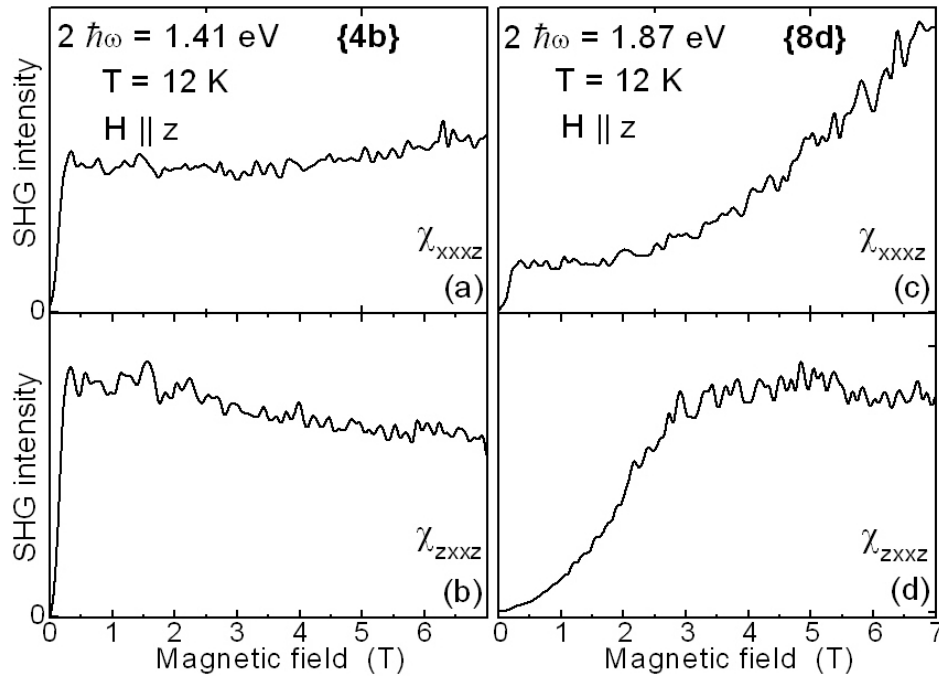
Figure 4.11: *Coupling of sublattices in CuB$_2$O$_4$. Magnetic field dependence of MFISH intensity at (a,b) 4b and (c,d) 8d sites at 11 K. The magnetic field is applied along the z axis of (010) oriented CuB$_2$O$_4$.*

of the MFISH intensity for both, 1.410 eV and 1.875 eV, displaying the transfer of the magnetic ordering from the 4b to the 8d site.

4.3.4   Magnetic phase diagrams of 4b and 8d sites

At $\mu_0 H \lesssim 1$ T, only A- and C-type MFISH are observed. A-type MFISH is shown, e.g. in Figs. 4.9(d) and 4.10(d), and is discussed above. C-type MFISH will be investigated more detailed in section 4.3.6. However, at $\mu_0 H > 1$ T and low temperature (T~6 K), Figs. 4.9(a), (b) and 4.10(a), (b) reveal B-type MFISH caused by field-induced phase transitions. The magnetic phase diagrams of CuB$_2$O$_4$ for $H \perp z$ and $H \parallel z$ geometries are shown by Fig. 4.12. The dependence of the phase boundaries in the magnetic phase diagram with applied magnetic field $H \perp z$ is found to be independent on the direction of H in the xy plane. The incommensurate purely antiferromagnetic phase I is suppressed in the magnetic field by the weakly ferromagnetic commensurate phases labelled II and III respective different directions of magnetization. At 0 K quenching appears at the extrapolated fields $\mu_0 H_x = 1.6$ T (I→II) and $\mu_0 H_z = 30$ T (I→III). The respective phase transitions are of second (I→II) and first (I→III) order, indicating gradual (I→II) and abrupt (I→III) reorientation of spins shown by the insets of Fig. 4.12. A comparison of our data with recent neutron diffraction data [162] revealing a magnetic phase transition for $\mu_0 H = 1.3$ T with $H \parallel [110]$ at 4.2 K evidences good agreement (neutron diffraction data are shown by grey triangle in Fig. 4.12(a)).
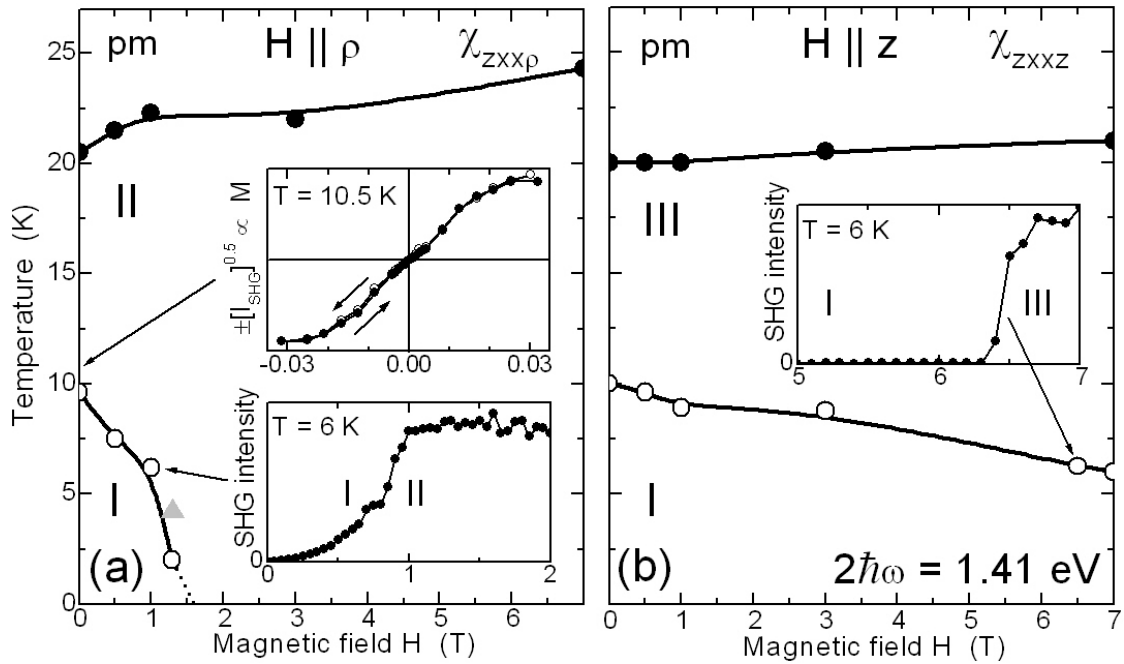
Figure 4.12: *Magnetic phase diagrams of CuB_2O_4. The magnetic field/temperature plane is shown for (a) in-plane ($H \parallel \rho$ with $\rho \perp z$) and (b) uniaxial ($H \parallel z$) magnetic field. Insets: SHG intensity I_{SHG} or magnetization $M \propto \pm I_{SHG}^{0.5}$ in dependence of magnetic field for selected points in the phase diagram. Grey triangle (a) corresponds to neutron diffraction data [162].*

In the case of the 8d site, the components χ_{xxxx} and χ_{xxxz} uncover similar magnetic phase boundaries as found for the 4b site (Fig. 4.12) indicating the partial coupling to the 4b site, while the components χ_{zxxx} and χ_{zxxz} display pure paramagnetic behavior in the hole phase diagram.

4.3.5   Determination of the magnetic symmetry

The magnetic symmetry will be determined by means of observation of non-vanishing MFISH tensor components according to the Neumann principle [83]. Therefore first the rotational anisotropy has to be studied in order to reveal non-vanishing tensor components.

The MFISH rotational anisotropy shown by Fig. 4.13 is recorded at $2\hbar\omega$=1.91 eV (4b site) in the commensurate antiferromagnetic phase (at 6 K with an applied magnetic field of 7 T along z) as a function of the azimuthal angle φ of the fundamental and the MFISH polarization for the $\mathbf{E}(2\omega) \parallel \mathbf{E}(\omega)$ and $\mathbf{E}(2\omega) \perp \mathbf{E}(\omega)$ geometries. These experimental data are modeled simultaneously for both geometries assuming the presence of the MFISH components χ_{xxxz} and χ_{zxxz}, which are observed in the MFISH spectra shown above. For the polarization geometry $\mathbf{E}(2\omega) \parallel \mathbf{E}(\omega)$, the SHG

Figure 4.13: *MFISH anisotropy in CuB_2O_4. The rotational anisotropy is measured at $2\hbar\omega =1.910$ eV in geometries $\mathbf{E}(2\omega) \parallel \mathbf{E}(\omega)$ (light shaded area and open circles) and $\mathbf{E}(2\omega) \perp \mathbf{E}(\omega)$ (dark shaded area and filled circles). Experimental data (dots) and simulations (shaded areas) are shown.*
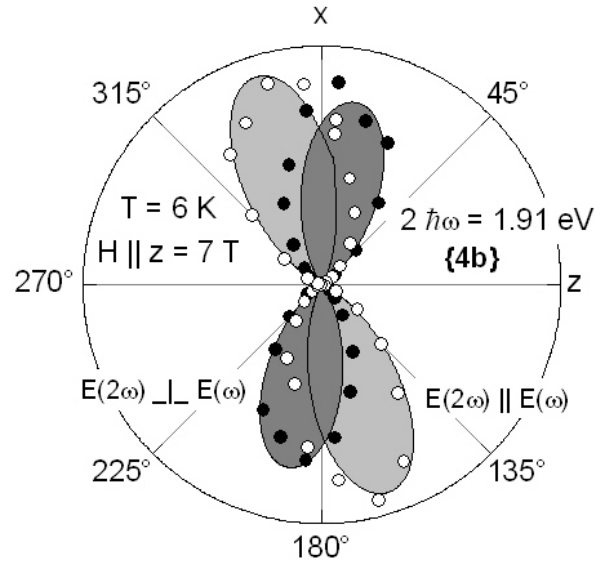
anisotropy is given by

$$I(2\omega)_{\parallel}^{MFISH} \propto |\frac{1}{4}\chi_{xxxz}[\cos(3\varphi) + 3\cos(\varphi)] + \frac{1}{4}\chi_{zxxz}[\sin(3\varphi) + \sin(\varphi)]|^2 \qquad (4.4)$$

and for the geometry $\mathbf{E}(2\omega) \perp \mathbf{E}(\omega)$

$$I(2\omega)_{\perp}^{MFISH} \propto |\frac{1}{4}\chi_{xxxz}[- \sin(3\varphi) - \sin(\varphi)] + \frac{1}{4}\chi_{zxxz}[\cos(3\varphi) + 3\cos(\varphi)]|^2 \qquad (4.5)$$

is calculated. The calculated curves (with parameters $\chi_{xxxz} = -\chi_{zxxz}$) are shown by lines with shaded areas. Good agreement between experimental and calculated MFISH intensities is found for rotational anisotropy indicating, that tensor components different to χ_{xxxz} and χ_{zxxz} are negligible for this geometry and this photon energy. In the case of $\mathbf{H} \parallel \mathbf{x}$, the components χ_{xxxx} and χ_{zxxx} contribute to the MFISH intensity (Fig. 4.7(a), (b)). In the case of the 8d site also the component χ_{zzzx} is observed (Fig. 4.7(c)).

MFISH described by Eq. (4.3) from χ_{xxxx}, χ_{zxxx} and χ_{zzzx} is allowed for the magnetic point groups 1, $\bar{1}$, 2, m, $\underline{2}/m$ and eight trigonal or hexagonal groups [83]. The trigonal and hexagonal groups are ignored due to their incompability with the tetragonal lattice. The groups $\underline{\bar{1}}$ and $\underline{2}/m$ do not allow a ferromagnetic moment and are not taken into account. Excluding monoclinic symmetry, only groups $\underline{2}$ and m remain. Group m with a twofold [110] symmetry axis points to a magnetic structure with a ferromagnetic moment parallel to the symmetry axis. In contrast group $\underline{2}$ indicates a magnetic structure with mirror plane (100), (010) or (001) and in-plane ferromagnetic moment. Figs. 4.9 and 4.10 and their respective discussion show, that the ferromagnetic moment can be oriented either along the x or z axis by an external magnetic field of 50 mT without further reduction of magnetic symmetry. Therefore the magnetic symmetry of the commensurate antiferromagnetic phase of CuB_2O_4 is found to be $\underline{2}$ with the mirror plane xz and an in-plane weak ferromagnetic moment.

4.3.6   Antiferromagnetic domain structure

4.3.6.1   Hysteresis of C-type MFISH

Magnetic fields below 50 mT can be used to align the weak Dzyaloshinskii-Moria type ferromagnetic moment in the xz plane (section 4.3.4). These manipulations of the weak ferromagnetic moment can be used to investigate the commensurate antiferromagnetic ordering and its respective domain structure. In the following part the MFISH of C-type will be considered in an applied magnetic field $H \parallel x$ in order to investigate the magnetic phase II. The saturation of the weak ferromagnetic moment along the x axis in a magnetic field leads to the generation of a single-domain state. MFISH of C-type is shown by Fig. 4.14(a). The dependence of the MFISH intensity on the temperature
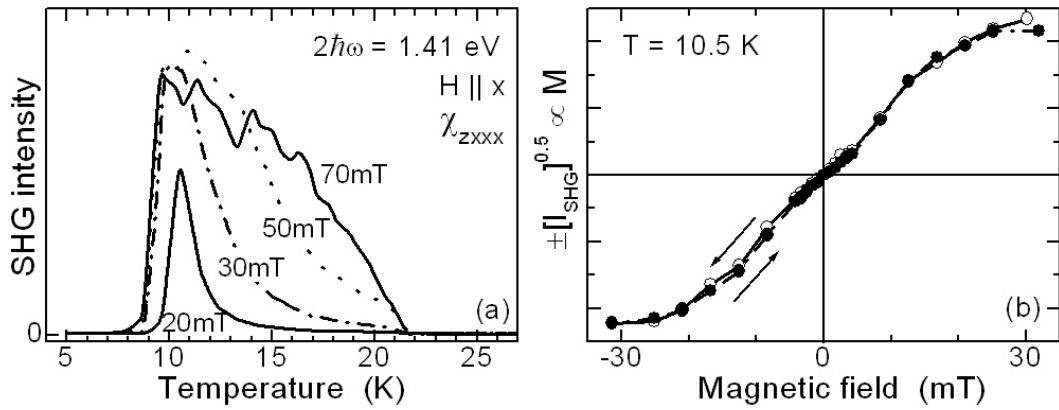
Figure 4.14: *Hysteresis in the magnetic phase II in CuB$_2$O$_4$. (a) Dependence of MFISH intensity on the temperature at low magnetic fields. Saturation of MFISH signal at $\mu_0 H_x < 30$ mT (11 K). (b) Hysteresis curve obtained by $M \propto \pm I_{SHG}^{0.5}$.*

at low magnetic fields reveals a saturation of the MFISH signal at $\mu_0 H_x < 30$ mT (11 K). Since the MFISH intensity couples quadratically to the external magnetic field as shown by the lower inset of Fig. 4.12(a) the hysteresis in Fig. 4.14(b) is obtained by $M \sim I_{SHG}^{0.5}$, where M is the magnetization. The coercive field of this hysteresis does not exceed the resolution limit of 0.5 mT. The formation process of domains within the hysteresis will be investigated in the following.

4.3.6.2   Domain structure

Before investigating the antiferromagnetic domain structure in phase II experimentally, group theoretical considerations will be done. The crystallographic symmetry of CuB$_2$O$_4$ is $\overline{4}2m$ with 8 symmetry elements given by Eq. (4.1) and thus the order of the non-magnetic symmetry group is 8. Additionally the time-inversion symmetry increases this number by a factor of 2 and altogether 16 symmetry elements exist, which leads to the order of the paramagnetic symmetry group of 16. The magnetic symmetry

of a single domain is determined to be $\underline{2}$ (section 4.3.5). The antiferromagnetic symmetry group $\underline{2}$ has the two symmetry elements 1 and $\underline{2}_z$ [83], and thus the order of the antiferromagnetic symmetry group is 2. The number of possible domains is given by the ratio of the order of the paramagnetic to that of the antiferromagnetic symmetry group, which is 16/2=8. Four orientational domains, with two 180°-domains each, can be present. The four different orientational domains are transformed into each other by the symmetry elements of the crystallographic point group $\overline{4}2m$, which are not present in the antiferromagnetic point group $\underline{2}_z$ combined with the time-inversion symmetry (section 1.1.2.4). Different 180°-domains are transformed into each other by application of the time inversion operator. Investigations of the domain structure of CuB_2O_4 will be rather complicated, since eight different domains are allowed accompanying the interactions between both sublattices. A distinction of 180°-domains requires an experimental phase-sensitive technique, which is explained in the following.

4.3.6.3   Phase-sensitive experimental setup

The experimental setup to investigate domains in CuB_2O_4 shown by Fig. 4.15 allows
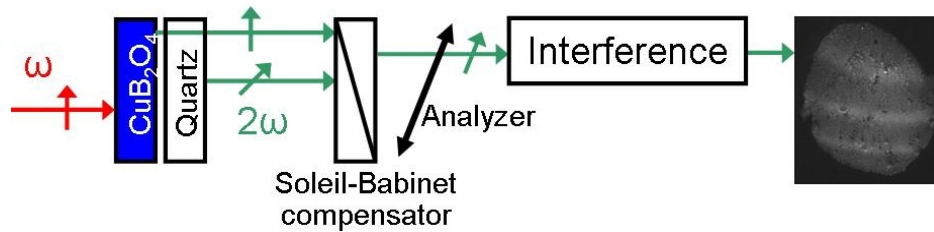
Figure 4.15: *Experimental setup to investigate the domain structure in CuB_2O_4. The technique is based on the interference of a crystallographic SHG contribution of quartz and a MFISH component of CuB_2O_4. A Soleil-Babinet compensator is used as a phaser shifter and allows phase-sensitive measurements. An analyzer is used to obtain a high contrast of interference by choosing a proper light polarization [79].*

the phase-sensitive investigation of MFISH [79]. The incident linearly polarized light at the frequency ω generates MFISH in the CuB_2O_4 crystal and crystallographic SHG in crystalline quartz. Polarizations of MFISH and SHG are chosen to be perpendicular to each other and coincide with the axes of the Soleil-Babinet compensator, which acts as a phase shifter. A Soleil-Babinet compensator offers different tunable refraction indices $n_\parallel \neq n_\perp$ because of a specific arrangement of quartz plates. This causes different phases for light waves propagating with polarizations parallel and perpendicular to the axes of the Soleil-Babinet compensator. By tuning the effective thickness of the wedge-shaped Soleil-Babinet compensator crystals, the phase between MFISH and SHG can be controlled. An analyzer projects both polarizations onto a certain axis allowing the detection of interference between MFISH and SHG. The angle of the analyzer is varied from 10°-80° with respect to the x axis of the CuB_2O_4 crystal in order to achieve the highest contrast of interference, which is observed if the MFISH and SHG intensity

are of the same magnitude ($I(2\omega)^{MFISH} \simeq I(2\omega)^{SHG}$). The transmitted light at the frequency 2ω is imaged onto a cooled CCD camera using a telephoto lens. The optical resolution is about 10 μm^2.

In the (010) oriented CuB$_2$O$_4$ crystal, the MFISH components χ_{xxxx} and χ_{zxxx} are generated by incident x-polarized light. The component χ_{xxxx} is suppressed by a proper polymer polarizing foil in front of the quartz crystal. Note that the special polarization foil transmits light at the fundamental frequency ω, which is polarized parallel to the x axis of the CuB$_2$O$_4$ crystal, with low absorption at 11 K in order not to suppress the generation of the crystallographic SHG contribution in quartz. The interference between χ_{zxxx} of CuB$_2$O$_4$ and χ_{xxx} of quartz is then studied phase-sensitive.

4.3.6.4   MFISH imaging

Since the crystallographic SHG contribution of quartz χ'_{xxx} is not influenced by the magnetic field, it acts as a reference to observe changes in the MFISH intensity and phase. Images of the CuB$_2$O$_4$ crystal are shown by Fig. 4.16. At zero field only SHG
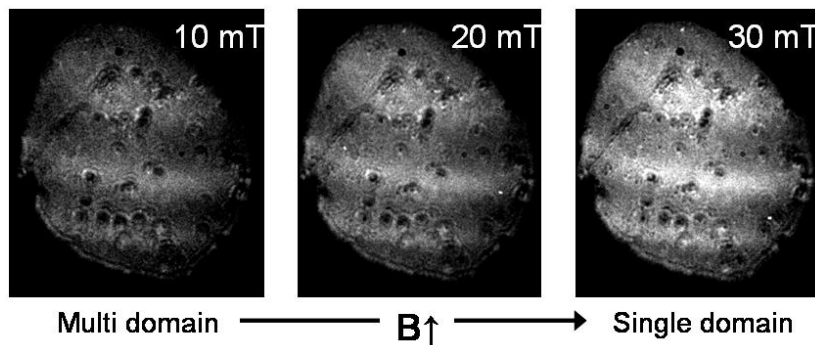
Figure 4.16: *Images of CuB$_2$O$_4$ crystal at different magnetic fields. Interference between the crystallographic SHG component χ'_{xxx} of quartz and the MFISH component χ_{zxxx} at 1.41 eV and 11 K is used in order to investigate the domain structure. Since no boarders but a gradual increase of the MFISH intensity is observed the domains size is believed to be below the optical detection limit (< 10 μm).*

signal from quartz is observed, since the MFISH signals caused by very small domains in CuB$_2$O$_4$ interfere destructively. An applied magnetic field influences the orientation of the weak ferromagnetic moment of the domains. With increasing field the MFISH component χ_{zxxx} increases leading to interference with the component χ'_{xxx}. A gradual increase of the MFISH intensity and the absence of domain walls are found below 30 mT. This points to a random distribution of domains with domain sizes below the optical detection limit (< 10 μm). The balance of the distribution of domain is changed by the magnetic field and finally approaches a single domain state with maximal MFISH signal at 30 mT. This result is not peculiar, since the domain structure and interactions between the sublattices are rather complicated and frustration of the antiferromagnetic ordering is possible.

Figure 4.17: *Phase measurement of MFISH signal in CuB$_2$O$_4$. Variation of the thickness of the Soleil-Babinet compensator crystal changes the relative phase between SHG and MFISH leading to the observed interference. E.g. a phase shift of $\Delta\phi^{MFISH} = 135°$ is observed for ±30 mT at $2\hbar\omega=1.41$ eV.*
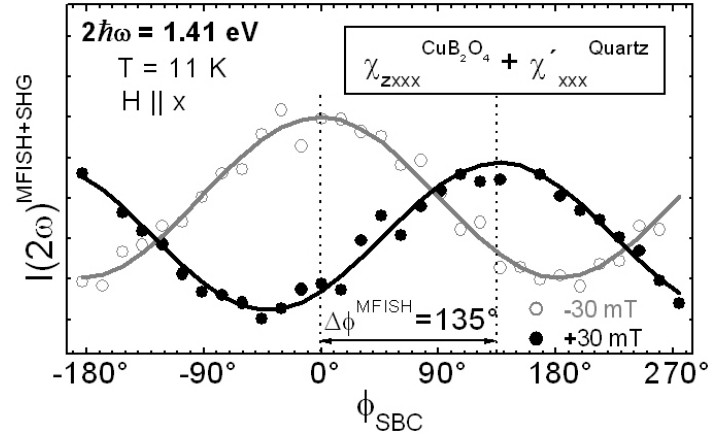
4.3.6.5 Phase sensitive measurements

Although the domains are too small for visualization, the alignment of the weak ferromagnetic moment by the applied magnetic field can be investigated by phase measurements of the MFISH signal shown by Fig. 4.17. A variation of the effective thickness of the Soleil-Babinet compensator crystal changes the relative phase between SHG and MFISH by ϕ_{SBC} leading to the detected interference signal. The interference signal is given by

$$
\begin{aligned}
I(2\omega)^{MFISH+SHG} \quad &\propto \quad |E'(2\omega)^{MFISH}|^2 + |E'(2\omega)^{SHG}|^2 \\
&+ \quad 2 \cdot |E'(2\omega)^{MFISH}| \cdot |E'(2\omega)^{SHG}| \cdot cos(\phi^{MFISH} - \phi^{SHG} + \phi_{SBC}),
\end{aligned}
\tag{4.6}
$$

where $E'(2\omega)^{MFISH} = E(2\omega)^{MFISH} \cdot cos(\beta)$ and $E'(2\omega)^{SHG} = E(2\omega)^{SHG} \cdot sin(\beta)$ are the projections of the light fields $E(2\omega)^{MFISH} \propto |\chi_{zxxx}| \cdot exp(i\phi^{MFISH})$ and $E(2\omega)^{SHG} \propto |\chi'_{xxx}| \cdot exp(i\phi^{SHG})$ generated in the CuB$_2$O$_4$ sample and the quartz reference, respectively, onto the polarization direction of the analyzer. β denotes the polarization direction of the analyzer and is given with respect to the x axis of the CuB$_2$O$_4$ sample. ϕ^{MFISH} and ϕ^{SHG} are the phases of the light fields. If tuning the phase ϕ_{SBC}, an interferogram as shown in Fig. 4.17 is obtained. E.g. at $2\hbar\omega=1.41$ eV a phase shift of $\Delta\phi^{MFISH} = 135°$ of the MFISH signal is observed for ±30 mT. The magnetic field dependence of the MFISH phase is shown for different MFISH energies in Fig. 4.18. Phase shifts of 90° at $2\hbar\omega=1.91$ eV and 180° at $2\hbar\omega=1.41$ eV are observed. 180° phase shifts are believed to indicate a spin-rotation as is known for 180°-domains [79]. The origin of the asymmetry of the phase hysteresis of the MFISH signal at $2\hbar\omega=1.41$ eV is not clarified. A possible explanation might be given by pinning effects, e.g. due to impurities or defects. The 90° phase shift at $2\hbar\omega=1.91$ eV might be caused by orientation domains. However, the phase shifts of 90° and 180° cannot be easily attributed to selected domains in CuB$_2$O$_4$. In addition, a comparison between MFISH phase and intensity (Fig. 4.18(b)) reveals hysteresis phenomena linked to different scales of the magnetic field, whose origin is not understood so far.
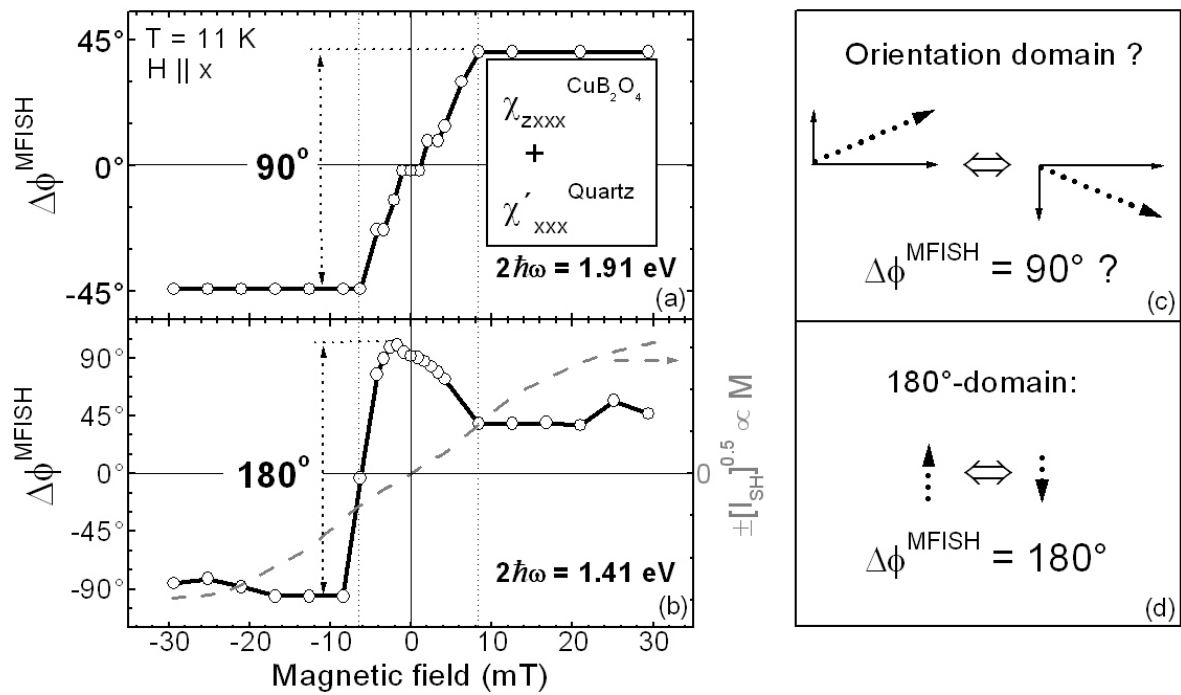
Figure 4.18: *Phase hysteresis of MFISH signal in CuB_2O_4. Magnetic field dependence of the MFISH phase is shown for different SHG energies. Observed phase shifts of 90° (a) and 180° (b) point to a correlation to the domain structure. The dashed line in (b) shows the magnetization $M \propto I_{MFISH}^{0.5}$. (c) and (d) show schematically the weak ferromagnetic moment of orientation domains and 180°-domains, respectively. The MFISH phase difference for two 180°-domains is expected to be $\Delta\phi^{MFISH} = 180°$ due to the domain definition [79]. In the case of orientation domains, a phase difference of $\Delta\phi^{MFISH} = 90°$ might be possible.*

In conclusion, access to the complicated domain structure is very difficult, since eight different domain contributions to the domain structure can be present in CuB_2O_4. Furthermore only very small domains are formed preventing their distinction.

4.4   Summary

Giant MFISH generation opens new degrees of freedom for investigating the magnetic and electronic properties of matter. CuB_2O_4 is used as a model system for an antiferromagnetic with a complicated magnetic structure possessing two inequivalent sublattices. Unusually sharp and intense spectral lines both in linear absorption and MFISH spectra are found. These spectral lines permit site selective access to the electronic and magnetic structure of CuB_2O_4. In opposite to linear optical techniques being whether insensitive to the magnetic ordering (linear absorption) or possessing other disadvantages, the MFISH is more advantageous to investigate the magnetic properties of CuB_2O_4. The MFISH signal reveals commensurate and incommensurate antiferromagnetic ordering and coupling of the MFISH signal to the weak ferromagnetic component for the 4b site is observed. Strong coupling between the sublattices transfers this order to the 8d site, where it coexists with a discoupled paramagnetic component of the Cu^{2+} moment. Spontaneous and magnetic-field-induced phase transitions are observed and magnetic phase diagrams are presented. Strong anisotropy of the MFISH signal is used to determine the magnetic symmetry. The investigation of the domain structure reveals a rather complicated magnetic structure with its multiplicity of different magnetic domains.

Since the spectral degree of freedom is shown to provide sublattice selectivity, sublattice dynamics can be studied by means of the MFISH technique. Another possibility is to investigate sublattice ordering and sublattice interactions in multiple ordered materials.

Chapter 5

Distribution of antiferromagnetic S and T domains in NiO

5.1 Introduction

Nickel oxide (NiO) is one of the most promising antiferromagnetic compounds for device applications (e.g. on the field of data storage based on the exchange bias effect [35]). NiO possesses a simple crystallographic and a well-known magnetic structure with an ordering temperature far above the room temperature. It is possible to grow large single crystals as well as thin films. The antiferromagnetic structure of NiO bulk crystals, surfaces and interfaces have been studied in Refs. [163, 78, 164, 165]. Furthermore the possibility of ultrafast manipulation of the antiferromagnetic order parameter of NiO bulk crystals was shown [40]. In particular, the exchange-bias properties of NiO have been studied both as static phenomenon [166, 167, 168] and in ultrafast experiments [169] in order to develop new possibilities for data storage.

This interest in applications of NiO shows the necessity for experimental techniques to investigate the antiferromagnetic ordering. Knowledge of the distribution of antiferromagnetic domains is necessary because the domain structure is relevant for strongly correlated systems [170], magnetization dynamics [171] and the exchange-bias effect [172]. However, imaging of antiferromagnetic domains is only possible with a few methods. Neutron diffraction possesses only low spatial resolution and fast time-resolved measurements are impossible. Linear optical experiments are sensitive to antiferromagnetic domains in specific cases only.

The antiferromagnetic domain structure of NiO was studied by polarization microscopy [173, 174], neutron diffraction [175] and x-ray diffraction [176] between about 1960 and 1980. Due to the fact that NiO forms 24 different antiferromagnetic domains most of the reported results were obtained for artificially prepared samples with simple domain structures only. Furthermore the distinction between different domains using polarization microscopy is only possible considering relative differences of the refractive index in the order of 10^{-5} [173, 174] and therefore is very sensitive to perturbations as strain or interfaces in multilayer structures. In the case of arbitrary samples forming

complex domain structures as used for contemporary experiments this approach is not suitable to access the domain structure. X-ray dichroism was used to image antiferromagnetic domains in NiO [78] but since diffraction experiments do not provide access to dynamical processes in antiferromagnetic domain structures on ultrafast time scales (< 100 ps) the development of an optical approach is necessary.

Therefore in this work the optical second harmonic generation (SHG) is used to investigate the antiferromagnetic domain structure in arbitrary NiO samples. A high degree of discrimination between all possible types of orientational domains is reached. Simulations of the rotational anisotropy of the SHG signal will be derived for all possible orientational domains as well as for typical superpositions of domains. Then the distribution of domains will be investigated experimentally in two types of bulk samples. As-grown crystals display a random distribution of all types of S and T domains with a size of < 1 μm. In contrast oxygen annealed samples reveal T domains with a size of ~ 100 μm and a random distribution of the three associated S domains of $\lesssim 1$ μm. Near T domain walls S domains of ~ 10 μm with the spin orientation pinned by the adjacent T domain are observed.

5.2 Theory

5.2.1 S and T domains in NiO

NiO belongs to the well-known group of binary $3d$-transition metal oxides RO ($R =$ Mn, Fe, Co, Ni, Cu) [177]. It possesses the centrosymmetric cubic structure of rock salt described by the point group $m3m$ above the Néel temperature $T_N = 523$ K. Below T_N the spins of the Ni^{2+} ions are ordered ferromagnetically in {111} planes along $\langle 11\bar{2} \rangle$ axes [178, 78], whereas adjacent {111} planes are ordered contrary forming an antiferromagnetic ordering. This leads to a contraction of the cubic unit cell along the stacking directions [179] of the ferromagnetic planes reducing the crystallographic point symmetry to $\bar{3}m$. The possible $\langle 111 \rangle$ stacking directions represent the four T domains (twin domains). Additional smaller contractions along the spin directions $\langle 11\bar{2} \rangle$ lead to a further symmetry reduction to $2/m$ as crystallographic and magnetic point symmetry describing the three S domains (spin domains) for each T domain. [178, 179]. Altogether 12 orientational domains shown by Table 5.1 can be formed by NiO. Considering also 180°-domains obtained by time-inversion (spin-reversal) of the S domains, altogether 24 domains can be distinguished. Since 180°-domains are also transformed into each other by a translation by $(\frac{1}{2}, \frac{1}{2}, \frac{1}{2})$ their definition is ambiguous and 180°-domains will not be considered in the following. Nevertheless their distinction would be possible with a phase-sensitive SHG technique as demonstrated in Section 4.3.6.3. The domain structure is shown schematically in Fig. 5.1(a) and (b).

Table 5.1: Crystallographic orientations of S and T domains in NiO. For each T domain shown in the upper row, the spin orientations of the accordant three S domains are given below. Note that the assignment of the T domains coincides with that chosen in Ref. [78], while the assignment of the S domains differs because of symmetry reasons employed in the following.

S\T	$T_1[1,1,1]$	$T_2[1,1,\bar{1}]$	$T_3[1,\bar{1},1]$	$T_4[\bar{1},1,1]$
S_1	$[1,1,\bar{2}]$	$[1,1,2]$	$[1,2,1]$	$[2,1,1]$
S_2	$[\bar{2},1,1]$	$[1,\bar{2},1]$	$[\bar{2},\bar{1},1]$	$[\bar{1},1,\bar{2}]$
S_3	$[1,\bar{2},1]$	$[\bar{2},1,\bar{1}]$	$[1,\bar{1},\bar{2}]$	$[\bar{1},\bar{2},1]$

5.2.2   Magnetic second harmonic generation (MSHG)

In opposite to linear optical effects like Faraday and Kerr rotation measuring the absolute magnetization and therefore being unsuitable for antiferromagnetic compounds, nonlinear optical processes like SHG also couple to the antiferromagnetic order parameter [7]. For NiO it was shown, that magnetic-dipole type SHG

$$P_i(2\omega) = \epsilon_0 \chi_{ijk}(\vec{\ell}^2) E_j(\omega) H_k(\omega) \tag{5.1}$$

is present below T_N [113, 111, 180]. Thereby the incident electromagnetic fields with the frequency ω denoted by $E_j(\omega)$ and $H_k(\omega)$ induce a polarization $P_i(2\omega)$ at the doubled frequency. The coupling between the incident electromagnetic fields and the induced polarization is described by the nonlinear susceptibility $\hat{\chi}(\vec{\ell}^2)$. This nonlinear susceptibility depends quadratically on the antiferromagnetic order parameter ℓ and therefore the MSHG intensity $I \propto |\vec{P}(2\omega)|^2$ can be used to investigate the antiferromagnetic structure of NiO [113].

(The terminology of MSHG (magnetic SHG) instead of MFISH (magnetic-field-induced SHG) is used here, since the MSHG also appears in zero magnetic field.)

5.2.3   MSHG in S and T domains

In order to calculate the rotational anisotropy of the MSHG signal in NiO for all 12 orientational domains and also for superpositions of related S and/or T domains, first the Cartesian coordinate systems (CCS) adopted to the orientation of the S domains, the T domains, the cubic crystal and the experimental geometry will be defined. Then non-zero susceptibilities $\chi_{ijk}(\vec{\ell}^2)$ will be determined on the basis of the magnetic point symmetries. These non-zero susceptibilities are identical for all 12 S domains, since the domains only differ due to their orientation but not due to their structure. Afterwards the tensor components will be transformed from the local CCS of any domain into the global CCS of the light beam probing the domain structure. Finally Eq. (5.1) in combination with the transformed nonlinear susceptibility tensor will be used to obtain the polarization dependence and so the rotational anisotropy of the MSHG signal.
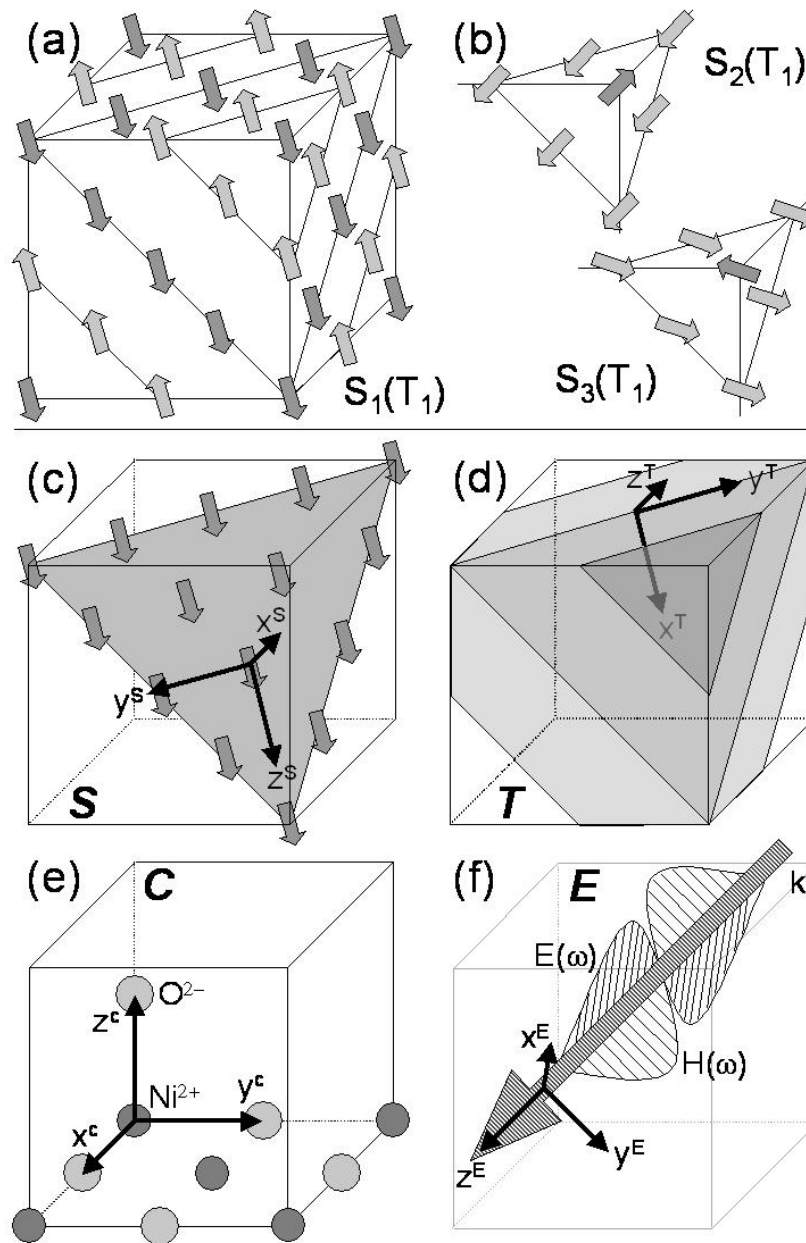
Figure 5.1: *Antiferromagnetic structure of NiO and Cartesian coordinate systems used to describe MSHG on T and S domains: (a) Orientation of Ni^{2+} spins along the $\langle 11\overline{2} \rangle$ direction in ferromagnetic planes stacked antiferromagnetically along the $\langle 111 \rangle$ axis. Here the $S_1(T_1)$ domain is shown. (b) Orientation of spins in the S_2 and S_3 domain of the T_1 domain. (c) CCS of an S domain. (d) CCS of a T domain. (e) CCS of the cubic crystal. (f) CCS of the experiment.*

5.2.3.1   Coordinate systems (CCS)

The four different CCS necessary for the tensor transformations from the local to the global CCS are shown in Fig. 5.1(c)-(f). The first CCS (label: S) is that of an S

domain. According to Ref. [83] its z^S and x^S axis lie along the, respectively, spin direction and stacking direction of the domain. The second CCS (label: T) is that of a T domain. According to Ref. [83] its y^T and z^T axis lie along the, respectively, spin direction and stacking direction of the domain. The third CCS (label: C) is that of the paramagnetic cubic crystal. Its x^C, y^C, and z^C axes are defined by the connection between a Ni^{2+} ion and its nearest O^{2-} neighbors. The fourth CCS (label: E) is that of the experiment. Its x^E and y^E axis are defined by the, respectively, electric and magnetic field of the incoming linearly polarized fundamental light with the wave vector $\vec{k} \parallel \vec{z}^E$. In the following the light will be considered to be incident perpendicular to one of the $\{111\}$ planes of the NiO crystal. This plane will be defined to be the $(111)^C$ plane and the T domain with stacking direction perpendicular to $(111)^C$ as T_1. Therefore the angle $\angle(\vec{k}, \vec{z}^T)$ is $0°$ for the domain T_1 and $70.5°$ for the domains $T_{2,3,4}$.

5.2.3.2   Tensor components

The tensor $\hat{\chi}(\vec{\ell}^2)$ is an axial third-rank i-tensor. The set of nonzero components is derived from Tables 7 and 3 in Ref. [83] with $\chi_{ijk} = \chi_{ikj}$ as additional constraint because of interchangeability of the two photons contributing to MSHG [180, 181]. If S domains are considered, the magnetic point symmetry $2/m$ leads to

$$
\begin{aligned}
&\chi^S_{zxx(S)}, \\
&\chi^S_{xxz(S)} = \chi^S_{xzx(S)}, \\
&\chi^S_{xyz(S)} = \chi^S_{xzy(S)}, \\
&\chi^S_{zzz(S)}, \\
&\chi^S_{zxy(S)} = \chi^S_{zyx(S)}, \\
&\chi^S_{zyy(S)}, \\
&\chi^S_{yyz(S)} = \chi^S_{yzy(S)}, \\
&\chi^S_{yxz(S)} = \chi^S_{yzx(S)}.
\end{aligned}
\tag{5.2}
$$

Here and in the following $ijk(X)$ stands for $i^X j^X k^X$, i.e., tensor components in the CCS labeled X.

5.2.3.3   Tensor transformation

In order to obtain the polarization dependence of the MSHG signal, the tensor components from Eq. (5.2) are transformed into the CCS of the experiment and inserted in Eq. (5.1). A transformation between CCS is described by

$$
\chi^{dst.}_{ijk} = R_{ii'} R_{jj'} R_{kk'} \chi^{src.}_{i'j'k'}. \tag{5.3}
$$

The vectors $\vec{R}_{1i}$, $\vec{R}_{2i}$, $\vec{R}_{3i}$ composing the transformation matrix $\hat{R}$ are given by the x, y and z axis of the source CCS (src.) in the coordinates of the destination CCS (dst.). For

NiO the transformation is composed of subsequent transformations $S \to T \to C \to E$ with the labels referring to the CCS defined above. In the exemplary case of the domain $S_1(T_1)$, this leads to

$$\hat{R}^{E \leftarrow S_1(T_1)} = \hat{R}^{E \leftarrow C} \hat{R}^{C \leftarrow T_1} \hat{R}^{T_1 \leftarrow S_1} \tag{5.4}$$

$$= \begin{pmatrix} 0 & \cos\varphi & \sin\varphi \\ 0 & -\sin\varphi & \cos\varphi \\ 1 & 0 & 0 \end{pmatrix}, \tag{5.5}$$

with

$$\hat{R}^{T_1 \leftarrow S_1} = \begin{pmatrix} 0 & 1 & 0 \\ 0 & 0 & 1 \\ 1 & 0 & 0 \end{pmatrix}, \tag{5.6}$$

$$\hat{R}^{C \leftarrow T_1} = \begin{pmatrix} 1/\sqrt{2} & 1/\sqrt{6} & 1/\sqrt{3} \\ -1/\sqrt{2} & 1/\sqrt{6} & 1/\sqrt{3} \\ 0 & -2/\sqrt{6} & 1/\sqrt{3} \end{pmatrix}, \tag{5.7}$$

$$\hat{R}^{E \leftarrow C} = \begin{pmatrix} \cos\varphi & \sin\varphi & 0 \\ -\sin\varphi & \cos\varphi & 0 \\ 0 & 0 & 1 \end{pmatrix} \cdot \begin{pmatrix} 1/\sqrt{2} & -1/\sqrt{2} & 0 \\ 1/\sqrt{6} & 1/\sqrt{6} & -2/\sqrt{6} \\ 1/\sqrt{3} & 1/\sqrt{3} & 1/\sqrt{3} \end{pmatrix}, \tag{5.8}$$

where φ is the rotation of the plane of polarization of the incident light with the $[1, -1, 0]^C$ direction defining $\varphi = 0°$ for $\vec{k} \parallel [111]^C$. For the other S domains the expression for the transformation is much more complex than in Eqs. (5.5)–(5.8) because of additional tilting of the involved CCS with respect to one another. Inserting Eq. (5.2) into Eq. (5.3) and the result of this into Eq. (5.1) reveals the components of the MSHG susceptibility in the CCS of the experiment. In the following the polarization dependence of the MSHG contribution $\vec{P}_{\parallel}(2\omega)$ polarized parallel to $\vec{E}(\omega)$ is determined. In the CCS of the experiment, this corresponds to $\vec{P}_{\parallel}(2\omega) \parallel \vec{E}(\omega) \parallel \vec{x}^E$ and $\vec{H}(\omega) \propto \vec{k} \times \vec{E}(\omega) \propto \vec{z}^E \times \vec{x}^E = \vec{y}^E$, so that only the susceptibility $\chi_{xxy(E)}$ has to be calculated. This leads to

$$\chi_{xxy(E)}^{S_1(T_1)}(\varphi) = \frac{1}{4}(\chi_{zyy(S)}^S - \chi_{zzz(S)}^S)(\cos(3\varphi) - \cos(\varphi))$$
$$+ \frac{1}{2}\chi_{yyz(S)}^S(\cos(3\varphi) + \cos(\varphi)), \tag{5.9}$$

$$\chi_{xxy(E)}^{S_2(T_1)}(\varphi) = \chi_{xxy(E)}^{S_1(T_1)}(\varphi - 120°), \tag{5.10}$$

$$\chi_{xxy(E)}^{S_3(T_1)}(\varphi) = \chi_{xxy(E)}^{S_1(T_1)}(\varphi + 120°) \tag{5.11}$$

for the S domains of the T_1 domain and to

$$
\begin{aligned}
\chi^{S_1(T_2)}_{xxy(E)}(\varphi) = \ & \frac{1}{27}(\frac{1}{4}\chi^S_{zzz(S)} - \frac{27}{12}\chi^S_{zyy(S)} + 2\chi^S_{zxx(S)} + 4\chi^S_{xxz(S)})(\cos(3\varphi) - \cos(\varphi)) \\
& - \frac{1}{6}\chi^S_{yyz(S)}(\cos(3\varphi) + \cos(\varphi)) \\
& + \frac{\sqrt{2}}{9}\chi^S_{yxz(S)}(\sin(3\varphi) + \sin(\varphi)) \\
& + \frac{\sqrt{2}}{9}(\chi^S_{zxy(S)} + \chi^S_{xyz(S)})(\sin(3\varphi) - \sin(\varphi)),
\end{aligned} \tag{5.12}
$$

$$
\begin{aligned}
\chi^{S_2(T_2)}_{xxy(E)}(\varphi) = \ & \frac{1}{6}\chi^S_{zzz(S)}(-\frac{\sqrt{3}}{2}\sin(3\varphi) - \frac{7\sqrt{3}}{12}\sin(\varphi) + \frac{5}{9}\cos(3\varphi) + \frac{7}{36}\cos(\varphi)) \\
& + \frac{1}{27}\chi^S_{zxx(S)}(3\sqrt{3}\sin(3\varphi) + 3\sqrt{3}\sin(\varphi) - \cos(3\varphi) + \cos(\varphi)) \\
& + \frac{1}{18}\chi^S_{zyy(S)}(-\frac{\sqrt{3}}{2}\sin(3\varphi) - \frac{\sqrt{3}}{4}\sin(\varphi) - \cos(3\varphi) - \frac{5}{4}\cos(\varphi)) \\
& + \frac{2}{27}\chi^S_{xxz(S)}(3\sqrt{3}\sin(3\varphi) - 3\sqrt{3}\sin(\varphi) - \cos(3\varphi) + \cos(\varphi)) \\
& + \frac{1}{18}\chi^S_{yyz(S)}(-\sqrt{3}\sin(3\varphi) - \frac{3\sqrt{3}}{2}\sin(\varphi) - 2\cos(3\varphi) + \frac{1}{2}\cos(\varphi)) \\
& + \frac{\sqrt{2}}{18}\chi^S_{xyz(S)}(-\sin(3\varphi) + \sin(\varphi) + \frac{5\sqrt{3}}{3}\cos(3\varphi) - \frac{5\sqrt{3}}{3}\cos(\varphi)) \\
& + \frac{\sqrt{2}}{9}\chi^S_{yxz(S)}(-\frac{1}{2}\sin(3\varphi) + \sin(\varphi) + \frac{5\sqrt{3}}{6}\cos(3\varphi) + \frac{2\sqrt{3}}{3}\cos(\varphi)) \\
& + \frac{\sqrt{2}}{9}\chi^S_{zxy(S)}(-\frac{1}{2}\sin(3\varphi) - \sin(\varphi) + \frac{5\sqrt{3}}{6}\cos(3\varphi) + \frac{2\sqrt{3}}{3}\cos(\varphi)),
\end{aligned} \tag{5.13}
$$

$$
\chi^{S_3(T_2)}_{xxy(E)}(\varphi) = \chi^{S_2(T_2)}_{xxy(E)}(\varphi + \varphi_0) \tag{5.14}
$$

with $\varphi_0 = 2\arctan(1/\sqrt{3^3}) = 21.79°$ for the S domains of the T_2 domain.

For the S domains of the T_3 and T_4 domains one gets

$$
\chi^{S_m(T_3)}_{xxy(E)}(\varphi) = \chi^{S_m(T_2)}_{xxy(E)}(\varphi + 120°), \tag{5.15}
$$

$$
\chi^{S_m(T_4)}_{xxy(E)}(\varphi) = \chi^{S_m(T_2)}_{xxy(E)}(\varphi - 120°). \tag{5.16}
$$

Note that the spins of the $S_2(T_n)$ and $S_3(T_n)$ domain ($n \in \{2, 3, 4\}$) include the same angle with the wavevector of the incoming light which explains the simple relation between Eq. (5.13) and Eq. (5.14). For fixed m, the $S_m(T_n)$ domains ($n \in \{2, 3, 4\}$) are transformed into one another by $\pm 120°$ rotations which explains the simple relation between Eqs. (5.12)–(5.14) and Eqs. (5.15) and (5.16).

The intensity of the MSHG signal from a single domain $S_m(T_n)$ is given by $I^{MSHG}(\varphi) \propto |\chi^{S_m(T_n)}_{xxy(E)}(\varphi)|^2$. Simulations of I_{MSHG} for all S domains on the basis of Eqs. (5.9)–(5.16) are shown in Figs. 5.2—5.5 and will be discussed in the experimental section.

5.2.3.4 Superposition of domains

In general, crystals are not in a single-domain state so that MSHG contributions from many domains overlap one another. Even if contributions from different domains are separated spatially, by imaging techniques interference occurs at the border between neighboring domains or for successive domains passed by the laser beam. Samples are characterized by the lateral dimension l_d of the domains in relation to the spatial resolution l_r of the detector. If the distance between spots in different domains is smaller than l_r the corresponding contributions to MSHG superpose coherently [182]. This is expressed by the equation

$$I_{\text{coh.}}(\varphi) \propto \left| \sum_{m,n} \chi_{xxy(E)}^{S_m(T_n)}(\varphi) \right|^2 . \tag{5.17}$$

In opposite incoherent superposition is expressed by

$$I_{\text{inc.}}(\varphi) \propto \sum_{m,n} \left| \chi_{xxy(E)}^{S_m(T_n)}(\varphi) \right|^2 . \tag{5.18}$$

If samples with only large domains ($l_d \gg l_r$) or small domains ($l_d \leq l_r$) are considered, the MSHG intensity can be exclusively described by Eq. (5.18) or Eq. (5.17), respectively. SHG in samples with medium sized domains is described by a weighted addition of Eqs. (5.17) and (5.18), but for clarity the discussion is restricted to the end cases only.

In panel (d) of Figs. 5.2–5.5 the anisotropy of the MSHG signal is shown for coherent superposition of MSHG contributions from a random distribution of small S domains within a large T domain. This leads to

$$\chi_{xxy(E)}^{T_1}(\varphi) = \frac{3}{4}(\chi_{zyy(S)}^{S} - \chi_{zzz(S)}^{S} + 2\chi_{yyz(S)}^{S}) \cos(3\varphi), \tag{5.19}$$

$$\chi_{xxy(E)}^{T_2}(\varphi) = -\frac{1}{18}(\chi_{zyy(S)}^{S} - \chi_{zzz(S)}^{S} + 2\chi_{yyz(S)}^{S})(\frac{7}{2}\cos(3\varphi) + \cos(\varphi))$$

$$+ \frac{\sqrt{2}}{3}(\chi_{yxz(S)}^{S} - \chi_{zxy(S)}^{S}) \sin(\varphi), \tag{5.20}$$

$$\chi_{xxy(E)}^{T_3}(\varphi) = \chi_{xxy(E)}^{T_2}(\varphi + 120°), \tag{5.21}$$

$$\chi_{xxy(E)}^{T_4}(\varphi) = \chi_{xxy(E)}^{T_2}(\varphi - 120°). \tag{5.22}$$

Likewise, panel (e) shows the result for the case that the S domains are not small so that incoherent superposition of the MSHG contributions occurs. Fig. 5.6 shows the anisotropy of the SHG signal for the case that SHG contributions from a random distribution of all 12 orientational domains superimpose in a coherent or incoherent way.
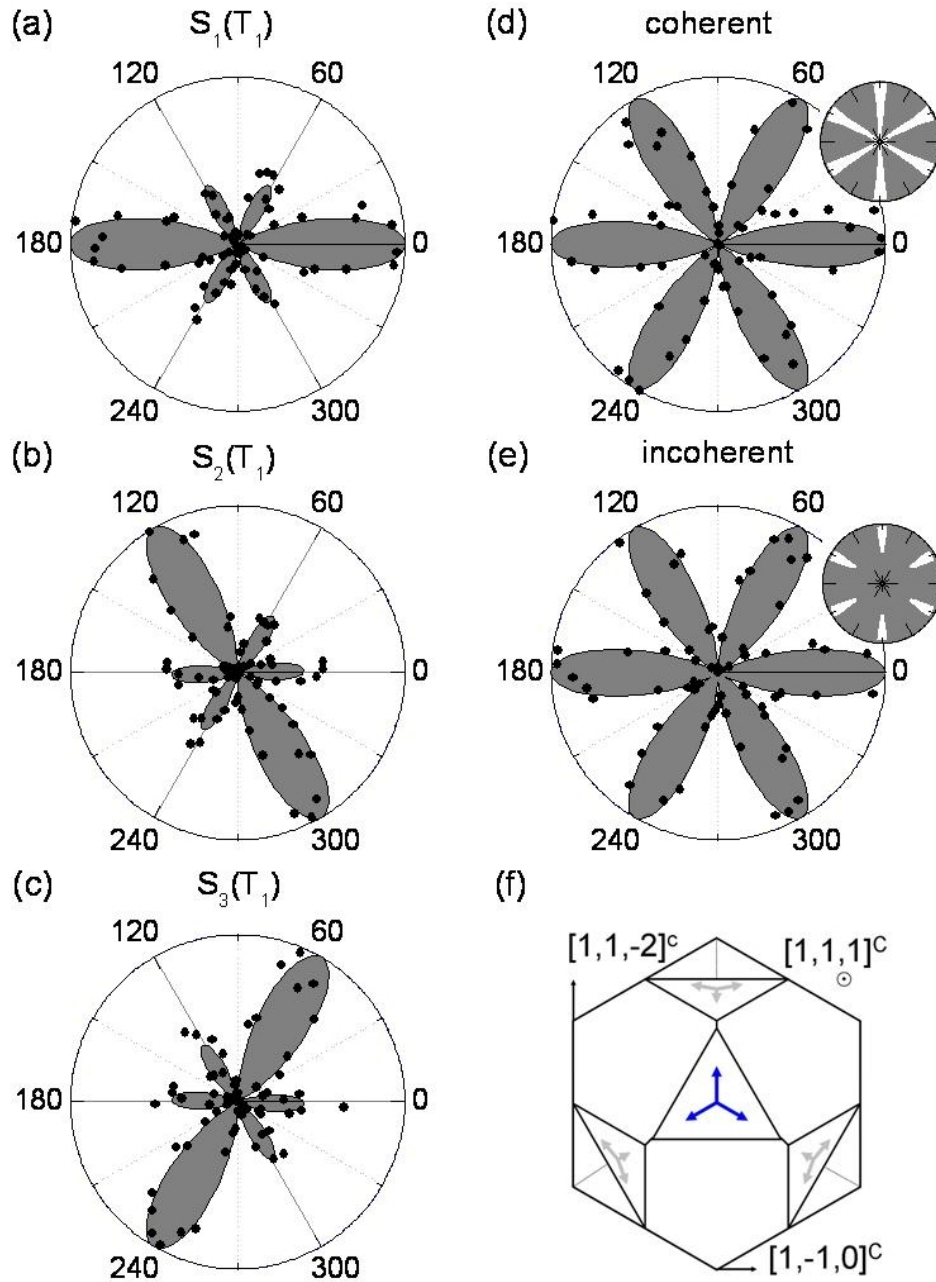
Figure 5.2: *Anisotropy of the MSHG signal from the S domains of the T_1 domain of NiO. Lines and grey areas are derived from an overall fit of MSHG susceptibilities. (a) Domain $S_1(T_1)$. (b) Domain $S_2(T_1)$. (c) Domain $S_3(T_1)$. (d) Coherent superposition of MSHG from a random assembly of the $S(T_1)$ domains. (e) Incoherent superposition of MSHG from a random assembly of the $S(T_1)$ domains. (f) Sketch of the 12 orientational domains with $S(T_1)$ domains emphasized. The insets in (d) and (e) are scaled to 10% of the associated anisotropy plots. The azimuthal angle refers to φ in Eq. (5.8).*
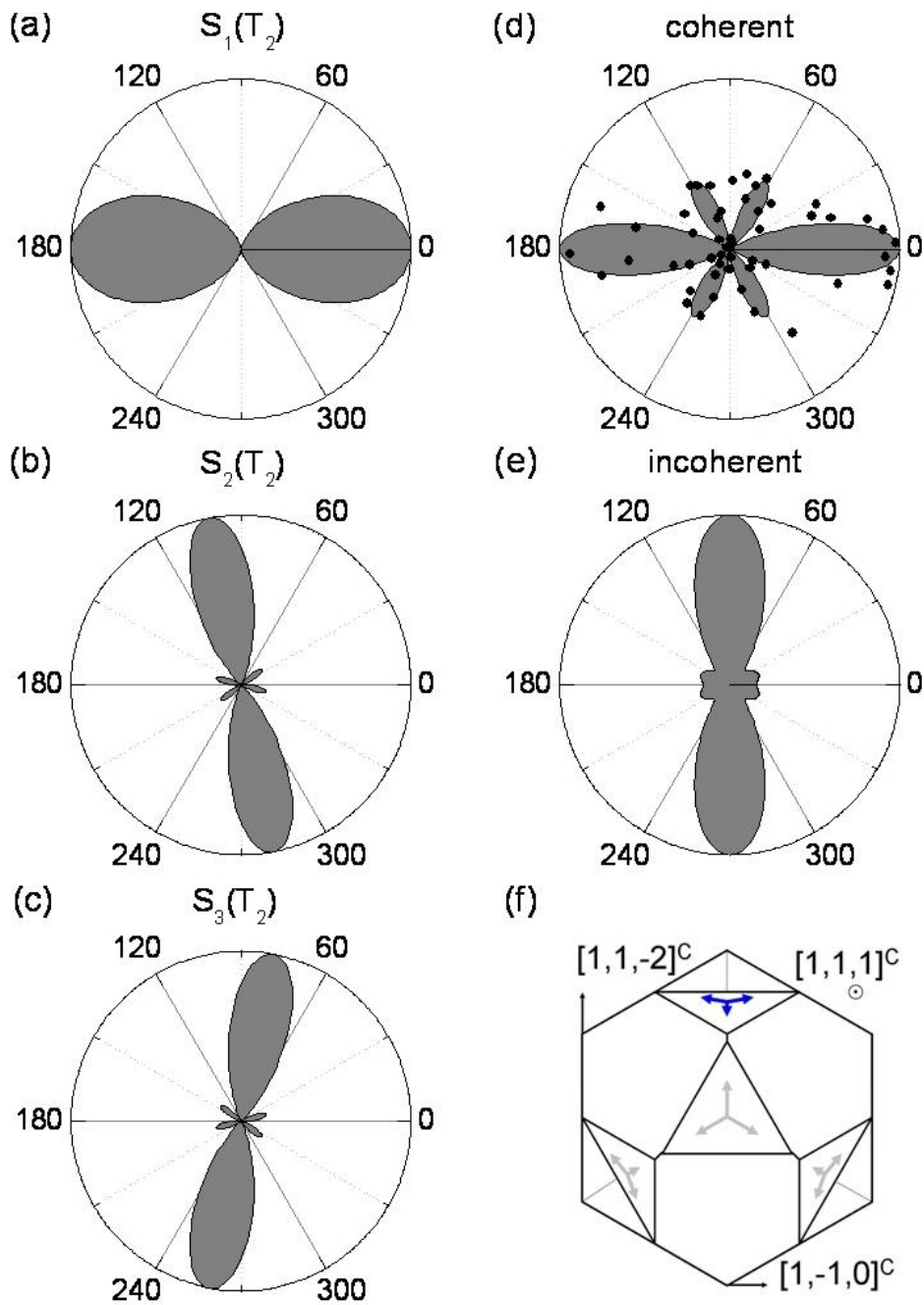
Figure 5.3: *Anisotropy of the MSHG signal from the S domains of the T_2 domain of NiO. Lines and grey areas are derived from an overall fit of MSHG susceptibilities. (a) Domain $S_1(T_2)$. (b) Domain $S_2(T_2)$. (c) Domain $S_3(T_2)$. (d) Coherent superposition of MSHG from a random assembly of the $S(T_2)$ domains.(e) Incoherent superposition of MSHG from a random assembly of the $S(T_2)$ domains. (f) Sketch of the 12 orientational domains with $S(T_2)$ domains emphasized. The azimuthal angle refers to φ in Eq. (5.8).*
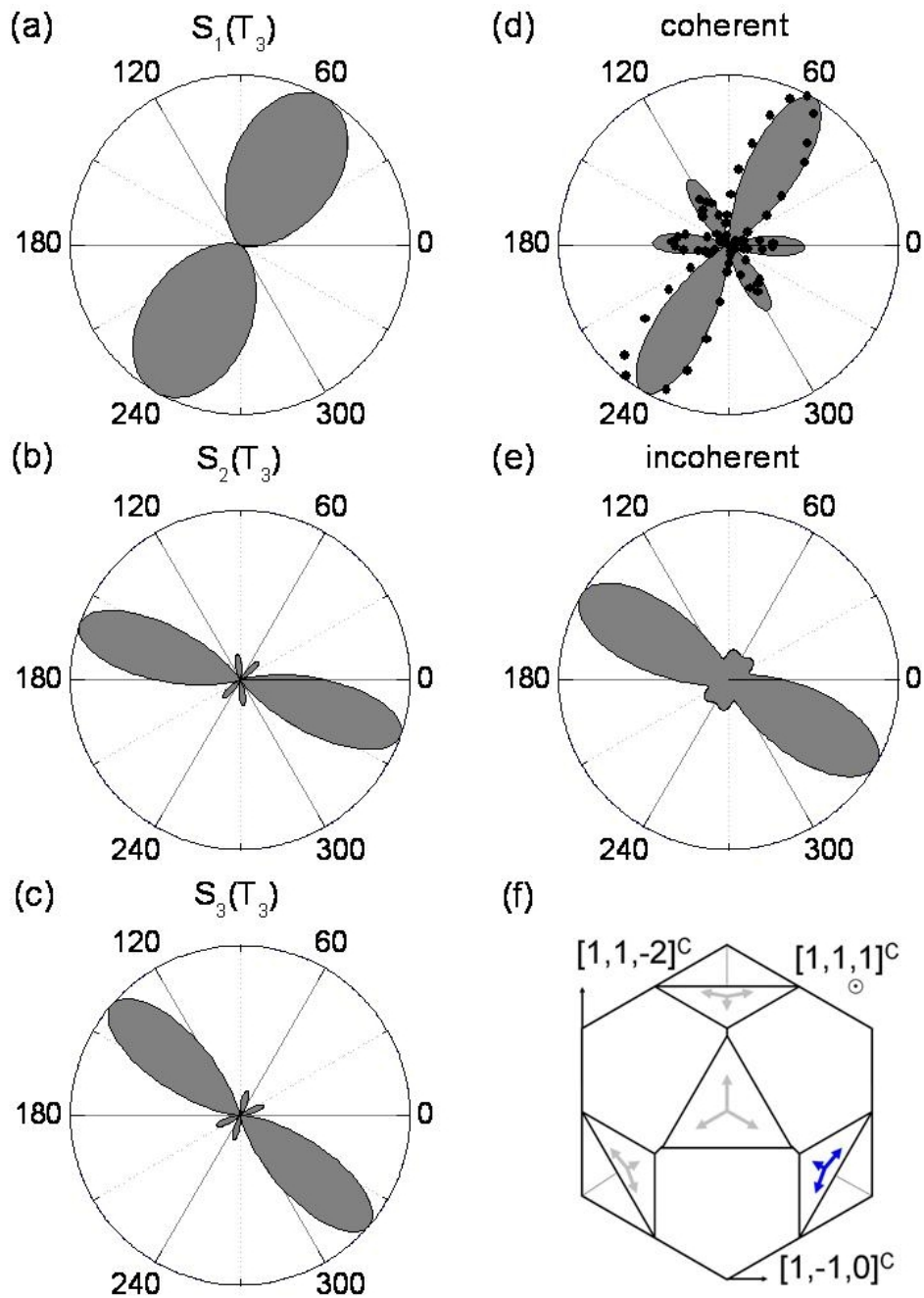
Figure 5.4: *Anisotropy of the MSHG signal from the S domains of the T_3 domain of NiO. Lines and grey areas are derived from an overall fit of MSHG susceptibilities. (a) Domain $S_1(T_3)$. (b) Domain $S_2(T_3)$. (c) Domain $S_3(T_3)$. (d) Coherent superposition of MSHG from a random assembly of the $S(T_3)$ domains. (e) Incoherent superposition of MSHG from a random assembly of the $S(T_3)$ domains. (f) Sketch of the 12 orientational domains with $S(T_3)$ domains emphasized. The azimuthal angle refers to φ in Eq. (5.8).*
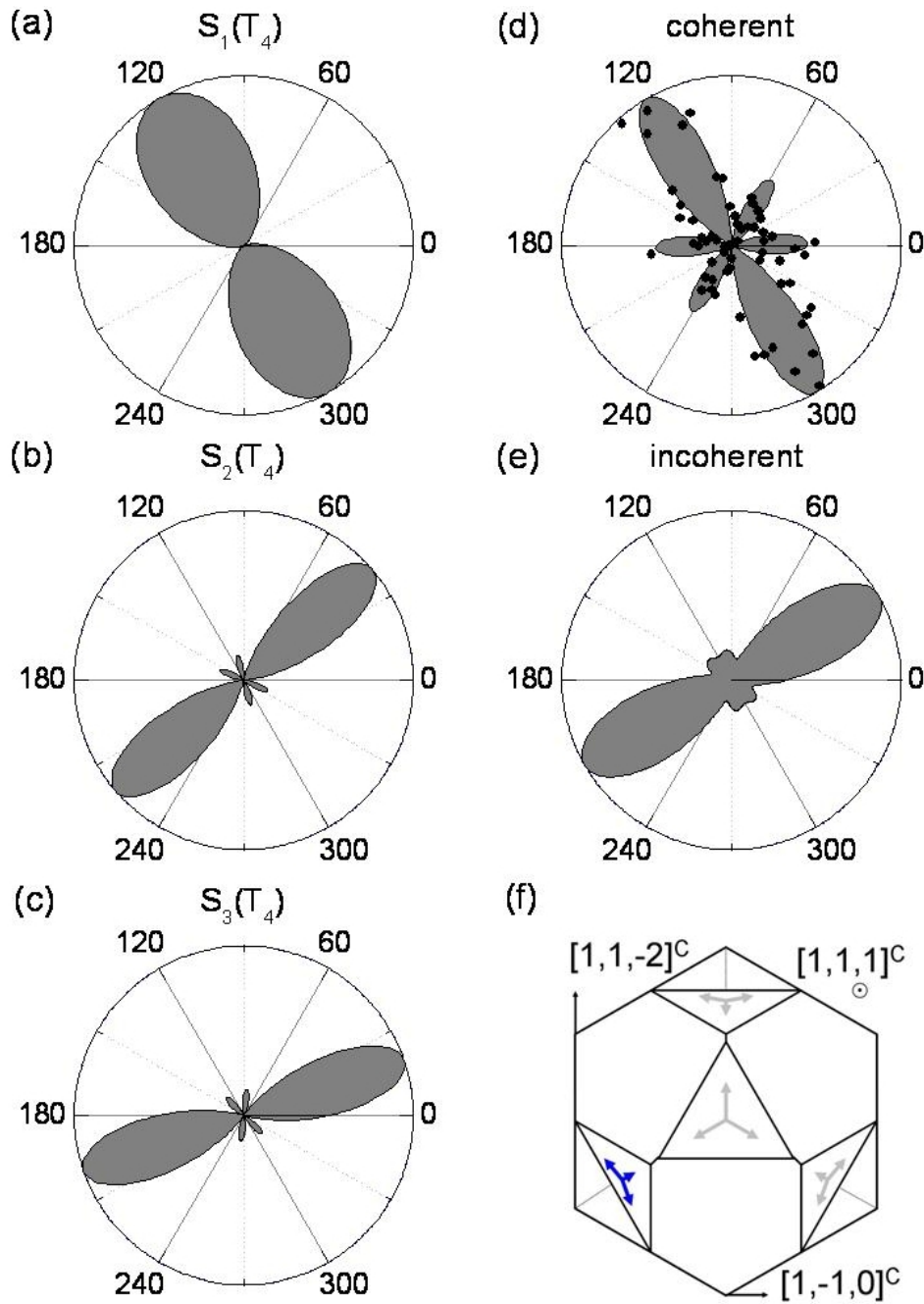
Figure 5.5: *Anisotropy of the MSHG signal from the S domains of the T_4 domain of NiO. Lines and grey areas are derived from an overall fit of MSHG susceptibilities. (a) Domain $S_1(T_4)$. (b) Domain $S_2(T_4)$. (c) Domain $S_3(T_4)$. (d) Coherent superposition of MSHG from a random assembly of the $S(T_4)$ domains. (e) Incoherent superposition of MSHG from a random assembly of the $S(T_4)$ domains. (f) Sketch of the 12 orientational domains with $S(T_4)$ domains emphasized. The azimuthal angle refers to φ in Eq. (5.8).*
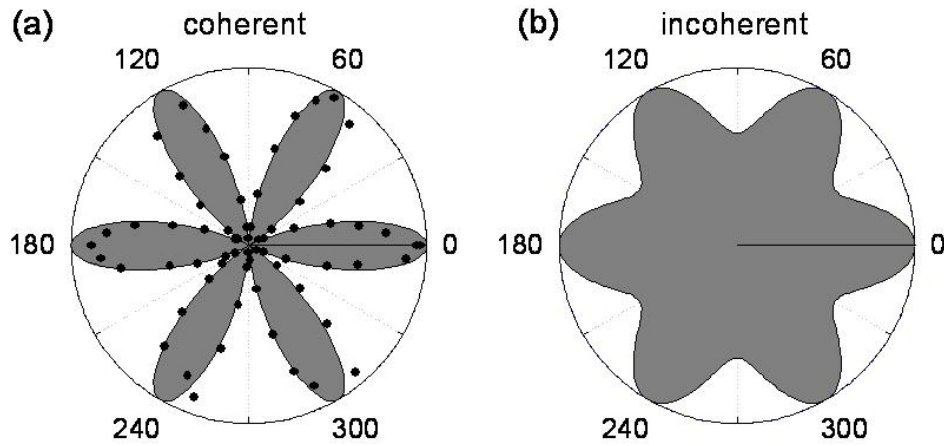
Figure 5.6: *Anisotropy of the MSHG signal from a random assembly of all 12 orientational domains. (a) Coherent superposition of contributions from different domains. (b) Incoherent superposition of contributions from different domains. The azimuthal angle refers to φ in Eq. (5.8).*

5.3   Experiment

5.3.1   Samples and setup

In the experiment (111) oriented samples prepared from bulk single crystals grown by the flame-fusion method are used. The samples are polished with Syton dispersion and vary in thickness between 50 and 100 μm. Both as-grown crystals and crystals annealed in oxygen are investigated. For annealing the samples are heated to 1400 K and cooled to room temperature at a rate of 2 K/min in a gas stream of 90% argon and 10% oxygen flowing at 10 l/min. Before annealing, crystals are brownish and domain structures are not noticeable by polarization microscopy. After annealing, samples are greenish and T domains in the order of ~ 100 μm are resolved.

   In order to conduct the experiments, the experimental setup shown by Fig. 1.16 is used. The anisotropy of the MSHG signal is measured by rotating the linear polarization of the incident light with an achromatic wave plate and transmitting only the component of the MSHG light polarized parallel to the incident light through a polymer polarizing foil. The MSHG light is imaged with a telephoto lens onto a cooled CCD camera. Because of the high Néel temperature of 523 K, the experiments are carried out at room temperature. At this temperature the largest MSHG intensity is observed at 2.06 eV, which is therefore chosen as MSHG photon energy [40]. Although the data of only one sample will be discussed in the following, results are reproduced on more than 5 different specimen.

5.3.2 Fit of MSHG data and distribution of domains

5.3.2.1 Data and fits

Figures 5.2–5.5 show the anisotropy of the MSHG signal measured on different spots of the sample annealed in oxygen. With few exceptions (see below), the sample displays only the four types of MSHG anisotropy shown in panel (d) of Figs. 5.2–5.5. Figures 5.3(d), 5.4(d), and 5.5(d) display a similar polarization dependence with twofold symmetry. They only differ by a phase of $\pm 120°$ in the angular dependence. In contrast to that, a sixfold symmetry of the MSHG is found in Fig. 5.2(d). This is exactly the behavior expressed by Eqs. (5.19)–(5.22). Therefore oxygen annealing is assumed to lead to a distribution of large T domains composed of a random distribution of small S domains. Based on this assumption, imaging experiments reveal the T domain structure sketched in Fig. 5.7.

Within one of the T_1 domain regions, whose twofold MSHG anisotropy stands in distinct contrast to the sixfold polarization dependence of the MSHG signal in Fig. 5.2(d) are observed. This points to the occurrence of single large $S(T_1)$ domains. Figs. 5.2(a)–5.2(c) show that all three S domains composing the T_1 domain are observed as single domains.

Further arguments confirming the assignment of domains in Figs. (5.2)–(5.5) are discussed in the following section.

A fit of the data in Figs. 5.2(a)–5.2(c) and Figs. 5.2(d)–5.5(d) reveals values for the tensor components $\chi_{ijk(S)}^S$. First Eqs. (5.9)–(5.11) are fitted to the SHG data for the $S(T_1)$ domains in Fig. 5.2(a)–(c) and

$$\frac{\chi_{zyy(S)}^S - \chi_{zzz(S)}^S}{\chi_{yyz(S)}^S} = 0.93 \pm 0.14 \tag{5.23}$$

is found for the tensor components involved. Next Eqs. (5.20)–(5.22) are fitted to the SHG data for the domains T_2, T_3, T_4 in panel (d) of Figs. 5.3–5.5. This leads to

$$\frac{\chi_{yxz(S)}^S - \chi_{zxy(S)}^S}{\chi_{zyy(S)}^S - \chi_{zzz(S)}^S + 2\chi_{yyz(S)}^S} = 0.009 \pm 0.006 \tag{5.24}$$

for the ratio between the tensor components contributing to the, respectively, sine and cosine contributions to the SHG anisotropy. Apparently SHG susceptibilities of the type χ_{ijk} with ijk as permutation of xyz are 1–2 orders of magnitude smaller than the dominating susceptibilities with 2 or 3 equal indices. This result is in compliance with the observation, that in none of the antiferromagnetic compounds investigated thus far SHG from a symmetry-allowed magnetic tensor component χ_{ijk} (with ijk as permutation of xyz) was observed [7]. The errors are given by fluctuations of the fit parameters obtained for different data sets as well as the fitting error itself.

Since single S domains of the T_2, T_3, T_4 domain are not observed, the remaining SHG susceptibilities in Eq. (5.2) cannot be fitted. In order to be able to illustrate the

symmetry relation between the SHG anisotropy of the S domains in Figs. 5.3–5.5 the following assumptions are made: (i) $\chi^S_{ijk(S)} = 0$ for any ijk which is a permutation of xyz. In view of Eq. (5.24) and the subsequent remarks this assumption is reasonable. (ii) $\chi^S_{zxx(S)} = \chi^S_{zyy(S)} = \chi^S_{xxz(S)} = \chi^S_{yyz(S)}$. This is an arbitrary assumption, only chosen for the purpose of illustration. With a different choice for the four tensor components the length of the double lobes making up Figs. 5.3(a) (domain $S_1(T_2)$) and 5.3(b) (domain $S_2(T_2)$) will change. However, the SHG anisotropy of all other S domains will change in accordance with this, because of the symmetry relations expressed by Eqs. (5.14)–(5.16).

5.3.2.2   Discussion of domain structures

Figures 5.2–5.5 and the associated Eqs. (5.9)–(5.16) show, that in general all 12 orientational domains possess a different SHG anisotropy. However, particularly when in addition to single domains random distributions of domains are considered, two types of degeneracy may occur:

(i) Coherent superposition of the signal from the three S domains making up the domain T_1 and coherent superposition of the signal from all 12 orientational domains lead to the same SHG anisotropy. This is the only true degeneracy, which occurs independent of the value of the susceptibilities $\chi^S_{ijk(S)}$. This ambiguity is easily solved by taking into account the overall distribution of domains in the sample. For a random distribution of all 12 orientational domains the anisotropy of the SHG signal will be uniform in the whole sample, whereas for a coexistence of the three S domains of the T_1 domain or a coexistence of three S domains making up the $T_{2,3,4}$ domain, regions with a different SHG anisotropy will be observed.

(ii) Additional accidental degeneracies may occur for specific values of the tensor components $\chi^S_{ijk(S)}$. For example, coherent superposition of the signal from the three S domains making up the domain T_2, T_3, or T_4 and SHG from the, respectively, $S_1(T_1)$, $S_3(T_1)$, or $S_2(T_1)$ single domain may lead to the same SHG anisotropy if $r = (\chi^S_{zyy(S)} - \chi^S_{zzz(S)})/\chi^S_{yyz(S)} = 10/9 = 1.11$. Ambiguities of this type can be solved in two ways. On the one hand, the accidental degeneracy will disappear when the photon energy is tuned because of the different spectral dependence of independent SHG susceptibilities. On the other hand, the overall distribution of domains in the sample can be taken into account just as in case (i). In the experiment both tests are applied in order to acquire the assignment of domains in Fig. 5.7. For example, the error margin of $r = 0.93$ in Eq. (5.23) for the SHG anisotropy in Figs. 5.2(a)–5.2(c) does not include the degeneracy value of 1.11 (note that in contrast one finds $r = 1.16$ for Fig. 5.3(d)). The regions exhibiting the SHG anisotropy in Figs. 5.2(a)–5.2(c) are all located within the T_1 domain and have a completely different structure than the other T domains. Both tests therefore point to single $S(T_1)$ instead of T domains with a random distribution of S domains.

The analysis of the domain structure on the basis of Eqs. (5.9) to (5.16) with additional tests for accidental degeneracies as described reveals the domain structure in Fig. 5.7 for one of the investigated samples. The sample exhibits all four T domains
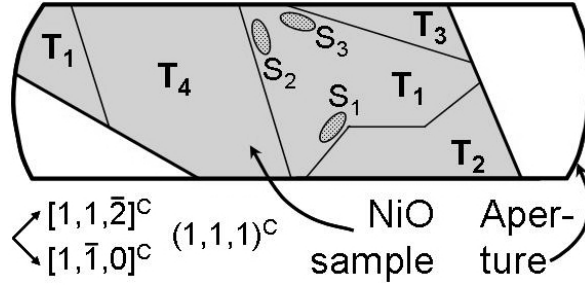
Figure 5.7: *Sketch of the domain structure after oxygen annealing which is found in the NiO sample discussed in the text.*

whose lateral dimensions are in the order of 100 μm. With few exceptions discussed below, the T domains consist of random distributions of the three S domains making up the respective T domain. The superposition of SHG contributions from the different S domains occurs coherently, which points to a lateral dimension of the S domains in the order of $\lesssim 1$ μm, i.e., below the resolution of the telephoto lens used in the experiment. Coherent interference according to Eq. (5.17) is clearly confirmed by the anisotropy of the SHG signals which resembles panel (d), but never panel (e), of Figs. 5.3–5.5. In the case of the T_1 domain, the distinction between coherent and incoherent SHG interference is more subtle than in the case of the other T domains, because it is given by the ratio between the minimum and the maximum value of the SHG intensity $I(\varphi)$. As shown in Figs. 5.2(d) and 5.2(e) this value is 0 and 6% for coherent and incoherent interference, respectively. A fit to the data points reveals a ratio of $(3 \pm 6)\%$ for SHG from the center of the T_1 domains and a ratio of $(12 \pm 6)\%$ for the sum of the SHG intensities from the three large S domains sketched in Fig. 5.7. In spite of the errors, this indicates the correct tendency for, respectively, coherent and incoherent superposition.

As depicted in Fig. 5.7, large $S(T_1)$ domains are only found near the boundary to a neighboring T domain. For all the large $S(T_1)$ domains observed in the vicinity of a domain T$\neq T_1$, $\cos \angle (z^{S(T_1)}, z^{T \neq T_1}) = 0.94$ is found, which is the highest possible value compatible with the magnetic structure of NiO. This points to a tendency of the Ni^{2+} spins to orient parallel to the stacking direction of ferromagnetic planes (and, thus, the distortion) in the adjacent T domain.

In contrast to the samples annealed in oxygen, the untreated samples do not display any domain structures. Fig. 5.6(a) reveals a sixfold anisotropy of the SHG signal, which is found on all spots of the sample. As mentioned in the discussion of case (i) in this Section, this corresponds to coherent superposition of SHG from all 12 orientational domains. Incoherent superposition can be excluded on the basis of Fig. 5.6(b). Thus, as-grown samples posses a random distribution of S and T domains with a size which is in the range of $\lesssim 1$ μm.

5.4   Summary and application

By means of MSHG it is possible to distinguish between the 12 orientational domains and between typical distributions of S or T domains in NiO. The distinction is made by measuring the anisotropy of the SHG signal. In contrast to other techniques, the discrimination between the three S domains of a selected T domain is particularly clear. Ambiguities in the assignment of domains are ruled out by tuning the frequency of the probe laser to the appropriate photon energy and by the analysis of the overall distribution of domains. SHG topography thus allows one to study arbitrary domain structures in as-grown crystals. Untreated NiO samples are found to possess a random distribution of all S and T domains with a lateral size in the order of $\lesssim 1$ μm. After annealing in oxygen, a distribution of T domains of ~ 100 μm made up by a random distribution of the three corresponding S domains of $\lesssim 1$ μm is observed. Next to a T domain wall, large S domains of ~ 10 μm are formed, apparently because of a tendency of the Ni^{2+} spins to orient along the stacking direction of ferromagnetic planes in the adjacent T domain.

SHG offers major advantages for investigating the distribution of domains in NiO as well as in other antiferromagnetic compounds. The high selectivity of the technique and spatial resolution in the order of $1 - 10$ μm allow to study complex compositions of domains as they are found in as-grown samples or heterostructures. Confusion from overlapping domain structures encountered by integrative techniques like polarization microscopy or neutron diffraction are avoided because only a region with the thickness of the optical absorption length contributes to the SHG signal. SHG is a robust technique, which is not hampered by defects, impurities, or strain and which is applicable to both, bulk samples and thin films or heterostructures. Surface contributions to the magnetic signal can be suppressed or enhanced by using, respectively, nanosecond or femtosecond laser pulses for probing the structure [14, 7]. Because of the unparalleled temporal resolution of optical experiments, SHG is the only technique allowing to study correlations between domain structures, which are known to play a major role in the physics of exchange-bias compounds [169, 172], and ultrafast magnetization processes. This is confirmed in recent experiments, which demonstrated a distinctly different temporal evolution of the antiferromagnetic state in NiO samples with large domains (~ 100 μm) as compared to NiO samples with small domains (< 1 μm) within 100 ps after the excitation with an intense 100-fs laser pulse [183]. The experiment confirms that nonlinear optics is not only a powerful alternative to the already existing techniques but, in fact, indispensable for studying contemporary aspects of antiferromagnetism.

Publications

Parts of this work are or will be published as follows:

1. *"Magnetic-Field-Induced Second Harmonic Generation*
   in the Semiconductor GaAs"
   V. V. Pavlov, A. M. Kalashnikova, and R. V. Pisarev
   I. Sänger, D. R. Yakovlev, and M. Bayer
   *Phys. Rev. Lett. **94**, 157404 (2005)*

2. *"Orbital Quantization of Electronic States in Magnetic Field as Origin*
   of Second Harmonic Generation in Diamagnetic Semiconductors"
   I. Sänger, D. R. Yakovlev, B. Kaminski, and M. Bayer
   V. V. Pavlov, and R. V. Pisarev
   In preparation (2006)

3. *"Magneto-optical second-harmonic generation*
   in semiconductors GaAs and CdTe"
   V. V. Pavlov, A. M. Kalashnikova, and R. V. Pisarev
   I. Sänger, D. R. Yakovlev, and M. Bayer
   SPIE (2006), in press

4. *"Spin and Orbital Quantization of Electronic States as Origins*
   of Second Harmonic Generation in Magnetic Semiconductors"
   I. Sänger, D. R. Yakovlev, and M. Bayer
   V. V. Pavlov, and R. V. Pisarev
   *Phys. Rev. Lett. **96**, 117211 (2006)*

5. *"Orbital vs. Spin Quantization of Electronic States as Independent Sources*
   of Second Harmonic Generation in Magnetic Semiconductors"
   I. Sänger, D. R. Yakovlev, B. Kaminski, and M. Bayer

V. V. Pavlov, and R. V. Pisarev
In preparation (2006)

6. *"Second-harmonic generation in the semiconductor (Cd, Mn)Te"*
   V. V. Pavlov, A. M. Kalashnikova, and R. V. Pisarev
   I. Sänger, D. R. Yakovlev, and M. Bayer
   J. Opt. Soc. Am. B **22***, 168 (2005)*

7. *"Magnetic-Field-Induced Second Harmonic Generation in CuB_2O_4"*
   R. V. Pisarev, **I. Sänger**, G. A. Petrakovskii, and M. Fiebig
   Phys. Rev. Lett. **93***, 37204 (2004)*

8. *"Linear and nonlinear optical studies of CuB_2O_4"*
   I. Sänger, R. V. Pisarev, G. A. Petrakovskii, and M. Fiebig
   In preparation (2006)

9. *"Magnetic phase diagram of CuB_2O_4"*
   M. Fiebig, **I. Sänger**, and R. V. Pisarev
   J. Appl. Phys. **93***, 6960 (2003)*

10. *"Second-harmonic as a tool for studying
    electronic and magnetic structures of crystals: review"*
    M. Fiebig, V. V. Pavlov, and R. V. Pisarev
    J. Opt. Soc. Am. B **22***, 96 (2005)*

11. *"Distribution of antiferromagnetic S and T domains in NiO"*
    I. Sänger, R. V. Pisarev, V. V. Pavlov, and M. Fiebig
    Submitted to Phys. Rev. B. (2005)

Symbols and abbreviations

symbol	meaning
$4b$, $8d$	Cu^{2+} sites in CuB_2O_4
a	lattice constant
$\mathbf{A}$	vector potential
α	fine structure constant, $\alpha \simeq 1/137$
a_B	Bohr radius
α, $\alpha(\omega)$	absorption coefficient
b	lattice constant
B	magnetic field
$\mathbf{B}$	magnetic induction
$B_J(y)$	Brillouin function
BBO	β-BaB_2O_4
c_0	speed of light in vacuum (299 792 458 m s^{-1})
C	Curie constant
CB	conduction band
CCD	charge-coupled device camera
CCS	Cartesian coordinate system
CdTe	cadmium telluride
$Cd_{1-x}Mn_xTe$	cadmium manganese telluride
Cr_2O_3	chromium oxide
Cu^{2+}	copper ions
CuB_2O_4	copper borate
d	label for d electrons
d_{e-h}	exciton diameter
DMS	diluted magnetic semiconductors
δ_{ij}	Dirac's delta function
ΔE	energy difference
ΔE_{GZ}	giant Zeeman splitting
ΔE_z	Zeeman splitting
Δ_{SO}	split-off energy between heavy and light hole bands

e	electron, unit charge ($1.602176 \cdot 10^{-19}$ C)
E, E_{ex}	energy, exchange energy
E_F	Fermi level
E_g	band gap energy
E($\mathbf{k}$), $E_{e,h}(\mathbf{k})$	dispersion, of the conduction/valence band
$\mathbf{E}$	electric field vector
E_i	i-th electric light field
ED	electric dipole
eV	electron volt ($1.602176 \cdot 10^{-19}$ J)
ε_r, ε_0	dielectric constant, in vacuum
fcc	face-centered cubic
FWHM	full width at half maximum
ϕ_{nlm}	eigenfunctions of the hydrogen atom
g_e	electron g factor
g_J	Lande factor
G	free enthalpy
GaAs	gallium arsenide
Γ_i	conduction ($i = 6$) or valence band ($i = 7, 8$) symmetry
Γ-point	point of high symmetry
h	hole
hh	heavy hole
$\hat{H}$	Hamiltonian
$H_{N_e}(y)$	Hermite polynomials
$\mathbf{H}$	magnetic field strength
H_C	coercive field strength
HeNe	helium-neon laser
$\hbar$	$h/2\pi = 1.054571 \cdot 10^{-34}$ J s$= 6.582118 \cdot 10^{-16}$ eV s
i	integer index $i = 0, 1, 2 \ldots$
i	complex unity
I	light intensity
$\hat{I}$	inversion operator
j	integer index $i = 0, 1, 2 \ldots$
$\mathbf{j}$	electric current
$\mathbf{J}$	total angular momentum
J_z	z-component of the angular momentum
J_{ij}	exchange integral
k_B	Boltzmann constant $1.38062 \cdot 10^{-23} J K^{-1}$
$\mathbf{k}$	wave vector

K	Kelvin
KD*P	KH_2PO_4
lh	light hole
l_{coh}	coherence length
l_d	lateral domain dimension
$\vec{\ell}$	antiferromagnetic order parameter
L	orbital angular momentum
L_z	z-component of the orbital momentum
LO, LA	longitudinal optical, longitudinal acoustic
λ	wavelength
m	z-component of the angular momentum
m_0	electron mass ($9.109381 \cdot 10^{-31}$ kg)
m*	effective mass
m_e^*, m_h^*, m_X^*	effective electron/hole/exciton mass
M	magnetization, magnetic dipole moment
M$_S$	saturated magnetization
Mn^{2+}	manganese ions
MD	magnetic dipole
MFISH	magnetic-field-induced second harmonic generation
MSHG	magnetic second harmonic generation
meV	milli electron volt
mJ	milli joule
μm	micrometer
μ	magnetic moment
μ	reduced mass
μ_r, μ_0	permeability, in vacuum
μ_B	Bohr magneton
$\mu(T)$	chemical potential
n	refractive index
$N_0\alpha, N_0\beta$	exchange integrals of the conduction, valence bands
$N(E_F)$	density of states at the Fermi level
Nd:YAG	yttrium aluminium garnet doped with neodymium
Ni^{2+}	nickel ions
NiO	nickel oxide
nm	nanometer
OPO	optical parametric oscillator
p	label for p (band) electrons
P	polarization, electric dipole moment
p	impulse operator
PL	photoluminescence

ps	picosecond
Ψ	wavefunction
$\hat{Q}$	electric quadrupole moment
R	resistivity, reflectivity
$\mathbf{r}, \mathbf{R}$	spatial position
Ryd	Rydberg constant
ϱ	electric charge density
s	label for s (band) electrons
S	entropy
$\mathbf{S}$	spin
$< \mathbf{S} >$	averaged spin
S_z	z-component of the spin
S$_0$	effective spin
S$_i$	spin of the i-th electron, ion or atom
S$_i$T$_j$	spin domain i of twin domain j
SHG	second harmonic generation
SO	split-off band
$\sigma_{\pm}$	circular polarization
$\sigma_{x,y,z}$	Pauli-matrices
t	time
T	temperature, Tesla
T$_0$	effective temperature
T$_a$	anomaly temperature
T$_C$	Curie temperature
T$_N$	Neel temperature
$\hat{T}$	time inversion operator
Θ	Neel temperature
τ	relaxation time
VB	valence band
ω_γ	photon frequency
ω_C	cyclotron frequency
Ω	Ohm
x	manganese concentration
X	exciton
$\chi_{para}, \chi_{dia}, \chi_{mag}$	para/dia/magnetic susceptibility
$\chi_{N_e}(\tilde{x})$	eigenfunctions of the harmonic oscillator
$\chi_{ijk..}$	nonlinear optical susceptibilities

Bibliography

[1] P. Franken, A. Hill, C. Peters, & G. Weinreich, Phys. Rev. Lett. **7**, 118 (1961).

[2] N. Bloemberg, *Nonlinear Optics* (Benjamin, New York, 1965).

[3] Y. Shen, *The Principles of Nonlinear Optics* (Wiley, New York, 1984).

[4] R. Boyd, *Nonlinear Optics* (Academic, New York, 1992).

[5] E. Matthias & F. Träger, Proceedings of the Topical Conference: Nonlinear Optics at Interfaces (NOPTI 1998), Appl. Phys. B **68** (1999).

[6] F. Träger, Proceedings of the Topical Conference: Nonlinear Optics at Interfaces (NOPTI 2001), Appl. Phys. B **74** (2002).

[7] M. Fiebig, V. V. Pavlov, & R. V. Pisarev, J. Opt. Soc. Am. B **22**, 96 (2005).

[8] K. Bennemann, *Nonlinear Optics in Metals* (Clarendon, Oxford, 1998).

[9] B. D. Bartolo, *Nonlinear Spectroscopy of Solids: Advances and Applications* (Plenum, New York, 1994).

[10] Y. Uesu, S. Kurimura, & Y. Yamamoto, Appl. Phys. Lett. **66**, 2165 (1995).

[11] A. Liebsch, Surf. Science **307**, 1007 (1994).

[12] J. Chen, S. Machida, & Y. Yamanoto, Opt. Lett. **23**, 676 (1998).

[13] K. Veenstra, A. Petukhov, A. de Boer, & T. Rasing, Phys. Rev. B **58**, R16020 (1998).

[14] A. Kirilyuk, J. Phys. D: Appl. Phys. **35**, R189 (2002).

[15] M. Fejer, G. Magel, D. Jundt, & R. Byer, IEEE J. Quantum Electron. **28**, 2631 (1992).

[16] V. V. Pavlov, A. M. Kalashnikova, R. V. Pisarev, I. Sänger, D. R. Yakovlev, & M. Bayer, Phys. Rev. Lett. **94**, 157404 (2005).

[17] V. Venkataramanan, K. Noguchi, M. Aono, & T. Suzuki, Appl. Phys. B **74**, 683 (2002).

[18] D. D. Awschalom, D. Loss, & N. Samarth, *Semiconductor Spintronics and Quantum Computation* (Springer-Verlag, Berlin, 2002).

[19] D. Bouwmeester, A. Ekert, & A. Zeilinger, *The Physics of Quantum Information* (Springer-Verlag, Berlin, 2000).

[20] C. F. Klingshirn, *Semiconductor Optics* (Springer Verlag, Berlin, 2005).

[21] W. Schäfer & M. Wegener, *Semiconductor Optics and Transport Phenomena* (Springer-Verlag, Berlin, 2002).

[22] G. Landwehr & E. I. Rashba, *Landau Level Spectroscopy* (Elsevier Science, Amsterdam, 1991).

[23] H. P. Wagner, M. Kühnelt, W. Langbein, & M. Hvam, Phys. Rev. B **58**, 10494 (1998).

[24] S. Bergfeld & W. Daum, Phys. Rev. Lett. **90**, 036801 (2003).

[25] R. V. Pisarev, I. Sänger, G. A. Petrakovskii, & M. Fiebig, Phys. Rev. Lett. **93**, 37204 (2004).

[26] Y. Ogawa, H. Akinaga, F. Takano, T. Arima, & Y. Tokura, J. Phys. Soc. Japan **73**, 2389 (2004).

[27] J. L. P. Hughes & J. E. Sipe, Phys. Rev. B **53**, 10751 (1996).

[28] S. N. Rashkeev, W. R. L. Lambrecht, & B. Segall, Phys. Rev. B **57**, 3905 (1998).

[29] B. Adolph & F. Bechstedt, Phys. Rev. B **57**, 6519 (1998).

[30] C. Kittel, *Introduction to Solid State Physics* (Wiley, New York, 2005).

[31] J. K. Furdyna, J. Appl. Phys. **64**, R29 (1988).

[32] B. B. Krichevtsov, R. V. Pisarev, A. A. Rzhevsky, V. N. Gridnev, & H.-J. Weber, Phys. Rev. B **57**, 14611 (1998).

[33] L. Néel, Ann. Phys. Paris **18**, 5 (1932).

[34] H. Bizette, C. Squire, & B. Tsai, Comptes Rendus Acad. Sci. Paris **207**, 449 (1938).

[35] W. H. Meiklejohn & C. P. Bean, Phys. Rev. **105**, 904 (1957).

[36] A. V. Kimel, A. Kirilyuk, A. Tsvetkov, R. V. Pisarev, & T. Rasing, Nature **429**, 850 (2004).

[37] P. W. Anderson, *The Theory of Superconductivity in the High-TC Cuprate Superconductors* (Princeton University Press, Princeton, 1997).

[38] C. Tsang, R. E. Fontana, T. Lin, D. E. Heim, V. S. Speriosu, B. A. Gurney, & M. L. Williams, IEEE Trans. Mag. **30**, 3801 (1994).

[39] S. S. P. Parkin, K. P. Roche, M. G. Samant, P. M. Rice, R. B. Beyers, R. E. Scheuerlein, E. J. OSullivan, S. L. Brown, J. Bucchigano, D. W. Abraham, Y. Lu, M. Rooks, P. L. Trouilloud, R. A. Wanner, & W. J. Gallagher, J. Appl. Phys. **85**, 5828 (1999).

[40] N. P. Duong, T. Satoh, & M. Fiebig, Phys. Rev. Lett. **93**, 117402 (2004).

[41] R. Gómez-Abal, O. Ney, K. Satitkovitchai, & W. Hübner, Phys. Rev. Lett. **92**, 227402 (2004).

[42] V. V. Pavlov, A. M. Kalashnikova, R. V. Pisarev, I. Sänger, D. R. Yakovlev, & M. Bayer, SPIE Proceedings, in press (2006).

[43] I. Sänger, B. Kaminski, D. R. Yakovlev, M. Bayer, V. V. Pavlov, & R. V. Pisarev, In preparation (2006).

[44] I. Sänger, D. R. Yakovlev, M. Bayer, V. V. Pavlov, & R. V. Pisarev, Phys. Rev. Lett. **96**, 117211 (2006).

[45] V. V. Pavlov, A. M. Kalashnikova, R. V. Pisarev, I. Sänger, D. R. Yakovlev, & M. Bayer, J. Opt. Soc. Am. B **22**, 168 (2005).

[46] I. Sänger, B. Kaminski, D. R. Yakovlev, M. Bayer, V. V. Pavlov, & R. V. Pisarev, In preparation (2006).

[47] M. Fiebig, I. Sänger, & R. V. Pisarev, J. Appl. Phys. **93**, 6960 (2003).

[48] I. Sänger, R. V. Pisarev, G. A. Petrakovskii, & M. Fiebig, In preparation (2006).

[49] I. Sänger, R. V. Pisarev, V. V. Pavlov, & M. Fiebig, Submitted to Phys. Rev. B (2005).

[50] W. Heisenberg, Z. Physik **49**, 619 (1928).

[51] W. Nolting, *Grundkurs theoretische Physik*, vol. 6 — Statistische Physik (Vieweg, Braunschweig / Wiesbaden, 1997).

[52] A. Cracknell, *Magnetism in Crystalline Materials* (Pergamon, Oxford, 1975).

[53] I. Dzyaloshinskii, Sov. Phys. JETP **5**, 6 (1957).

[54] L. Néel, Ann. de Phys. **4**, 249 (1949).

[55] Y. Y. Li, Phys. Rev. **101**, 1450 (1956).

[56] S. Foner, Phys. Rev. **130**, 183 (1963).

[57] R. Griffiths, Phys. Rev. Lett. **24**, 1479 (1970).

[58] K. Wilson, Rev. Mod. Phys. **47**, 773 (1975).

[59] N. F. Kharchenko, J. Phys.: Condens. Mat. **10**, 4707 (1998).

[60] D. Lee, J. Joannopoulus, J. Negele, & D. Landau, Phys. Rev. Lett. **52**, 433 (1984).

[61] P. Weiss, J. Physique Rad. **6**, 661 (1907).

[62] L. Néel, Proceedings of International Conference in Theoretical Physics Kyoto (Science Council of Japan, Tokyo, 1953).

[63] H. Barkhausen, Z. Physik **20**, 401 (1919).

[64] K. Honda & S. Saya, Sci. Rept. Tohoku Imp. Univ. (1926).

[65] G. Slack, J. Appl. Phys. **31**, 1571 (1960).

[66] W. Roth, J. Appl. Phys. **31**, 2000 (1960).

[67] L. Landau & E. Lifschitz, *Lehrbuch der theoretischen Physik*, vol. VIII — Elektrodynamik der Kontinua (Akademie, Berlin, 1970).

[68] A. Hubert & R. Schfer, *Magnetic Domains* (Springer, Berlin, 2000).

[69] P. J. Brown, Physica B **192**, 14 (1993).

[70] M. Fiebig, D. Fröhlich, G. Sluyterman, & R. Pisarev, Appl. Phys. Lett. **66**, 2906 (1995).

[71] M. Fiebig, D. Fröhlich, & H. Thiele, Phys. Rev. B **54**, R12681 (1996).

[72] G. A. Petrakovskii, M. A. Popov, B. Roessli, & B. Ouladdiaf, J. Exp. Theor. Physics **93**, 809 (2001).

[73] M. Faraday, Phil. Trans. Roy. Soc. **136**, 1 (1846).

[74] J. Baruchel, Physica B **192**, 79 (1993).

[75] L. Dobrzynski & K. Blinowski, *Neutrons and Solid State Physics* (Ellis Horwood, London, 1994).

[76] H. Blank & S. Amelinckz, Appl. Phys. Lett. **2**, 140 (1963).

[77] S. Saito, J. Phys. Soc. Jpn. **17**, 1287 (1962).

[78] F. U. Hillebrecht, H. Ohldag, N. B. Weber, C. Bethke, U. Mick, M. Weiss, & J. Bahrdt, Phys. Rev. Lett. **86**, 3419 (2001).

[79] S. Leute, T. Lottermoser, & D. Fröhlich, Opt. Lett. **24**, 1520 (1999).

[80] M. Fiebig, *Nichtlineare Spektroskopie und Topografie an antiferromagnetischen Domänen*, Ph.D. thesis, Universität Dortmund (1996).

[81] T. Hahn, ed., *International Tables for X-Ray Crystallography, Vol. A: Space-Group Symmetry* (Reidel, Boston, 1987).

[82] A. Shubnikov & N. Belov, *Colored Symmetry* (Pergamon, Oxford, 1964).

[83] R. R. Birss, *Symmetry and Magnetism* (North-Holland, Amsterdam, 1966).

[84] G. Koster, J. Dimmock, J. Wheeler, & H. Statz, *Properties of the Thirty-Two Point Groups* (M.I.T. Press, Cambridge/Massachusetts, 1963).

[85] S. Joshua, *Symmetry Principles and Magnetic Symmetry in Solid State Physics* (Adam Hilger, New York, 1991).

[86] J. Nye, *Physical Properties of Crystals* (Oxford University Press, London, 1969).

[87] J.-M. Jancu, R. Scholz, F. Beltram, & F. Bassani, Phys. Rev. B **57**, 6493 (1998).

[88] Y. R. Lee & A. K. Ramdas, Phys. Rev. B **38**, 10600 (1998).

[89] Y. Tanabe & S. Sugano, J. Phys. Soc. Jpn. **9**, 753 (1954).

[90] D. Langer & S. Ibuki, Phys. Rev. **138**, A809 (1965).

[91] B. E. Larson & H. Ehrenreich, Phys. Rev. B **39**, 1747 (1989).

[92] B. E. Larson, K. C. Hass, H. Ehrenreich, & A. E. Carlsson, Phys. Rev. B **37**, 4137 (1988).

[93] B. E. Larson, K. C. Hass, & R. L. Aggarwal, Phys. Rev. B **33**, 1789 (1986).

[94] J. K. Furdyna & N. Samarth, J. Appl. Phys. **61**, 3526 (1987).

[95] S. Nagata, R. R. Galaka, D. P. Akbarzadeh, J. K. Furdyna, & P. H. Keesom, Phys. Rev. B **22**, 3331 (1980).

[96] W. Ossau & B. Kuhn-Heinrich, Physica B **184**, 422 (1993).

[97] J. A. Gaj, R. Planel, & G. Fishman, Solide State Commun. **29**, 435 (1979).

[98] D. R. Yakovlev, U. Zehnder, W. Ossau, A. Waag, G. Landwehr, T. Wojtowicz, G. Karczewski, & J. Kossut, J. Magn. Magn. Mater. **191**, 25 (1999).

[99] S. P. McAllister, J. K. Furdyna, & W. Giriat, Phys. Rev. B **29**, 1310 (1984).

[100] M. A. Novak, O. G. Symko, D. J. Zheng, & S. Oseroff, Phys. Rev. B **33**, 6391 (1986).

[101] D. R. Yakovlev, *Habilitation: Exciton Magnetic Polarons in Diluted Magnetic Semiconductor Heterostructures (in Russian)* (A. F. Ioffe Physico-Technical Insitute, St.Petersburg, Russia, 1998).

[102] D. D. Awschalom, J. M. Hong, L. L. Chang, & G. Grinstein, Phys. Rev. Lett. **59**, 1733 (1987).

[103] M. Sawicki, M. A. Brummell, P. A. J. de Groot, G. J. Tomka, D. E. Ashenford, & B. Lunn, J. Cryst. Growth **138**, 900 (1994).

[104] J. Pietruczanis, W. Marc, A. Twardowski, G. Karczewski, A. Zakrzewski, E. Janik, T. Wojtowicz, & J. Kossut, Material Science Forum **182**, 687 (1995).

[105] S. H. Liu, Phys. Rev. **121**, 451 (1961).

[106] J. K. Furdyna & J. Kossut, *Semiconductors and Semimetals* (Academic Press, Boston, 1998).

[107] A. K. Bhattacharjee, G. Fishman, & B. Coqblin, Physica **118**, 449 (1983).

[108] T. Maiman, Nature **187**, 493 (1960).

[109] A. Schawlow & C. Townes, Phys. Rev. **112**, 1940 (1958).

[110] J. D. Jackson, *Classical Electrodynamics* (John Wiley and Sons, New York, 1975).

[111] P. S. Pershan, Phys. Rev. **130**, 919 (1963).

[112] R. Loudon, *The Quantum Theory of Light* (Clarendon, Oxford, 1983).

[113] M. Fiebig, D. Fröhlich, T. Lottermoser, V. V. Pavlov, R. V. Pisarev, & H.-J. Weber, Phys. Rev. Lett. **87**, 137202 (2001).

[114] V. Muthukumar, R. Valent, & C. Gros, Phys. Rev. Lett. **75**, 2766 (1995).

[115] L. Landau & E. Lifschitz, *Lehrbuch der theoretischen Physik*, vol. I — Mechanik (Akademie, Berlin, 1970).

[116] F. Kneubühl & M. Sigrist, *Laser* (Teubner, Stuttgart, 1995).

[117] A. Yariv, *Optical Waves in Crystals* (John Wiley and Sons, Inc., New York, 1984).

[118] K. Kato, IEEE J. Quantum Electron. **22**, 1013 (1986).

[119] A. Fix, *Untersuchung der spektralen Eigenschaften von optischen parametrischen Oszillatoren aus dem optisch nichtlinearen Material Betabariumborat*, Ph.D. thesis, Universität Kaiserslautern (1995).

[120] T. Dekorsy, V. A. Yakovlev, W. Seidel, M. Helm, & F. Keilmann, Phys. Rev. Lett. **90**, 055508 (2003).

[121] Q. T. Vu, H. Haug, O. D. Mucke, T. Tritschler, M. Wegener, G. Khitrova, & H. M. Gibbs, Phys. Rev. Lett. **92**, 217403 (2004).

[122] A. Fiore, V. Berger, E. Rosencher, P. Bravetti, & J. Nagle, Nature **391**, 463 (1998).

[123] M.-Z. Huang & W. Y. Ching, Phys. Rev. B **47**, 9464 (1993).

[124] V. N. Gridney, V. V. Pavlov, & R. V. Pisarev, Phys. Rev. B **63**, 184407 (2001).

[125] S. V. Popov, Y. P. Svirko, & N. I. Zheludev, *Susceptibility Tensors for Nonlinear Optics* (Institute of Physics Publishers, Philadelphia, 1995).

[126] Y. V. Zhilyaev, N. K. Poletaev, V. M. Botnaryuk, T. A. Orlova, L. M.Fedorov, S. A. Yusupova, A. Owens, M. Bavdaz, A. Peacock, B. O'Meara, & H. Helava, Phys. Stat. Sol. (C) **0**, 1024 (2003).

[127] E. Palik, *Optical Constants of Solids* (Academic Press, New York, 1985).

[128] J. Jerphagnon & S. K. Kurtz, J. Appl. Phys. **41**, 1667 (1970).

[129] S. I. Gubarev, T. Ruf, M. Cardona, & K. Ploog, Phys. Rev. B **48**, 1647 (1993).

[130] R. P. Seisyan & B. P. Zakharchenya, *Landau Level Spectroscopy, Ch.7* (Elsevier Science, Amsterdam, 1991).

[131] L. D. Landau & E. M. Lifshitz, *Quantum Mechanics* (Pergamon Press, Oxford, 1977).

[132] Landolt-Börnstein, *Numerical Data and Functional Relationships, New Series, Group III, Vol.* **41 A1** (Springer, Berlin, 2001).

[133] J. C. Nash, *Compact numerical methods for computers* (Adam Hilger, Bristol, 1979).

[134] Landolt-Börnstein, *Numerical Data and Functional Relationships, New Series, Group III, Vol.* **41b** (Springer, Berlin, 1999).

[135] H. Ohno, J. Magn. Magn. Mater. **200**, 110 (1989).

[136] K. C. Ku, S. J. Potashnik, R. F. Wang, S. H. Chun, P. Schiffer, N. Samarth, M. J. Seong, A. Mascarenhas, E. Johnston-Halperin, R. C. Myers, A. C. Gossard, & D. D. Awschalom, Appl. Phys. Lett. **82**, 2302 (2003).

[137] J. A. Gaj, R. R. Gatazka, & M. Nawrocki, Solide State Commun. **25**, 193 (1978).

[138] V. V. Pavlov, R. V. Pisarev, A. Kirilyuk, & T. Rasing, Phys. Rev. Lett. **78**, 2004 (1997).

[139] Y. Ogawa, H. Akinaga, F. Takano, T. Arima1, & Y. Tokura, J. Phys. Soc. Japan **73**, 2389 (2004).

[140] C. Gourdon, V. Jeudy, M. Menant, D. Roditchev, L. A. Tu, E. L. Ivchenko, & G. Karczewski, Appl. Phys. Lett. **82**, 230 (2003).

[141] L. Kowalczyk, B. Koziarska-Glinka, L. V. Khoi, R. R. Gazka, & A. Suchocki, Opt. Mater. **14**, 161 (2000).

[142] A. Zappettini, S. M. Pietralunga, A. Milani, M. Martinelli, & A. Mycielski, Synthetic Metals **124**, 261 (2001).

[143] B. Kaminski, *Zweiphotonenspektroskopie an Halbleitern*, Master's thesis, Universität Dortmund (2006).

[144] G. Dolling, T. M. Holden, V. F. Sears, J. K. Furdyna, & W. Giriat, J. Appl. Phys. **53**, 7644 (1982).

[145] A. N. Bogdanov, U. K. Rößler, M. Wolf, & K. H. Müller, Phys. Rev. B **66**, 214410 (2002).

[146] B. Roessli, J. Schefer, G. A. Petrakovskii, B. Ouladdiaf, M. Boehm, U. Staub, A. Vorotinov, & L. Bezmaternikh, Phys. Rev. Lett. **86**, 1885 (2001).

[147] G. A. Petrakovskii, A. D. Balaev, & A. M. Vorotinov, Phys. Solid State **42**, 321 (1999).

[148] M. Boehm, S. Martynov, B. Roessli, G. Petrakovskii, & J. Kulda, Journ. Magn. Magn. Mater. **250**, 313 (2002).

[149] M. Fiebig, C. Degenhardt, & R. Pisarev, Phys. Rev. Lett. **88**, 027203 (2002).

[150] M. Martinez-Ripoli, S. Martinez-Carrera, & S. Garcia-Blanco, Acta. Cryst. B **27**, 677 (1971).

[151] H. Nakamura, Y. Fujii, H. Kikuchi, & H. H. Chiba, submitted (2005).

[152] A. I. Pankrats, G. A. Petrakovskii, M. A. Popov, K. A. Sablina, L. A. Prozorova, S. S. Sosin, G. Szimczak, R. Szimczak, & M. Baran, JETP Lett. **78**, 569 (2003).

[153] H. R. Christer, *Grundlagen der allgemeinen und anorganischen Chemie* (Verlag Sauerländer-Salle, Frankfurt a. M., 1969).

[154] G. A. Petrakovskii, K. A. Sablina, D. A. Velikanov, A. M. Vorotinov, N. V. Volkov, & A. F. Bovina, Crystallogr. Rep. **45**, 853 (2000).

[155] I. Sänger, *Zweiphotonenspektroskopie und -topographie an antiferromangetischem Nickeloxid und Kupferborat*, Master's thesis, Universität Dortmund (2002).

[156] T. C. Oakberg, SPIE Proceedings **2873**, 17 (1996).

[157] Y. Tokura, S. Koshihara, T. Arima, H. Takagi, S. Ishibashi, T. Ido, & S. Uchida, Phys. Rev. B **41**, 11657 (1990).

[158] M. Bassi, P. Camagni, R. Rolli, G. Samoggia, F. Parmigiani, G. Dhalenne, & A. Revcolevschi, Phys. Rev. B **54**, 11030 (1996).

[159] Y. Okimoto, Y. Tomioka, Y. Onose, Y. Otsuka, & Y. Tokura, Phys. Rev. B **57**, 9377 (1998).

[160] R. V. Pisarev, private communication (2005).

[161] G. F. Imbusch, Proceedings of the Seventh International Symposium on Physics and Chemistry of Luminescent Materials 1 (1998).

[162] J. Shefer, M. Boehm, B. Roessli, G. A. Petrakovskii, B. Ouladdiaf, & U. Staub, Appl. Phys. A **74**, 1740 (2002).

[163] J. Stöhr, T. Regan, S. Anders, J. Lüning, M. Scheinfein, H. Padmore, & R. White, Phys. Rev. Lett. **83**, 1862 (1999).

[164] H. Ohldag, T. J. Regan, J. Stöhr, A. Scholl, F. Nolting, J. Lüning, S. A. C. Stamm, & R. L. White, Phys. Rev. Lett. **87**, 247201 (2001).

[165] A. Barbier, C. Mocuta, W. Neubeck, M. Mulazzi, F. Yakhou, K. Chesnel, A. Sollier, C. Vettier, & F. de Bergevin, Phys. Rev. Lett. **93**, 257208 (2004).

[166] Z. Y. Liu, Appl. Phys. Lett. **85**, 4971 (2004).

[167] Z. Y. Liu & S. Adenwalla, Phys. Rev. B **67**, 184423 (2003).

[168] M. Fraune, U. Rüdiger, G. Güntherodt, S. Cardoso, & P. Freitas, Appl. Phys. Lett. **77**, 3815 (2000).

[169] G. Ju, A. V. Nurmikko, R. F. C. Farrow, R. F. Marks, M. J. Carey, & B. A. Gurney, Phys. Rev. Lett. **82**, 3705 (1999).

[170] N. D. Mathur, G. Burnell, S. P. Isaac, T. J. Jackson, B. S. Teo, J. L. MacManus-Driscoll, L. F. Cohen, J. E. Evetts, & M. G. Blamire, Nature **387**, 266 (1997).

[171] T. Satoh, N. P. Duong, & M. Fiebig, submitted (2005).

[172] P. Borisov, A. Hochstrat, X. Chen, W. Kleemann, , & C. Binek, Phys. Rev. Lett. **94**, 117203 (2005).

[173] H. Kondoh & T. Takeda, J. Phys. Soc. Jpn. **19**, 2041 (1964).

[174] S. Saito, M. Miura, & K. Kurosawa, J. Phys. C: Solid St. Phys. **13**, 1513 (1980).

[175] J. Baruchel, M. Schlenker, K. Kurosawa, & S. Saito, Phil. Mag. B **43**, 853 (1981).

[176] J. Baruchel, M. Schlenker, K. Kurosawa, & S. Saito, Phil. Mag. B **43**, 861 (1981).

[177] Landolt-Börnstein, *Numerical Data and Functional Relationships, New Series, III/17g* (Springer, Berlin, 1984).

[178] M. T. Hutchings & E. J. Samuelsen, Phys. Rev. B **6**, 3447 (1972).

[179] K. Nakahigashi, N. Fukuoka, & Y. Shimomura, J. Phys. Soc. Jpn. **38**, 1634 (1975).

[180] Y. R. Shen, *The Principles of Nonlinear Optics* (Wiley, New York, 1984).

[181] T. Satoh, T. Lottermoser, & M. Fiebig, Appl. Phys. B **79**, 701 (2004).

[182] K. Pedersen & O. Keller, J. Opt. Soc. Am. B **6**, 2412 (1989).

[183] T. Satoh, T. Lottermoser, & M. Fiebig, J. Magn. Magn. Mater., to be published (2006).

List of Figures

Index

Curriculum vitae

Personal details

Name: Ingo Sänger

Date of birth: 06.05.1977

Place of birth: Dortmund

Family status: married, one child

Education and qualifications

08.1983 - 07.1987 Basic primary school: Landgrafen-Grundschule, Dortmund

09.1987 - 06.1996 Grammar school: Mallinckrodt-Gymnasium, Dortmund

09.1996 - 09.1997 Alternative civilian service

10.1997 - 01.2003 Diploma course of studies: physics

                   Diploma thesis:

                   "Zweiphotonenspektroskopie und -topographie

                     an antiferromagnetischem Nickeloxid und Kupferborat"

                   Diploma thesis supervisor: Priv.-Doz. Dr. Manfred Fiebig

                   University of Dortmund

since 02.2003   Research associate at the chair of Prof. Dr. M. Bayer

                   Topic of the presented doctoral dissertation:

                   "Magnetic-field-induced second harmonic generation

                     in semiconductors and insulators"

                   Doctoral thesis supervisor: Priv.-Doz. Dr. D. R. Yakovlev

                   University of Dortmund

Acknowledgements

Finally, I would like to thank my parents Roswitha and Karl-Heinz Sänger for always encouraging me and for their support in all situations. My beloved wife Alexandra Sänger and my lovely daughter Lara Sänger have always encouraged me: